EFFECTS OF ELECTRON-ELECTRON, ELECTRON-PHONON AND SPIN-ORBIT INTERACTIONS IN LOW-DIMENSIONAL SYSTEMS

Kuntal Bhattacharyya



School of Physics University of Hyderabad Telangana- 500 046, Hyderabad, India

EFFECTS OF ELECTRON-ELECTRON, ELECTRON-PHONON AND SPIN-ORBIT INTERACTIONS IN LOW-DIMENSIONAL SYSTEMS

A thesis to be submitted in the partial fulfilment for the degree of

Doctor of Philosophy

in

Physics

by

Kuntal Bhattacharyya

(Registration number-16PHPH03)

under the supervision of

Prof. Ashok Chatterjee



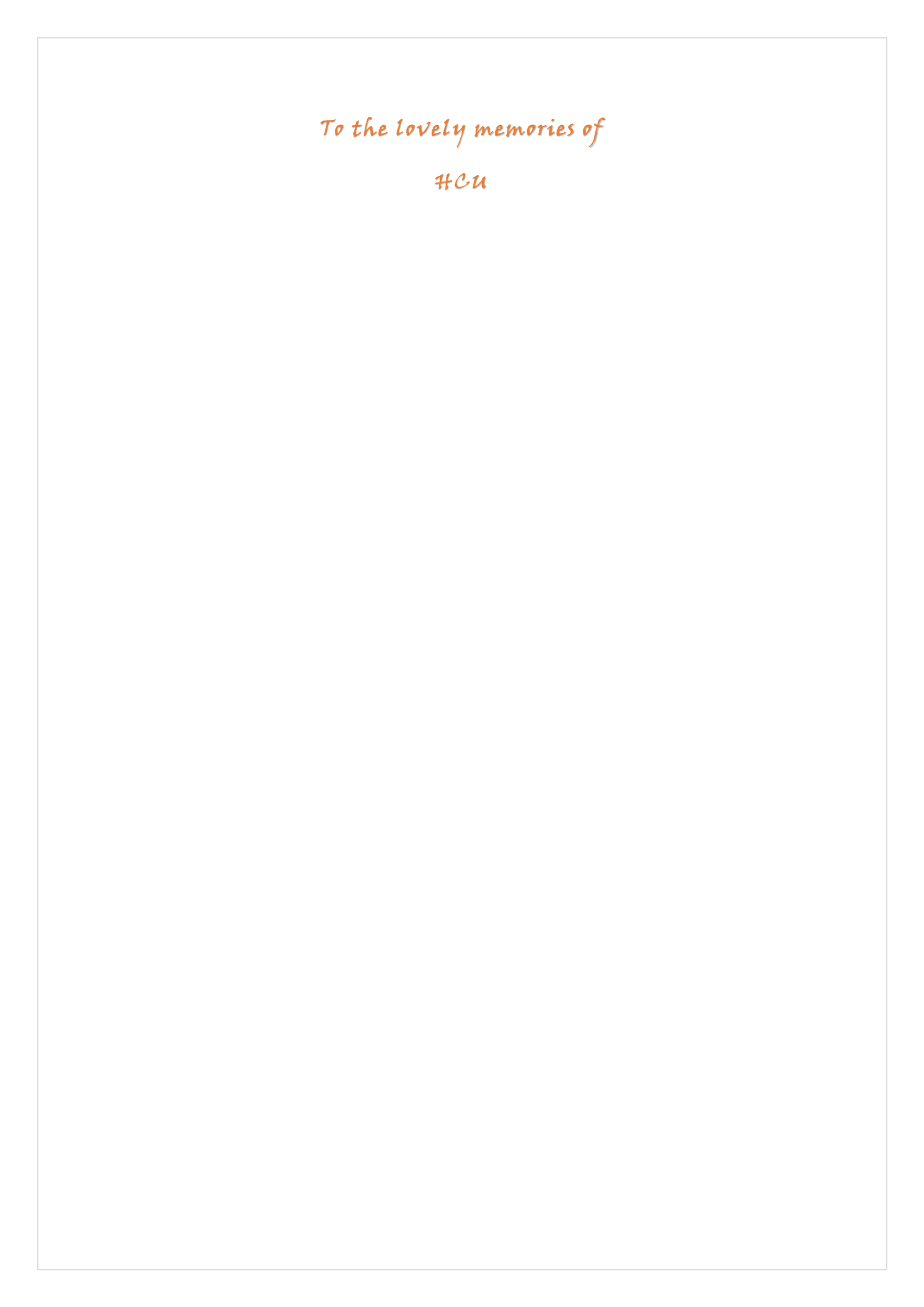


School of Physics

University of Hyderabad

Telangana- 500 046, Hyderabad, India

December 2022



DECLARATION





I, Kuntal Bhattacharyya, hereby declare that the work reported in this thesis entitled "Effects of electron-electron, electron-phonon and spin-orbit interactions in low-dimensional systems" has been carried out by me in the School of Physics, University of Hyderabad, India, under the supervision of Prof. Ashok Chatterjee as per the Ph.D. ordinances of the University. I declare, to the best of my knowledge, that no part of this thesis has been submitted previously for the award of a research degree or diploma at any other University or Institution. I also declare that the work is original and free from plagiarism. I therefore agree that my thesis can be deposited in Shodhganga/INFLIBNET.

A report on plagiarism statistics from the University librarian is enclosed.

Date: 28-12-2022

Place: School of Physics, University of Hyderabad.

Telangana-500 046, India.

Kuntal Bhattacharyya

Kanta Rhallishary

(Reg. No.-16PHPH03)

CERTIFICATE





This is to certify that the thesis entitled "Effects of electron-electron, electron-phonon and spin-orbit interactions in low-dimensional systems" is being submitted to the University of Hyderabad by Kuntal Bhattacharyya with registration id 16PHPH03, in partial fulfilment for the award of the degree of Doctor of Philosophy in Physics, is a record of bonafide work carried out by him under my supervision and is free of plagiarism.

This matter embodied in this report has not been submitted to any other University or Institution for the award of any degree or diploma.

Further, the student has the *following publications* in international peer reviewed journals and conference proceedings before the submission of the thesis for adjudication.

PAPERS/MANUSCRIPTS THAT ARE PART OF THE THESIS

- 1. *K. Bhattacharyya*, D. Debnath, and A. Chatterjee. *Role of Rashba spin-orbit interaction on polaron Zeeman effect in a two-dimensional quantum dot with parabolic confinement*. J. Magn. Magn Mater. **506**, 166745 (2020).
- 2. **K. Bhattacharyya**, M. Kalla, and A. Chatterjee. *Temperature dependent nonequilibrium magneto-transport in a correlated polar single molecular transistor with quantum dissipation*. J. Appl. Phys. **132**, 194303 (2022).
- 3. **K.** Bhattacharyya, M. Kalla, S. Sil, and A. Chatterjee. Spin-transport across a two-dimensional metal-semiconductor interface with infinite potential in presence of spin-orbit interactions: Double refraction and spin-filtering effect. (Accepted in 'Micro and Nanostructures', to appear)

- 4. **K.** Bhattacharyya, D. Debnath, and A. Chatterjee. Spin filtering by Rashba coupling in a correlated polar dissipative molecular transistor at finite temperature in a magnetic field. (Under review)
- 5. **K.** Bhattacharyya, P. J. Monisha, and A. Chatterjee. Persistent currents in a correlated mesoscopic Holstein-Hubbard ring in the presence of bulk inversion asymmetry. (To be communicated)

PAPERS/MANUSCRIPTS THAT ARE NOT INCLUDED IN THE THESIS

- 1. D. Debnath, *K. Bhattacharyya*, and A. Chatterjee. *A semi-exact study of self-trapping transition in a one-dimensional Holstein-Hubbard model*. Physica B Condens. Matter. **646**, 414357 (2022).
- 2. D. Debnath, *K. Bhattacharyya*, and A. Chatterjee. *A semi-exact analytical study of the phase diagram of a two-dimensional Extended Holstein-Hubbard model.* (*Under review*)
- 3. D. Debnath, *K. Bhattacharyya*, and A. Chatterjee. *Quantum transport in a bi-molecular transistor*. (*Manuscript under process*)
- 4. *K. Bhattacharyya*, S. Sil, and A. Chatterjee. *Persistent currents in a correlated Bernevig-Hughes-Zhang (BHZ) topological quantum ring.* (*Manuscript under process*)

LIST OF PAPERS IN CONFERENCE PROCEEDINGS

1. *K. Bhattacharyya*, M. Kalla, and A. Chatterjee. *Effect of finite temperature and external magnetic field on non-equilibrium transport in a single molecular transistor with quantum dissipation: Anderson-Holstein-Caldeira-Leggett model.* Materials Today: Proceedings 55, 1–3 (2022).

- 2. **K. Bhattacharyya**, M. Kalla, and A. Chatterjee. *Phonon mediated spin-filtering in a molecular junction-transistor at a non-zero temperature*. Materials Today: Proceedings **66**, 3250-3252 (2022).
- 3. **K.** Bhattacharyya and A. Chatterjee. Polaronic and bound polaronic effects in the energy states of an electron in a two-dimensional parabolic quantum dot in the presence of Rashba spin-orbit interaction. AIP Conference Proceedings 2142, 090008 (2019).

The student has attended the following *conferences and workshops*.

LIST OF CONFERENCES AND WORKSHOPS ATTENDED

September 18-22, 2022: <u>Poster Presentation</u>, entitled "Spin-filtering effect in a correlated single molecular spintronics- transistor: Anderson-Holstein-Caldeira-Leggett-Rashba model" in "Annual Conference on Quantum Condensed Matter (QMAT 2022)", at IIT Kanpur, India.

September 9-10, 2022: <u>Poster Presentation</u>, entitled "Spin-filtering effect in a correlated single molecular spintronics-transistor: Anderson-Holstein-Caldeira-Leggett-Rashba model" in "International Conference on Frontier Areas of Science and Technology (ICFAST 2022)", at University of Hyderabad, Telangana-500 046, India. (Received the best poster award)

December 15-19, 2021: <u>Poster Presentation (online)</u>, entitled "Dissipative Quantum Transport in Single Molecular at Finite Temperature and Magnetic Field: A Tuneable Spin-Filter" in "DAE SSPS 2021", at DAE Convention Centre, Anushaktinagar, Mumbai, India.

December 10-12, 2021: <u>Oral Presentation (online)</u>, entitled "Phonon mediated spin-filtering of a molecular-junction at a non-zero temperature" in "29th National (Virtual) Conference on Condensed Matter Days (CMDAYS21)", at Central University of jharkhaand, India. <u>Selected for publication</u> as <u>Conference Proceedings</u>, Materials today: Proceedings **66**, 3250-3252 (2022).

December 8-11, 2021: <u>Poster Presentation (online)</u>, entitled "Dissipative Quantum Transport in Single Molecular at Finite Temperature and Magnetic Field: A Tuneable Spin-Filter" in "QMAT 2021", at TIFR, Mumbai, India.

September 16-17, 2021: <u>Oral Presentation (online)</u>, entitled "Effect of finite temperature and external magnetic field on non-equilibrium transport in a single molecular transistor with quantum dissipation: Anderson-Holstein-Caldeira-Leggett model" in "9th National Conference on

Condensed Matter Physics and Applications (CMPA-2021)" at Dept. of Physics, Manipal Institute and Technology, India. <u>Selected for publication</u> as <u>Conference Proceedings</u>, Materials today: Proceedings **55**, 1-3 (2022).

February 5–6, 2021: <u>Oral Presentation (online)</u>, entitled "Effect of finite temperature and magnetic field on the quantum transport through a dissipative single molecular transistor in the presence of electron-electron and electron-phonon interaction" in "International Conference on Physical Sciences (ICPS-2021)" at SVNIT, Surat-395007, India. (<u>Received the best oral presentation award</u>)

February 7-9, 2019: <u>Poster Presentation</u>, entitled "Polaronic and Bound Polaronic Effects in The Energy States of an Electron in a Two-Dimensional Parabolic Quantum Dot in The Presence of Rashba Spin-Orbit Interaction" in "International Conference on Advanced and Basic sciences (ICABS-19)", at GDC Memorial College, Bahal, Haryana, India. <u>Selected for publication</u> as **Conference Proceedings** AIP Conference Proceedings **2142**, 090008 (2019).

July 16 – August 10, 2018: <u>Attended the workshop</u> on "Integrable systems in Mathematics, Condensed matter and Statistical Physics" hosted by international Centre for Theoretical Sciences (ICTS), Bengaluru, India.

October 2017: <u>Attended National Conference</u> on "Physics at Small Scale and Advanced Material" organized by School of Physics, University of Hyderabad, India.

The student has also worked as a *teaching assistant* in School of Physics for the following courses.

Course code	Title of the course	Taught by
PY455	Quantum Mechanics-II	Prof. M. Sivakumar
PY804	Advanced Condensed Matter Physics	Prof. A. Chatterjee
PY577	Quantum Theory of Solids	Prof. A. Chatterjee

The student has passed the following courses towards the fulfilment of *coursework* requirement for Ph.D.



School of Physics University of Hyderabad

PO: Central University Campus Gachibowli, Hyderabad-500 046, India Phones: (office) 040-23134300/4400 (Direct) 040-23012455 Email: deany qualityd.ac in

Prof. K.C. James Raju Professor & Dean



COURSE WORK CERTIFICATE

This is to certify that Mr. Kuntal Bhattacharyya bearing the enrollment No. 16PHPH03 has carried out the Ph.D. (Physics) research under the supervision of Prof. Ashok Chatterjee, in the School of Physics, University of Hyderabad, Hyderabad. He passed the following courses which are a pre-requisite for registration to Ph.D. Programme as per UGC norms.

So. No.	Course No.	Title of the Course	Credits
1.	PY801	Research Methodology	4
2.	PY802	Advanced Quantum Mechanics	4
3.	PY803	Advanced Experimental Techniques	4
4	PY804	Advanced Mathematical Methods	4

Dated: 21/11/2022

Dean

School of Physics DEAN

School of Physics University of Hyderabad HYDERABAD - 500 046

Dean

CDEAN

M. Thanashyam.

School of Physics School of Physics
University of Hyderabad
HYDERABAD - 500 046

Date: 28-12-2022

Place: School of Physics, University of Hyderabad

Prof. Ashok Chatterjee

(Thesis Supervisor)

Prof. ASKOK CHATTERJEE SCHOOL OF PHYSICS UNIVERSITY OF HYDERABAD HYDERABAD - 500 044 INDI-

ACKNOWLEDGEMENTS

As my PhD journey has come to an end, I am reminded of the people whose direct or indirect involvement over all these years made my job much easier, more exciting and memorable. I would like to take this opportunity to express my heartfelt thanks to all those who have been supportive all these years. At the same time, I express my sincere apologies to those I missed acknowledging.

First of all, I would like to give my warmest thanks to my supervisor *Prof. Ashok Chatterjee* for giving me the opportunity to pursue my research under his supervision. From day one, he has given me the confidence and a sense of comfort that made me feel I was in the right place. His passion and understanding towards Physics and life beyond Physics really motivated me. I am grateful to him for introducing me to this beautiful field of Condensed Matter Physics. I consider him the finest teacher I had in my life. He has provided me with freedom in every respect, which put me in the right frame of mind to carry out my research work. I learnt a lot about the subject both from his classroom teaching and the endless discussions that we had during our "tea time". Those discussions encouraged me every time, and I felt confident. His guidance, like a father, always helped me think better in so many different ways. I will be indebted to him forever. I also want to express my deepest gratitude to him for being concerned about things that are not so academic, which to my thinking, makes him the rarest. He provided that space where we could share anything related to things starting from the not-so-happy ones like family issues, health issues, financial needs etc. to the most joyful ones like sports, music, poetry, shayaries, palm reading, cracking jokes, sharing childhood memories, even politics sometimes and what not. Those moments I enjoyed every time which gave me refreshments and mental stability, and that brings me to the next person whom I want to acknowledge, our beloved Ma'am Dr. Soma Mukhopadhyay. I can't thank her enough for her genuine affection, care and support towards my research and other things over all these years. Particularly, I would like to give her special thanks for spending some wonderful times together with Sir and other group mates during festivals and special occasions. She always provided a homely atmosphere which made all of us very comfortable. I must mention that I enjoyed some of the best foods there, homemade or otherwise. Those are the moments I will never forget. I would also like to thank Abhinava for sometimes joining us and adding a different taste to it. I had a great time with them, and I will cherish it forever!

I would like to sincerely thank my doctoral committee members, *Prof. S. Srinath* and *Prof. S.V.S Nageswara Rao*, for their valuable comments, questions and suggestions which helped

me improve my understanding of the subject. I want to extend my sense of gratitude to the non-academic staff of the School of Physics (SoP) for taking care of the official procedures and to our present Dean, Prof. K.C. James Raju and all the former Deans for providing the facilities and assistance to carry out my research activities. I am thankful to my group members Zahid Malik, Manasa Kalla, Dr. Hemant Kumar Sharma, Pooja Saini and Debika Debnath for their fruitful discussions and support. I am very much delighted to give a special thanks to my senior P.J. Monisha for her enormous help, constructive suggestions and good wishes. You are a fantastic person to work with. I wish I could have had your assistance and guidance in person during my PhD.

Thank you, Jaydev, my junior from the mathematics department, for teaching me the technicalities of MATLAB and helping me with your valuable insights while writing some of the codes. I wish to acknowledge my seniors of SoP, Dr. Shiva Rama Krishna S and Dr. Sujay, for their help and suggestions. I sincerely want to express my gratitude to Dr. Ashoka S Vudayagiri of SoP for giving me his valuable time to check the plagiarism of my papers and the thesis. It is my genuine pleasure to thank Madhvi Ma'am of the UoH admin section for her kind support and commitment in dealing with the fellowship issues, especially during Covid times. A special credit goes to our health centre staff, doctors, guest house staff and officials for their undisputed caring, support and advice during my Covid days. Thank you, Kittu Bhai, for getting me the paper bindings, prints, xerox etc., wherever I needed them. You were just a phone call away, and I didn't have to think of any other option to get them done, which undoubtedly saved a lot of time. I had a good time with our night-canteen man Sanjay Bhaiya. We used to chat about the HCU campus life, its past stories, current incidents and many other things while having his special 'egg noodles' and 'bread poach'. I will miss them. I admire you for the warmth you bring in every time and get us some delicious food in the middle of the night. Thank you for your company. On the same note, I thank Mujaid Bhai as well.

I want to express my deepest gratitude and regards to my M.Sc. teachers *Dr. Arunabha Adhikari*, *Dr. Bibhas Bhattacharyya*, *Dr. Molly De Raychaudhury*, *Dr. Subhajit Sarkar*, *Dr. Sunandan Gangopadhyay*, *Dr. Jaydip Mitra* and *Dr. Anirban Saha* for teaching me the basic and advanced courses during M.Sc. Their excellent teaching, guidance and motivation made me feel interested in going for research as a future option. I am indeed grateful to them for their love and support. Here I want to mention my Maths teacher during the old school days, *Dr. Srimanta Sinha Roy*. His teaching and motivations left an impact on me to choose a mainstream science subject like Physics as a major subject at the undergraduate level.

Friends are an integral part of life. It is my utmost delight to thank some of my friends who stood by me in good and bad times. I am eternally grateful to *Apurba*, *Arijit*, *Bappa*, *Tasnim*

and *Debika* for some of the greatest moments of the campus life that you all shared with me. To mention a few, cooking, jungle safari, rock climbing and our much-celebrated Saraswati puja are the ones I will never forget. Apart from these, we spent some lovely time discussing sports, music, musical instruments, movies, literature, childhood memories, socio-political issues, personal ups and downs, science and many more. Your associations made me a better and more mature person. We grew up together. Thank you for all the lovely memories; I will cherish each of those forever! Special thanks to *Apurba*, one of my old friends since my school days, for being there like a true friend. I can't repay you back for what you have done for me! Thank you, *Anik*, your presence and friendship since my college days have enriched me in many ways. Thank you for all your love, warmth, guidance and moral support.

I also want to thank my fellow scholar friends and juniors, *Saddam, Soutrick, Subham, Suman, Somnath, Golu, Pabitra, Sourav, Sayantan, Olivia, Soumen, Abhisek, Panja, Sovan, Nurul, Anupam, Jaydev, Alamgir, Mainak, Arunava, Kailash, Munna, Bihari Ji and my seniors Sugata da, Navendu da, Sudipta da and Suman da for all your love, support, guidance and also some funny and cheerful moments that we spent together. Thank you all for making my hostel and campus life exciting.*

I sincerely acknowledge the Department of Science and Technology (DST), India for providing financial support with the DST-INSPIRE fellowship for JRF and SRF.

Finally, I express my love and gratitude to *my parents*, my sister *Kuntalika* and my brother *Alapon* for standing by my side and being incredibly supportive throughout my life. Any 'thank you' will be too little for them!

Kuntal Bhattacharyya

LIST OF ABBREVIATIONS

LDS Low-dimensional systems

BOA Born-Oppenheimer approximation

e-e Electron-electron

e-p Electron-phonon

SO Spin-orbit

HM Hubbard model

MIT Metal-insulator transition

1D One-dimensional

2D Two-dimensional

3D Three-dimensional

ND N-dimensional

GS Ground state

ES Excited state

BA Bethe ansatz

SDW Spin density wave

CDW Charge-density wave

A-B Aharonov-Bohm

PC Persistent current

PCC Persistent charge current

PSC Persistent spin current

QD Quantum dot

QW Quantum well

QR Quantum ring

SMT Single molecular transistor

SET Single electron transistor

FET Field effect transistor

DOS Density of state

FM Fröhlich model

RSPT Raleigh-Schrödinger perturbation theory

LLP Lee, Low and Pines

LLPH Lee-Low-Pines-Huybrechts

ZS Zeeman splitting

RZ Rashba-Zeeman

TBM Tight-binding model

LFT Lang-Firsov transformation

HHM Holstein-Hubbard model

H-H Holstein-Hubbard

2DEG Two-dimensional electron gas

SE Schrödinger equation

FU Feynman units

SOI Spin-orbit interaction

TRS Time-reversal symmetry

SIS Spatial-inversion symmetry

SIA Structural inversion asymmetry

BIA Bulk inversion asymmetry

DSOI Dresselhaus SOI

RSOI Rashba SOI

KE Kinetic energy

PE Potential energy

NN Nearest neighbour

TB Tight-binding

PBC Periodic boundary condition

PPF Peierls phase factor

PP Peierls phase

AHCL Anderson-Holstein-Caldeira-Leggett

PQD Parabolic QD

LO Longitudinal optical

ZS Zeeman splitting

RZ Rashba-Zeeman

HF Hartree-Fock

MFA Mean-field approximation

MF Mean-field

RBZ Reduced Brillouin zone

SF Spectral function

NEGF Non-equilibrium Green function

RC Raju and Chatterjee

C-L Caldeira-Leggett

RSO Rashba SO

LIST OF PAPERS BASED ON WHICH THE THESIS HAS BEEN WRITTEN

- 1. *K. Bhattacharyya*, D. Debnath, and A. Chatterjee. *Role of Rashba spin-orbit interaction on polaron Zeeman effect in a two-dimensional quantum dot with parabolic confinement*. J. Magn. Magn Mater. **506**, 166745 (2020). [Chapter 2 is written based on this paper]
- 2. **K. Bhattacharyya**, M. Kalla, S. Sil, and A. Chatterjee. Spin-transport across a two-dimensional metal-semiconductor interface with infinite potential in presence of spin-orbit interactions: Double refraction and spin-filtering effect. (Accepted in 'Micro and Nanostructures', to appear)

[Chapter 3 is written based on this paper]

- 3. **K.** Bhattacharyya, P. J. Monisha, and A. Chatterjee. Persistent currents in a correlated mesoscopic Holstein-Hubbard ring in the presence of bulk inversion asymmetry. (To be communicated).

 [Chapter 4 is written based on this paper]
- 4. *K. Bhattacharyya*, M. Kalla, and A. Chatterjee. *Temperature dependent nonequilibrium magneto-transport in a correlated polar single molecular transistor with quantum dissipation*. J. Appl. Phys. **132**, 194303 (2022). [Chapter 5 is written based on this paper]
- 5. **K.** Bhattacharyya, D. Debnath, and A. Chatterjee. Spin filtering by Rashba coupling in a correlated polar dissipative molecular transistor at finite temperature in a magnetic field. (Under review).

[Chapter 6 is written based on this paper]

PREFACE

The present thesis embodies our work on the role of electron-phonon (e-p), electron-electron (e-e) and spin-orbit (SO) interactions in low-dimensional systems (LDS). In LDS, e.g., quantum dot (QD), quantum well (QW), and quantum ring (QR), the electron is confined to one or more dimensions and as a result, the system shows discrete electronic energy levels. The shape and size of the confining potential give rise to different electronic properties. In a QD system, the commonly used harmonic (parabolic) oscillator potential is considered to be the simplest confining potential to start with. However, people have also considered more physical potentials with different shapes, such as a Gaussian potential. The size of a QD is of the order of nanometres which can contain one to many atoms.

The electrons in confined systems can interact with themselves and also with the lattice giving rise to e-e and e-p interactions which can influence the electronic properties in LDS. In a polar crystal, an extra electron in the conduction band interacts with the vibrating lattice (phonons) leading to a distortion in the lattice. This distortion causes a polarization potential in which the electron may get trapped. The electron together with the distortion behaves like a quasi-particle which is commonly known as a polaron. If the electron is slow, then the potential will be shallow and the distortion can spread over many lattice points and as a result a large polaron is produced. The polaron of this type is known as Fröhlich polaron and its properties are studied in the continuum model. Since impurity is a rule rather than an exception for a real physical system, one may also consider a simple hydrogenic impurity in a polar QD. In such a case, the electron of the hydrogenic impurity interacts with both the impurity ion and the lattice and the resulting polaron is called a bound polaron.

The study of polaron becomes important in the presence of an external magnetic field. An external magnetic field causes Zeeman splitting in a parabolic QD. It has been seen in the context of a magnetopolaron confined in a two-dimensional QD that the Zeeman splitting is suppressed and the suppression becomes strongly size dependent when the size of the QD is reduced to a few nanometres. Another important interaction which lies at the heart of spintronics applications is the spin-orbit (SO) interaction (SOI) through which the spin of the electron can be manipulated. The very first spintronic device was proposed in the context of a spin field-effect transistor by Datta and Das. During the fabrication of a QD, an asymmetric potential is formed at the interface of a QW heterostructure which can be tuned by an externally applied gate voltage. Due to this structural inversion asymmetry (SIA), an electric field is produced by which an effective magnetic field is generated in the electron's rest frame. This effective magnetic field couples to the spin of the electron giving rise to SOI. The

spins can precess around the effective SO magnetic field with a frequency. This type of SOI originating from SIA is known as the Rashba SOI (RSOI), whose strength can be tuned by the external gate voltage. Interestingly, there exist some crystals which lack inversion symmetry in the bulk and the SOI produced by this bulk inversion asymmetry (BIA) is known as Dresselhaus SOI (DSOI). The SOI can lead to additional spin-splitting of the electronic energy levels which is different from the usual Zeeman splitting that occurs due to an external magnetic field. Therefore, it is intriguing to study the interplay of SOI and polaronic interaction in the context of the Zeeman splitting of a magnetopolaron in a QD.

It is well known that in a mesoscopic QR system where an array of atoms is designed in the form of a ring, a magnetic flux of Aharonov-Bohm (A-B) type gives rise to a persistent current (PC) that flows through the entire ring caused by the quantum interference effect of the electronic wavefunctions. People have studied several interesting mesoscopic effects in the presence of interactions in this kind of low-dimensional system. The tunneling junction devices such as a single molecular transistor (SMT), which resembles a metal-QD-metal structure, show potential applications in the field of charge and spin transport. In such systems, especially in a single-electron transport, the e-e interaction in the central QD plays a vital role which leads to some exciting phenomena like the Coulomb blockade and the Kondo effec. Also, in recent times, many important studies have been witnessed in this area where people have studied strongly correlated transport properties in the presence of e-p and SO interactions in the SMT systems.

The thesis is organized as follows.

In **Chapter 1** of the thesis, we present the motivations behind the work and introduce the continuum and discrete models used in this thesis and the basic formulations of the interactions mentioned above. In the continuum model, we describe the Fröhlich polaron, bound polaron and magnetopolaron and also Rashba and Dresselhaus SOIs. In the discrete model, we present the Hubbard and Holstein models for a narrow-band system. Next, we discuss how PC can be generated in a QR. We introduce the Hamiltonians for RSOI and DSOI in a QR. Finally, we present the model Hamiltonian for an SMT system and discuss the different processes involved in this system.

In **Chapter 2**, we investigate the role of RSO interaction on the polaron Zeeman effect in a two-dimensional parabolic QD. We formulate the system Hamiltonian using the well-known Fröhlich model and calculate the polaronic corrections to the energy states of the QD by employing an all-coupling Lee-Low-Pines-Huybrechts variational method and the second-order Raleigh-Schrödinger perturbation theory. We also study the interplay between e-p and RSO interactions in the context of RSOI-induced Zeeman splitting.

Chapter 3 of the thesis describes the combined effect of both the SOIs on the spin-transport across a metal-semiconductor interface in the presence of a delta-function scatterer at the interface. The tunnelling current, conductance and spin-polarization are calculated using appropriate boundary conditions and the effects of RSOI and DSOI on the reflected and refracted spin-resolved currents and spin polarizations are studied.

In **Chapter 4**, we study the effect of DSOI on the persistent charge and spin currents in a one-dimensional mesoscopic QR threaded by an A-B flux in the presence of e-e and e-p interactions. In such a narrow-band system, we have a small polaron which is best described by the Holstein model and the e-e interactions can be treated by the Hubbard model. We therefore use the Holstein-Hubbard-Dresselhaus model to study the system. After decoupling the e-p interaction by the much-celebrated Lang-Firsov transformation and eliminating the DSOI by a unitary transformation, we treat the Hubbard correlation at the Hartree-Fock mean-field level and finally obtain the energy and current using a self-consistent numerical diagonalization method. The effects of temperature and chemical potential on charge and spin currents have also been investigated.

In Chapter 5, we consider a three-terminal device configured as a metal-QD-metal structure placed on an insulating substrate and investigate finite-temperature nonequilibrium quantum magneto-transport in the presence of local e-p and onsite Hubbard interactions and quantum dissipation. The interaction between substrate phonons and the local QD phonon has been incorporated by the linear Caldeira-Leggett model. This interaction is partially eliminated by a unitary transformation which produces a dissipative effect in the phonon frequency which in turn influences the tunnelling current. The e-p interaction is dealt with the Lang-Firsov transformation. The transport properties such as spectral function, tunnelling current, conductance and spin-polarization are finally calculated using the nonequilibrium Keldysh Green function technique. We study the contrasting effects of temperature and magnetic field on the transport properties mentioned above.

In **Chapter 6**, we study the RSOI-induced quantum transport through a QD embedded in a two-arm quantum loop of a single molecular transistor at finite temperature in the presence of e-p and Hubbard interactions, an external magnetic field and quantum dissipation. The electrons from the source can tunnel to the drain following two paths, one through the arm of the loop that contains the QD and the other through the other arm of the loop that does not contain any QD. Our study focuses on how the Rashba coupling alone causes a zero-field spin-splitting in the spin-up and spin-down currents in an SMT system. We have also studied the combined effects of polaronic and SO interactions on the transport properties in different regimes of temperature and field. The effect of e-e interaction on spin-resolved conductances has also been studied. In this study, we have also analyzed the condition required to achieve

the maximum spin-polarization for a particular strength of the RSOI and magnetic field at zero temperature in the SMT system.

Our results may find important applications in the fabrication of efficient spin-filtering devices in which the spin-filtering can be tuned by controlling the external magnetic field, RSOI and the e-p interaction in different temperature regimes.

Finally, in **Chapter 7**, we summarize and conclude our findings.

Kuntal Bhattacharyya

CONTENTS

Declaration Certificate Acknowled List of abb List of pap Preface	ii Igements vii
	Introduction
Chapter 1	1.1 Motivations so far
	Role of Rashba spin-orbit interaction on polaron Zeeman effect in a two-dimensional quantum dot with parabolic confinement
Chapter 2	Abstract

Spin-transport across a two-dimensional metalsemiconductor interface with infinite potential in presence of spin-orbit interactions: Double refraction and spin-filtering effect

	Abstract	68
C6t	3.1 Introduction	69 70
Chapter 3	3.2 Analytical model and formulation	70 76
		90
	3.4 Conclusions References	92
	txejerences	72
	Persistent currents in a correlated mesoscopic	
	Holstein-Hubbard ring in the presence of bulk	
	inversion asymmetry	
	Abstract	94
	4.1 Introduction	95
	4.2 Analytical model and formulation	96
	4.3 Numerical results and discussions	102
Chapter 4	4.3.1 Results for persistent charge current	102
	4.3.2 Results for persistent spin current	108
	4.4 Conclusions	113
	References	114
	Temperature dependent nonequilibrium magneto-	
	transport in a correlated polar single molecular	
	transistor with quantum dissipation	
	Abstract	116
	5.1 Introduction	117
_	5.2 Analytical model and formulation	118
Chapter 5	5.2.1 The Keldysh formalism: Spectral function, tunnelling current and	122
	differential conductance	
	5.3 Numerical results and discussions	128
	5.4 Conclusions	146
	References	147
	Spin-filtering by Rashba coupling in a correlated	
	polar dissipative molecular transistor at finite	
	temperature in a magnetic field	
	J	
	Abstract	150
Chapter 6	6.1 Introduction	151
2.005 001 0	6.2 Analytical model and formulation	152

	6.2.1 Rashba induced spin-polarized tunnelling via Keldysh method 6.3 Numerical results and discussions	157 159 174 175
Chapter 7	Summary and conclusions	178

CHAPTER 1

Introduction

The study of modern condensed matter physics provides a suitable ground to investigate the electronic and transport properties of quantum materials, both theoretically and experimentally. It explores fundamental properties of matter which originate from the interactions between atoms and electrons. The exciting phenomena in condensed matter physics emerge from the non-trivial quantum mechanical interactions and the interplay between them. At one side it deals with the active research areas like strongly correlated phenomena, phase transitions and critical phenomena, on the other side, it triggers technological inventions which revolutionize modern civilization.

1.1 MOTIVATIONS SO FAR

A solid containing ions and electrons is a crystalline condensed system where the electrons can interact with themselves as well as with the ions. The dynamics of an electron is very much modified by these interactions. However, the Born-Oppenheimer approximation (BOA) allows the ions to be approximated in many cases as static as they are much heavier than the electrons. Usually, the interactions such as electron-electron (e-e) and electron-phonon (e-p) interactions can influence many interesting physics in condensed matter systems, e.g., quantum phase transitions, high-temperature (T_c) superconductivity, quantum Hall effects and many other phenomena. In the last few decades, investigations on low-dimensional systems (LDS) have opened up many intriguing research areas. In LDS, the charge carriers are confined to a length scale which is lower than the de Broglie wavelengths of the carriers [1, 2]. Low-dimensional semiconducting materials such as two-dimensional (2D) quantum wells (QWs), one-dimensional (1D) quantum wires, quantum ring (QR) and zero-dimensional (0D) quantum dots (QDs) and also their hybrid structures have potential applications in electronic, optoelectronic and flexible devices like field effect transistors, photodiodes, photodetectors, high performance data storage devices etc. On the other hand, spintronics physics have become an emergent phenomenon which requires the spin manipulation mechanisms driven by the spin-orbit (SO) interaction (SOI) [3, 4]. Due to the development of

modern fabrication technique, it is possible to fabricate spintronics devices like magnetic storage devices, computer nano chips, memory devices, magneto-resistive devices, magnetic tunnel junction devices, spin valve etc. The spin Hall effect where an electrical current induces a transverse spin current due to the SOI may also open up new functionalities in spin-torque switching devices. In this thesis, we mainly present our work on the semiconductor LDS. To see how efficient the semiconductor nanodevices are, we must take the interactions experienced by the carrier with the surroundings into account.

It is important to consider e-e interactions in strongly correlated systems for the understanding of electronic and magnetic properties like metal-insulator transition (MIT), band magnetism, half-metallic behaviour, heavy fermions, high- T_c superconductivity, spincharge separation etc. In a many-body interacting system, the free-electron model does not provide sufficient information to describe the aforementioned properties. The most successful model for this purpose has been the *Hubbard model* (HM) [5] named after John Hubbard. This model introduces an onsite Coulomb energy term U to the usual tight-binding Hamiltonian. It can produce both a metallic state and an insulating state depending on the strength of U. The HM has been applied to describe the behaviour of transition metal oxides, high- T_c cuprates, spin density wave (SDW), p/d-wave superconductor, topological phase transitions, spin-liquid and many other ground-breaking phenomena [6]. Another interesting area where e-e interactions in LDS (such as in QDs) [7-14] have led to many exciting properties is qubits, though, designing qubits including e-e interactions has its own challenges, for they are very delicate to control. Silicon (Si) is a good host material to form QD-qubits because of their long coherence time. For this reason, Si-QDs can be potentially applied to quantum computation. Due to their long spin lifetimes and coherent spin control, they have shown promising aspects in spin-based qubits which can operate even at moderately high temperature (> 100 mK) [13, 15, 16]. Although, most of the time, the effect of long range e-e interactions has not been emphasized in the gate-controlled QD systems, they can play an important role in spin-qubits operation. The Kondo effect [17-22] and Coulomb blockade [23, 24] are two other important aspects in tunnel junction molecular devices such as single molecular transistor (SMT), single electron transistor (SET), spin field effect transistor (FET) etc. Coulomb blockade refers to a mesoscopic phenomenon where the electrical conductance gets reduced due to the Coulomb repulsion between the electrons confined in a mesoscopic device. It can be observed in any tunnel junction device where the electrons coming from a source (metallic or superconducting) enter into a QD and then go to the drain. The flow of the electrons is governed by a bias voltage. If the size of the device is very small (size of a few atoms), then electrons in the QD experience a strong Coulomb repulsion which prevents further flow of the electrons from the source. As a result,

conductance decreases and current-voltage characteristic does not remain Ohmic, rather it shows a staircase like pattern which signifies electric charge quantization. It can be used as single electron charging in an SET system. Interestingly, under the application of a magnetic field, it provides a suitable ground to study spin blockade [25] and valley blockade [26]. Another important phenomenon in low-temperature many-body physics is the Kondo effect. Although it was theoretically explained more than fifty years ago [27] by Jun Kondo who used higher order perturbation technique in describing the minimum of the resistivity vs temperature curve of dilute magnetic alloys, it remains one of the crucial phenomena to be looked into in molecular junction devices. In the context of low temperature electron transport, it describes a spin-spin exchange interaction between the conduction band (s-band) electrons and the localized magnetic impurity (d-band electrons), commonly known as s-d exchange interaction. When the coupling between leads and QD in an SMT system increases, higher order tunnelling processes also occur where below a certain temperature the s-d electron scattering between the conduction electrons of the metallic leads and localized spin of the impurity becomes important. This temperature is usually known as Kondo temperature T_K . These exchange processes cause spin-flip of the impurity state. An impurity containing a single electron-energy level with a specific spin orientation (either up or down spin state) prevents further accumulation of electrons tunnelling from the metallic lead due to Coulomb repulsion U. But the electron with a particular spin state in the localized impurity energy level can tunnel quantum mechanically and go to a virtual energy level outside the impurity creating an empty space for the metallic electrons with opposite spin state to enter and fill the localized level. It is important to mention that the impurity coexists with the conduction electrons of the leads acting like a Fermi-sea with all the states occupied below the Fermi energy. Hence, when a few such spin-slip excitations take place, a resonance (Kondo resonance) peak appears in the density of state (DOS) with the energy close to the Fermienergy which also reflects in the conductance spectrum. As a result of these s-d scattering processes, the resistivity increases when the leads are cooled below T_K . For a very small mesoscopic device, both the Coulomb blockade and the Kondo resonance become crucial. The Hubbard type of e-e interaction also produces a resistive effect in strongly correlated mesoscopic transport systems like a QR structure [28, 29]. Therefore, e-e interaction is an essential interaction to be taken into account in the study of LDS. Attempts have indeed been made along this direction, but a lot of scope still exists for a better understanding the e-e interaction in LDS. In this thesis, we have studied the e-e interaction both in mesoscopic QR structure and tunnel junction systems.

The e-p interaction is another key element which helps understand many fundamental phenomena in condensed matter systems. Mobile electrons get scattered by the vibrating lattice i.e., the phonon modes. Apart from the e-e interaction, it is another scattering process which produces resistivity in the system. In an ionic or polar crystal, an extra electron attracts the positive ion and repels the negative ions, thereby a distortion in the crystal structure of the lattice is created in the vicinity of the electron. This distortion gives rise to polarization in the lattice. As a consequence of this interaction between a fermionic-charged particle and a bosonic field, a change in the effective mass of the electron occurs. This electron along with the lattice distortion can be treated as a quasi-particle which is known as *polaron* [30-32]. If the interaction is weak, the distortion spreads over a few lattice sites, and resulting polaron is called a large polaron. On the other hand, if the interaction is strong enough, the distortion gets confined within one or two lattice sites. In other words, the electron may get trapped in the confining potential well developed in the lattice. We call it a small polaron. The idea of polaron was first conceived by Landau a long time ago [33]. Later, Landau and Pekar [34] proposed a semi-classical model to study the behaviour of an electron moving in the conduction band of an ionic crystal. But the fully quantum mechanical model was introduced by Fröhlich [35], who proposed a model Hamiltonian, known as the Fröhlich model (FM) which describes the motion of a slow or low-lying electron in a polar or ionic lattice. Under the framework of the FM, the lattice can be considered as a continuum as in this limit, the de Broglie wavelength of the electron is much larger than the lattice spacing. Consequently, the polaron can move throughout the lattice in this limit. Therefore, the Fröhlich-polaron is known as a continuum polaron. In the case of strong e-p interaction, the FM is not the obvious choice as the structure of the lattice is ignored in this model. The strong coupling theory deals with the localization of the polaron where the electron gets trapped in the potential well produced due to strong distortion of the static lattice. In this limit, the motion of the lattice is much faster than that of the electron. So, in the reference frame of the electron, the ionic motion is adiabatic. Fröhlich obtained the Landau-Pekar solution from his Hamiltonian using the variational method. Afterwards, attempts have been made to find an all-coupling theory which encompasses the entire range of the e-p coupling. Among them, Lee-Low-Pines-Huybrechts (LLPH) [36, 37] method has drawn significant attention. This method is a modified version of the LLP method. In this dissertation, we will restrict ourselves to the polaron problem in a confined geometry. From the experimental point of view, it is important to study polaronic cyclotron mass in the presence of an external magnetic field. Mukhopadhyay et al. [38, 39] studied the magneto-polaron problem using the second-order Raleigh-Schrödinger perturbation theory (RSPT) and all-coupling non-diagonal Green's function method and showed that e-p interaction suppresses Zeeman splitting quite significantly when the size of the QD is reduced to a few nanometres. With the recent development in modern fabrication techniques like molecular beam epitaxy, etching

techniques, and selective ion implantation etc. it is possible to design nano semiconductor QD devices with spatial confinement in all directions. As these artificial atoms are of the order of a few nanometres, the quantum mechanical treatment of the problem becomes essential. In semiconductor ODs, the fast carrier transitions between the confined discrete energy levels determine high intensity of luminescence and the QD laser operation. The polaron problem has been extensively studied in QDs, QWs, graphene QD and other nano systems [40-55]. The transport and other important properties in QDs are also greatly influenced by the e-p interaction. The FM is best suited for a large continuum polaron. In this thesis, we are also interested in discussing the narrow-band electrons for which the tightbinding model (TBM) is the most suitable model. Polarons in such systems are best described by the celebrated Holstein model [56-57] where the polaron is considered to be tightly bound to the lattice sites and may be referred to as a Holstein polaron. To calculate the GS of this model, one may perform the well-known Lang-Firsov transformation (LFT) [58] to decouple the e-p interaction. Due to the polaron formation, the electronic energy is reduced by a factor which is dependent on the strength of the e-p interaction. The hopping amplitude is also decreased by a factor dependent on the e-p interaction coefficient, known as the Holstein factor. Thus, electronic band narrowing occurs due to the polaron formation. The Holstein polaron model in the presence of the Coulomb correlation has shown some promising results in narrow-band systems. To study the interplay between the e-p interaction and the e-e interaction, the Holstein-Hubbard model (HHM) is believed to be one of the most suitable models. If the e-p interaction is strong, the system settles into a bipolaronic charge-density wave (CDW) GS that corresponds to a paramagnetic Peierls insulator. On the other hand, if the e-p interaction is not so strong to overcome the repulsive e-e Coulomb interaction, the GS behaves as a polaronic SDW state, which resembles an antiferromagnetic Mott insulator. Therefore, it is interesting to study the SDW-CDW transition driven by the competition between the repulsive e-e interaction and the phonon-induced attractive e-e interactions which may lead to some intermediate phase. Application of this concept may give rise to some interesting results in the field of high- T_c superconductivity. There have been a few quite investigations on this issue in recent years by Chatterjee and collaborators and others [59-63]. Another phenomenon that can be described by the HHM model is self-trapping transition [64-66]. As the e-p coupling increases, the depth of polarization potential created by the polaronic interaction also increases and as a result the polaron loses its mobility making the electron self-trapped. Hence, due to the increase in the e-p coupling strength it is possible for the polaron to undergo a transition from a large (mobile) polaron to a small (self-trapped) polaron state.

The effect of magnetic field in a TB mesoscopic system is also an important phenomenon to study. There have been a large number of investigations on the Aharonov-Bohm (A-B) effect in closed confined geometries, for e.g., in a 1D TB QR, where the effect of A-B flux leads to a persistent current (PC) in the ring [67-75]. This mesoscopic phenomenon occurs due to a quantum interference effect and is greatly affected by the size of the QR, temperature and interactions present in the system. Though the e-p interaction has been investigated in LDS by several authors, there are still some exciting phenomena that have not been addressed before. In this thesis, we study the role of e-p interaction in confined systems and its effects on mesoscopic and spintronics transport.

The SOI in LDS can be used to manipulate the spin degrees of freedom which is at the heart of Spintronics which deals with spin transport, spin dynamics and spin relaxation in electronic materials. In Spintronics, we deal with three types of questions: (i) how to polarize the spin, (ii) how long the system will remember the spin polarization, (iii) how to detect the spin. The spin-polarization can be achieved in many ways, one of them being the spin injection from a magnetic electrode to the sample which accumulates the spin-polarized electrons (spin accumulation). The rate of spin accumulation is dependent on the spin relaxation mechanism which brings back the spins to their equilibrium configuration and the timescale of spin relaxation is typically of the order of nanosecond. The SOI becomes especially important in the context of spin relaxation mechanism and the detection of spin states. It has been suggested in analogy with quantum Hall effect that SOI can generate a dissipationless spin current in a hole-doped semiconductor [76]. Also, SOI has a special role in topological systems [77-82] where the relativistic SO term induces band inversion phenomenon. The study of spintronics has seen an upsurge after the pioneering work done by Datta and Das [83] who proposed a spin-FET model where the electrons can enter from the source and get collected at the drain giving rise to a current (ON state) if the electron spins are parallel to the spins of the drain and zero current (OFF state) if spins are antiparallel to the drain spins. This spin-orientation is controlled by a gate voltage connected to the substrate which exhibits an effective SO magnetic field arising from the SOI by which the spins precess. Hence, modifying the gate voltage one can make the spins either parallel (ON) or antiparallel (OFF) at the drain and control the current. However, this model requires various techniques of spin injection and accumulation of spin-polarized current through transport across different hetero-junctions or optical pumping techniques to polarize the spins and mechanisms of spin relaxation. There are several spin relaxation or spin dephasing mechanisms in metals or semiconductors. Among these, the D'yakonov-Perel' mechanism [84] is an efficient spin relaxation mechanism that can be realized in systems lacking inversion symmetry. Examples of systems with inversion asymmetry are the group III-V zinc blende semiconductors (e.g., GaAs). The inversion asymmetry can also be induced externally by forming a heterostructure (such as GaAs/AlGaAs QWs) which produces an asymmetric confining potential. Thus, one can classify inversion asymmetries into two types leading to two types of SOIs. One is the bulk inversion asymmetry (BIA) and the other is structural inversion asymmetry (SIA). The most common example of SOI due to SIA is the Rashba SOI (RSOI) [85-87] and the one due to BIA is the *Dresselhaus SOI* (DSOI) [88]. These two types of SOIs will be discussed qualitatively later in the Sec.1.3.2. The subject of spintronics covers a vast area of theoretical and experimental research of spin-polarized transport in spin-based tunnelling junction systems like ferromagnet-insulator-superconductor interface, magnetic tunnel junction, semiconductor FET, bipolar transistor, metal-semiconductor-metal SMT systems, SET systems, spin-filters, spin-diodes, spin FET and nanostructure spin qubits where tunnelling conductance and spin-polarization are studied for different spin-splitting states due to SOIs. These nanostructures are useful to get zero-field splitting [89-91] due to RSOI or DSOI, or both SOIs, which gives rise to many interesting phenomena in spin polarized mesoscopic transport [89, 92-101]. There are some promising materials which are used for high spin-polarization, for e.g., CMR materials, half metallic oxides such as CrO₂, Fe₃O₄, ferromagnetic semiconductor such as CrBr₃, high carrier density compounds like (III,Mn)V compounds, and double perovskites materials. Therefore, it is important to explore the effect of SOI in LDS which can lead to exciting applications in spin-based nanodevice systems. In a three-terminal structure like SMT, the effects of e-e, e-p and SO interactions and their influence on spin-polarized transport phenomena have been studied [17-24, 102-119]. In this thesis, the role of SOIs in creating zero field spin splitting states and the corresponding spin-spilt tunnelling current, conductance and spin-polarization have been examined in detail. Also, some interesting competing effects of SOIs and e-p interaction in a QD and other spintronics transport system have been studied.

We have discussed above the motivation to study certain interactions in quantum systems. In Sec.1.2-1.5, we provide an introduction to LDS and the important interactions in the continuum and discrete models that will be used in the thesis. Finally, in Sec.1.6, we present the outline of the thesis.

1.2 LOW-DIMENSIONAL STRUCTURES

Due to advancement in fabrication techniques, the low-dimensional physics has become a subject of great interest where the motion of electrons is restricted at least in one direction. This is called *quantum confinement*. Of late, the quantum confinement and size effects in

semiconductor or metallic structures have led to many emergent phenomena in the fields of mesoscopic physics, cold atom physics and many more. Confining the system is described by the characteristic lengths (λ) of the systems, for example, mean free path in transport studies or Fermi-wavelength for quantization etc. If the dimension of a particular direction (x, y or z) is comparable with the characteristic length, λ of the system, then the motion of the particle is restricted fully along that direction, while it is free to move along other available directions. Therefore, confinement restricts the degrees of freedom in one or more directions along which the quantum effects become strongly pronounced.

1.2.1 Two-dimensional quantum well (one-dimensional confinement)

In these kinds of structures, the motion of the particle is confined in one direction specifically, the dimension of that particular direction, L_x , L_y or L_z is shrunk to a size which is comparable to the system's characteristic length, λ . Here, 'two' refers to the number of directions available for to particle to move. This can be best described by the *two-dimensional electron gas* (2DEG) model or the well-known *particle in a box problem* in quantum mechanics. Here, it should be named as a particle in a 1D box problem. Let's say, the confinement is created along z-direction which implies there exists a non-zero confinement potential V(z) along z-direction, whereas, in x and y directions, the potential is zero as the motion is free along x and y. The Schrödinger equation (SE) for the particle confined in such a geometry is given by

$$\left[\frac{\hbar^2}{2m}\left(\frac{\partial^2}{\partial x^2} + \frac{\partial^2}{\partial y^2} + \frac{\partial^2}{\partial z^2}\right) + V(z)\right]\psi(x, y, z) = \varepsilon\psi(x, y, z). \tag{1.1}$$

The total energy can be divided into two parts as

$$\varepsilon = \varepsilon_{x,y}(k_x, k_y) + \varepsilon_z(k_z^{n_z}), \tag{1.2}$$

where, $\varepsilon_{x,y}$ is the free-particle energy along x and y with continuous k_x , k_y values given as

$$\varepsilon_{x,y}(k_x, k_y) = \frac{\hbar^2}{2m^*} (k_x^2 + k_y^2), \tag{1.3}$$

where, m^* is the effective mass in the band. The quantized $k_z^{n_z}$ -momentum due to the confinement along z specified by the quantum number n_z is given by

$$k_z^{n_z} = \frac{n_z \pi}{L_z}, n_z = 0, 1, 2, \dots$$
 (1.4)

Therefore, all the k_z -values are not allowed along z. Unlike the continuum energy along x and y directions, the quantized energy in the z-direction for the n^{th} – sub-band is given by

$$\varepsilon_{z}(k_{z}^{n}) = \frac{\hbar^{2}(k_{z}^{n_{z}})^{2}}{2m} = \frac{\hbar^{2}}{2m} \left(\frac{n_{z}^{2}\pi^{2}}{L_{z}^{2}}\right), n_{z} = 0,1,2,...$$
 (1.5)

Hence, finite sample size drastically alters the allowed energy levels bringing in gap in the energy spectrum. We can also calculate the 2D density of states DOS per unit area within a band and below a particular n^{th} state as

$$g_{2D}(\varepsilon) = \frac{m^*}{\pi \hbar^2} \sum_{j=1}^n H(\varepsilon - \varepsilon_j), \qquad (1.6)$$

where, $H(\varepsilon - \varepsilon_j)$ is the Heaviside step function given as $H(\varepsilon - \varepsilon_j) = 0$ for $\varepsilon < \varepsilon_j$ and 1 for $\varepsilon > \varepsilon_j$. The practical example of this kind is semiconductor QWs, for e.g., $GaAs/Al_xGa_{1-x}As$ hetero-structures system. As the Ga and As have two different band gaps, a potential well can be generated and the system exhibits bound states. Metal-oxide-semiconductor is another example where 2DEG is formed at the semiconductor-insulator interface. Another known example of 2D system is graphene quantum wells where the dimension of the wavefunction is of the order of the entire 2D graphene-sheet. One can think of a 2DEG system as almost a free-electron system in 2D where the particle has a large mean free path which means the scattering with the defects can be ignored.

1.2.2 ONE-DIMENSIONAL QUANTUM WIRE (TWO-DIMENSIONAL CONFINEMENT)

In these structures, the degree of confinement is one-step stronger compared to the quantum well structures. When the confinement occurs in two directions, let's say along x and z directions, and another direction i.e., y-direction is available for the particle to move freely, then we refer it to a quantum wire. Here, 'one' denotes the number of direction available for

the particle to exhibit the free particle nature. As discussed above, in this case, the SE of the particle in a 2D box is given by

$$\left[\frac{\hbar^2}{2m}\left(\frac{\partial^2}{\partial x^2} + \frac{\partial^2}{\partial y^2} + \frac{\partial^2}{\partial z^2}\right) + V(x, z)\right]\psi(x, y, z) = \varepsilon\psi(x, y, z). \tag{1.7}$$

Now, the total energy of the particle ε with free (continuum) nature in 1D (along y) and confined (discrete) nature in 2D (along x and z) can be expressed as

$$\varepsilon = \varepsilon_{y}(k_{y}) + \varepsilon_{x,z}(k_{x}^{n_{x}}, k_{z}^{n_{z}}), \tag{1.8}$$

where, $\varepsilon_y(k_y)$, the free energy with all-allowed continuum k_y -momentum is written as

$$\varepsilon_{y}(k_{y}) = \frac{\hbar^{2}}{2m^{*}}k_{y}^{2},\tag{1.9}$$

and the quantized energy $\varepsilon_{x,z}(k_{x,z}^{n_x,n_z})$ specified by the two quantum numbers n_x , n_z is given as

$$\varepsilon_{x,z}(k_x^{n_x}, k_z^{n_z}) = \frac{\hbar^2}{2m} \left(\frac{n_x^2 \pi^2}{L_x^2}\right) + \frac{\hbar^2}{2m} \left(\frac{n_z^2 \pi^2}{L_z^2}\right); n_x, n_z = 0,1,2,... \quad (1.10)$$

Also, the 1D DOS per unit length is given by

$$g_{1D}(\varepsilon) = \frac{\sqrt{m^*}}{\sqrt{2\pi\hbar}} \varepsilon^{-\frac{1}{2}}.$$
 (1.11)

1.2.3 Zero-dimensional quantum dot (threedimensional confinement)

In the extreme case of confinement, the particle can be confined in all possible directions, meaning all the three-dimensions of the box L_x , L_y and L_z are typically of the order of characteristic length λ . Therefore, in true sense, this is the ideal confinement where the particle has 'zero' number of directions available to move freely. In this case, the SE of the particle in a 3D box is given by

$$\left[\frac{\hbar^2}{2m}\left(\frac{\partial^2}{\partial x^2} + \frac{\partial^2}{\partial y^2} + \frac{\partial^2}{\partial z^2}\right) + V(x, y, z)\right]\psi(x, y, z) = \varepsilon\psi(x, y, z). \quad (1.12)$$

By the quantization condition of $\vec{k}(k_x, k_y, k_z)$ as expressed in Eq. (1.4), the quantized energy of these zero-dimensional objects specified by the three quantum numbers n_x , n_y and n_z can be written as

$$\varepsilon \left(k_x^{n_x}, k_y^{n_y}, k_z^{n_z}\right) = \frac{\hbar^2}{2m} \left(\frac{n_x^2 \pi^2}{L_x^2}\right) + \frac{\hbar^2}{2m} \left(\frac{n_y^2 \pi^2}{L_y^2}\right) + \frac{\hbar^2}{2m} \left(\frac{n_z^2 \pi^2}{L_z^2}\right); \; n_x, n_y, n_z = 0, 1, 2, \dots \; (1.13)$$

The DOS for the QD can be calculated as

$$g_{0D}(\varepsilon) = 2\sum_{i} \delta(\varepsilon - \varepsilon_{i}).$$
 (1.14)

Hence, the DOS of the QD shows the sharp Dirac-delta spikes denoting the true confined nature. The factor of '2' comes from the spin degrees of freedom. The typical size of a QD ranges from 2 to 10 nanometres containing around 100 to 1000 electrons or 10 to 50 atoms along diameter. This size is usually less than the quantum coherence length because of which the coherence can be achieved throughout at low temperature. The QD can be thought of as a mesoscopic analogue of a single atom, often referred as 'artificial atom' as confining the particle gives rise to quantized states in the energy spectrum.

1.2.3.1 FABRICATION OF QUANTUM DOT

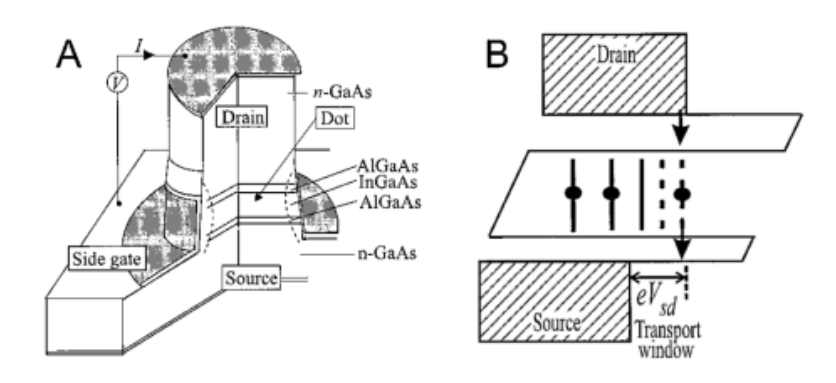
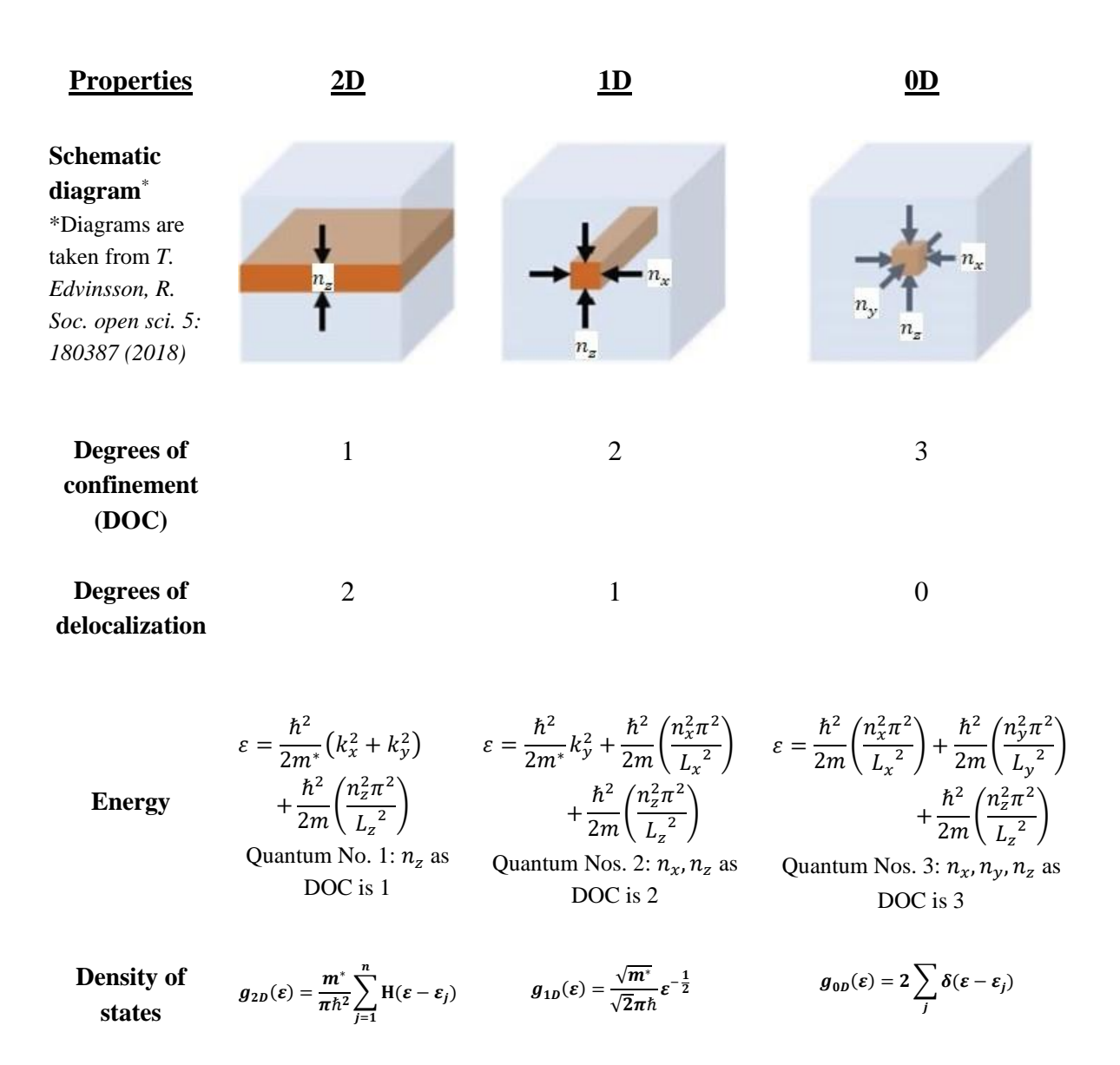


Fig.1.1 Schematic representation of QD fabrication (Picture courtesy: Tarucha *et al. Science* **278**, 1788 (1997)).

Normally, one of the known techniques of fabricating QD is the molecular beam epitaxy, where the QD gets self-assembled by depositing a semiconductor having a larger lattice constant (for example, Ge or InAs) onto another semiconductor having a smaller lattice constant (for example, Si or Ga). As it is shown in Fig.1.1, QD can be fabricated experimentally by depositing several layers of such different semiconductor hetero-structures of different thickness, most commonly a three-layer structure of insulating InGaAs sandwiched between two AlGaAs layers and the whole system is connected two n-doped GaAs contacts as the source and the drain substrate and a voltage is applied to the substrate. The Fermi energy of the GaAs contacts lies above the conduction band of InGaAs and the conduction band edge of AlGaAs lies above the InGaAs conduction band edge. This configuration creates a sharp confining potential like a double QW potential which allows the accumulation of electrons inside the InGaAs region when no voltage is applied. A gate voltage is also applied to move the QW structure spatially, which results in a variable number of bound states in the dot. When a constant bias voltage is applied, the Fermi energies of the contacts shifts and a window of transport opens up. Though the InGaAs layer is insulating, but it is thin enough to tunnel the electrons from source to drain which gives rise to sharp current peaks in the current-voltage characteristics where each peak corresponds to a single electron transport. This was experimentally demonstrated by Tarucha et al. [120] in 1996. Theoretically, the QD systems are treated by assuming different confining potentials; amongst them harmonic oscillator potential (parabolic QD) is widely used. Although the parabolic potential is not physical, it can provide the most useful features of the confined system [121-123]. In nanodevice applications, a double QD model resembling a two-level system can serve as the most elementary quantum qubits in quantum computation applications. Also, it has potential applications in the nano-electronic circuit, where one or a few QDs connected to metallic leads (source or drain) controlled by bias and gate voltages can be considered a nano-resister or capacitor. These kinds of molecular transistor structures can be extremely important to study many exciting phenomena such as Coulomb blockade, Kondo effect, resonant tunnelling, Kondo-Fano effect etc.

To summarize, we present a table containing the key-points about these low-dimensional systems as following



Next, we would like to present a few theoretical models and basic characteristics of these models that have been used in this thesis to describe our work. We start with the continuum model and then we will discuss discrete lattice models.

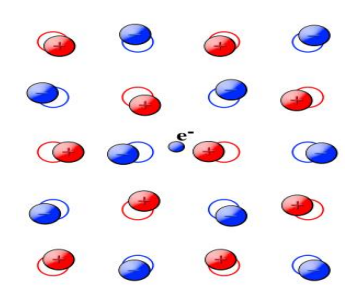
1.3 CONTINUUM MODELS

In the continuum limit, the discreteness of the lattice becomes unimportant. This model would be valid for a slowly moving electron in a lattice. The de Broglie wavelength of a slow electron is much bigger than the lattice constant which means the wavefunction associated to the electron spreads over many lattice-sites which makes it difficult for the electron to distinguish one lattice-site from another. So, the change in the wavefunction over a lattice spacing can be approximated to be negligibly small and under this circumstance, the lattice

essentially appears as a *continuum* to the electron. As a result, the momentum vector \vec{k} becomes continuous and the energy spectrum of the electron looks like a closely spaced band just like a free particle case. Although, this is the *continuum approximation* of lattice model, but it serves as a good starting point to study the low-lying states or long-wavelength excitations such as electrons in the conduction band of a metal, low-temperature phenomenon, transport in low-temperature and small fields etc. We will now discuss the e-p interaction, e-e interaction and SO interactions in the continuum limit.

1.3.1 Electron-phonon interaction: Fröhlich polaron model

In the simple Bloch picture, electrons experience a periodic potential created by the lattice ions in an ideal crystal. In such an ideal scenario, the conduction band electron can be approximated as a free electron with an effective Bloch mass m^* (different from the bare mass of the electron) and the kinetic energy of the electron is given by $\vec{p}^2/2m^*$, where \vec{p} is the momentum of the Bloch electron. However, ions oscillate in a real crystal. Therefore, it is essential to consider the motion of the ions which produces a displacement of ions from their equilibrium positions shown in Fig.1.2. In an ionic crystal or a polar semiconductor, the e-p interaction is modelled by the Fröhlich polaron Hamiltonian. In the framework of the FM, the ionic displacement gives rise to a time-dependent polarization field which interacts with an extra conduction band electron. As the electron is slow, the de Broglie wavelength or the wavefunction associated with this low-lying electron spreads over many lattice points, which means the discrete nature of the lattice is irrelevant to the electron. Therefore, the radius of the polaron is much larger than the lattice spacing, which is why the Fröhlich polaron is known as a large polaon. As a result, the lattice essentially seems to be a continuum to the electron and the electron dressed with the lattice distortion (a complex or quasi-particle) can move throughout the crystal shown in the Fig.1.3. In field theory, an electron can be treated as a source of phonons and the interaction between the electron with the oscillating lattice can be described by the phonon emission and absorption processes. These processes can be explained through Feynman diagrams. Fig.1.4 displays a process in which an electron with a momentum \vec{k} emits a phonon with momentum \vec{q} and goes into a state with momentum $\vec{k} - \vec{q}$. This is called one-phonon emission process. Fig.1.5 describes a different process where the electron with a momentum \vec{k} absorbs a phonon with momentum \vec{q} and goes into a state with momentum $\vec{k} + \vec{q}$. This is called one-phonon absorption process. The electron and phonon propagators meet at a point, which is called the vertex, where the total momentum should be conserved. These processes give rise to scattering phenomena in transport mechanisms.



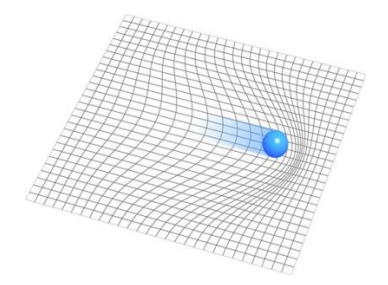
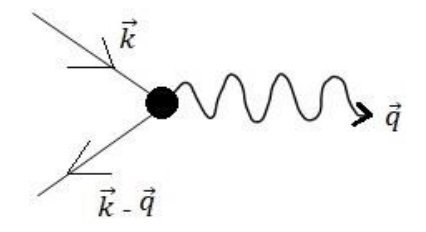
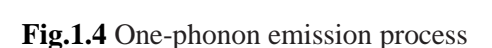


Fig.1.2 Displacement of ions in a lattice (picture source: *internet*).

Fig.1.3 Movement of polaron in lattice (picture source: *internet*).





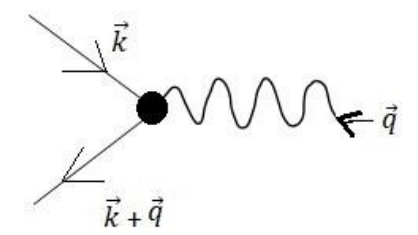


Fig.1.5 One-phonon absorption process

The FM is described by the following Hamiltonian:

$$H = H_e + H_{ph} + H_{e-p}, (1.15)$$

where H_e , H_{ph} and H_{e-p} denote respectively the Hamiltonians for a free electron, free phonons and the e-p interaction which are written as

$$H_e = -\frac{\hbar^2}{2m^*} \nabla^2_{\vec{r}'}, \tag{1.16}$$

$$H_{ph} = \hbar \omega_0 \sum_{\vec{q}'} b_{\vec{q}'}^{\dagger} b_{\vec{q}'}, \qquad (1.17)$$

$$H_{e-p} = \sum_{\vec{q}'} \left(\xi'_{\vec{q}'} e^{-i\vec{q}' \cdot \vec{r}'} b_{\vec{q}'}^{\dagger} + h.c. \right). \tag{1.18}$$

Here all vectors in general can be N-dimensional (ND) for a ND lattice. \vec{r}' is the position vector of the electron, m^* is the effective mass, ω_0 is the dispersionless LO phonon frequency, $b_{\vec{q}'}^{\dagger}$ ($b_{\vec{q}'}$) is the creation (annihilation) operator of an LO phonon of wavevector \vec{q}' , $\xi'_{\vec{q}'}$ is the electron-phonon interaction coefficient. We shall use the Feynman units (FU) [124] in which the energy is scaled by $\hbar\omega_0$, length by r_0 which is the inverse of the wavevector q_0 i.e., q_0^{-1} , q_0 defined by $\frac{\hbar^2 q_0^2}{m^*} = \hbar\omega_0$, wavevectors by q_0 . Such scalings are equivalent to putting $\hbar = m^* = \omega_0 = 1$. Hamiltonian (1.15) in this unit can be written as

$$H = -\frac{1}{2}\nabla_{\vec{r}}^2 + \sum_{\vec{q}} b_{\vec{q}}^{\dagger} b_{\vec{q}} + \sum_{\vec{q}} \left(\xi_{\vec{q}} e^{-i\vec{q}.\vec{r}} b_{\vec{q}}^{\dagger} + h.c.\right), \tag{1.19}$$

where $\xi_{\vec{q}}$ is given as

$$|\xi_{\vec{q}}|^2 = \left[\frac{\Gamma\left(\frac{N-1}{2}\right) 2^{N-\frac{3}{2}} \pi^{\frac{N-1}{2}}}{V_N q^{N-1}} \right] \alpha, \tag{1.20}$$

where V_N is the volume of the *N*-dimensional lattice and α is the dimensionless e-p coupling constant given by

$$\alpha = \frac{e^2}{\sqrt{2}r_0} \frac{1}{\hbar\omega_0} \left(\frac{1}{\varepsilon_\infty} - \frac{1}{\varepsilon_0}\right). \tag{1.21}$$

1.3.1.1 BOUND POLARON

In practice, a crystal is not free from impurities. If the impurity contains electric charge, it will interact with the vibrating ions by electrostatic interaction as an electron does. Let us consider a hydrogenic impurity (also called a Coulomb impurity). In this case, both the electron and the nucleus, interact with the phonons to form a bound polaron. The bound polaron problem was formulated in the continuum lattice by extending the FM by Platzman [125]. The Platzman model for the bound polaron can be written in the FU as

$$H = -\frac{1}{2}\nabla_{\vec{r}}^{2} - \frac{\tilde{\beta}}{|\vec{r} - \vec{\tilde{r}}|} + \sum_{\vec{q}} \tilde{b}_{\vec{q}}^{\dagger} \tilde{b}_{\vec{q}} + \sum_{\vec{q}} \left(\xi_{\vec{q}} \left(e^{-i\vec{q}.\vec{r}} - e^{-i\vec{q}.\vec{\tilde{r}}} \right) \tilde{b}_{\vec{q}}^{\dagger} + h.c. \right), \quad (1.22)$$

where the second term represents the impurity-electron interaction, \vec{r} being the position of the Coulomb impurity, and $\tilde{\beta}$ the dimensionless impurity-electron coupling strength given by $\tilde{\beta} = \frac{e^2}{\hbar \omega_0 r_0 \varepsilon_\infty}$. The last term represents the e-p and impurity-phonon interactions. For simplicity, the impurity can be considered to be located at $\vec{r} = 0$. The impurity-phonon coupling can be eliminated exactly by employing the following canonical transformations

$$b_{\vec{q}} = \tilde{b}_{\vec{q}} - \xi_{\vec{q}}, \qquad b_{\vec{q}}^{\dagger} = \tilde{b}_{\vec{q}}^{\dagger} - \xi_{\vec{q}}^{*}.$$
 (1.23)

Eq. (1.22) is transformed to

$$H = -\frac{1}{2}\nabla_{\vec{r}}^{2} - \frac{\tilde{\beta}}{r} + \sum_{\vec{q}} \left(b_{\vec{q}}^{\dagger} + \xi_{\vec{q}}^{*}\right) \left(b_{\vec{q}} + \xi_{\vec{q}}\right) + \sum_{\vec{q}} \left(\xi_{\vec{q}} \left(e^{-i\vec{q}.\vec{r}} - 1\right) \left(b_{\vec{q}}^{\dagger} + \xi_{\vec{q}}^{*}\right) + h.c.\right)$$

$$= -\frac{1}{2}\nabla_{\vec{r}}^{2} - \frac{\tilde{\beta}}{r} + \sum_{\vec{q}} b_{\vec{q}}^{\dagger} b_{\vec{q}} + \sum_{\vec{q}} \left(\xi_{\vec{q}} e^{-i\vec{q}.\vec{r}} b_{\vec{q}}^{\dagger} + h.c.\right) + \sum_{\vec{q}} \left(\left|\xi_{\vec{q}}\right|^{2} e^{-i\vec{q}.\vec{r}} + h.c.\right) - \sum_{\vec{q}} \left|\xi_{\vec{q}}\right|^{2}$$

$$(1.24)$$

where the 5th term can be calculated by substituting Eq. (1.20) for $|\xi_{\vec{q}}|^2$ (for N=3) and converting the \vec{q} -summation into an integral over \vec{q} as

$$\sum_{\vec{q}} \left(\left| \xi_{\vec{q}} \right|^2 e^{-i\vec{q}.\vec{r}} + h.c. \right) \to \frac{4\sqrt{2}\pi}{V} \alpha \frac{V}{8\pi^3} \int d\vec{q} \frac{e^{-i\vec{q}.\vec{r}}}{q^2} = \frac{\sqrt{2}}{r} \alpha. \tag{1.25}$$

We can neglect the infinite constant term $\sum_{\vec{q}} |\xi_{\vec{q}}|^2$. Therefore, the Hamiltonian for the bound polaron becomes

$$H = -\frac{1}{2}\nabla_{\vec{r}}^2 - \frac{\beta}{r} + \sum_{\vec{q}} b_{\vec{q}}^{\dagger} b_{\vec{q}} + \sum_{\vec{q}} \left(\xi_{\vec{q}} e^{-i\vec{q}.\vec{r}} b_{\vec{q}}^{\dagger} + h.c. \right), \tag{1.26}$$

where β is given as $\beta = \tilde{\beta} - \sqrt{2}\alpha$.

1.3.1.2 POLARON IN THE PRESENCE OF AN EXTERNAL MAGNETIC FIELD: MAGNETOPOLARON

To observe the polaron formation experimentally, one has to determine two characteristic quantities, the polaron radius $r_0 = \sqrt{\hbar/m^*\omega_0}$ and the e-p coupling constant $\alpha = \left(\frac{e^2}{\sqrt{2}r_0\hbar\omega_0}\right)\left(\frac{1}{\varepsilon_\infty}-\frac{1}{\varepsilon_0}\right)$. The Bloch band mass m^* can be obtained from mobility data and once this is obtained, one can determine α provided ω_0 , ε_∞ and ε_0 are known. To determine the polaron mass m_p^* , one may require from cyclotron resonance experiments the cyclotron mass $m_c^* = eB/\omega_c^* c$, where B is the magnetic field and ω_c^* the cyclotron frequency. The m_c^* essentially gives the measure of m_p^* . Therefore, it is important to study the polaron problem in the presence of an external magnetic field.

The model Hamiltonian of a polaron in an external magnetic field \vec{B} (0,0, B) can be written in the FU as

$$H = \frac{1}{2} \left(-i \nabla_{\vec{r}} - \frac{e \vec{A}}{c} \right)^2 + \sum_{\vec{q}} b_{\vec{q}}^{\dagger} b_{\vec{q}} + \sum_{\vec{q}} \left(\xi_q \ e^{-i \vec{q} \cdot \vec{r}} b_{\vec{q}}^{\dagger} + h.c. \right), \tag{1.27}$$

where \vec{A} is the magnetic vector potential which can be chosen under the Landau gauge as $\vec{A} = (-By, 0,0)$. Under this gauge the Hamiltonian () is modified as

$$H = \frac{1}{2}(p_x + \overline{\omega}_c y)^2 + \frac{1}{2}(p_y^2 + p_z^2) + \sum_{\vec{q}} b_{\vec{q}}^{\dagger} b_{\vec{q}} + \sum_{\vec{q}} \left(\xi_q e^{-i\vec{q}.\vec{r}} b_{\vec{q}}^{\dagger} + h.c. \right), \quad (1.28)$$

where $\overline{\omega}_c$ is given by

$$\overline{\omega}_c = \frac{\omega_c}{\omega_0}, \quad \omega_c = \frac{eB}{m_c^* c}.$$
 (1.29)

1.3.2 SPIN-ORBIT INTERACTIONS

SOI leads to many important phenomena in semiconductor physics. It can be heuristically derived from the relativistic Dirac equation. When an electron moves in an electric field it experiences an effective magnetic field in its own inertial reference frame which then couples

to the spin of the electron giving rise to SOI effect. The full-relativistic Hamiltonian of an electron moving in an effective magnetic field is governed as

$$\left[\frac{1}{2m}\left(\vec{p}-\frac{e}{c}\vec{A}\right)^2-\frac{e\hbar}{2mc}\vec{\sigma}.\left(\vec{\nabla}\times\vec{A}\right)-\frac{\vec{p}^4}{8m^3c^3}+\frac{e\hbar^2}{8m^2c^2}\vec{\nabla}.\vec{\nabla}\varphi-\frac{e\hbar}{4m^2c^2}\vec{\sigma}.\left(\vec{\nabla}\varphi\times\vec{p}\right)\right]\psi$$

$$= [E^{NR} - e\varphi]\psi, \tag{1.30}$$

where the first term refers to the non-relativistic motion. The interaction between the spin-1/2 particle (spin operator $\vec{s} = \hbar \vec{\sigma}/2$) and the magnetic field $\vec{B} = \vec{\nabla} \times \vec{A}$ is given by the second term. The third term refers to the relativistic mass correction. The fourth term is the *Darwin term*. The fifth term is the contribution coming from the spin-orbit interaction, also known as the *Thomas term*. For a spherically symmetric potential, the electric field is given as $\vec{E} = -\frac{d\varphi}{dr}\frac{\vec{r}}{r}$ and $\vec{r} \times \vec{p} = \vec{l}$, \vec{l} being the angular momentum of the electron. The Thomas term for such a case can also be written as

$$H_T = -\frac{e\hbar}{4m^2c^2}\vec{\sigma}.(\vec{\nabla}\varphi \times \vec{p}) = -\frac{e}{2m^2c^2}\frac{1}{r}\frac{d\varphi}{dr}\vec{l}.\vec{s} . \qquad (1.31)$$

The typical value of the SOI energy varies widely in semiconductor materials. The usual expression for SOI-energy goes like $E_{SO} \sim \left(\frac{ze^2}{\hbar c}\right)^2 \frac{me^4}{\hbar^2} \propto z^2$, where z is the atomic number. Therefore, we can say, the bigger the atom, the bigger the SOI strength. Depending on the symmetry properties of the solids, the SOI can be classified into two major divisions namely (A) symmetry-independent SOI and (B) symmetry-dependent SOI.

1.3.2.1 SYMMETRY-INDEPENDENT SPIN-ORBIT INTERACTION

This type of SOI is present in all kinds of crystals. It can be discussed without considering the special symmetry properties of the lattice which is almost similar to that of atoms. Fig.1.6 illustrates the band splitting due to the usual SOI in a bulk semiconductor. The conduction band (CB) with orbital angular momenta l=0 (s-band) and the valance band (VB) with l=1 (p-band) are separated by a band gap $E_{\rm g}$. Each band is two-fold degenerate for spin-up (s=1/2) and spin-down (s=-1/2) states and the total angular momenta quantum number j is given by $\vec{j}=\vec{l}+\vec{s}$. The heavy hole (hh with j=3/2, $J_z=\pm 3/2$) and the light hole (lh with j=1/2, $J_z=\pm 1/2$) bands are separated intrinsically, but degenerate at Γ_8 point.

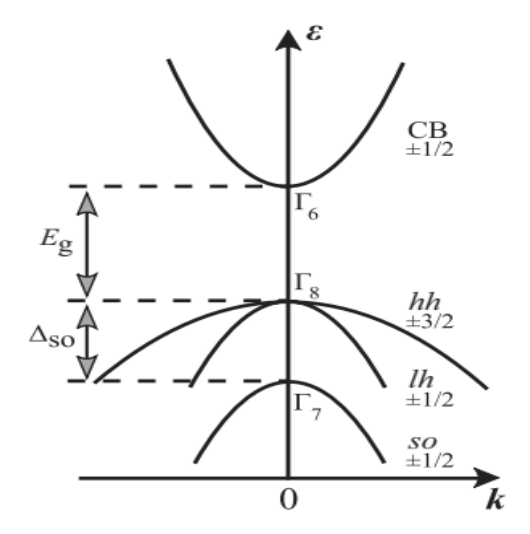


Fig.1.6 Splitting in bulk GaAs semiconductor energy bands vs. k near the Γ-point (k = 0) (picture courtesy: *Dissertation, V. Lechner, p. 9, 2012*).

Due to SOI $(\vec{l}.\vec{s})$ term) the 3-fold degeneracy of the VB (p-band) with projection $m_l = -1,0,+1$ is broken and they are separated by a SO split band gap Δ_{SO} measured from Γ_7 point to the Γ_8 point, although the CB (s-band) does not split. However, all the bands are 2-fold degenerate for two spin orientations.

1.3.2.2 SYMMETRY-DEPENDENT SPIN-ORBIT INTERACTION

This kind of SOI may be explained considering the special symmetry of the lattice. To discuss this, we first present two most elementary symmetry operations in crystals, which are (1) time-reversal symmetry and (2) spatial-inversion symmetry.

- (1) The former is a theoretical concept where time evolves backwards to describe an event, or in physics, all the motions are reversed under a mathematical operation $\mathcal{T}\colon t \to -t$, then time-reversal symmetry (TRS) is preserved if all the physical properties remain unchanged back in time. Under \mathcal{T} -operation, the physical quantities transform as follows
 - Position vector, $\vec{r} \rightarrow \vec{r}$ as $t \rightarrow -t$ (even in TRS).
 - Linear momentum, $\vec{k} \rightarrow -\vec{k}$ as $t \rightarrow -t$ (odd in TRS).
 - Orbital angular momentum, $\vec{l} \rightarrow -\vec{l}$ as $t \rightarrow -t$ (odd in TRS).
 - Spin angular momentum, $\vec{s} \rightarrow -\vec{s}$ as $t \rightarrow -t$ (odd in TRS).

Therefore, $\vec{l} \cdot \vec{s}$ term is even under \mathcal{T} i.e., TRS is preserved for SOI case and the energy dispersion obeys the following relation: $E_{\vec{s}}(\vec{k}) = E_{-\vec{s}}(-\vec{k})$.

- (2) The other type of symmetry operation is the spatial-inversion symmetry (SIS) which is governed by the operation $\mathcal{R}: \vec{r} \to -\vec{r}$. Under this operation, if the physical properties remain unchanged going backwards in position, then the inversion-symmetry is preserved. The physical quantities change under \mathcal{R} -operation as follows
 - Linear momentum, $\vec{k} \rightarrow -\vec{k}$ as $\vec{r} \rightarrow -\vec{r}$ (odd in SIS).
 - Orbital angular momentum, $\vec{l} \rightarrow \vec{l}$ as $\vec{r} \rightarrow -\vec{r}$ (even in SIS).
 - Spin angular momentum, $\vec{s} \rightarrow \vec{s}$ as $\vec{r} \rightarrow -\vec{r}$ (even in SIS).

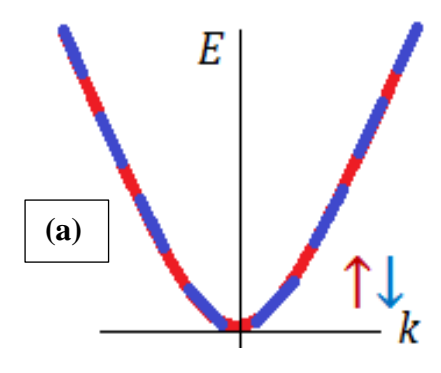
Therefore, the energy dispersion under SIS satisfies the following relation: $E_{\vec{s}}(\vec{k}) = E_{\vec{s}}(-\vec{k})$. In this context, one can bring in the concept of *centrosymmetric* and *non-centrosymmetric* crystals.

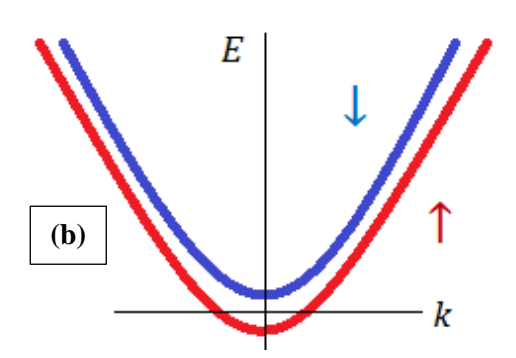
1.3.2.2.1 Spin-orbit interaction in centrosymmetric crystals

This is analogous to the symmetry-independent SOI described above where the bands splitting due to atomic l-s coupling may occur. If the crystal is symmetric i.e., all the properties are exactly same with respect to the centre of inversion then it's known as centrosymmetric crystals. In these types of crystals, the energy dispersion holds the following identity under \mathcal{T} and \mathcal{R} -symmetry operations

$$E_{\vec{s}}(\vec{k}) \underset{t \to -t}{=} E_{-\vec{s}}(-\vec{k}) \underset{\vec{r} \to -\vec{r}}{=} E_{-\vec{s}}(\vec{k}) \Rightarrow E_{\vec{s}}(\vec{k}) = E_{-\vec{s}}(\vec{k})$$
(1.32)

Hence, two different spin states i.e., up-spin (\vec{s},\uparrow) and down-spin $(-\vec{s},\downarrow)$ states have same energy which means they are degenerate when both TRS and SIS are maintained shown in Fig.1.7(a). The degenerate equation $E_{\vec{s}}(\vec{k}) = E_{-\vec{s}}(-\vec{k})$ as $t \to -t$ is known as *Kramer's doublets* followed by *Kramer's theorem* which states that all the eigenstates are at least doubly-degenerate if TRS is preserved. However, the degeneracy can be lifted by applying external magnetic field, \vec{B} and then the Kramer's doublets separate due to the TRS breaking as shown in Fig. 1.7(b).





TRS + SIS both preserved

TRS breaking + SIS preserved

Fig.1.7 (a) Degenerate bands in centrosymmetric case: Both TRS and SIS are preserved. (b) Degeneracy lifted by applying external \vec{B} : TRS is broken, but SIS is present.

The bands will split vertically in E-axis. This is known as Zeeman splitting which is determined in terms of the effective Landé factor g^* which strongly differs from the free-electron g-factor which is given by: $g_0 = 2$. However, it was first shown by Roth $et\ al.$ [23] through $\vec{k}.\vec{p}$ method that this effective g-factor is greatly influenced by SOI and given by [24]:

$$\frac{g^*}{g_0} = 1 - \frac{\Delta_{SO}}{3E_{\rm g} + 2\Delta_{SO}} \left(\frac{m_0}{m^*} - 1\right),\tag{1.33}$$

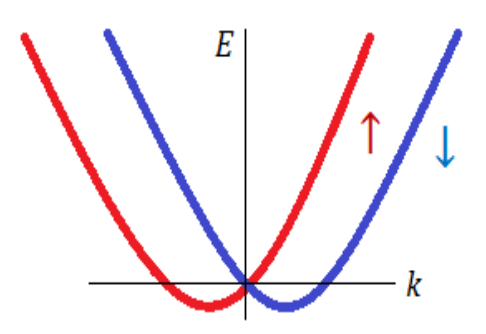
where, m^* is the effective band mass and m_0 is the bare mass of the free electron.

1.3.2.2.2 SPIN-ORBIT INTERACTION IN NON-CENTROSYMMETRIC CRYSTALS

If the crystal loses its symmetry properties when inverted around the centre, then it's no longer symmetric under inversion and it can be called a *non-centrosymmetric crystal*. For this kind of crystals, although the above dispersion satisfies TRS, but does not satisfy the equality with respect to SIS and holds a different relation which is given by

$$E_{\vec{s}}(\vec{k}) \underset{t \to -t}{=} E_{-\vec{s}}(-\vec{k}) \neq E_{-\vec{s}}(\vec{k}), \tag{1.34}$$

which causes *additional spin-splitting* at $\vec{k} \neq 0$ due to SIS breaking, even when external magnetic field is zero. This is commonly referred to as 'zero-field splitting' shown in Fig.1.8. This is a left-right splitting along k-axis owing to removal of spin-degeneracies. From the above equation, one can notice that SIS is broken, but TRS is preserved and hence, Kramer's doublets continue to exist at some k-points.



TRS preserved + SIS breaking

Fig.1.8 Bands split in non-centrosymmetric crystals even when $\vec{B} = 0$. TRS is present. But SIS is broken.

We will mainly focus on SOI in non-centrosymmetric crystals. These types of SIS breaking phenomena can be induced as well as they can be intrinsically present in the crystal itself. One can understand it by looking at the Thomas term $H_T = -\frac{e\hbar}{4m^2c^2}\vec{\sigma}.(\vec{\nabla}\varphi\times\vec{p})$. Here, the quantity $\vec{\nabla}\varphi$, the gradient of crystal potential can either be made asymmetric externally or it can be intrinsically asymmetric in a non-centrosymmetric crystal, which leads to two different kinds of SOI in a crystal. One type of SIS breaking can be accomplished by forming a heterostructure by combining materials of different band gaps. As a result, this causes an asymmetry in the crystal structure specifically at the interface of the hetero junction which can be controlled externally. This is known as SIA.

The other type is an asymmetry which is intrinsically present in the bulk-crystal due to the lack of inversion centre. This is known as BIA. A very common example of this kind of crystal is Zinc-blende (ZnS) like semiconductor structure (shown in Fig.1.9) such as GaAs, GaSb, GaP, InAs, InSb, ZnSe, CdSe, CdTe etc. Also, SIA can be induced in these structures and that will cause additional spin-splitting.

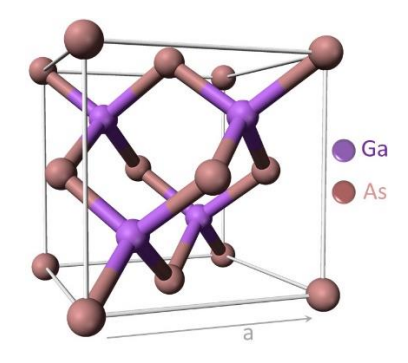


Fig.1.9 Diagram of the non-centrosymmetric crystal structure of GaAs semiconductor (picture courtesy: *internet*).

1.3.2.2.1 Dresselhaus spin-orbit interaction

We first like to discuss a few aspects of the SOI due to BIA. The SOI arising due to BIA is commonly known as the DSOI. As discussed above, SOI induces splitting in bulk bands of GaAs semiconductor (Fig.1.6). But in Fig.1.6, the spin-degeneracy in LH and HH bands is still intact. Due to the DSOI present in non-centrosymmetric crystals, there will be an additional spin-splitting which will lift the spin-degeneracy of the LH and HH bands along k-axis. This effect is more pronounced as we lower the dimension of the material because with lowering the dimension, the symmetry also gets reduced. We want to study this effect in a 2D QW structure where the electrons are confined along a particular direction giving rise to quantization effect in the energy bands. To incorporate the equal spin-splitting along $\pm k$ -axis around $\vec{k}=0$, one can add a linear spin-dependent term which is the lowest-order perturbative term to the Hamiltonian due to SOI in a 2DEG as

$$H = \frac{\vec{p}^2}{2m^*} \mathbb{I} + H_{SOC} = \frac{\vec{p}^2}{2m^*} \mathbb{I} + \frac{1}{\hbar} \sum_{ij} \beta_{ij} \sigma_i p_j,$$
 (1.35)

where \vec{p} is the momentum operator, β_{ij} in the second term refers to a material-dependent pseudo tensor of rank 2, \mathbb{I} is the 2×2 identity matrix and σ_i is the Pauli matrix. This term can be expanded into symmetric and antisymmetric components which gives BIA and SIA respectively as

$$\sum_{ij} \beta_{ij} \sigma_i p_j = \sum_{ij} (\beta_{ij}^{sym} \{ \sigma_i, p_j \} + \beta_{ij}^{anti-sym} [\sigma_i, p_j]) \equiv H_{SOC}^{BIA} + H_{SOC}^{SIA}.$$
 (1.36)

The H_{SOC} term can also be expressed as following

$$H_{SOC} = \frac{\hbar}{2} \vec{\sigma} \cdot \vec{\Omega}(\vec{k}), \tag{1.37}$$

where $\overrightarrow{\Omega}(\vec{k})$ is the \vec{k} -dependent effective magnetic field which can be interpreted as the effective Larmor frequency with which the spins precess. Therefore, the effective zero-field spin-splitting energy between up and down spin states becomes $\hbar |\overrightarrow{\Omega}(\vec{k})|$. One may also notice from Eq. (1.37), that for TRS to be preserved, $\overrightarrow{\Omega}(\vec{k})$ must satisfy $\overrightarrow{\Omega}(-\vec{k}) = -\overrightarrow{\Omega}(\vec{k})$. Now if SIS is also present in addition, then $\overrightarrow{\Omega}(-\vec{k}) = \overrightarrow{\Omega}(\vec{k})$ and hence, the only possible solution for $\overrightarrow{\Omega}(\vec{k})$ is $\overrightarrow{\Omega}(\vec{k}) = 0$. Therefore, for H_{SOC} to be non-vanishing, SIS must be broken. Here, this term is obviously non-zero as there is no SIS for a non-centrosymmetric crystal, but TRS may be preserved as long as we do not apply any external magnetic field.

The BIA can be influenced by changing the width of the QW, charge carrier density or temperature. In 3D bulk structure, the SOI term can be expressed by the power series expansion of \vec{k} as

$$H_{SOC}^{3D} = \gamma_c \left[\sigma_x k_x \left(k_y^2 - k_z^2 \right) + \sigma_y k_y (k_z^2 - k_x^2) + \sigma_z k_z \left(k_x^2 - k_y^2 \right) \right], \quad (1.38)$$

where γ_c is a material-dependent parameter. This Hamiltonian gives rise to the k^3 terms in the bulk conduction band. The contribution of linear-k terms seen in the lower dimension (for e.g., in 2D) can be derived from the above Hamiltonian. Let us consider a 2DQW structure of a zinc-blende crystal which is an ideal candidate for the systems with BIA. One should note that in 2DQW, both linear-k and cubic-k terms may appear in the conduction band spectrum. But we can neglect the k^3 -spin-splitting terms unless the temperature or the carrier concentration is too high. Therefore, we mainly focus on linear-k contribution to the spin-splitting in low-temperature regime. To obtain this we need to consider the effect of quantum confinement. This allows us to make the following tricks considering the crystal growth direction along z-direction ([001]). We can replace k_z and k_z^2 terms by their expectation values as: $\langle k_z \rangle = 0$ and $\langle k_z^2 \rangle \neq 0$ (as $\langle k_z^2 \rangle \approx \pi^2/l_{QW}^2$). Also, we can disregard the terms containing k^3 -contributions such as $\sigma_x k_x k_y^2$ and $\sigma_y k_y k_x^2$ as we want to obtain the linear-k SOI spectrum. By these approximations, the linear-DSOI Hamiltonian originates from BIA as

$$H_D^{2D} = \gamma_c \langle k_z^2 \rangle \left(-\sigma_x k_x + \sigma_y k_y \right) = \beta_D \left(\sigma_y k_y - \sigma_x k_x \right), \tag{1.39}$$

where β_D is the coefficient of the DSOI. The Hamiltonian for a 2DQW in the presence of DSOI can be written as

$$H = \frac{\vec{p}^2}{2m^*} \mathbb{I} + \frac{\beta_D}{\hbar} (\sigma_y p_y - \sigma_x p_x), \tag{1.40}$$

and the 2D eigenstate of this Hamiltonian is given by

$$\psi_{k\sigma}(\vec{r}) = \frac{1}{2\pi\hbar\sqrt{2}} \left(\sigma \cdot \frac{1}{k_x - ik_y}\right) e^{i\vec{k}\cdot\vec{r}},\tag{1.41}$$

where, σ is the spin-index: $\sigma = \pm 1$ and \vec{k} stands for the 2D momentum vector: $\vec{k} = (k_x, k_y)$. The energy spectrum of this system is given by

$$E_{\pm}(k) = \frac{\hbar^2}{2m^*} k^2 \pm \beta_D k, \tag{1.42}$$

where, k is the magnitude of the 2D \vec{k} -vector given by $k^2 = k_x^2 + k_y^2$. Hence, we can see a zero-field spin-splitting in the energy spectrum where, '+' sign represents the energy of the up-spin branch and '-' sign represents that of the down-spin branch. The energy dispersion and contours are shown in Fig.1.10.

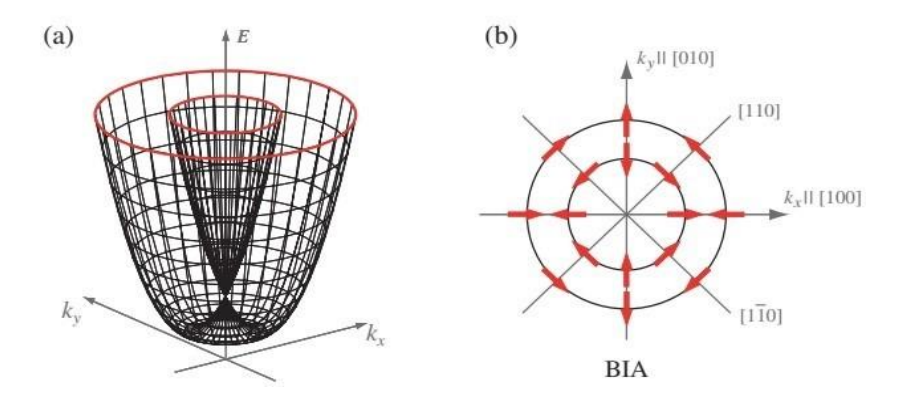


Fig.1.10 (a) Energy dispersion of the DSOI Hamiltonian (b) Contours of constant energy i.e., the Fermi surface containing two concentric circles of oppositely oriented up and down spins in k_x - k_y plane (picture courtesy: *Dissertation, V. Lechner, p. 13, 2012*).

1.3.2.2.2.2 RASHBA SPIN-ORBIT INTERACTION

Next, we discuss the SOI due to SIA in a 2DQW structure. This type of SOI is usually referred as the RSOI. The very first experimental observation in this context was studied by Stein et al. [126] in 1983, where they observed a zero-field spin-splitting in the electron-spin-resonance spectra of a 2D GaAs/Al_xGa_{1-x}As heterostructure. In the same year, Störmer et al. [127] also reported by combined magneto-transport and cyclotron-resonance experiments that the spin-degeneracy is lifted for finite \vec{k} which gives rise to two cyclotron masses in 2D GaAs/Al_xGa_{1-x}As heterostructure. Next year, in 1984, Bychkov and Rashba [128] theoretically explained the lifting of two-fold spin degeneracy following the SIS-breaking theory developed by Rashba in 1960 [86].

Before deriving the RSOI Hamiltonian we rewrite the Thomas term (1.31) as

$$H_T = -\frac{e\hbar}{4m^2c^2}\vec{\sigma}.(\vec{\nabla}\varphi \times \vec{p}) = -\frac{e\hbar}{4m}\vec{\sigma}.B_{SO}(\vec{p}) = -\frac{1}{2}\mu_B\vec{\sigma}.B_{SO}(\vec{p}), \qquad (1.43)$$

where, B_{SO} is the momentum dependent effective magnetic field experienced by the electron in its rest frame:

$$B_{SO}(\vec{p}) = \frac{1}{mc^2} (\vec{\nabla}\varphi \times \vec{p}) = -\frac{1}{mc^2} (\vec{p} \times \vec{E}), \tag{1.44}$$

and μ_B is the Bohr magneton which is given by $\mu_B = e\hbar/2m$. One can see that the potential, φ appearing in the above Eq. (1.44) can be made asymmetric by forming a 2DQW structure shown in the above Fig.1.11. Here in this diagram, it can be clearly seen that at the interface the band-mixing is non-uniform which generates a non-spherically symmetric potential (triangular like with left sharp edge and right curved edge) in space and consequently a non-zero electric field, $\vec{\mathcal{E}}$ is produced inside the QW.

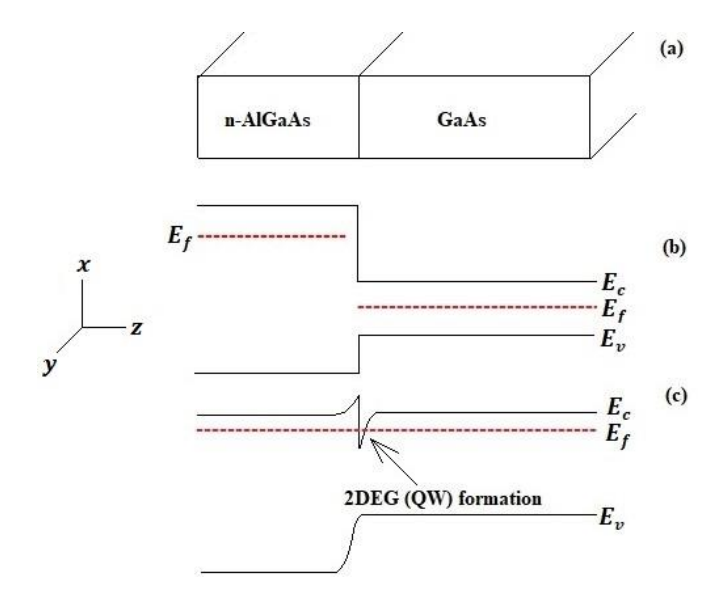


Fig.1.11 Structural inversion asymmetry in a 2DQW heterostructure.

Let us consider that this electric field, $\vec{\xi} = -\vec{\nabla}\varphi$ is directed along the crystal growth direction \hat{z} , then the Thomas term (1.31) can be expressed as the RSOI Hamiltonian as

$$H_{R} = -\frac{e\hbar}{4m^{2}c^{2}}\vec{\sigma}.\left(\vec{\nabla}\varphi \times \vec{p}\right)$$

$$= \frac{e\hbar\mathcal{E}}{4m^{2}c^{2}}\hat{z}.\left(\vec{\sigma}\times\vec{p}\right)$$

$$= \frac{\alpha_{R}}{\hbar}\left(\sigma_{x}p_{y} - \sigma_{y}p_{x}\right), \tag{1.45}$$

where α_R denotes the coefficient of the RSOI given as $\alpha_R = e\hbar^2 E/4m^2c^2$. The above RSOI Hamiltonian is just the second term of Eq. (1.36) originating from SIA. One should note that if the asymmetric potential at the interface is formed keeping the sharp edge right and curved edge left, then the electric field $E\hat{z}$ and hence the RSOI strength α_R flips its sign. This is the consequence of the SIA in a 2DQW heterostructure. Importantly, the Rashba parameter α_R can be tuned externally by applying a gate voltage.

The 2DQW Hamiltonian in the presence of the RSOI can be written as

$$H = \frac{\vec{p}^2}{2m^*} \mathbb{I} + \frac{\alpha_R}{\hbar} (\sigma_x p_y - \sigma_y p_x). \tag{1.46}$$

The 2D eigenstates and energy spectrum of this Hamiltonian are respectively given by

$$\psi_{k\sigma}(\vec{r}) = \frac{1}{2\pi\hbar\sqrt{2}} \left(-\sigma \cdot \frac{k_y - ik_x}{k}\right) e^{i\vec{k}\cdot\vec{r}},\tag{1.47}$$

and

$$E_{\pm}(k) = \frac{\hbar^2}{2m^*} k^2 \pm \alpha_R k \ . \tag{1.48}$$

Here also we can see a zero-field spin-splitting in the energy spectrum for up (+) and down (-) spin states. The contour is shown in Fig.1.12. For each k, the spin-splitting due to RSOI is $\Delta = E_+(k) - E_-(k) = 2\alpha_R k$.

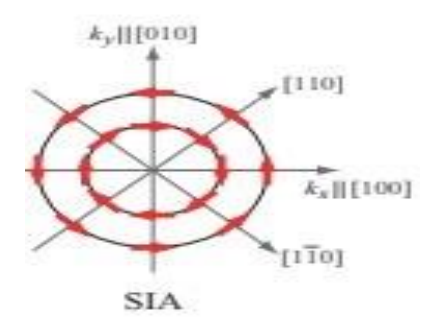


Fig.1.12 Fermi contours of two concentric circles of two oppositely oriented spin states for RSOI. (Picture courtesy: *Dissertation, V. Lechner, p. 13, 2012*).

In a 1D quantum wire, the 1D-RSOI Hamiltonian can be written as

$$H = \frac{\vec{p}^2}{2m^*} \mathbb{I} - \frac{\alpha_R}{\hbar} \sigma_y p_x. \tag{1.49}$$

The 1D eigenstates and energies are respectively given as

$$\psi_{k_x\sigma}(x) = \frac{1}{\sqrt{2\pi\hbar}\sqrt{2}} {1 \choose -i\sigma} e^{ik_x x}, \qquad (1.50)$$

$$E_{\pm}(k_x) = \frac{\hbar^2}{2m^*} k_x^2 \pm \alpha_R k_x. \tag{1.51}$$

If both the RSOI and DSOI are present in a 2DQW, such as a zinc-blende semiconductor, the Hamiltonian for such system can be written as

$$H = \frac{\vec{p}^2}{2m^*} \mathbb{I} + \frac{\alpha_R}{\hbar} (\sigma_x p_y - \sigma_y p_x) + \frac{\beta_D}{\hbar} (\sigma_y p_y - \sigma_x p_x). \tag{1.52}$$

The eigenstates of this Hamiltonian can be expressed as

$$\psi_{k\sigma}(\vec{r}) = \frac{1}{2\pi\hbar\sqrt{2}} \left(\sigma \frac{\alpha_R(k_y - ik_x) + \beta_D(k_x - ik_y)}{\sqrt{(\alpha_R k_x - \beta_D k_y)^2 + (\alpha_R k_y - \beta_D k_x)^2}} \right) e^{i\vec{k}.\vec{r}}, \quad (1.53)$$

and the eigenenergies are given by

$$E_{\pm}(k) = \frac{\hbar^2}{2m^*} k^2 \pm \sqrt{(\alpha_R k_x - \beta_D k_y)^2 + (\alpha_R k_y - \beta_D k_x)^2}.$$
 (1.54)

In polar coordinates the eigenstates and the energy spectrum are respectively written as

$$\psi_{k\sigma}(\vec{r}) = \frac{1}{2\pi\hbar\sqrt{2}} {\sigma \choose ie^{i\varphi}} e^{i\vec{k}\cdot\vec{r}},\tag{1.55}$$

$$E_{\sigma}(k) = \frac{\hbar^2}{2m^*} \left[\left(k + \sigma \zeta(\eta, \theta, \phi_{\vec{k}}) \right)^2 - \left(\zeta(\eta, \theta, \phi_{\vec{k}}) \right)^2 \right], \tag{1.56}$$

where $\zeta(\eta,\theta,\phi_{\vec{k}})$ is the SOI dependent momentum and is given by $\zeta(\eta,\theta,\phi_{\vec{k}}) = \eta\sqrt{1+\sin2\theta\sin2\phi_{\vec{k}}}$ which describes an angular anisotropy of the spin-splitting where η and θ are respectively given by: $\eta=m^*\sqrt{\alpha_R^2+\beta_D^2}/\hbar^2$ and $\theta=\tan^{-1}(\beta_D/\alpha_R)$. One may notice the spinor phase φ in the wavefunction and energy is related to the RSOI and DSOI coefficients as: $\varphi=Arg[\alpha_R\exp(i\phi_{\vec{k}})+i\beta_D\exp(-i\phi_{\vec{k}})]$.

1.4 DISCRETE LATTICE MODELS

So far, we have discussed the interactions in continuum approximation. In reality, the discrete lattice models are more suitable for studying the interactions in LDS. The TBM is the

most studied models as a lattice model, where the electron is considered to be strongly bound to the individual atom and therefore the discrete nature of the lattice becomes important. If the wavelength of the electron is greater than a lattice constant, then electronic wavefunctions can overlap and as a result the electron can hop to the neighbouring atomic site and then the system behaves a metal. However, for such hopping to happen, the bands have to be partially filled. On the other hand, if the wavefunctions do not overlap, it is difficult for the electron to hop from one site to the other, giving rise to an insulating state of the system. This situation results when the electrons belong to completely filled or empty bands. Therefore, the TBM provides a suitable ground to explain the MIT in narrow-band systems. In this section, we present the models applicable to narrow-band systems under the TB approximation.

1.4.1 THE HOLSTEIN MODEL

Holstein formulated this model based on the TBM which can be written as

$$H = H_e + H_{ph} + H_{e-ph}, (1.57)$$

where,

$$H_e = \epsilon_0 \sum_{i\sigma} c_{i\sigma}^{\dagger} c_{i\sigma} - t \sum_{\langle ij \rangle \sigma} c_{i\sigma}^{\dagger} c_{j\sigma} + h.c., \qquad (1.58)$$

$$H_{ph} = \hbar\omega_0 \sum_{i} \left(b_i^{\dagger} b_i + \frac{1}{2} \right), \tag{1.59}$$

$$H_{e-p} = g_1 \sum_{i\sigma} n_{i\sigma} (b_i + b_i^{\dagger}). \tag{1.60}$$

In Eq. (1.58), the first term represents the total onsite energy, ϵ_0 being the on-site energy per site, $c_{i\sigma}^{\dagger}(c_{i\sigma})$ being the creation (annihilation) operator of an electron at the i^{th} site with the spin-index σ , the second term is the nearest-neighbour (NN) hopping term, i and j being the nearest neighbours and t the hopping amplitude. In Eq.(1.59), $b_i^{\dagger}(b_i)$ is the creation (annihilation) operator for a phonon at the i^{th} site with a dispersionless frequency ω_0 . In Eq.(1.60), $n_{i\sigma}(c_{i\sigma}^{\dagger}c_{i\sigma})$ is the number operator for the electron at site i with spin σ , $c_i = \begin{pmatrix} c_{i\uparrow} \\ c_{i\downarrow} \end{pmatrix}$ and g_1 is the e-p coupling strength.

1.4.2 THE HUBBARD MODEL

In 1963, Hubbard used this model to study the electronic correlations in narrow-band systems [129, 130]. Around the same time, this model was proposed independently by Gutzwiller [131] and Kanamori [132] to study the ferromagnetism in transition metals. Later, Hubbard gave an improved solution which could predict that the lattice at half-filling (one electron per site) undergoes the Mott MIT which otherwise was understood to be always metallic according to the band theory. For the 1D HM, the exact ground state (GS) solution using the Bethe ansatz (BA) was first given by Lieb and Wu [133] which predicts the absence of the Mott MIT at a non-zero Hubbard strength, U. Later, Essler et al. [134] have obtained the complete solution of 1D HM using the BA. The total Hamiltonian of a solid comprises the kinetic energy (KE) and potential energy (PE) parts as $H = H_{kin} + H_{pot}$, where the KE part contains electronic and ionic parts which is given as $H_{kin} = H_{kin-e} + H_{kin-ion}$, and the PE part contains the contributions from interaction between electrons, electrons and ions and ions which can be written as $H_{pot} = H_{e-e} + H_{e-ion} + H_{ion-ion}$. In the limit of the BOA, the ionic motions can be neglected and one can write: $H_{kin-ion} \approx 0$ and $H_{ion-ion} \approx \text{constant}$ (negligibly small). The total Hamiltonian under these approximations takes the form as

$$H = H_{kin-e} + H_{e-ion} + H_{e-e} = -\frac{\hbar^2}{2m} \sum_{j} \nabla_j^2 + \sum_{n} \sum_{j} V(\vec{R}_n - \vec{r}_j) + H_{e-e}, \quad (1.61)$$

where the first term represents the sum of the KEs of the electrons, and the second term represents the average potential acting on the *j*th electron created by the ions. Combining these two terms the above Hamiltonian looks like

$$H = \sum_{j} h_{j} + H_{e-e}, \tag{1.62}$$

where, h_i represents the single electron operator which can be written as

$$h_j = -\frac{\hbar^2}{2m} \nabla_j^2 + \sum_n V(\vec{R}_n - \vec{r}_j).$$
 (1.63)

In the second quantized notation the first term of the Eq. (1.62) can be expressed as

$$\sum_{i} h_{j} = \sum_{ij\sigma} \langle i\sigma | h_{j} | j\sigma \rangle c_{i\sigma}^{\dagger} c_{j\sigma}, \qquad (1.64)$$

where $\langle i\sigma | h_j | j\sigma \rangle = \int \phi_{i\sigma}^{\dagger}(\vec{r}) h_j \phi_{j\sigma}(\vec{r}) = t_{ij}$, where $\phi_{i\sigma}$ is the localized Wannier wave function of the electron centred at the i^{th} site with spin index σ denoting either the up-spin (\uparrow) or the down-spin (\downarrow) and t_{ij} is the amplitude of the overlap integral between any i^{th} and j^{th} sites. The e-e interaction can be represented as

$$H_{e-e} = \frac{1}{2} \sum_{i \neq j} \frac{e^2}{|\vec{r}_i - \vec{r}_j|'}$$
(1.65)

where \vec{r}_i denotes the position of the electron at i^{th} lattice site. In the second quantized notation the H_{e-e} can be expressed as

$$H_{e-e} = \frac{1}{2} \sum_{i,j,k,l} \sum_{\mu\nu\sigma\tau} \langle i\mu, j\nu \left| \frac{e^2}{|\vec{r} - \vec{r}'|} \right| k\sigma, l\tau \rangle c_{i\mu}^{\dagger} c_{j\nu}^{\dagger} c_{l\tau} c_{k\sigma},$$
(1.66)

where,

$$\langle i\mu, j\nu \left| \frac{e^2}{|\vec{r} - \vec{r}'|} \right| k\sigma, l\tau \rangle = e^2 \int \frac{\phi_{i\mu}^{\dagger}(\vec{r})\phi_{j\nu}^{\dagger}(\vec{r}')\phi_{l\tau}(\vec{r}')\phi_{k\sigma}(\vec{r})}{|\vec{r} - \vec{r}'|} d\vec{r} d\vec{r}' = U_{ijkl}.$$
 (1.67)

As these localized wavefunctions fall off exponentially, t_{ij} is most significant when i and j are NN sites. Therefore, t_{ij} becomes $t_{ij} = -t$ and $\sum_j h_j$ takes the following form

$$\sum_{j} h_{j} = -t \sum_{\langle ij \rangle \sigma} c_{i\sigma}^{\dagger} c_{j\sigma}, \tag{1.68}$$

where $\langle ij \rangle$ denotes the NN hopping. For the same reason mentioned above, U_{ijkl} is expected to decrease rapidly as $|\vec{r}_i - \vec{r}_j|$ increases. Therefore, the most valued contribution comes from the on-site term when i = j = k = l. Then, U_{ijkl} becomes $U_{ijkl} = U_{iiii} \equiv U$. So, H_{e-e} can be written for the on-site Coulomb interaction as

$$H_{e-e} = \frac{1}{2}U \sum_{i\sigma,\sigma=\uparrow,\downarrow} c_{i,-\sigma}^{\dagger} c_{i,\sigma}^{\dagger} c_{i,\sigma} c_{i,-\sigma}$$

$$= \frac{1}{2} U \sum_{i\sigma,\sigma=\uparrow,\downarrow} c_{i,-\sigma}^{\dagger} c_{i,-\sigma} c_{i,\sigma}^{\dagger} c_{i,\sigma}$$

$$= \frac{1}{2} U \left[\sum_{i} c_{i,\downarrow}^{\dagger} c_{i,\downarrow} c_{i,\uparrow}^{\dagger} c_{i,\uparrow} + \sum_{i} c_{i,\uparrow}^{\dagger} c_{i,\uparrow} c_{i,\downarrow}^{\dagger} c_{i,\downarrow} \right]$$

$$= U \sum_{i} n_{i\uparrow} n_{i\downarrow} , \qquad (1.69)$$

where $n_{i\sigma}$ is the number operator for the electrons at the i^{th} site and is written as $n_{i\sigma} = c_{i\sigma}^{\dagger} c_{i\sigma}$. Combining Eqs. (1.68) and (1.69), we finally get the Hubbard Hamiltonian as

$$H = -t \sum_{\langle ij \rangle \sigma} c^{\dagger}_{i\sigma} c_{j\sigma} + U \sum_{i} n_{i\uparrow} n_{i\downarrow}. \tag{1.70}$$

1.4.3 PERSISTENT CURRENT IN A MESOSCOPIC RING AND GEOMETRIC PHASES

In mesoscopic physics, the system's size is considered to be in the intermediate regime between the microscopic (atoms or molecules) objects and macroscopic ones, where the quantum coherence effects play a significant role. There exists a characteristic length L_{ϕ} over which the charge carrier can travel without the loss of their quantum phase (ϕ) coherence. This also corresponds to a finite phase breaking time τ_{ϕ} . Therefore, the coherence is maintained over a length scale or a time scale $L < L_{\phi}$ or $\tau < \tau_{\phi}$ respectively. In mesoscopic devices, the phase coherence can be lost leading to a decoherence effect due to the scattering processes and high temperature. The typical time and length scale of mesoscopic semiconductor devices at a low temperature (sub-Kelvin) are of the order of picoseconds and micrometres respectively. Most of the promising mesoscopic effects are seen in LDS such as 2DEG of semiconductor heterostructures (2DQW), 1D quantum wires and QDs. One of the most exciting phenomena in mesoscopic effects is A-B oscillations observed in conductance spectrum of a metallic QR [135]. Surprisingly, in a tiny 1D mesoscopic QR, the PCs can occur due to the A-B effect even if the ring is non-magnetic. The A-B effect is a quantum mechanical effect that arises when electrons move along two different paths of a closed contour (such as a QR) and a magnetic flux is made to pierce through the centre of the closed contour, then the magnetic field produces a phase (known as the Aharonov-Bohm phase) shift in the wavefunction of the electrons. The phase difference between two paths is proportional to the magnetic flux enclosed by the QR and is given by

$$\Delta \phi_{AB} = \frac{q}{\hbar} \oint \vec{A} \cdot \overrightarrow{dl} = \frac{q}{\hbar} \Phi, \tag{1.71}$$

where \vec{A} is the magnetic vector potential and Φ is the magnetic flux (A-B flux) enclosed by the QR. The A-B effect in a QR results from a gauge invariance of electromagnetic potential. Consider a particle moving through a region where $\vec{B} = 0$, $\vec{A} \neq 0$ and \vec{V} is the electrostatic potential. The SE for such case can be written as

$$i\hbar \frac{\partial \psi}{\partial t} = \left[\frac{1}{2m} \left(\frac{\hbar}{i} \vec{\nabla} - \frac{q\vec{A}}{c} \right)^2 + V \right] \psi. \tag{1.72}$$

Now applying a transformation $\psi = U\psi_0 = e^{ig(\vec{r})}\psi_0$ where $g(\vec{r}) = \frac{q}{\hbar} \int_0^{\vec{r}} \vec{A}(\vec{r}') \cdot \vec{dr}'$ the above equation (1.72) can be transformed to

$$i\hbar \frac{\partial \psi_0}{\partial t} = \left[-\frac{\hbar^2}{2m} \nabla^2 + V \right] \psi_0. \tag{1.73}$$

We can see that under the transformation, as $\psi \to \psi_0$, the vector potential \vec{A} is gone and the above SE (1.73) holds for the wavefunction ψ_0 . The phase factor $g(\vec{r})$ is analogous to the A-B phase ϕ_{AB} which leads to quantum interference effects. To see how quantum interference effect gives rise to a current we consider a 1D TB-QR consisting of N number of identical atomic sites as shown in the figure below (Fig.1.13).

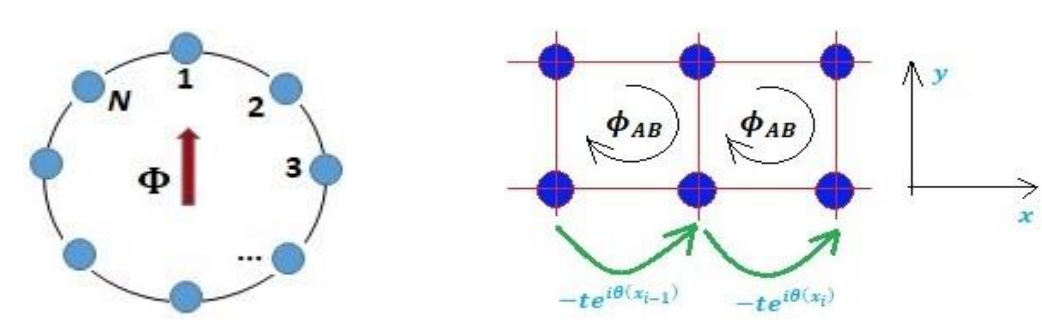


Fig.1.13 A 1D QR threaded by an A-B flux Φ. **Fig.1.14** 2D lattice hopping with Peierls phase θ .

Consider a 1D QR (in the TB scheme) with periodic boundary condition (PBC): $|N+1\rangle = |1\rangle$ which allows the quantization of the momenta $k=\frac{2\pi m}{N}, m=0,1,2,...,N-1$. The wavefunction ψ_0 (solution for $\vec{A}=0$) satisfies $\psi_0(\varphi+2\pi)=\psi_0(\varphi)$, while the new wavefunction ψ ($\vec{A}\neq 0$ solution) satisfies the *twisted PBC* as

$$\psi(\varphi + 2\pi) = e^{iN\theta}\psi(\varphi) = e^{i\phi_{AB}}\psi(\varphi) = e^{i\frac{2\pi\Phi}{\Phi_0}}\psi(\varphi), \tag{1.74}$$

where θ is the *Peierls phase factor* (PPF) which usually appears in the NN hopping term of a TB Hamiltonian of a crystal under the application of an external magnetic field \vec{B} and is related to the A-B phase as $\phi_{AB} = \frac{2\pi\Phi}{\Phi_0} = N\theta$, Φ being the A-B flux and $\Phi_0 = hc/e$ which is the magnetic flux quantum. The hopping term in Eq. (1.58) modifies after the inclusion of the *Peierls phase factor* (without spin) as

$$-t\sum_{\langle ij\rangle}c_i^{\dagger}c_j \to -t\sum_{\langle ij\rangle}c_i^{\dagger}\left(e^{i\int_{\vec{x}_i}^{\vec{x}_j}\vec{A}.\vec{dx}}\right)c_j = -t\sum_{\langle ij\rangle}c_i^{\dagger}e^{i\theta(\vec{x})}c_j, \tag{1.75}$$

where, $\theta(\vec{x}) = e^{i\int_{\vec{x}_i}^{\vec{x}_j} \vec{A} \cdot d\vec{x}}$ is the PP which originates when the electron hops from the lattice point \vec{x}_i to \vec{x}_j and is proportional to \vec{A} . This phase factor directly determines the A-B phase ϕ_{AB} which is obtained by summing all the PPs over the closed path shown in Fig.1.14. Hence, for a 1D QR the A-B phase is the sum of PPs of *N* lattice sites. Eq. (1.74) can be achieved by writing the TB Hamiltonian in terms of the PP as

$$H = -t \sum_{\langle ij \rangle} \left(e^{i\theta} c_i^{\dagger} c_j + h.c. \right) = -t \sum_{\langle ij \rangle} \left(e^{i\frac{\Phi_{AB}}{N}} c_i^{\dagger} c_j + h.c. \right)$$
$$= -t \sum_{\langle ij \rangle} \left(e^{i\frac{2\pi\Phi}{N\Phi_0}} c_i^{\dagger} c_j + h.c. \right), \tag{1.76}$$

The TB energy for this Hamiltonian (1.76) is obtained as

$$E = -2t\cos\left(k - \frac{2\pi\Phi}{N\Phi_0}\right),\tag{1.77}$$

The total PC (I_{PC}) in enclosed by the QR can be derived as follows. In the Heisenberg picture, the current at m^{th} site can be defined as

$$\frac{dn_m}{dt} = -\frac{i}{\hbar}[n_m, H],\tag{1.78}$$

where n_m is the number operator of the electron at m^{th} site of the QR. Calculating the commutation relation, Eq. (1.78) is expressed as

$$\frac{dn_m}{dt} = \frac{it}{\hbar} \left(e^{i\frac{\phi_{AB}}{N}} c_m^{\dagger} c_{m+1} - e^{-i\frac{\phi_{AB}}{N}} c_{m+1}^{\dagger} c_m - e^{i\frac{\phi_{AB}}{N}} c_{m-1}^{\dagger} c_m + e^{-i\frac{\phi_{AB}}{N}} c_m^{\dagger} c_{m-1} \right). \tag{1.79}$$

The continuity equation for n_m is given in terms of particle current j_m as

$$\frac{dn_m}{dt} = -(j_m - j_{m-1}),\tag{1.80}$$

Comparing Eqs. (1.79) and (1.80), we can write

$$j_{m} = -\frac{it}{\hbar} \left(e^{i\frac{\phi_{AB}}{N}} c_{m}^{\dagger} c_{m+1} - e^{-i\frac{\phi_{AB}}{N}} c_{m+1}^{\dagger} c_{m} \right), \quad (1.81)$$

The total particle current can be obtained as

$$J = \frac{1}{N} \sum_{m=1}^{N} j_m = -\frac{it}{N\hbar} \sum_{m=0}^{N-1} \left(e^{i\frac{\phi_{AB}}{N}} c_m^{\dagger} c_{m+1} - e^{-i\frac{\phi_{AB}}{N}} c_{m+1}^{\dagger} c_m \right) = \frac{\partial H}{\partial \phi_{AB}} = \frac{\Phi_0}{2\pi} \frac{\partial H}{\partial \Phi}. \quad (1.82)$$

For the electric current we can write $J_e = -eJ$. Therefore, in stationary state the total PC can be calculated as

$$I_{PC} = -\frac{\Phi_0}{2\pi} \langle \psi \left| \frac{\partial H}{\partial \Phi} \right| \psi \rangle = -\frac{\Phi_0}{2\pi} \frac{\partial E}{\partial \Phi} \,. \tag{1.83}$$

Therefore, both the energy and current are periodic in A-B flux Φ with period Φ_0 .

1.4.4 Spin-orbit interactions in a quantum ring

The Rashba and Dresselhaus SOIs in a 1D QR can be incorporated in a TB Hamiltonian as $H = H_0 + H_{SO}$, where H_0 represents the TB Hamiltonian (without SOI) and H_{SO} is the SO Hamiltonian. H_0 and H_{SO} are given by

$$H_0 = -t \sum_{i} \left(c_i^{\dagger} c_{i+1} + h.c. \right), \tag{1.84}$$

$$H_{SO} = -i\alpha_R \sum_{i} \left[c_i^{\dagger} (\sigma_x \cos \varphi_{i,i+1} + \sigma_y \sin \varphi_{i,i+1}) c_{i+1} + h.c. \right]$$

$$+i\beta_{D}\sum_{i}\left[c_{i}^{\dagger}(\sigma_{y}\cos\varphi_{i,i+1}+\sigma_{x}\sin\varphi_{i,i+1})c_{i+1}+h.c.\right],\tag{1.85}$$

where φ is the azimuthal coordinate of the ring: $\varphi_{i,i+1} = \frac{\varphi_i + \varphi_{i+1}}{2}$ where $\varphi_i = \frac{2\pi(i-1)}{N}$, i = 1,2,3,...N, α_R and β_D are respectively the strengths of RSOI and DSOI. Now, we define a unitary operator: $\mathcal{U} = \left(\frac{\sigma_x + \sigma_y}{2}\right)\sigma_z$ which transforms the Pauli matrices as

$$\mathcal{U}\sigma_{x}\mathcal{U}^{\dagger} = -\sigma_{y}, \qquad \mathcal{U}\sigma_{y}\mathcal{U}^{\dagger} = -\sigma_{x}, \qquad \mathcal{U}\sigma_{z}\mathcal{U}^{\dagger} = -\sigma_{z}.$$
 (1.86)

The total Hamiltonian after employing the unitary transformation transforms as

$$\begin{split} \widetilde{H} &= \mathcal{U}H\mathcal{U}^{\dagger} = \mathcal{U}H_{0}\mathcal{U}^{\dagger} + \mathcal{U}H_{SO}\mathcal{U}^{\dagger} \\ &= -t\sum_{i}\left(\tilde{c}_{i}^{\dagger}\,\tilde{c}_{i+1} + h.\,c.\right) \\ &+ i\alpha_{R}\sum_{i}\left[\tilde{c}_{i}^{\dagger}(\sigma_{y}\cos\varphi_{i,i+1} + \sigma_{x}\sin\varphi_{i,i+1})\,\tilde{c}_{i+1} + h.\,c.\right] \\ &- i\beta_{D}\sum_{i}\left[\tilde{c}_{i}^{\dagger}(\sigma_{x}\cos\varphi_{i,i+1} + \sigma_{y}\sin\varphi_{i,i+1})\,\tilde{c}_{i+1} + h.\,c.\right], \end{split} \tag{1.87}$$

where $\tilde{c}_i = \mathcal{U}c_i$ and $\tilde{c}_i^{\dagger} = c_i^{\dagger}\mathcal{U}^{\dagger}$. By comparing Eqs. (1.85) and (1.87), we see that the RSOI and DSOI strengths are interchanged in the new basis. Therefore, the RSOI and DSOI are

unitary conjugate to each other. Interestingly, if $\alpha_R = \beta_D$, H and \widetilde{H} become identical which means the total Hamiltonian is invariant if the strengths of RSOI and DSOI become equal.

1.5 MOLECULAR JUNCTION TRANSISTOR: SMT MODEL WITH DISSIPATION

Molecular junction transistors are interesting for their potential applications in single electron charge and spin transport, high gain switching devices, spintronics applications, quantum interference phenomena, phenomena related to Kondo effect and Coulomb blockade, molecular superconducting devices and so on. In this thesis, we wish to study the effect of the interactions discussed earlier and the interplay between these interactions on the quantum transport in an SMT system. As shown in Fig.1.15, an SMT system contains at its centre a molecule or a QD connected to two conducting leads which act as a source (S) and a drain (D). The S-QD-D system is placed on a substrate to which is attached a gate. The electrons in S and D can be treated as free electrons with continuous momentum states. The central QD contains discrete energy levels and so the QD electrons are described by localized states. Because of the application of a bias voltage, electrons from S can travel to D by tunnelling through QD which can also be controlled by the gate voltage. The tunneling of electrons from S to QD and QD to D and vice versa can be described by a hybridization term. The central QD can exhibit e-p, Hubbard and SO interactions and the QD-phonons can interact with the substrate phonons which will produce quantum dissipations. The model Hamiltonian for such a system can be described by the Anderson-Holstein-Caldeira-Leggett (AHCL) Hamiltonian as

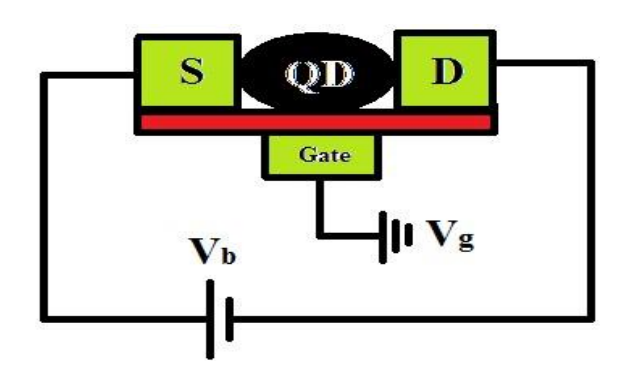


Fig.1.15 Schematic representation of an SMT device.

$$H = H_{S,D} + H_{OD} + H_T + H_V , (1.88)$$

where,

$$H_{S,D} = \sum_{k\sigma \in S,D} \varepsilon_k \, n_{k\sigma} \,, \tag{1.89}$$

$$H_{\rm QD} = \sum_{d\sigma} (\varepsilon_d - eV_g) n_{d\sigma} + \sum_{d} U n_{d\uparrow} n_{d,\downarrow} + \left(\frac{p_0^2}{2m_0} + \frac{1}{2} m_0 \omega_0^2 x_0^2 \right) + g \sum_{d\sigma} n_{d\sigma} x_0, (1.90)$$

$$H_T = \sum_{kd\sigma} \left[V_k \left(c_{kS,\sigma}^{\dagger} c_{d\sigma} + c_{kD,\sigma}^{\dagger} c_{d\sigma} \right) + h.c \right], \tag{1.91}$$

$$H_V = H_{BO} + H_{QD-B} \equiv \sum_{i=1}^{N} \left[\frac{p_i^2}{2m_i} + \frac{1}{2} m_i \omega_i^2 x_i^2 \right] + \sum_{i=1}^{N} \beta_i x_i x_0.$$
 (1.92)

In Eq. (1.89), $n_{k\sigma}(=c_{k\sigma}^{\dagger}c_{k\sigma})$ denotes the number operator for free electrons in S and D with momentum k and spin σ . In QD Hamiltonian (H_{QD}) (Eq.1.90), $n_{d\sigma}(=c_{d\sigma}^{\dagger}c_{d\sigma})$ is the number operator for the QD electrons in the single localized energy level ε_d , U refers to the onsite correlation energy. The third term of H_{QD} is the Hamiltonian for the local lattice mode of QD, where (x_0, p_0) are the coordinate and the corresponding canonical momentum of the QD oscillator with mass m_0 and frequency ω_0 . The fourth term represents the e-p coupling of the QD, where g gives the strength of the coupling between the electrons and phonon of the QD. The tunnelling Hamiltonian (1.91) gives tunneling of electrons from S to QD and QD to D, where V_k refers to the hybridization strength of the coupling between the QD and the leads. The Hamiltonian (1.92) is the vibrational part of the SMT system where x_i, p_i, m_i and ω_i denote respectively the position, momentum, mass and frequency of the ith bath-oscillator and β_i gives the measure of coupling strength between the QD phonon and the i-th bath phonon. This term generates dissipation in the QD phonon dynamics which essentially increases the tunnelling current as shown by Raju and Chatterjee [116].

1.6 OUTLINE OF THE THESIS

The thesis is organized as follows.

In Chapter 1 of the thesis, we present the motivations behind the work and introduce the continuum and discrete models used in this thesis and the basic formulations of the interactions mentioned above. In the continuum model, we describe the Fröhlich polaron, bound polaron and magnetopolaron and also Rashba and Dresselhaus SOIs. In the discrete model, we present the Hubbard and Holstein models for a narrow-band system. Next, we discuss how PC can be generated in a QR. We introduce the Hamiltonians for RSOI and DSOI in a QR. Finally, we present the model Hamiltonian for an SMT system and discuss the different processes involved in this system.

In Chapter 2, we investigate the role of RSO interaction on the polaron Zeeman effect in a two-dimensional parabolic QD. We formulate the system Hamiltonian using the well-known Fröhlich model and calculate the polaronic corrections to the energy states of the QD by employing an all-coupling Lee-Low-Pines-Huybrechts variational method and the secondorder Raleigh-Schrödinger perturbation theory. It is found that the e-p and RSO interactions influence each other in the presence of a magnetic field, while this interplay is missing in the absence of the field.

Chapter 3 of the thesis describes the combined effect of both the SOIs on the spintransport across a metal-semiconductor interface in the presence of a delta-function scatterer at the interface. The tunnelling current, conductance and spin-polarization are calculated using appropriate boundary conditions and the effects of RSOI and DSOI on the reflected and refracted spin-resolved currents and spin polarizations are studied. It is shown that the spinpolarization is greater when both the SOIs are present as compared to when only RSOI is present. The infinite potential across the interface reduces the tunnelling current and conductance and also makes the reflected spin-polarization zero. However, the refracted spinpolarization strongly depends on SOIs strength. We would like to mention that the delta potential does not have any effect on the magnitude of spin filtering.

In Chapter 4, we study the effect of DSOI on the persistent charge and spin currents in a one-dimensional mesoscopic QR threaded by an A-B flux in the presence of e-e and e-p interactions. In such a narrow-band system, we have a small polaron which is best described by the Holstein model and the e-e interactions can be treated by the Hubbard model. We therefore use the Holstein-Hubbard-Dresselhaus model to study the system. After decoupling the e-p interaction by the much-celebrated Lang-Firsov transformation and eliminating the DSOI by a unitary transformation, we treat the Hubbard correlation at the Hartree-Fock mean-field level and finally obtain the energy and current using a self-consistent numerical diagonalization method. It is observed that the DSOI enhances both the charge and spin currents and hence the spin-polarization significantly, while the e-p interaction reduces them.

As the mesoscopic phenomena strongly depend on the electronic number density and temperature, the effect of chemical potential and temperature have also been studied.

Molecular junction systems such as a single molecular transistor (SMT) show potential applications in nano-electronic, nano-photonic and spintronics devices. In **Chapter 5**, we consider a three-terminal device configured as a metal-QD-metal structure placed on an insulating substrate and investigate finite-temperature nonequilibrium quantum magneto-transport in the presence of local e-p and onsite Hubbard interactions and quantum dissipation. Following the approach of Raju and Chatterjee [116], the interaction between substrate phonons and the local QD phonon has been incorporated by the linear Caldeira-Leggett model. This interaction is partially eliminated by a unitary transformation which produces a dissipative effect in the phonon frequency which in turn influences the tunnelling current. The e-p interaction is dealt with the Lang-Firsov transformation. The transport properties such as spectral function, tunnelling current, conductance and spin-polarization are finally calculated using the nonequilibrium Keldysh Green function technique. It is observed that a magnetic field produces a spin-filtering effect in spectral function, tunnelling current and conductance while the temperature diminishes the spin-filtering effect.

In Chapter 6, we study the RSOI-induced quantum transport through a QD embedded in a two-arm quantum loop of a single molecular transistor at finite temperature in the presence of e-p and Hubbard interactions, an external magnetic field and quantum dissipation. The electrons from the source can tunnel to the drain following two paths, one through the arm of the loop that contains the QD and the other through the other arm of the loop that does not contain any QD. It is shown that in the absence of the magnetic field, the Rashba coupling alone separates the spin-up and spin-down currents which are equal and opposite with respect to the RSOI phase, causing a zero-field spin-polarization. Although, the spin-up and spindown currents behave differently in the presence of a magnetic field. We have also studied the combined effects of polaronic and SO interactions on the transport properties in different regimes of temperature and field. There exists a critical value of e-e interaction at which the gap between the spin-up and spin-down currents becomes maximum, causing a sharp discontinuity in the conductance spectrum. The polaronic interaction enhances the zero-field spin-polarization substantially. It is important to mention that the spin-polarization can be manipulated by tuning the Rashba strength, magnetic field and temperature. In this study, we have also analyzed the condition required to achieve the maximum spin-polarization for a particular strength of the RSOI and magnetic field at zero temperature in the SMT system.

Our results may find important applications in the fabrication of efficient spin-filtering devices in which the spin-filtering can be tuned by controlling the external magnetic field, RSOI and the e-p interaction in different temperature regimes.

Finally, in **Chapter 7**, we summarize and conclude our findings.

REFERENCES

- 1. A.D. Yoffe, Advances in Physics **42**:2, 173-262 (1993).
- 2. T. Edvinsson, R. Soc. open sci. 5: 180387 (2018).
- 3. I. Žutić, J. Fabian, and S. D. Sarma, Rev. Mod. Phys. **76**, 323 (2004).
- 4. S. A. Wolf et al., Science **294**, 1488 (2001).
- 5. J. Hubbard, Proc. R. Soc. Lond. A **276**, 238-257 (1963).
- 6. P. A. Lee, Rep. Prog. Phys. **71**, 012501 (2008).
- 7. S. Bednarek, B. Szafran, and J. Adamowski, Phys. Rev. B 59, 20 (1999).
- 8. U. Merkt, J. Huser, and M. Wagner, Phys. Rev. B 43, 9 (1991).
- 9. A. Matulis, J. O. Fjærestad, and K. A. Chao, Int. J. Mod. Phys. B **11**, 8 (1997).
- 10. M. Fujito, A. Natori, and H. Yasunaga, Phys. Rev. B 53, 15 (1996).
- 11. K. Keren, A. Stern, and U. Sivan, Eur. Phys. J. B 18, 311–318 (2000).
- 12. I. Ozfidan1, M. Korkusinski, and P. Hawrylak, Phys. Status Solidi RRL **10**, 1, 13–23 (2016).
- 13. L. Petit *et al.*, Nature **580**, 355-359 (2020).
- 14. H. E. Ercan, S. N. Coppersmith, and M. Friesen, Phys. Rev. B **104**, 235302 (2021).
- 15. L. Petit et al., Phys. Rev. Lett. **121**, 076801 (2018).
- 16. C. H. Yang et al., Nature **580**, 350-354 (2020).
- 17. D. G.-Gordon, H. Shtrikman, D. Mahalu, D. A.-Magder, U. Meirav, and M. A. Kastner, Nature **391**, 156 (1998).
- 18. D. Bing, and X. L. Lei, Phys. Rev. B **63**, 235306 (2001).
- 19. L. H. Yu and D. Natelson, Nano Lett. **4**, 79 (2003).
- 20. W. Liang, M. P. Shores, M. Bockrath, J. R. Long, and H. Park, Nature **417**, 725 (2002).
- 21. G. Gonzalez, M. N. Leuenberger, and E. R. Mucciolo, Phys. Rev. B **78**, 054445 (2008).
- 22. G. V. Scott and D. Natelson, ACS Nano 4, 7 (2010).
- 23. U. V. Pipit, A. Yasuo, S. Masanori, T. Toshiharu, and M. Yutaka, Mater. Res. Express 4, 024004 (2017).
- 24. M. C. Luffe, J. Koch, and F. von Oppen, Phys. Rev. B 77, 125306–7 (2008).
- 25. B. B. Chen et al., Phys. Rev. B 95, 035708 (2017).

- 26. J. K. Perron et al., Phys. Rev. B 96, 205302 (2017).
- 27. J. Kondo, Prog. Theor. Phys. 32 (1): 37-49 (1964).
- 28. P. J. Monisha, I. V. Sankar, S. Sil, and A. Chatterjee, Sci. Rep. 6, 20056 (2016).
- 29. A. Chatterjee, M. O. Smolkina, and I. Y. Popov, Nanosystems: Phys., Chem., Maths. **10** (1), 50-62 (2019).
- 30. A. Chatterjee and S. Mukhopadhyay, *Polarons and Bipolarons: An introduction*, CRC press, Taylors & Francis group (2019).
- 31. J. T Devreese, *Polarons in ionic crystals and polar semiconductors*, North Holland Publishing Company, Amsterdam, the Netherlands (1972).
- 32. A.S. Alexandrov, *Polarons in Advanced Materials*, Springer (2007).
- 33. L. D. Landau, Z. Phys. 3, 664 (1933).
- 34. L. D. Landau and S. I. Pekar, JETP 18, 341 (1948).
- 35. H. Fröhlich, Advances in Physics 3, 11 (1954).
- 36. W. J. Huybrechts, J. Phys. C: Solid State Phys. **10**, 3761 (1977).
- 37. A. Chatterjee, Ann. Phys. NY 202, 320 (1990).
- 38. S. Mukhopadhyay and A. Chatterjee, Phys. Rev. B 59, 12 (1999).
- 39. S. Mukhopadhyay and A. Chatterjee, Int. J. Mod. Phys. B 14, 32 (2000).
- 40. T. Stauber and R. Zimmermann, Phys. Rev. B **62**, 11 (2000).
- 41. F. Comas and Nelson Studart, Phys. Rev. B 69, 235321 (2004).
- 42. M. Bissiri et al., Phys. Rev. B **62**, 4642 (2000).
- 43. E. Cappelluti, C. Grimaldi, and F. Marsiglio, Phys. Rev. B 78, 085334 (2007).
- 44. C. Grimaldi, Phys. Rev. B 77, 024306 (2008).
- 45. J. T Devreese, J. Phys.: Condens. Matter 19, 255201 (2007).
- 46. Y.H. Ren *et al.*, Eur. Phys. J. B **7**, 651-656 (1999).
- 47. B. S. Kandemir and T. Altanhan, Phys. Rev. B 77, 045426 (2008).
- 48. A. Mogulkoc, M. Modarresi, and B.S. Kandemir, Eur. Phys. J. B 88:49 (2015).
- 49. C. H. Park, F. Giustino, M. L. Cohen, and S. G. Louie, Nano Lett. 8, 12 (2008).
- 50. G. S. N Eliel et al., Nat. Commun. 9, 1221 (2018).
- 51. A. Liu and A. M. Finkel'stein, Phys. Rev. B **101**, 241401 (R) (2020).
- 52. L. A. Ribeiro et al. J. Phys. Chem. Lett. 6, 510-514 (2015).
- 53. A. Privitera and W. Hofstetter, Phys. Rev. B **82**, 063614 (2010).
- 54. B. Kain and H. Y. Ling, Phys. Rev. A 96, 033627 (2017).
- 55. B. Kain and H. Y. Ling, Phys. Rev. A **94**, 013621 (2016).
- 56. T. Holstein, Ann. Phys. NY 8, 325 (1959).
- 57. T. Holstein, Ann. Phys. NY **8**, 343 (1959).
- 58. I. G. Lang and Y. A. Firsov, Sov. Phys. JETP **16**, 1301 (1962).

- 59. Y. Takada and A. Chatterjee, Phys. Rev. B 67, 081102 (R) (2003).
- 60. P. M. Krishna and A. Chatterjee, Physica C **457**, 55–59 (2007).
- 61. I. V Sankar and A. Chatterjee, Physica B: Condensed Matter 489, 17-22 (2016).
- 62. Ch. U. Lavanya, I. V Sankar, A. Chatterjee, Sci. Rep. 7, 1, 1-11 (2017).
- 63. D. Debnath, M. Z. Malik, A. Chatterjee, Sci. Rep. 11, 1, 1-14 (2021).
- 64. P. M. Krishna, S. Mukhopadhyay and A. Chatterjee, Physics Letters A **327**, 67–72 (2004).
- 65. I. V. Sankar, S. Mukhopadhyay, A. Chatterjee, Physica C: Superconductivity **480**, 55-60 (2012).
- 66. I. V. Sankar and A. Chatterjee, Eur. Phys. J. B 87, 7 (2014).
- 67. M. Büttiker, Y. Imry, and R. Landauer, Phys. Lett. A **96**, 365–367 (1983).
- 68. L. K Castelano, G.-Q Hai, B. Partoens, and F. M. Peeters, Phys. Rev. B **78**, 195315 (2008).
- 69. P. A. Orellana and M. Pacheco, Phys. Rev. B **71**, 235330 (2005).
- 70. S. K. Maiti, M. Dey, S. Sil, A. Chakrabarti, and S. N. Karmakar, EPL **95**, 57008 (2011).
- 71. M. Patra and S. K. Maiti, Annals of Physics **375**, 337-350 (2016).
- 72. E. M. Q. Jariwala, P. Mohanty, M. B. Ketchen, and R. A. Webb, Phys. Rev. Lett. **86**, 1594–1597 (2001).
- 73. R. Deblock, R. Bel, B. Reulet, H. Bouchiat, and D. Mailly, Phys. Rev. Lett. **89**, 206803 (2002).
- 74. H. Bluhm, N. C. Koshnick, J.A. Bert, M.E. Huber, and K. A. Moler, Phys. Rev. Lett. **102**, 136802 (2009).
- 75. P. J. Monisha, I. V. Sankar, S. Sil, and A. Chatterjee, Sci. Rep. 6, 20056 (2016).
- 76. S. Murakami, N. Nagaosa, and S. C. Zhang, Science 301 (2003).
- 77. B. A. Bernevig, T. L. Hughes, and S. C. Zhang, Science **314** (2006).
- 78. C. L. Kane and E. J. Mele, Phys. Rev. Lett. **95**, 226801 (2005).
- 79. X. L. Qi and S. C. Zhang, Rev. Mod. Phys. **83**, 4 (2011).
- 80. L. Tian et al., J. Phys. Chem. Lett. 11, 24, 10340–10347 (2020).
- 81. I. Aguilera, C. Friedrich, and S. Blugel, Phys. Rev. B 88, 165136 (2013).
- 82. L. Zhang, and X. J. Liu, arXiv:1806.05628v1 (2018).
- 83. S. Datta and B. Das, Appl. Phys. Lett. **56**, 665 (1990).
- 84. M. I. D'yakonov and V. I. Perel, Sov. Phys. Solid State 13, 3023–3026 (1971).
- 85. E. I. Rashba, Fiz. Tverd. Tela (Leningrad) 2, 1224 (1960).
- 86. E. I. Rashba, Sov. Phys. Solid State 2, 1109 (1960).
- 87. Yu. A. Bychkov and E. I. Rashba, J. Phys. C: Solid State Phys. 17 6039 (1984).

- 88. G. Dresselhaus, Phys. Rev. 100, 580 (1955).
- 89. V. M. Ramaglia, D. Bercioux, V. Cataudella, G. D. Filippis, C. A. Perroni, J. Phys. Condens. Matter **16**, 9143-9154 (2004).
- 90. T. Yokoyama, Y. Tanaka, J. Inoue, Phys. Rev. B 74, 035318 (2006).
- 91. J. C. Egues, C. Gould, G. Richter, L.W. Molenkamp, Phys. Rev. B **64**, 195319 (2001).
- 92. F. Meier, D. Loss, Phys. Rev. Lett. **90**, 16, 167204(4) (2003).
- 93. J. Schliemann, M. Lee, J. C. Egues, D. Loss, Phys. Rev. Lett. 90, 146801 (2003).
- 94. K. C. Hall, W. H. Lau, K. Gündoğdu, M. E. Flatté, T. F. Boggess, Appl. Phys. Lett. **83**, 14, 2937-2939 (2003).
- 95. A. Slobodskyy, C. Grould, T. Slobodskyy, C. Becker, G. Schmidt, W. Molenkamp, Phys. Rev. Lett. **90**, 24, 246601(4) (2003).
- 96. I. Žutić, S. D. Sarma, Phys. Rev. B **60**, 24, 16322(4) (1999).
- 97. U. Zülicke, C. Schroll, Phys. Rev. Lett. **88**, 2, 029701(1) (2001).
- 98. J.-Q. Lu, Y. Guo, F. Zhai, B.-L. Gu, J.-Z. Yu, Y. Kawazoe, Phys. Letts. A **299**, 616–621 (2002).
- 99. T. Koga, J. Nitta, H. Takayanagi, S. Datta, Phys. Rev. Lett. 88, 12, 126601(4) (2002).
- 100. B. Srisongmuang, P. Pairor, M. Berciu, Phys. Rev. B 78, 155317 (2008).
- 101. S. Bandyopadhyay, M. Cahay, J. Ludwick, Phys. Scr. **96**, 065806 (2021).
- 102. Y. Meir, N. S. Wingreen, and P. A. Lee, Phys. Rev. Lett. 66, 3048 (1991).
- 103. A. P. Jauho, N. S. Wingreen, and Y. Meir, Phys. Rev. B 50, 5528 (1994).
- 104. Z. Z. Chen, R. Lü, and B. F. Zhu, Phys. Rev B 71, 165324 (2005).
- 105. A. Khedri, T. A. Costi, and V. Meden, Phys. Rev. B 98, 195138 (2018).
- 106. F. Mireles and G. Kirczenow, Phys. Rev. B **66**, 024426 (2001).
- 107. M. H. Larsen, A. M. Lunde, and K. Flensberg, Phys. Rev. B 66, 033304 (2002).
- 108. M. Zarea, S. E. Ulloa, and N. Sandler, Phys. Rev. Lett. 108, 046601 (2012).
- 109. J. Moser et al., Phys. Rev. Lett. 99, 056601 (2007).
- 110. M. W. Wu, J. Zhou, and Q. W. Shi, Appl. Phys. Lett. 85, 2547 (2004).
- 111. F. Mahfouzi, N. Nagaosa, and B. K. Nikolic', Phys. Rev. Lett. 109, 166602 (2012).
- 112. J. R. Petta, S. K. Slater, and D. C. Ralph, Phys. Rev. Lett. 93, 13 (2004).
- 113. Q.-feng Sun, J. Wang, and H. Guo, Phys. Rev. B **71**, 165310 (2005).
- 114. R. G. Alvar, W. Lejia, D. B. Enrique, and A. N. Christian, Nat. Commun. **7**, 11595 (2016).
- 115. J. O. Thomas et al., Nat. Commun. 10, 4628 (2019).
- 116. N. R. Chebrolu and A. Chatterjee, Sci. Rep. 6, 18511 (2016).
- 117. M. Kalla, N. R. Chebrolu, and A. Chatterjee, Sci. Rep. 9, 16510 (2019).

- 118. M. Kalla, N. R. Chebrolu, and A. Chatterjee, Sci. Rep. 11, 10458 (2021).
- 119. M. Kalla, N. R. Chebrolu, and A. Chatterjee, Sci. Rep. 12, 9444 (2022).
- 120. Tarucha et al. Science 278, 1788 (1997).
- 121. S. Bednarek, B. Szafran, and J. Adamowski, Phys. Rev. B **59**, 20 (1999).
- 122. M. A. Reed, J. N. Randall, R. J. Aggarwal, R. J. Matyi, T. M. Moore, and A. E. Wetsel, Phys. Rev. Lett. **60**, 6 (1988).
- 123. U. Merkt, J. Huser, and M. Wagner, Phys. Rev. B 43, 9 (1991).
- 124. R.P. Feynman, Phys. Rev. 97, 3 (1955).
- 125. P. M. Platzman, Phys. Rev. **125**, 1961 (1962).
- 126. D. Stein, K. von Klitzing and G. Weimann, Phys. Rev. Lett. **51**, 130–3 (1983).
- 127. H. L. Störmer et al., Phys. Rev. Lett. **51**, 126 (1983).
- 128. Yu. A. Bychkov and E. I. Rashba, JETP Lett. 39, 2 (1984).
- 129. J. Hubbard, Proc. R. Soc. A **276**, 237–257 (1963).
- 130. J. Hubbard, Proc. R. Soc. A **281**, 401–419 (1964).
- 131. M. C. Gutzwiller, Phys. Rev. Lett. 10, 159–162 (1963).
- 132. J. Kanamori, Prog. Theor. Phys. **30**, 275–289 (1963).
- 133. E. H. Lieb, F. Y. Wu, Phys. Rev. Lett. 20, 1445 (1968).
- 134. F. H. L. Essler, V. E. Korepin, and K. Schoutens, Phys. Rev. Lett. **67**, 27 (1991).
- 135. R. A. Webb, S. Washburn, C. P. Umbach, and R. B. Laibowitz, Phys. Rev. Lett. **54**, 25 (1985).

CHAPTER 2

ROLE OF RASHBA SPIN-ORBIT INTERACTION ON POLARON ZEEMAN EFFECT IN A TWO-DIMENSIONAL QUANTUM DOT WITH PARABOLIC CONFINEMENT

ABSTRACT

We calculate the energies of the ground and the first excited states of a free polaron and that of a polaron bound to a Coulomb impurity in a QD with harmonic confinement in the presence of RSOI by employing the variation theory of Lee, Low and Pines as modified by Huybrechts for an all-coupling range of the e-p interaction and arbitrary confinement length. We show that in both cases, the RSOI removes the two-fold spin degeneracy of the first-excited states even in the absence of any applied magnetic field, though the ground state does not show any such spin splitting. The self-energy corrections due to the polaronic effect are however not affected by RSOI. We also investigate the combined effect of Rashba and polaronic interactions in the presence of an external magnetic field using the Rayleigh-Schrödinger perturbation theory. Application of our results to GaAs and CdS QDs shows that the suppression of the phonon-induced size-dependent Zeeman splitting in a QD is reduced by RSOI.

2.1 INTRODUCTION

Of late, the study of spin-physics in LDS has drawn tremendous attention for its application in the very important and emerging field of spintronics where the transport and other properties of the micro-electronic devices can be tuned by using the phenomenon of spinpolarization [1-6]. The spin polarization is caused by RSOI [7-10] which originates when the confinement potential of the nanostructures lacks the symmetry under the operation of structural inversion [11-12]. RSOI removes the spin-degeneracy of the electrons giving rise to spin-splitting which is tuneable by an external field [13-14]. In recent times, both theoretical and experimental studies have been carried out to explore the effects of SOI in quantum systems [15-31].

The coupling between electrons and phonons has been shown to have a key contribution in understanding electronic and several other important properties of quantum structures [32-40] and therefore it would be naturally interesting to investigate the combined effect of e-p interaction and SOI in QDs. Attempts have already been made in this direction, but to our knowledge, these studies seem to be restricted only to either weak or strong e-p coupling regime [41-55]. In the present work, we wish to determine the GS and the first excited state (ES) energies of an electron moving in a 2D PQD for all-e-p coupling in the presence of RSOI employing the LLPH method [32-39, 56-59]. We also extend our study to the case of a bound polaron. Imperfections being a rule rather than the exception, this study is more realistic and thus worth investigation. Finally, we examine the combined effect of RSOI and e-p interaction on the electron energies in a 2D PQD placed in a magnetic field applied perpendicular to the QD plane using the second-order RSPT. Our main goal here is to investigate the interplay between the RSOI and e-p interaction in the context of phononinduced Zeeman suppression in a polar QD. We consider two specific materials namely, GaAs and CdS QDs to which we apply our theory for the sake of concreteness. We observe that RSOI enhances the Zeeman splitting and thus opposes the suppressive effect of polaronic interaction.

ANALYTICAL MODELS AND FORMULATIONS 2.2

In this section, we formulate the model Hamiltonian and discuss the analytical techniques that we have used. This section comprises two parts. First, we formulate the model of a 2D PQD in the presence of e-p interaction and RSOI and calculate the GS and ES energies of the system and the polaronic corrections to these energies using LLPH all-coupling variational method in the absence of magnetic field. Next, we consider the system in the presence of an external magnetic field and calculate the polaronic corrections to the GS energy using RSPT. We also calculate the effective Zeeman splitting modified by the RSOI to see the interplay between e-p interaction and RSOI.

2.2.1 2D POLARON IN THE PRESENCE OF RSOI WITH PARABOLIC CONFINEMENT

We consider an electron of band mass m^* in a 2D PQD in the presence of RSOI. The electron also interacts with the longitudinal optical (LO) phonons of dispersionless frequency ω_0 . We shall work in FU [32-39,60] in which $\hbar=m^*=\omega_0=1$. The system can be modelled by the Hamiltonian in FU as

$$H = H_e + H_p + H_{ep}, (2.1)$$

where the electronic Hamiltonian H_e , the phonon Hamiltonian H_p and the e-p interaction Hamiltonian H_{ep} are given by

$$H_e = -\frac{1}{2} \left(\frac{1}{\rho} \frac{\partial}{\partial \rho} + \frac{\partial^2}{\partial \rho^2} + \frac{1}{\rho^2} \frac{\partial^2}{\partial \phi^2} \right) I + V_c(\rho) I + \alpha_R \sigma_z \frac{dV_c(\rho)}{d\rho} \left(-\frac{i}{\rho} \frac{\partial}{\partial \phi} \right), \quad (2.2)$$

$$H_p = \sum_{\vec{q}} b_{\vec{q}}^{\dagger} b_{\vec{q}} ,$$
 (2.3)

$$H_{ep} = \sum_{\vec{q}} (\xi_{\vec{q}} e^{-i\vec{q}.\vec{\rho}} b_{\vec{q}}^{\dagger} + h.c.), \qquad (2.4)$$

where everything is dimensionless and I is 2D unit matrix. In Eq. (2.1), ρ (ρ , φ) refers to the electron position vector, $V_c(\rho)$ is the confinement potential of the QD given by $V_c(\rho) = \frac{1}{2}\omega_h^2\rho^2$, ω_h being the frequency of the harmonic dot, and the third term describes RSOI, α_R denoting the RSOI coefficient and σ_z the z-component of the Pauli spin matrix. In Eq. (2.2), $b_q^{\dagger}(b_q)$ stands for the creation (annihilation) operator of a LO phonon of wave vector \mathbf{q} and frequency ω_0 . In Eq. (2.3), ξ_q is the e-p interaction coefficient given by: $|\xi_{\vec{q}}|^2 = (\sqrt{2}\pi/Vq)\alpha$, V being the QD area and α the electron-phonon (e-p) coupling constant given by $\alpha = 0$

 $(e^2/2\hbar\omega_0)(2m\omega_0/\hbar)^{1/2}(\epsilon_\infty^{-1}-\epsilon_0^{-1})$ [32-39]. We employ the LLPH technique and prescribe the variational function as

$$|\Psi\rangle = U_1 U_2 |0\rangle |\psi^{\nu}\rangle, \tag{2.5}$$

where the LLPH transformations U_1 and U_2 are respectively given by

$$U_1 = e^{S_1} = \exp\left[-ia\sum_{\vec{q}}(\vec{q}.\vec{\rho}) b_{\vec{q}}^{\dagger} b_{\vec{q}}\right], \tag{2.6}$$

$$U_2 = e^{S_2} = \exp\left[\sum_{\vec{q}} (f_{\vec{q}} b_{\vec{q}}^{\dagger} - f_{\vec{q}}^* b_{\vec{q}})\right]. \tag{2.7}$$

 $|0\rangle$ is the zero-phonon state. The choice of the electronic wavefunction $|\psi^{\nu}\rangle$ depends on the binding of the electron. As the confinement potential is a harmonic oscillator potential and the system has a cylindrical symmetry, we choose the following form of the trial wavefunction

$$|\psi^{v}\rangle = \left(\frac{\mu^{2|m|+2}}{\pi|m|!}\right)^{\frac{1}{2}} e^{im\varphi - \frac{\mu^{2}\rho^{2}}{2}} \rho^{|m|} \chi_{\sigma},$$
 (2.8)

where $\chi_{\sigma} = \begin{pmatrix} 1 \\ 0 \end{pmatrix}$ or $\begin{pmatrix} 0 \\ 1 \end{pmatrix}$, $m = 0, \pm 1, \pm 2, \dots$, and $a, f_{\vec{q}}$ and μ as variational parameters. The LLPH energy of the 2D PQD is calculated as following

$$E_{LLPH} = \langle \Psi | H | \Psi \rangle, \tag{2.9}$$

Where the wavefunction $|\Psi\rangle$ is given by Eq. (2.5). Therefore, E_{LLPH} can be expressed as

$$E_{LLPH} = \langle \psi^{v} | \langle 0 | \widetilde{\tilde{H}} | 0 \rangle | \psi^{v} \rangle, \tag{2.10}$$

where $\widetilde{\widetilde{H}}$ is calculated as $\widetilde{\widetilde{H}} = U_2^{-1}U_1^{-1}HU_1U_2$ which in other words can be calculated by the Baker-Campbell-Hausdorff formula as

$$\widetilde{H} = e^{S}He^{-S} = H + [S, H] + \frac{1}{2!}[S, [S, H]] + \cdots$$
 (2.11)

Therefore, the transformed Hamiltonian $\widetilde{\widetilde{H}}$ is obtained as

$$\widetilde{H} = e^{-S_{2}}e^{-S_{1}}He^{S_{1}}e^{S_{2}}$$

$$= \frac{\vec{p}^{2}}{2} + \frac{1}{2}\omega_{h}^{2}\rho^{2} + \sum_{\vec{q}}\left(1 + \frac{\alpha^{2}q^{2}}{2} - \alpha\vec{p}.\vec{q}\right)\left(b_{\vec{q}}^{\dagger} + f_{\vec{q}}^{*}\right)\left(b_{\vec{q}} + f_{\vec{q}}\right)$$

$$+ \frac{\alpha^{2}}{2}\sum_{\vec{q},\vec{q}'}(\vec{q}.\vec{q}')\left(b_{\vec{q}}^{\dagger} + f_{\vec{q}}^{*}\right)\left(b_{\vec{q}'}^{\dagger} + f_{\vec{q}'}^{*}\right)\left(b_{\vec{q}} + f_{\vec{q}}\right)\left(b_{\vec{q}'}^{\dagger} + f_{\vec{q}'}^{\dagger}\right)$$

$$+ \sum_{\vec{q}}(\xi_{\vec{q}} e^{-(1-\alpha)\vec{q}.\vec{\rho}}\left(b_{\vec{q}}^{\dagger} + f_{\vec{q}}^{*}\right) + h.c.\right) + \alpha_{R}\sigma_{z}\frac{dV_{c}(\rho)}{d\rho}\left(-\frac{i}{\rho}\frac{\partial}{\partial\varphi}\right). \quad (2.12)$$

The zero-phonon average of the transformed Hamiltonian is written as

$$\langle 0|\widetilde{\widetilde{H}}|0\rangle = -\frac{1}{2} \left[\frac{1}{\rho} \frac{\partial}{\partial \rho} + \frac{\partial^{2}}{\partial \rho^{2}} + \frac{1}{\rho^{2}} \frac{\partial^{2}}{\partial \varphi^{2}} \right] + \frac{1}{2} \omega_{h}^{2} \rho^{2}$$

$$+ \sum_{\vec{q}} \left[1 + \frac{a^{2}q^{2}}{2} + ia \vec{\nabla} \cdot \vec{q} \right] |f_{\vec{q}}|^{2} + \frac{a^{2}}{2} \sum_{\vec{q}, \vec{q}'} \vec{q} \cdot \vec{q}' |f_{\vec{q}}|^{2} |f_{\vec{q}'}|^{2}$$

$$+ \sum_{\vec{q}} (\xi_{\vec{q}} e^{-(1-a)\vec{q}\cdot\vec{\rho}} f_{\vec{q}}^{*} + h.c.) + \alpha_{R} \sigma_{Z} \frac{dV_{c}(\rho)}{d\rho} \left(-\frac{i}{\rho} \frac{\partial}{\partial \varphi} \right). \tag{2.13}$$

The energy E_{LLPH} is then calculated by taking the expectation with respect to the trial wavefunction $|\psi^{\nu}\rangle$ as

$$\begin{split} E_{LLPH} &= \langle \psi^{v} | \langle 0 \left| \widetilde{\widetilde{H}} \right| 0 \rangle | \psi^{v} \rangle \\ &= \frac{1}{2} \mu^{2} (1 + |m|) + \frac{1}{2} \frac{\omega_{h}^{2}}{\mu^{2}} (1 + |m|) \end{split}$$

$$+ \sum_{\vec{q}} \left[1 + \frac{a^2q^2}{2} + ia \, \langle \psi^v \big| \vec{\nabla} \big| \psi^v \rangle.\, \vec{q} \right] \big| f_{\vec{q}} \big|^2 + \frac{a^2}{2} \sum_{\vec{q},\vec{q}'} \vec{q}.\, \vec{q}' \big| f_{\vec{q}} \big|^2 \big| f_{\vec{q}'} \big|^2$$

$$+\sum_{\vec{q}} \left[\xi_{\vec{q}} \langle \psi^{\nu} | e^{-i(1-\alpha)\vec{q}.\vec{\rho}} | \psi^{\nu} \rangle f_{\vec{q}}^* + h.c. \right] \pm \alpha_R m \omega_h^2. \tag{2.14}$$

Next, we use symmetric QD approximation: $\sum_{\vec{q}} \vec{q} |f_{\vec{q}}|^2 = 0$. Under this approximation E_{LLPH} becomes

$$E_{LLPH} = \frac{1}{2}\mu^{2}(1+|m|) + \frac{1}{2}\frac{\omega_{h}^{2}}{\mu^{2}}(1+|m|) + \sum_{\vec{q}} \left[1 + \frac{a^{2}q^{2}}{2}\right] |f_{\vec{q}}|^{2} + \sum_{\vec{q}} \left[\xi_{\vec{q}}\lambda_{\vec{q}}^{*}f_{\vec{q}}^{*} + h.c.\right] \pm \alpha_{R}m\omega_{h}^{2}, \qquad (2.15)$$

where $\lambda_{\vec{q}}$ is given by

$$\lambda_{\vec{q}} = \langle \psi^{\nu} | e^{i(1-a)\vec{q}\cdot\vec{\rho}} | \psi^{\nu} \rangle. \tag{2.16}$$

To calculate E_{LLPH} we must minimize E_{LLPH} with respect to the variational parameters $f_{\vec{q}}$ ($f_{\vec{q}}^*$), a and μ . Minimizing with respect to $f_{\vec{q}}^*$ we obtain $f_{\vec{q}}$ as

$$\frac{\partial E_{LLPH}}{\partial f_{\vec{q}}^*} = 0 \Rightarrow \left[1 + \frac{\alpha^2 q^2}{2} \right] f_{\vec{q}} + \xi_{\vec{q}} \, \lambda_{\vec{q}}^* = 0 \Rightarrow f_{\vec{q}} = -\frac{\xi_{\vec{q}} \, \lambda_{\vec{q}}^*}{1 + \frac{\alpha^2 q^2}{2}}. \tag{2.17}$$

Substituting this form of $f_{\vec{q}}$ from Eq. (2.17) in Eq. (2.15), we express E_{LLPH} as

$$E_{LLPH} = \frac{1}{2}\mu^{2}(1+|m|) + \frac{1}{2}\frac{\omega_{h}^{2}}{\mu^{2}}(1+|m|) - \sum_{\vec{q}} \frac{\left|\xi_{\vec{q}}\right|^{2}\left|\lambda_{\vec{q}}\right|^{2}}{1+\frac{\alpha^{2}q^{2}}{2}} \pm \alpha_{R}m\omega_{h}^{2}, \quad (2.18)$$

where $\left|\lambda_{\vec{q}}\right|^2$ can be computed by Eq. (2.16) as

$$\left|\lambda_{\vec{q}}\right|^2 = \left|L_{-1-|m|}\left(-\frac{(1-a)^2q^2}{4\mu^2}\right)\right|^2.$$
 (2.19)

Hence, substituting Eq. (2.19) in Eq. (2.18), the variational energy of the 2D polaron with a parabolic confinement in the presence of RSOI is obtained as

$$E_{LLPH} = \frac{(1+|m|)}{2} \mu^2 + \frac{(1+|m|)}{2\mu^2 l_0^4} \pm \frac{\alpha_R m}{l_0^4}$$
$$-\frac{\alpha}{\sqrt{2}} \int_0^\infty \left| L_{-(1+|m|)} \left(-\frac{(1-a)^2 q^2}{4\mu^2} \right) \right|^2 \left(1 + \frac{a^2 q^2}{2} \right)^{-1} dq, \qquad (2.20)$$

where, the confinement length l_0 is related to confining harmonic frequency ω_h as $l_0 = \sqrt{\omega_h}$ which gives the effective size of QD and $L_{-(1+|m|)}(-(1-a)^2q^2/4\mu^2)$ is the Laguerre polynomial.

Next, we want to discuss two limiting cases for two extreme values of a. First, a=1 corresponds to the extended-state (weak coupling) limit and variation of E_{LLPH} with respect to μ in this case yields for the GS and ES energies respectively as following

$$E_{GS} = l_0^{-2} - \left(\frac{\pi\alpha}{2}\right),\tag{2.21}$$

$$E_{ES} = 2l_0^{-2} - \left(\frac{\pi\alpha}{2}\right) \pm \frac{\alpha_R}{l_0^4}.$$
 (2.22)

The localized state (strong coupling) limit can be obtained by putting a = 0, and following the same procedure as above, we obtain:

$$E_{GS} = l_0^{-2} - \frac{\sqrt{\pi}\alpha}{2l_0},\tag{2.23}$$

$$E_{ES} = 2l_0^{-2} - 11\left(\frac{\sqrt{\pi}\alpha}{32l_0}\right). \tag{2.24}$$

The actual variational energy E is obtained numerically by varying E_{LLPH} with respect to a and μ . The polaronic correction is defined as

$$\Delta E = E(\alpha) - E(\alpha = 0). \tag{2.25}$$

Thus, the GS and ES polaronic corrections for a 2D PQD can be respectively written as

$$\Delta E_{GS} = E_{GS} - l_0^{-2}, (2.26)$$

and

$$\Delta E_{ES} = E_{ES} - 2l_0^{-2}. (2.27)$$

In the bound polaron case [32-39,59,61], the electronic Hamiltonian H_e contains an extra Coulomb term: $-\beta/\rho$ (see Sec.1.3.1.1 for model Hamiltonian), where $\beta=e^2/\varepsilon_{\infty}$, ε_{∞} denoting the permittivity of QD in the high-frequency limit and the energy reads

$$E_{\beta} = E_{LLPH} - \left[\frac{\beta \mu \Gamma(|m| + \frac{1}{2})}{|m|!} \right]. \tag{2.28}$$

2.2.2 2D Magnetopolaron in the presence of RSOI

In the case of a 2D magnetopolaron in a PQD with RSOI, the effective electronic Hamiltonian in Eq. (2.1) is modified by the presence of a magnetic field as

$$H_e = -\frac{1}{2} \left(\frac{1}{\rho} \frac{\partial}{\partial \rho} + \frac{\partial^2}{\partial \rho^2} + \frac{1}{\rho^2} \frac{\partial^2}{\partial \phi^2} \right) I + \frac{1}{2} \omega^2 \rho^2 I - \frac{i\omega_c}{2} \frac{\partial}{\partial \phi} + \frac{1}{2} \mu_B g_s B \sigma_z$$

$$+\alpha_R \sigma_Z \frac{dV_c(\rho)}{d\rho} \left(-\frac{i}{\rho} \frac{\partial}{\partial \varphi} + \frac{\omega_c \rho}{2} \right), \tag{2.29}$$

where $\omega = (\omega_h^2 + \omega_c^2/4)^{1/2}$, $\omega_c = eB/m^*c$, B being the external magnetic field, μ_B the Bohr magneton, g_s the effective Landé-g factor and all other symbols have the same meaning as defined earlier. Our aim is to study the synergetic effect of e-p interaction and RSOI. The Hamiltonian (2.29) is exactly soluble and the eigenstates and eigenvalues [16-29] of H_e are given respectively by

$$\psi_{nm\sigma}^{(0)}(\boldsymbol{\rho},\varphi) = \left[\frac{\Omega_{\sigma} n!}{\pi(n+|m|!)}\right]^{1/2} (\Omega_{\sigma} \rho^2)^{\frac{|m|}{2}} e^{\frac{im\varphi - \Omega_{\sigma}\rho^2}{2}} L_n^{|m|} (\Omega_{\sigma}\rho^2) \chi_{\sigma}, \qquad (2.30)$$

$$E_{nm\sigma}^{(0)} = (2n + |m| + 1)\Omega_{\sigma} + \frac{m}{2}\omega_c + \sigma\left(\frac{g_s}{4}\omega_c + \alpha_R m\omega_h^2\right), \tag{2.31}$$

where Ω_{σ} is expressed as following

$$\Omega_{\sigma} = \sqrt{\omega_h^2 + \frac{\omega_c^2}{4} + \sigma \alpha_R \omega_h^2 \omega_c}, \qquad (2.32)$$

the spin function χ_{σ} in Eq. (2.30) is mentioned earlier where $\sigma=\pm 1$ correspond to the spin-polarization in the magnetic field direction and $L_n^{|m|}$ is the associated Laguerre polynomial. The polaron self-energy correction to electron energy to second order in RSPT reads

$$\Delta E_{nm\sigma} = -\sum_{n'm'} \sum_{\mathbf{q}} \frac{\left| \left\langle \psi_{n'm'\sigma}^{(0)}(\boldsymbol{\rho}, \boldsymbol{\varphi}) \right| \xi_{q} e^{-i\mathbf{q}.\boldsymbol{\rho}} \left| \psi_{nm\sigma}^{(0)}(\boldsymbol{\rho}, \boldsymbol{\varphi}) \right\rangle \right|^{2}}{\left(E_{n'm'\sigma}^{(0)} - E_{n,m,\sigma}^{(0)} + 1 \right)}$$

$$= -\left| \xi_{q} \right|^{2} \left\langle \psi_{nm\sigma}^{(0)} \right| e^{-i\mathbf{q}.(\boldsymbol{\rho}-\boldsymbol{\rho}')} G(\boldsymbol{\rho}, \boldsymbol{\rho}') \left| \psi_{nm\sigma}^{(0)} \right\rangle, \tag{2.33}$$

where $G(\rho, \rho')$ is the Green function corresponding to Hamiltonian (2.27) and is given by [64-66]

$$G(\boldsymbol{\rho}, \boldsymbol{\rho}') = \sum_{n'm'} \frac{\psi_{n'm'\sigma}^{(0)*}(\boldsymbol{\rho}, \varphi) \, \psi_{n'm'\sigma}^{(0)}(\boldsymbol{\rho}', \varphi)}{E_{n'm'\sigma}^{(0)} - E_{nm\sigma}^{(0)} + 1}$$

$$= \int dt \, \frac{\Omega_{\sigma} e^{-\left(1 - E_{n,m,\sigma}^{(0)}\right)t - \frac{\Omega_{\sigma}}{2}\left(\rho^{2} + {\rho'}^{2}\right) \coth(\Omega_{\sigma}t) - 2\,\rho \cdot \rho' \frac{\cosh\left(\frac{\omega_{c}\,t}{2}\right)}{\sinh(\Omega_{\sigma}t)}}{2\pi\,\sinh(\Omega_{\sigma}t)} e^{-2i\left(x'y - y'x\right)\frac{\sinh\left(\frac{\omega_{c}\,t}{2}\right)}{\sinh(\Omega_{\sigma}t)}},$$
(2.34)

which is valid for the entire range of the magnetic field for GS and for weak magnetic field $(\Omega_{\sigma} + \frac{\omega_c}{2} < 1)$ for the first two ESs. The perturbed energy of the system can be written as

$$E_{n,m,\sigma} = E_{n,m,\sigma}^{(0)} + \Delta E_{n,m,\sigma}, \tag{2.35}$$

where the polaronic corrections $\Delta E_{n,m,\sigma}$ for the GS and ESs are respectively given as

$$\Delta E_{0,0,\sigma} = -\frac{\alpha}{2} \sqrt{\pi \Omega_{\sigma}} \int_{0}^{\infty} dt \, e^{-t} \left[1 - e^{-\Omega_{\sigma} t} \cosh\left(\frac{\omega_{c} t}{2}\right) \right]^{-\frac{1}{2}}, \quad (2.36)$$

$$\Delta E_{0,\pm 1,\sigma} = -\frac{1}{2} \alpha \sqrt{\pi \Omega_{\sigma}} \int_{0}^{\infty} dt \, e^{-\left(1 - \Omega_{\sigma} \mp \frac{\omega_{c}}{2}\right)t} (1 - e^{-2\Omega_{\sigma}t})^{-1}$$

$$\times \left[2f_{\sigma} \left(g_{\sigma} \mp h_{\sigma} \right) + h_{\sigma}^{2} - f_{\sigma}^{2} \right] \left[f_{\sigma} \left(g_{\sigma} f_{\sigma} + h_{\sigma}^{2} \right) \right]^{-3/2}, \quad (2.37)$$

where,

$$f_{\sigma} = \left[1 + \coth(\Omega_{\sigma}t) - \cosh\left(\frac{\omega_{c}t}{2}\right) \sinh^{-1}(\Omega_{\sigma}t)\right], \tag{2.38}$$

$$g_{\sigma} = \left[1 + \coth(\Omega_{\sigma}t) + \cosh\left(\frac{\omega_{c}t}{2}\right)\sinh^{-1}(\Omega_{\sigma}t)\right], \tag{2.39}$$

$$h_{\sigma} = \sinh\left(\frac{\omega_{\rm c} t}{2}\right) \sinh^{-1}(\Omega_{\sigma} t). \tag{2.40}$$

We are interested in studying the level splitting as a function of both α and l_0 . Eqs. (2.36) and (2.37) clearly suggest that both the GS and ES polaronic corrections are linear in α . From the experimental point of view, it would be useful to define the renormalized cyclotron frequencies as

$$\omega_{c\sigma}^{\pm} = E_{0,\pm 1,\sigma} - E_{0,0,\sigma} \,, \tag{2.41}$$

and the Zeeman (or level) splitting (ZS) as

$$\Delta_{ZS} = \omega_{c_{\sigma}}^+ - \omega_{c_{\sigma}}^-. \tag{2.42}$$

The dipole selection rule allows the transitions

$$\omega_{c+}^{+} = E_{0,1,1} - E_{0,0,1}, \tag{2.43}$$

$$\omega_{c_{-}}^{+} = E_{0,1,-1} - E_{0,0,-1}, \tag{2.44}$$

$$\omega_{c_{-}} = E_{0,-1,-1} - E_{0,0,-1}, \tag{2.45}$$

$$\omega_{c_{+}}^{-} = E_{0,-1,1} - E_{0,0,1}. \tag{2.46}$$

In the absence of RSOI, $\omega_c^+_+ = \omega_c^+_-$ and $\omega_c^-_- = \omega_c^-_+$. But the inclusion of RSOI results in a few more Zeeman lines because of an additional splitting due to RSOI. Here we present our numerical results for GaAs and CdS QDs. As shown above, one can define four Rashba-Zeeman (RZ) splittings. We consider, for example, the frequency difference $(\omega_c^+_+ - \omega_c^-_-)$ which we will call Δ_{RZ} . Therefore, throughout the numerical analysis we refer Δ_{RZ} as

$$\Delta_{RZ} = \left(\omega_{c_+}^+ - \omega_{c_-}^-\right). \tag{2.47}$$

2.3 NUMERICAL RESULTS AND DISCUSSIONS

In this section, we numerically compute the energies of the 2D polaron in the presence of RSOI with parabolic confinement both in the absence and presence of the magnetic field. At first, we show the results for the 2D polaron in the absence of the external magnetic field. Later, we present the same for the magnetopolaron case.

2.3.1 Results for 2D polaron without the external magnetic field

In the free-polaron case, Eq. (2.20) is minimized with respect to α and μ numerically to get the energy for all values of the coupling constant α . We take the values of α from Ref. [62,63].

Fig.2.1 provides the results for the size-dependence of the GS and the first ES energies of the polaron in a GaAs QD for a particular value of the RSOI coefficient α_R . It is clear from the figure that in the presence of RSOI, the two-fold spin-degeneracy of the first ES of the 2D PQD is lifted even in the absence of a magnetic field and as a result, the ES bifurcates into two levels corresponding to the two different eigenvalues of the spin operator, though

GS does not undergo any such split [16-30]. The splitting becomes more pronounced as the size of the QD is reduced. The spin-splitting also occurs in higher excited states in the $m \neq 0$ sectors (not shown here).

Fig.2.2 shows the plot of GS and ES energies with respect to α . The splitting of the ES is again visible but interestingly, the splitting energy is independent of α .

Figs.2.3(a) and 2.3(b) show the variation of the GS and ES polaronic corrections respectively for a 2D PQD of GaAs with respect to l_0 for three α values with $\alpha_R = 0$ and 0.05. From the figures, one can see that e-p interaction leads to significantly large polaron self-energies (ΔE) at small values of effective QD size l_0 . As l_0 is increased, ΔE s initially decreases very rapidly, but beyond a certain l_0 , they decrease very slowly, asymptotically reaching the bulk values. Also, the plots for $\alpha_R = 0$ are identical to those for $\alpha_R = 0.05$ for different values of α . Thus, we are led to conclude that the polaron self-energies for GS and the first ESs of a 2D PQD are unaffected by RSOI for a 2D PQD.

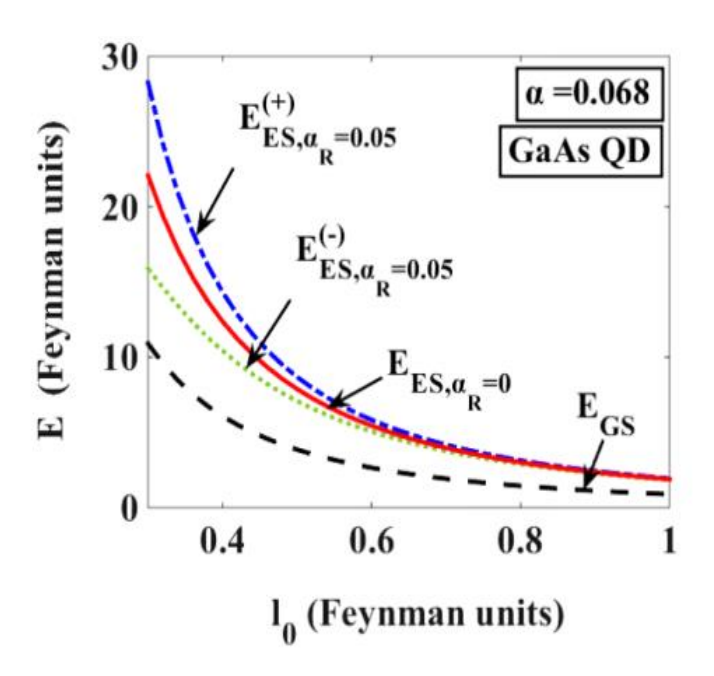


Fig.2.1 GS and first ES energies (*E*) of a free polaron (in FU) vs. dot size, l_0 (in FU) with $\alpha_R = 0$ and 0.05 (in FU) for a GaAs QD.

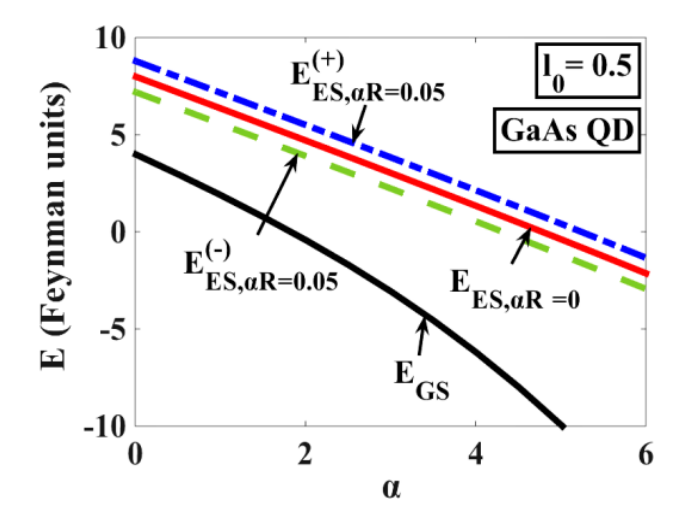


Fig.2.2 GS and first ES energies(*E*) of a free polaron (in FU) vs. α with $\alpha_R = 0$ and 0.05 (in FU) for a GaAs QD.

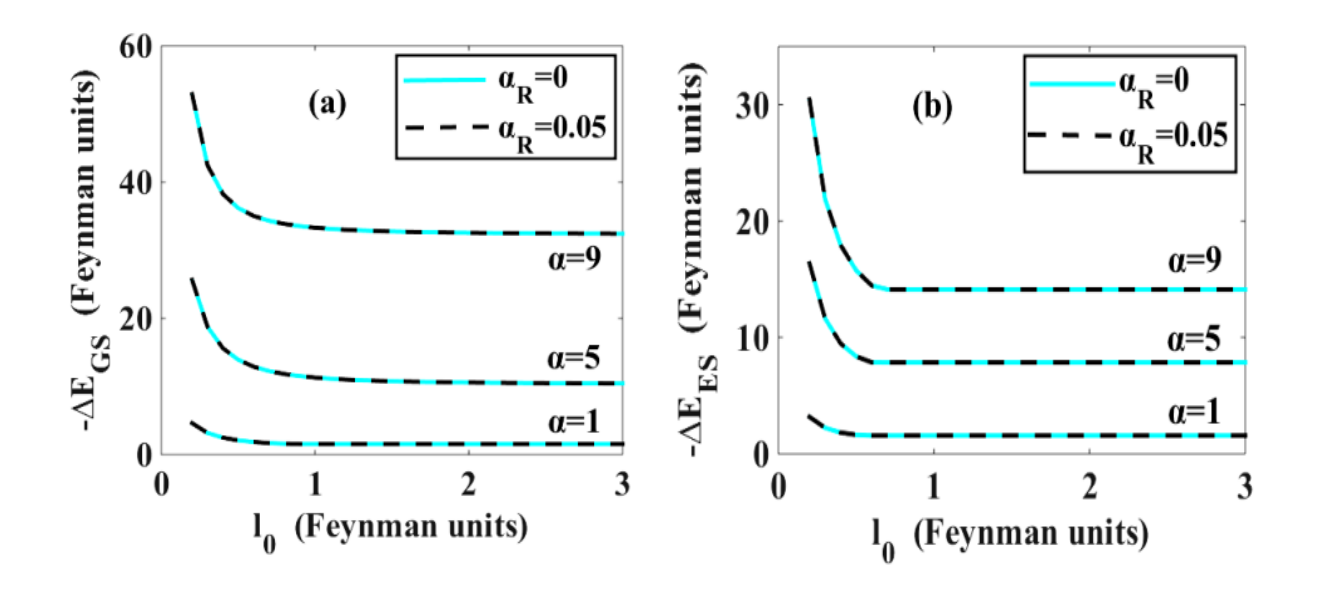


Fig.2.3. Polaronic corrections for (a) GS $(-\Delta E_{GS})$ (b) ES $(-\Delta E_{ES})$ vs. l_0 for $\alpha = 1, 5, 9$ and $\alpha_R = 0, 0.05$.

We define the transition frequencies as $\omega^{\pm} = E_{ES}^{\pm} - E_{GS}$ and Rashba spin-splitting energy as $\Delta_R = E_{ES}^+ - E_{ES}^- = \omega^+ - \omega^-$. It is observed that spin-splitting energy Δ_R does not depend on e-p interaction, α (not shown here) which confirms the observations made in Fig.2.3. But Δ_R indeed depends on the size of the QD which can be seen in Fig.2.4. For small l_0 , the effect is considerably large and it decreases as l_0 increases and eventually reduces to zero in the bulk limit. Thus, this size-dependent spin-splitting is purely a quantum phenomenon that arises when the length scale reaches the quantum domain.

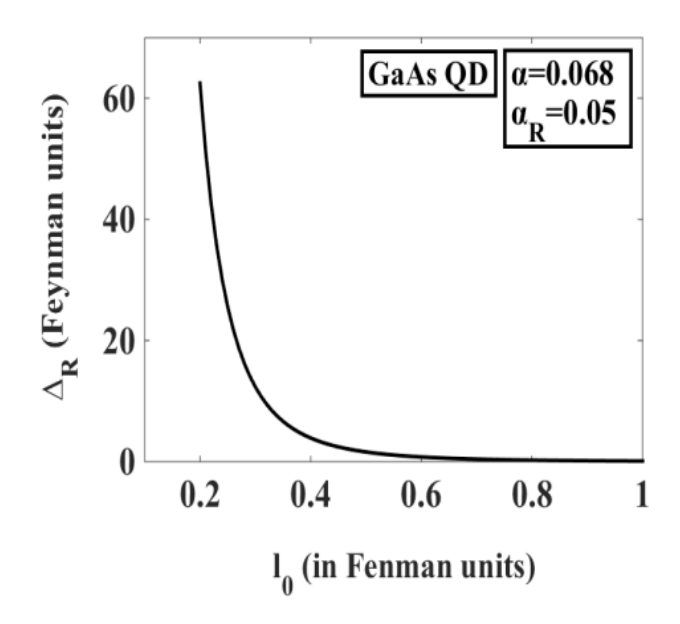


Fig.2.4 Spin-splitting energy, Δ_R vs. l_0 for a GaAs QD with $\alpha_R = 0.05$.

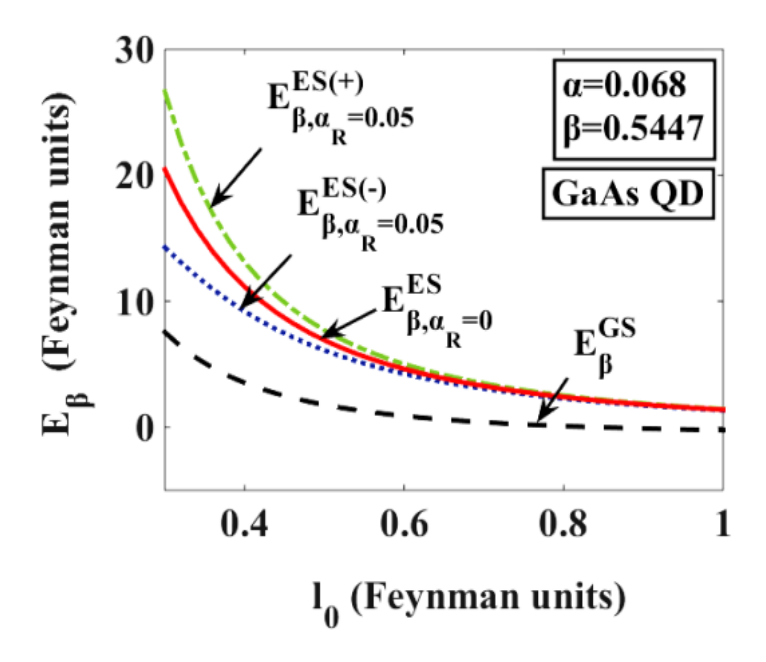


Fig.2.5 Bound polaron energy, E_{β} for GS and first ES vs. l_0 in FU for a GaAs QD with $\alpha_R = 0$, 0.05.

Figs.2.5 and 2.6 show the GS and ES energies for a bound polaron case. The results have qualitatively the same nature as those obtained for the free polaron. We have also studied the behaviour of the GS and ES polaron self-energies with respect to the effective QD size (not shown here). The behaviour is similar to the free polaron case.

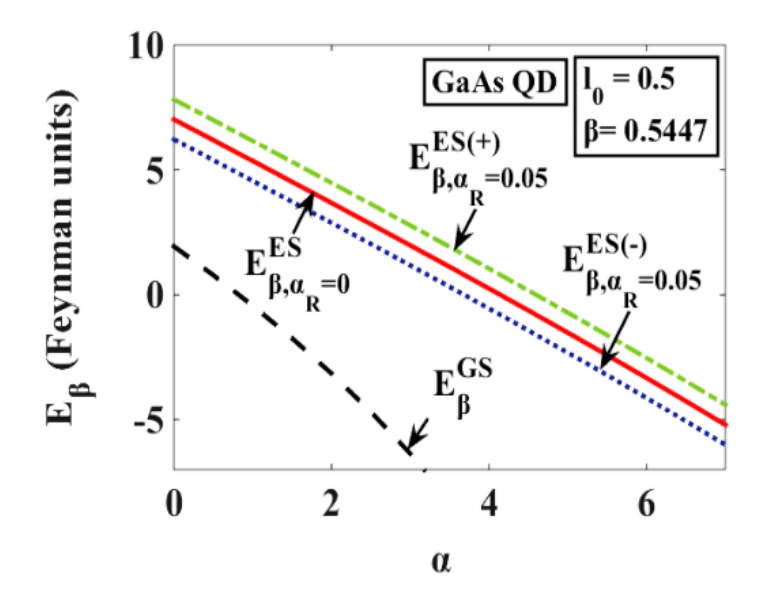


Fig.2.6 E_{β} vs. α for GS and first ES in a GaAs QD with $\alpha_R=0$ or 0.05 and $l_0=0.5$ in FU.

2.3.2 RESULTS FOR 2D MAGNETOPOLARON WITH THE EXTERNAL MAGNETIC FIELD

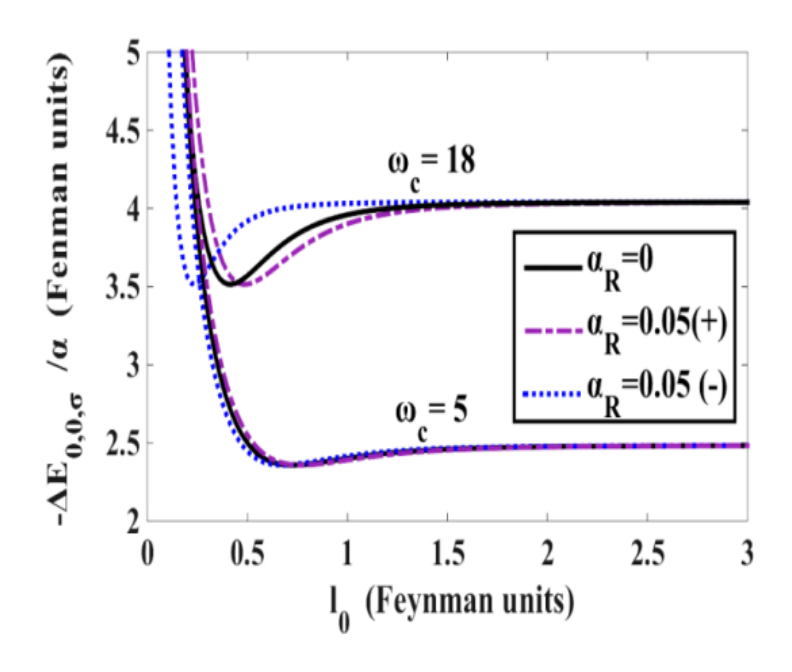


Fig.2.7 GS self-energy correction $\Delta E_{0,0,\sigma}$ (in FU) of a 2D magnetopolaron vs. l_0 (in FU) for two values of ω_c (in FU).

Fig.2.7 displays the behaviour of the GS polaron self-energy, $\Delta E_{0,0,\sigma}$ with respect to l_0 in the absence and presence of RSOI for two values of B. At a large magnetic field, polaronic

corrections become different for the spin-up (+) and spin-down (-) electronic states leading to a splitting of GS due to RSOI. Similar splitting also occurs for the excited states (not shown here). Interestingly enough, the e-p interaction and RSOI get intertwined in the presence of a magnetic field.

Fig.2.8 shows the dependence of RZ splitting, Δ_{RZ} on α for $\alpha_R = 0$ and 0.05 with $\omega_c = 0.3$ and $l_0 = 2.0$. Δ_{RZ} is found to be a linearly decreasing function of α both in the absence and presence of RSOI. The suppression of ZS caused by e-p interaction in a QD was predicted to be size-dependent by Mukhopadhyay and Chatterjee and Chatterjee and collaborators [67-69]. Fig.2.8 suggests that in the presence of RSOI, ZS becomes slightly larger for a small value of α_R which implies that RSOI enhances ZS. However, RSOI can be tuned by applying an external electric field and RSOI-induced ZS can be increased. Thus, the suppressive effect of the polaronic interaction on ZS is reduced because of the interplay between e-p interaction and RSOI.

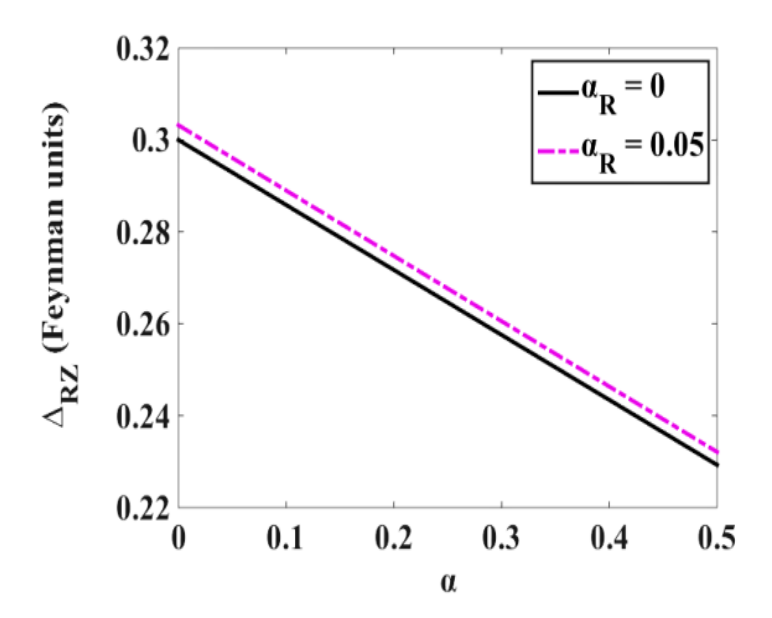


Fig.2.8 Δ_{RZ} (in FU) vs. α for GaAs QD with $\omega_c = 0.3$ (in FU) and $l_0 = 2.0$ (in FU).

To see the size-dependence of RZ splitting, we plot in Fig.2.9, Δ_{RZ} as a function of l_0 for GaAs and CdS QDs. The figure unequivocally shows that in the case of $\alpha = 0 = \alpha_R$, ZS is independent of l_0 . As was predicted earlier [67-69], in the presence of e-p interaction alone, below a certain l_0 , ZS becomes size-dependent and decreases rapidly with decreasing l_0 . However, ZS has a weak dependence on RSOI at low l_0 and the splitting increases rather slowly as the QD size decreases. Thus, RSOI has an opposite effect on ZS as compared to e-p interaction. However, this effect is normally smaller than that due to e-p interaction and

therefore, overall ZS will still decrease with decreasing QD size, but the decrease becomes less rapid in the presence of RSOI. The important to note is that RSOI can be increased by an external electric field and therefore RSOI-induced enhancement of ZS can be tuned. Thus, because of the interplay between e-p interaction and RSOI, ZS in a polar semiconductor QD can be controlled by tuning both the QD size and the external field and a desired resonant transition can be obtained. The interplay of e-p interaction and RSOI in the presence of a magnetic field can give rise to some interesting effects.

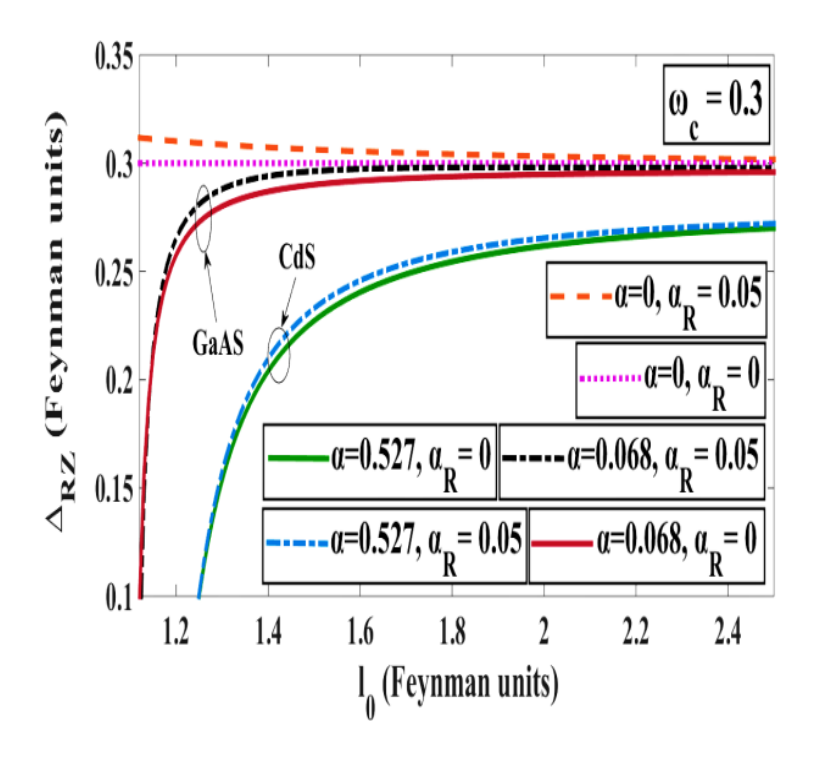


Fig.2.9 Δ_{RZ} for GaAs and CdS QDs as a function of l_0 with $\omega_c = 0.3$.

2.3 CONCLUSIONS

The polaron self-energy corrections for the GS and the first ESs of a 2D polar PQD with an arbitrary size have been calculated using an all-coupling variational theory incorporating the effect of RSOI. We observe that the two-fold degeneracy of the first ESs with respect to spin is lifted by RSOI even in the absence of a magnetic field leading to a discernible splitting of the first ESs, GS does not show any such splitting. Similar results are also observed for the bound polaron problem. Our calculation, when applied to a GaAs QD, suggests that though the polaron self-energies of both free and bound polarons are considerably large for small QDs, they remain unaffected by RSOI.

We have next considered the same QD system placed in a magnetic field and obtained the polaronic corrections for GS and the first ESs using the 2nd-order RSPT. In contrast to the B=0 case, the polaronic corrections now depend on RSOI for a sufficiently high magnetic field. Application of our theory to GaAs and CdS QDs reveals that the effects of e-p interaction and RSOI on ZS are opposite and both are size-dependent. While the e-p interaction suppresses ZS, RSOI enhances it, though the enhancement by RSOI is normally much small. However, in the presence of an external electron field, RSOI-induced ZS can be enhanced. Thus, in conclusion, the suppression of ZS caused by e-p interaction in a polar QD is reduced by RSOI. This interplay between e-p interaction and RSOI can give rise to some interesting effects in the presence of a magnetic field.

REFERENCES

- 1. E. A. de Andrada e Silva, Phys. Rev. B **60**, 8859 (1999).
- 2. C. Ming Hu, J. Nitta, T. Akazaki, J. Osaka, P. Pfeffer, and W. Zawadzki, Phys. Rev. B 60, 7736 (1999).
- 3. A. Voskoboynikov, S. Shin Liu, C. P. Lee, and O. Tretyak, J.Appl. Phys. 87, 1 (2000).
- 4. E. A. de Andrada e Silva, G. C. La Rocca, and F. Bassani, Phys. Rev. B 55, 16 293 (1997).
- 5. B. E. Kane, Nature (London) 393, 133 (1998).
- 6. S. Datta and B. Das, Appl. Phys. Lett. **56**, 665 (1990).
- 7. T. Koga, J. Nitta, H. Takayanagi, and S. Datta, Phys. Rev. Lett. 88, 126601 (2002).
- 8. A.W. Cummings, R. Akis, and D. K. Ferry, Appl. Phys. Lett. **89**, 172115 (2006).
- 9. F. Mei, S. Zhang, N. Tang, J. Duan, F. Xu, Y. Chen, W. Ge and B. Shen, Sci. Rep. 4, 4030 (2014).
- 10. E. N. Bulgakov and A. F. Sadreev JETP Letters 73, 505 (2001).
- 11. E. I. Rashba, Fiz. Tverd. Tela (Leningrad) 2, 1224 (1960).
- 12. E. I. Rashba, Sov. Phys. Solid State 2, 1109 (1960).
- 13. R. Dingle, A. C. Gossard, and W. Wiegmann, Phys. Rev. Lett. 34, 1327 (1975).
- 14. W. J. Skocpol, L. D. Jackle, E. L. Hu, R. E. Howard, and L. A. Fetter, Phys. Rev. Lett. 49, 951 (1982).
- 15. J. Nitta, T. Akazaki, H. Takayanagi, and T. Enoki, Phys. Rev. Lett. 78, 1335 (1997).
- 16. J. Lee, H. N. Spector, W. C. Chou, and C. S. Chu, J. Appl. Phys. 99, 113708 (2006).
- 17. T. Chakraborty and P. Pietiläinen, Phys. Rev. B **71**, 133305 (2005).

- 18. D.S Kumar, S. Mukhopadhyay and A. Chatterjee, Physica E 47, 270 (2013).
- 19. D. S. Kumar, S. Mukhopadhyay, A. Chatterjee, Physica B 501, 129 (2016).
- 20. O. Voskoboynikov, O. Bauga, C. P. Lee, and O. Tretyak, J. Appl. Phys. 94, 5891 (2003).
- 21. E. A. de Andrada e Silva, G. C. La Rocca, and F. Bassani, Phys. Rev. B 55, 16293 (1997).
- 22. V. Moroz and C. H. W. Barnes, Phys. Rev. B 61, R2464 (2000).
- 23. V. Moroz and C. H. W. Barnes, Phys. Rev. B 60, 14272 (2000).
- 24. W. H. Kuan, C. S. Tang, and W. Xu, J. Appl. Phys. 95, 6368 (2004).
- 25. D.S Kumar, A. Boda, S. Mukhopadhyay and A. Chatterjee, Superlattices and Microstructures 88, 174 (2015).
- 26. P. Pietiläinen and T. Chakraborty, Phys. Rev. B **73**, 155315 (2006).
- 27. R. Winkler, Spin-Orbit Coupling Effects in Two-Dimensional Electron and Hole System, Springer (2003).
- 28. Z. H. Liu, R. Li, X. Hu and J. Q. You, Sci. Rep. 8, 2302 (2018).
- 29. T. Chakraborty and P. Pietiläinen, Phys. Rev. Lett. 95, 136603 (2005).
- 30. O. Voskoboynikov, C. P. Lee and O. Tretyak, Phys. Rev. B 63, 165306 (2001).
- 31. E. Tsitsishvili, G. S. Lozano, and A. O. Gogolin, Phys. Rev. B 70, 115316 (2004).
- 32. A. Boda, B. Boyacioglu, U. Erkaslan and A. Chatterjee, Physica B 498, 43 (2016).
- 33. F. Herzog, H. Hardtdegen, T. Schäpers, D. Grundler and M. A Wilde, arXiv: cond-mat/1703.07143v1 (2017).
- 34. K. Premasiri, S. K. Radha, S. Sucharitakul, U. R. Kumar et al. Nano Lett., **18**, 4403 (2018).
- 35. S. D. Stranks and P. Plochocka, Nature Mat. 17, 381 (2018).
- 36. P. J. Monisha, I. V. Sankar, S. Sil and A. Chatterjee, Sci. Rep. 6, 20056 (2016).
- 37. P. Wójcik, A. Bertoni and G. Goldoni, Phys. Rev. B **97**, 165401 (2018).
- 38. D. S. Kumar, S. Mukhopadhyay, A. Chatterjee, J. Mag Mag Mat 418, 169 (2016).
- 39. P. Saini, A. Boda and A. Chatterjee, J. Mag Mag Mat 485, 407 (2019).
- 40. A. Chatterjee and S. Mukhopadhyay, *Polarons and Bipolarons: An Introduction, Taylor and Francis* (2018).
- 41. T.K. Mitra, A. Chatterjee and S. Mukhopadhyay, Phys. Rep. 153, 91 (1987).
- 42. S.Schmitt-Rink, D.A.B Miller and D.S. Chemla Phys. Rev. B 35, 8113 (1987).
- 43. S.Nomura and T. Kobayashi Phys. Rev. B 45, 1305 (1992).
- 44. K.D Zhu and S.W Gu Phys. Lett. A **163**, 435 (1992).
- 45. S. Mukhopadhyay and A. Chatterjee, Phys. Lett. A 204, 411 (1995).
- 46. S. Mukhopadhyay and A. Chatterjee, Int. J. Mod. Phys. B 10, 2781 (1996).
- 47. A. Chatterjee, S. Mukhopadhyay, Acta Phys. Pol. B 32, 473 (2001).
- 48. P. M. Krishna, S. Mukhopadhyay, A. Chatterjee, Solid State Commun. 138, 285 (2006).

- 49. Z. Li, Z. Ma, A. Wright and C. Zhang, App. Phys. Lett., **90**, 112103-1-3 (2007).
- 50. P. M. Krishna, S. Mukhopadhyay, A. Chatterjee, Phys. Lett. A 360, 655 (2007).
- 51. A. Chatterjee, M. O. Smolkina, I. Y. Popov, Nanosystems: Physics, Chemistry, Mathematics **10**, 50 (2019).
- 52. I.V. Shankar, P.J. Monisha, S.Sil and A.Chatterjee, Physica E 73, 175-180 (2015).
- 53. C. Grimaldi, Phys. Rev. B 77, 024306 (2008).
- 54. L.Covaci and M. Berciu, Phys. Rev. Lett. 102,186403 (2009).
- 55. A.Vartanian, A. Kirakosyan, and K.Vardanyan, Superlattices and Microstructures **109**, 655 (2017).
- 56. Z. X. Li, J. X. Wang, L. Kun Wang, Physica B **462**, 76 (2015).
- 57. X. J. Ma and J. L. Xiao, J. At. Mol. Sci. 4, 2, 138 (2013).
- 58. Z. X. Li, C. H Yin and X. Y. Zhu, Mod. Phys. Lett. B **29**, 1550124 (2015).
- 59. W.J Huybrechts, J. Phys. C: Solid State Phys. 10, 3761 (1977).
- 60. A. Chatterjee, Ann. Phys., NY **202**, 320 (1990).
- 61. R. P. Feynman, Phys. Rev. 97, 3 (1955).
- 62. A. Chatterjee, Phys. Lett. A 135, 380 (1989).
- 63. S. Mukhopadhyay, A. Chatterjee, Phys. Rev. B **55**, 9279 (1997).
- 64. E. Kartheuser, in *Polaron in Ionic Crystals and Polar Semiconductors*, edited by J.T. Devreese ~North-Holland, Amsterdam, p 717 (1972).
- 65. E. H. Sondheimer and A. H. Wilson, Proc. R. Soc. London, Ser. A 210, 173 (1952).
- 66. Y. Lepine and D. Matz, Can. J. Phys. 54, 1979 (1976).
- 67. S. Mukhopadhyay and A. Chatterjee, Phys. Rev. B 59, R7833 (1999).
- 68. S. Mukhopadhyay, A. Chatterjee, Int. J. Mod. Phys. B 14, 3897 (2000).
- 69. S. Mukhopadhyay, B. Boyacioglu, M. Saglam and A. Chatterjee, Physica E **40**, 776 (2008).

CHAPTER 3

SPIN-TRANSPORT ACROSS A TWO-DIMENSIONAL METAL SEMICONDUCTOR INTERFACE WITH INFINITE POTENTIAL IN PRESENCE OF SPIN-ORBIT INTERACTIONS: DOUBLE REFRACTION AND SPIN-FILTERING EFFECT

ABSTRACT

The spin-transport across a 2D metal-semiconductor junction with a Dirac-delta function potential at the interface and the RSOI and DSOI in the semiconductor region is studied exactly using discontinuous boundary conditions and the spin-polarized reflected and refracted current density and differential conductance are calculated. It is shown that in the presence of an infinite interface potential, an increase in the incident electron's energy reduces the spin splitting. It is also shown that the reflected and refracted coefficients, the spin-polarized currents and the corresponding differential conductance depend strongly on the SOIs. The reflected spin polarization, however, becomes zero due to the infinite potential. The RSOI enhances the refracted spin polarization while the DSOI reduces it. Thus, the maximum in polarization occurs at small values of DSOI and large values RSOI. Interestingly, though the presence of delta-potential at the interface does not change the magnitude of the spin-filtering, it causes a constant shift in the spin polarization.

3.1 Introduction

The SOI effect which has been studied quite extensively for the last few decades in semiconductor heterostructures and several other surface-alloy systems, lies at the heart of Spintronics [1,2] which is a new branch of modern condensed matter physics where spinsplitting due to SOI is used to manipulate properties and fabricate spin-based nano-devices. The very first spintronic device was proposed in the context of spin-FET by Datta and Das [3]. Due to the wide range of applicability, many research groups have studied the SOI effects in LDS [4-15]. Because of the advancement in experimental techniques such as electron-spin resonance, spin-resolved photoemission spectroscopy, scanning tunnelling microscopy etc., it is now possible to achieve spin-polarized transport in realistic systems like ferromagnet-semiconductor-ferromagnet interface [16],ferromagnet-superconductor interface [17], graphene spin-filter [18] and so on. But the Schottky barrier [19] across the semiconductor-metal interface should be carefully reduced by implementing suitable fabrication techniques [20] in order to get high transmissivity. These semiconductors are useful to get zero-field splitting [21-23] due to RSOI or DSOI, or both SOIs, which gives rise to many interesting phenomena in spin polarized mesoscopic transport [5, 21, 24-32].

Spin-filtering phenomenon based on SOI was first studied by Koga et al. [30] in a nonmagnetic tunnelling diode which was a proposed device based on RSOI. Srisongmuang et al. [31] have theoretically shown that under certain conditions, the tunnelling conductance in a metal-semiconductor junction system can be increased by increasing the spin-flip scattering potential at the interface. Very recently, Bandyopadhyay et al. have studied the reflection and refraction of an electron spin at a quasi-2D semiconductor (without SOI)-semiconductor (with SOI) junction [32] and also separately studied the same at a quasi-2D semiconductortopological insulator junction [33]. Khodas et al. [34] have shown that an unpolarized electron beam obliquely incident on a heterostructure interface separating two regions with different SOI strengths can undergo double refraction leading to two transmitted beams with different spin-polarized angles. They have, however, considered only RSOI to achieve this double refraction. Recently, Kalla et al. [35] have extended this idea to a 2D metalsemiconductor junction in the presence of both SOIs and found that the presence of DSOI causes a stronger spin-filtering effect. However, they have studied the system in the absence of a scattering potential at the interface. In this paper, we consider an infinite Dirac-delta potential at the metal-semiconductor interface and investigate the combined effect of RSOI and DSOI on doubly-refracted spin polarization using finite discontinuity condition in the first derivative of the wave functions at the interface. We show that the presence of deltascatterer has interesting effects on the reflection and transmission of electrons and hence on spin-polarized tunnelling current and conductance. We however observe that the infinite barrier does not change the angle of the refracted beams.

3.2 ANALYTICAL MODEL AND FORMULATION

The system considered in our study is an infinite 2D model system lying in the x-y plane where the region: x < 0 (region-I) denotes a metal and the region: x > 0 (region-II) denotes a semiconductor which has non-zero RSOI and DSOI. We write the Hamiltonian of the system as

$$H = H_I + H_{II} + H_{\Lambda} \,. \tag{3.1}$$

Here H_I represents the metallic region and can be written as

$$H_I = \frac{q_x^2}{2m} + \frac{q_y^2}{2m}$$
, for $-\infty \le x < 0$, (3.2)

where $q(q_x = q \cos \theta_i, q_y = q \sin \theta_i)$ is the momentum vector of the free electrons, θ_i being the incident angle and m is the electronic mass. The Hamiltonian H_{II} describing the semiconductor region is written as

$$H_{II} = \frac{p_x^2}{2m^*} + \frac{p_y^2}{2m^*} + \frac{\alpha}{\hbar} \left(\sigma_y p_x - \sigma_x p_y \right) + \frac{\beta}{\hbar} \left(\sigma_x p_x - \sigma_y p_y \right) + V_0 \text{, for } 0 < x \le \infty \text{, (3.3)}$$

where $p(p_x, p_y)$ and m^* represent respectively the momentum and the effective mass of the electrons in semiconductor region, the third and fourth terms describe respectively RSOI and DSOI in the region II with α and β being the respective strengths of the two interactions and V_0 gives the barrier height in region-II. H_{Δ} describes the interface Hamiltonian which is modelled by

$$H_{\Delta} = \Delta \delta(x) , \qquad (3.4)$$

where, $\delta(x)$ is the Dirac delta-function, Δ being the strength of the scattering potential. We can write the Schrödinger equation (SE) for the region-I as

$$H_I \psi_I = \varepsilon_a \psi_I \,, \tag{3.5}$$

where ψ_I is the electron wave function for the region-I and ε_q is the corresponding energy given by: $\varepsilon_q = \hbar^2 (q_x^2 + q_y^2)/2m = \hbar^2 q^2/2m$, m and $q(q_x, q_y)$ being the Bloch mass and wave function of the electron respectively. The wave function ψ_I corresponding to energy ε_q in the region-I can be expressed as a linear combination of incoming and reflected wave functions:

$$\psi_I(x,y) = \left(\frac{1}{\sqrt{2}} \begin{bmatrix} 1\\1 \end{bmatrix} e^{iq_x x} + \begin{bmatrix} b_\uparrow \\ b_\downarrow \end{bmatrix} e^{-iq_x x} \right) e^{iq_y y} \quad \text{, for } -\infty \le x < 0, \tag{3.6}$$

which has an x-part and a y-part. The x-part contains both the incident wave function and the reflected wave function. As the spins are not polarized in the metallic region-I, the x-part of the incident wave function consists of equally probable spin-up $\begin{bmatrix} 1\\0 \end{bmatrix}$ and spin-down $\begin{bmatrix} 0\\1 \end{bmatrix}$ configurations. We assume that the x-part of the reflected state is associated with probability amplitudes b_{\uparrow} and b_{\downarrow} for spin-up and spin-down electrons respectively. As the system has translational invariance along y-direction, the y-part for both incident and reflected wave functions is same. We can write the SE for the region-II as

$$H_{II}\psi_{II} = E_k\psi_{II} , \qquad (3.7)$$

where ψ_{II} can be written as

$$\psi_{II}(x,y) = \left(\begin{bmatrix} A_{II}^{(1)} \\ A_{II}^{(2)} \end{bmatrix} e^{ik_{x}x} + \begin{bmatrix} B_{II}^{(1)} \\ B_{II}^{(2)} \end{bmatrix} e^{-ik_{x}x} \right) e^{ik_{y}y} , \text{ for } 0 < x \le \infty,$$
 (3.8)

where in general, $A_{II}^{(1)}$ and $A_{II}^{(2)}$ denote the transmission amplitudes of spin-up and spin-down respectively in region-II and $B_{II}^{(1)}$ and $B_{II}^{(2)}$ denote the same for reflected part. Since there is no wave reflecting from region-II we can write $B_{II}^{(1)} = B_{II}^{(2)} = 0$. Using Eqs.(3.6) and (3.8), we obtain the eigen energies of region-II as

$$E_{k\pm} = \varepsilon_k + V_0 \pm k\lambda(\theta_k) \,, \tag{3.9}$$

where $\varepsilon_k = \hbar^2 (k_x^2 + k_y^2)/(2m^*) = \hbar^2 k^2/2m^*$ and $\lambda(\theta_k)$ being the angle-dependent effective SOI strength given by

$$\lambda(\theta_k) = \sqrt{\alpha^2 + \beta^2 + 4\alpha\beta \sin\theta_k \cos\theta_k} , \qquad (3.10)$$

where θ_k is the angle of refraction for the electron in the semiconductor region and is given by $\theta_k = tan^{-1}(k_y/k_x)$. In Eq. (3.9) we can see the energy splitting of the spin-up (+) and spin-down (–) states due to SOI. The wavefunction corresponding to $E_{k^{\pm}}$ then becomes

$$\psi_{II}(x,y) = \left(A_{II}^{(1)} \begin{bmatrix} 1 \\ -e^{-i\phi_{k^{+}}} \end{bmatrix} e^{ik_{x}^{+}x} + A_{II}^{(2)} \begin{bmatrix} e^{i\phi_{k^{-}}} \\ 1 \end{bmatrix} e^{ik_{x}^{-}x} \right) e^{ik_{y}y} \quad (3.11)$$

where $\phi_k = tan^{-1} \left(\frac{\alpha \cos \theta_k + \beta \sin \theta_k}{\alpha \sin \theta_k + \beta \cos \theta_k} \right)$. We also obtain the magnitude of energy-dependent momenta, k^{\pm} , as

$$k^{\pm} = -k_{SO} + \sqrt{k_{SO}^2 + \frac{2m(E_{k^{\pm}} - V_0)}{\hbar^2}} , \qquad (3.12)$$

with $k_{SO}=[m\lambda(\theta_{k^\pm})/\hbar^2]$, $k_x^\pm=k^\pm\cos\theta_{k^\pm}$ and $k_y^\pm=k^\pm\sin\theta_{k^\pm}$. Due to the translational invariance along the y-axis, the projection of the momentum vector should be continuous at x=0 i.e., $q_y=k_y^\pm$, which leads to $\theta_{k^\pm}=\sin^{-1}\{(q/k^\pm)\sin\theta_i\}$, where the θ_{k^+} and θ_{k^-} denote respectively the spin-up and spin-down splitting angles of the incoming wave in the region-II. Using θ_{k^\pm} – equations, we get $\lambda(\theta_{k^\pm})$ from Eq. (3.10) and we get E_{k^\pm} from Eq. (3.9) and then solving Eq. (3.12) self-consistently, we obtain k^\pm and corresponding energies E_{k^\pm} . The refractive indices corresponding to the two refracted waves are given by $n_{k^\pm}=(k^\pm/q)=(\sin\theta_i/\sin\theta_{k^\pm})$. There will be no transmission of incident wave when $\theta_i>\pi/2$. Therefore, there exist two critical angles, θ_c^+ and θ_c^- , in the region-II for each of the refracted waves which read

$$n_{k^{\pm}} = \sin \theta_c^{\pm} = \frac{m\lambda \left(\frac{\pi}{2}\right)}{\hbar\sqrt{2m\varepsilon_q}} \left[\mp 1 + \left(1 + \frac{2\hbar^2 \left(E_{k^{\pm}}\left(\frac{\pi}{2}\right) - V_0\right)}{m\left(\lambda \left(\frac{\pi}{2}\right)\right)^2}\right)^{1/2} \right]. \quad (3.13)$$

To calculate the probability amplitudes $A_{II}^{(1)}$, $A_{II}^{(2)}$, b_{\uparrow} and b_{\downarrow} , we employ the following boundary conditions [28,31]:

$$\psi_I(x=0,y) = \psi_{II}(x=0,y) = \psi(x=0,y), \qquad (3.14)$$

$$\left[\frac{\partial}{\partial x}\psi_I(x,y)\right]_{x=0} - \frac{m}{m^*} \left[\frac{\partial}{\partial x}\psi_{II}(x,y)\right]_{x=0} = \left(\frac{2m}{\hbar^2}\Delta + i\frac{m}{m^*}k_{SO}\,\sigma_y\right)\psi(x=0,y). \quad (3.15)$$

The discontinuity in the 2^{nd} boundary condition arises due to the presence of infinite barrier and SOI. We obtain

$$b_{\uparrow} = A_{II}^{(1)} - A_{II}^{(2)} e^{i\phi_{k^{+}}} - \frac{1}{\sqrt{2}} , \qquad (3.16)$$

$$b_{\downarrow} = A_{II}^{(1)} e^{-i\phi_{k^{-}}} + A_{II}^{(2)} - \frac{1}{\sqrt{2}}, \tag{3.17}$$

where,

$$A_{II}^{(1,2)} = \frac{\sqrt{2} \left[\left(1 + p_{kx}^{\pm} \right) \left(1 \pm e^{\pm i\phi_{k^{\pm}}} \right) + \xi \left(e^{\pm i\phi_{k^{\pm}}} \mp 1 \right) \right]}{M + N} , \qquad (3.18)$$

with, $M = (1 + p_{kx}^- + \xi e^{-i\phi_{k^-}})(1 + p_{kx}^+ + \xi e^{i\phi_{k^+}})$ and $N = [e^{-i\phi_{k^-}}(1 + p_{kx}^-) - \xi][e^{i\phi_{k^+}}(1 + p_{kx}^+) - \xi]$, where,

$$p_{kx}^{\pm} = \frac{m}{m^*} \frac{k_x^{\pm}}{q_x} - \frac{2mi}{\hbar^2} \frac{\Delta}{q_x} , \qquad (3.19)$$

$$\xi = \frac{m}{m^*} \frac{\lambda(\theta_{k^{\pm}})}{g_r}.\tag{3.20}$$

The reflection and transmission coefficients are given by

$$R_{\uparrow,\downarrow} = \left| b_{\uparrow,\downarrow} \right|^2 , \qquad (3.21)$$

$$T_{\uparrow,\downarrow} = \frac{m}{m^*} \left| A_{II}^{(1,2)} \right|^2 \left(\frac{k_x^{+,-} \pm k_{SO} \cos \theta_{k_x^{+,-}}}{q_x} \right). \tag{3.22}$$

From the second boundary condition (3.15), the current continuity equation at the interface (x = 0) can be expressed as

$$\left[\frac{1}{m^*}\left(\hat{p}_x + \hbar k_{SO}\sigma_y - \frac{2i}{\hbar}\Delta\right)\psi_{II}(x,y)\right]_{x=0} = \left[\frac{1}{m}\hat{p}_x\psi_I(x,y)\right]_{x=0},\tag{3.23}$$

where $\hat{p}_x = -i\hbar\partial/\partial x$. To see the conservation of probability current we multiply Eq. (3.23) with the Hermitian conjugate of $\psi_I(x,y)$ i.e., ${\psi_I}^{\dagger}(x,y)$ from the left-hand side which can be written at x = 0 as

$$\[\psi_I^{\dagger}(x,y) \frac{1}{m^*} \Big(\hat{p}_x + \hbar k_{SO} \sigma_y - \frac{2i}{\hbar} \Delta \Big) \psi_{II}(x,y) \Big]_{x=0} = \left[\psi_I^{\dagger}(x,y) \frac{1}{m} \hat{p}_x \psi_I(x,y) \right]_{x=0}. \quad (3.24)$$

Using the first boundary condition at x = 0, the above equation can be re-expressed as

$$\[\psi_{II}^{\dagger}(x,y) \frac{1}{m^*} \Big(\hat{p}_x + \hbar k_{SO} \sigma_y - \frac{2i}{\hbar} \Delta \Big) \psi_{II}(x,y) \Big]_{x=0} = \left[\psi_I^{\dagger}(x,y) \frac{1}{m} \hat{p}_x \psi_I(x,y) \right]_{x=0}.$$
 (3.25)

Equating the real parts on both sides of Eq. (3.25), in general, we get the probability current continuity equation as

$$\frac{\hbar k_{x}^{+}}{m^{*}} \left[\left| A_{II}^{(1)} \right|^{2} - \frac{1}{2} Re \left(A_{II}^{*(2)} A_{II}^{(1)} \right) (\cos \phi_{k^{+}} - \cos \phi_{k^{-}}) + \frac{1}{2} Im \left(A_{II}^{*(2)} A_{II}^{(1)} \right) (\sin \phi_{k^{+}} - \sin \phi_{k^{-}}) \right]$$

$$+\frac{\hbar k_{x}^{-}}{m^{*}}\left[\left|A_{II}^{(2)}\right|^{2}-\frac{1}{2}Re\left(A_{II}^{*(1)}A_{II}^{(2)}\right)(\cos\phi_{k^{+}}-\cos\phi_{k^{-}})-\frac{1}{2}Im\left(A_{II}^{*(1)}A_{II}^{(2)}\right)(\sin\phi_{k^{+}}-\sin\phi_{k^{-}})\right]$$

$$+\frac{\hbar k_{SO}}{m^*} \left[\left| A_{II}^{(1)} \right|^2 \sin \phi_{k^+} - \left| A_{II}^{(2)} \right|^2 \sin \phi_{k^-} \right]$$

$$-\frac{\hbar k_{SO}}{m^*} \left[\frac{1}{2} Im \left(A_{II}^{*(1)} A_{II}^{(2)} \right) + \frac{1}{2} Im \left(A_{II}^{*(1)} A_{II}^{(2)} \right) cos(\phi_{k^+} + \phi_{k^-}) \right. \\ \left. - \frac{1}{2} Re \left(A_{II}^{*(1)} A_{II}^{(2)} \right) sin(\phi_{k^+} + \phi_{k^-}) \right] \\ \left. - \frac{1}{2} Re \left(A_{II}^{*(1)} A_{II}^{(2)} \right) sin(\phi_{k^+} + \phi_{k^-}) \right] \\ \left. - \frac{1}{2} Re \left(A_{II}^{*(1)} A_{II}^{(2)} \right) sin(\phi_{k^+} + \phi_{k^-}) \right] \\ \left. - \frac{1}{2} Re \left(A_{II}^{*(1)} A_{II}^{(2)} \right) sin(\phi_{k^+} + \phi_{k^-}) \right] \\ \left. - \frac{1}{2} Re \left(A_{II}^{*(1)} A_{II}^{(2)} \right) sin(\phi_{k^+} + \phi_{k^-}) \right] \\ \left. - \frac{1}{2} Re \left(A_{II}^{*(1)} A_{II}^{(2)} \right) sin(\phi_{k^+} + \phi_{k^-}) \right] \\ \left. - \frac{1}{2} Re \left(A_{II}^{*(1)} A_{II}^{(2)} \right) sin(\phi_{k^+} + \phi_{k^-}) \right] \\ \left. - \frac{1}{2} Re \left(A_{II}^{*(1)} A_{II}^{(2)} \right) sin(\phi_{k^+} + \phi_{k^-}) \right] \\ \left. - \frac{1}{2} Re \left(A_{II}^{*(1)} A_{II}^{(2)} \right) sin(\phi_{k^+} + \phi_{k^-}) \right] \\ \left. - \frac{1}{2} Re \left(A_{II}^{*(1)} A_{II}^{(2)} \right) sin(\phi_{k^+} + \phi_{k^-}) \right] \\ \left. - \frac{1}{2} Re \left(A_{II}^{*(1)} A_{II}^{(2)} \right) sin(\phi_{k^+} + \phi_{k^-}) \right] \\ \left. - \frac{1}{2} Re \left(A_{II}^{*(1)} A_{II}^{(2)} \right) sin(\phi_{k^+} + \phi_{k^-}) \right] \\ \left. - \frac{1}{2} Re \left(A_{II}^{*(1)} A_{II}^{(2)} \right) sin(\phi_{k^+} + \phi_{k^-}) \right] \\ \left. - \frac{1}{2} Re \left(A_{II}^{*(1)} A_{II}^{(2)} \right) sin(\phi_{k^+} + \phi_{k^-}) \\ \left. - \frac{1}{2} Re \left(A_{II}^{*(1)} A_{II}^{(2)} \right) sin(\phi_{k^+} + \phi_{k^-}) \right] \\ \left. - \frac{1}{2} Re \left(A_{II}^{*(1)} A_{II}^{(2)} \right) sin(\phi_{k^+} + \phi_{k^-}) \\ \left. - \frac{1}{2} Re \left(A_{II}^{*(1)} A_{II}^{(2)} \right) sin(\phi_{k^+} + \phi_{k^-}) \\ \left. - \frac{1}{2} Re \left(A_{II}^{*(1)} A_{II}^{(2)} \right) sin(\phi_{k^+} + \phi_{k^-}) \\ \left. - \frac{1}{2} Re \left(A_{II}^{*(1)} A_{II}^{(2)} \right) sin(\phi_{k^+} + \phi_{k^-}) \\ \left. - \frac{1}{2} Re \left(A_{II}^{*(1)} A_{II}^{(2)} \right) sin(\phi_{k^+} + \phi_{k^-}) \\ \left. - \frac{1}{2} Re \left(A_{II}^{*(1)} A_{II}^{(2)} \right) sin(\phi_{k^+} + \phi_{k^-}) \\ \left. - \frac{1}{2} Re \left(A_{II}^{*(1)} A_{II}^{(2)} \right) sin(\phi_{k^+} + \phi_{k^-}) \\ \left. - \frac{1}{2} Re \left(A_{II}^{*(1)} A_{II}^{(2)} \right) sin(\phi_{k^+} + \phi_{k^-}) \\ \left. - \frac{1}{2} Re \left(A_{II}^{*(1)} A_{II}^{(2)} \right) sin(\phi_{k^+} + \phi_{k^-}) \\ \left. - \frac{1}{2} Re \left(A_{II}^{*(1)} A_{II}^{(2)} \right) sin(\phi_{k^+} + \phi_{k^+}) \\ \left. - \frac{1}{2}$$

$$+\frac{\hbar k_{SO}}{m^*} \left[\frac{1}{2} Im \left(A_{II}^{*(2)} A_{II}^{(1)} \right) + \frac{1}{2} Im \left(A_{II}^{*(2)} A_{II}^{(1)} \right) cos(\phi_{k^+} + \phi_{k^-}) \right. \\ \left. - \frac{1}{2} Re \left(A_{II}^{*(2)} A_{II}^{(1)} \right) sin(\phi_{k^+} + \phi_{k^-}) \right] \\ \left. - \frac{1}{2} Re \left(A_{II}^{*(2)} A_{II}^{(1)} \right) sin(\phi_{k^+} + \phi_{k^-}) \right] \\ \left. - \frac{1}{2} Re \left(A_{II}^{*(2)} A_{II}^{(1)} \right) sin(\phi_{k^+} + \phi_{k^-}) \right] \\ \left. - \frac{1}{2} Re \left(A_{II}^{*(2)} A_{II}^{(1)} \right) sin(\phi_{k^+} + \phi_{k^-}) \right] \\ \left. - \frac{1}{2} Re \left(A_{II}^{*(2)} A_{II}^{(1)} \right) sin(\phi_{k^+} + \phi_{k^-}) \right] \\ \left. - \frac{1}{2} Re \left(A_{II}^{*(2)} A_{II}^{(1)} \right) sin(\phi_{k^+} + \phi_{k^-}) \right] \\ \left. - \frac{1}{2} Re \left(A_{II}^{*(2)} A_{II}^{(1)} \right) sin(\phi_{k^+} + \phi_{k^-}) \right] \\ \left. - \frac{1}{2} Re \left(A_{II}^{*(2)} A_{II}^{(1)} \right) sin(\phi_{k^+} + \phi_{k^-}) \right] \\ \left. - \frac{1}{2} Re \left(A_{II}^{*(2)} A_{II}^{(1)} \right) sin(\phi_{k^+} + \phi_{k^-}) \right] \\ \left. - \frac{1}{2} Re \left(A_{II}^{*(2)} A_{II}^{(1)} \right) sin(\phi_{k^+} + \phi_{k^-}) \right] \\ \left. - \frac{1}{2} Re \left(A_{II}^{*(2)} A_{II}^{(1)} \right) sin(\phi_{k^+} + \phi_{k^-}) \right] \\ \left. - \frac{1}{2} Re \left(A_{II}^{*(2)} A_{II}^{(1)} \right) sin(\phi_{k^+} + \phi_{k^-}) \right] \\ \left. - \frac{1}{2} Re \left(A_{II}^{*(2)} A_{II}^{(1)} \right) sin(\phi_{k^+} + \phi_{k^-}) \right] \\ \left. - \frac{1}{2} Re \left(A_{II}^{*(2)} A_{II}^{(1)} \right) sin(\phi_{k^+} + \phi_{k^-}) \right] \\ \left. - \frac{1}{2} Re \left(A_{II}^{*(2)} A_{II}^{(1)} \right) sin(\phi_{k^+} + \phi_{k^-}) \right] \\ \left. - \frac{1}{2} Re \left(A_{II}^{*(2)} A_{II}^{(1)} \right) sin(\phi_{k^+} + \phi_{k^-}) \\ \left. - \frac{1}{2} Re \left(A_{II}^{*(2)} A_{II}^{(1)} \right) sin(\phi_{k^+} + \phi_{k^-}) \right] \\ \left. - \frac{1}{2} Re \left(A_{II}^{*(2)} A_{II}^{(1)} \right) sin(\phi_{k^+} + \phi_{k^-}) \\ \left. - \frac{1}{2} Re \left(A_{II}^{*(2)} A_{II}^{(1)} \right) sin(\phi_{k^+} + \phi_{k^-}) \\ \left. - \frac{1}{2} Re \left(A_{II}^{*(2)} A_{II}^{(1)} \right) sin(\phi_{k^+} + \phi_{k^-}) \\ \left. - \frac{1}{2} Re \left(A_{II}^{*(2)} A_{II}^{(1)} \right) sin(\phi_{k^+} + \phi_{k^-}) \\ \left. - \frac{1}{2} Re \left(A_{II}^{*(2)} A_{II}^{(1)} \right) sin(\phi_{k^+} + \phi_{k^-}) \\ \left. - \frac{1}{2} Re \left(A_{II}^{*(2)} A_{II}^{(1)} \right) sin(\phi_{k^+} + \phi_{k^-}) \\ \left. - \frac{1}{2} Re \left(A_{II}^{*(2)} A_{II}^{(1)} \right) sin(\phi_{k^+} + \phi_{k^+}) \\ \left. - \frac{1}{2} Re \left(A_{II}^{*(2)} A_{II}^{(1)} \right) sin(\phi_{k^+} + \phi_{k^+}) \\ \left. - \frac{$$

$$+\frac{\Delta}{m^{*}\hbar} \left[Im \left(A_{II}^{*(1)} A_{II}^{(2)} \right) (\cos \phi_{k^{+}} - \cos \phi_{k^{-}}) - Re \left(A_{II}^{*(1)} A_{II}^{(2)} \right) (\sin \phi_{k^{+}} - \sin \phi_{k^{-}}) \right]$$

$$+\frac{\Delta}{m^{*}\hbar} \left[Im \left(A_{II}^{*(2)} A_{II}^{(1)} \right) (\cos \phi_{k^{+}} - \cos \phi_{k^{-}}) + Re \left(A_{II}^{*(2)} A_{II}^{(1)} \right) (\sin \phi_{k^{+}} - \sin \phi_{k^{-}}) \right]$$

$$= \frac{\hbar q_{x}}{m} \left[1 - |b_{\uparrow}|^{2} - |b_{\downarrow}|^{2} \right].$$

$$(3.26)$$

In deriving Eq. (3.26) we have assumed both the angle of refractions θ_{k^+} and θ_{k^-} and hence φ_{k^+} and φ_{k^-} are real. If the region-II does not contain SOCs which means $\alpha=0=\beta$ so that $\varphi_{k^+}=0=\varphi_{k^-}$, $\lambda(\theta_k)=0$, $k_{SO}=0$, $\theta_{k^+}=\theta_{k^-}$, $k_x^+=k_x^-=k_x$ and $A_{II}^{(1)}=A_{II}^{(2)}$, then double refraction does not occur and in that limit with the help of Eqs. (3.21) and (3.22), Eq. (3.26) satisfies the usual current continuity equation as following

$$\frac{m}{m^*} \frac{k_x}{q_x} \left[\left| A_{II}^{(1)} \right|^2 + \left| A_{II}^{(2)} \right|^2 \right] \equiv T_{\uparrow} + T_{\downarrow} = 1 - R_{\uparrow} - R_{\downarrow}. \tag{3.27}$$

Next, we consider the zero-temperature refracted and reflected currents $(J_{\uparrow\downarrow}^{Refr}, J_{\uparrow\downarrow}^{Refl})$ which can be expressed as a function of bias voltage V as

$$J_{\uparrow\downarrow}^{Refr,Refl}(eV) = \frac{el^2q_f}{2\pi h} \int_0^{eV} d\varepsilon_q \int_{-\theta_m}^{\theta_m} d\theta_i \cos\theta_i \sqrt{1 + \left(\frac{\varepsilon_q}{E_f}\right)} \left(T_{\uparrow,\downarrow}, R_{\uparrow\downarrow}\right) , \quad (3.28)$$

where l^2 is the area of the metal, is the maximum possible angle of the incident wave given by

$$\theta_m = \sin^{-1}\left(\frac{k^-}{q}\right). \tag{3.29}$$

and E_f and q_f are the Fermi energy and Fermi wave vector respectively. We also calculate the spin-polarized differential conductance in the region-II as

$$G_{\uparrow,\downarrow}(V) \equiv \frac{dJ_{\uparrow\downarrow}(V)}{dV} = \frac{e^2 l^2 q_f}{2\pi h} \int_{-\theta_m}^{\theta_m} d\theta_i \cos \theta_i \sqrt{1 + \left(\frac{eV}{E_f}\right)} T_{\uparrow,\downarrow}. \quad (3.30)$$

To understand the spin-dependent tunnelling conductance more concretely, we define the spin-polarization of conductance as

$$P_J^{Refr,Refl} = \frac{J_{\uparrow}^{Refr,Refl} - J_{\downarrow}^{Refr,Refl}}{J_{\uparrow}^{Refr,Refl} + J_{\downarrow}^{Refr,Refl}} . \tag{3.31}$$

3.3 Numerical results and discussions

A schematic representation of the system is shown in Fig.3.1. We set V_0 =12 meV, m/m^* =0.042 and $k_{SO} = 0.05q_f$. One can see for normal incidence i.e., θ_i =0, there is no refraction. Due to the presence of RSOI and DSOI, the momenta and the corresponding refracting angles split into spin-up (+) and spin-down (-) branches in the semiconductor region. We obtain the reflection and transmission coefficients and the spin resolved current densities and tunnelling conductance of this system in the presence of the infinite delta potential and the SOIs.

In Fig.3.2(a), we show the variation of two refracted angles, θ_{k+} and θ_{k-} with respect to the angle of incidence (θ_i) in the presence of delta-function-scatterer at the metalsemiconductor junction for different strengths of RSOI (α) and DSOI (β). The values of the Fermi energy, bias voltage and the incident energy of the electrons are chosen as $E_f = 15$ meV, eV = 25 meV and $\varepsilon_q = 20$ meV respectively, for the purpose of concreteness. It has been observed that RSOI alone can cause spin-splitting of spin-up and spin-down electrons, but in the presence of both SOIs the angle of refraction reduces for both spin-up and spindown electrons. However, the spin-down refraction angle reduces much more than the spinup refraction angle and as a result the gap between the refracted beams of electrons of two different spin orientations increases. Thus, the spin-polarization is greater when both RSOI and DSOI are present as compared to when only RSOI is present. One can also observe that spin-up electrons can undergo a total internal reflection at a critical angle though the spindown electrons do not show any such effect. This feature was also suggested by Khodas et al. [34]. Kalla et al. [35] have studied this behaviour using continuous boundary conditions in the absence of the infinite potential at the interface. Here we have studied the system in the presence of an infinite delta potential at the metal-semiconductor interface using discontinuous boundary conditions. It is interesting to point out that the behaviour of double refracted waves for two different spin projections due to SOIs with respect to θ_i is exactly the same for $\Delta = 0$ and $\Delta \neq 0$. Therefore, the presence of an infinite potential at the junction does

not change the path of the spin-up and spin- down refracted electrons with respect to θ_i . We also plot $\theta_{k^{\pm}}$ vs. θ_i in Fig.3.2(b) to show the effect of incident energy on the refracted angles of the spin-up and spin-down electrons at particular strengths of RSOI and DSOI keeping E_f and eV fixed at 15 meV and 25 meV respectively. It is seen clearly that for $\Delta \neq 0$, the incident energy decreases the refracted angle of the spin-up electrons and increases that of the spin-down electrons, while for $\Delta = 0$, the scenario is completely opposite (inset).

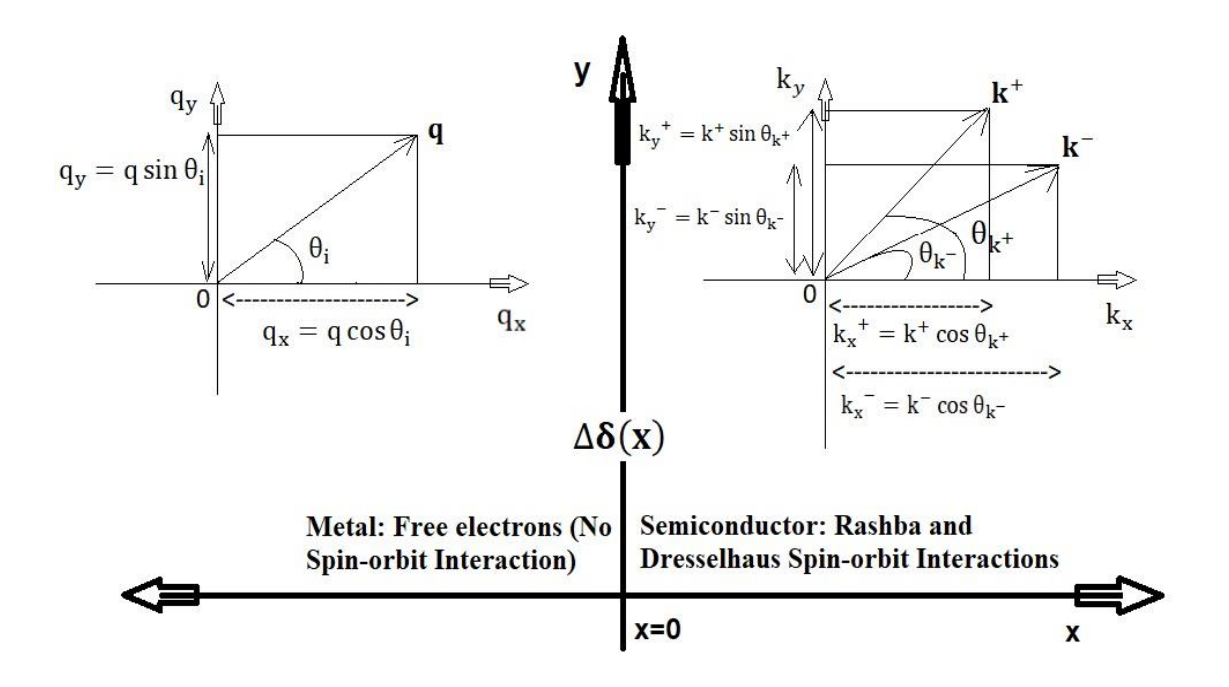


Fig.3.1 Sketch of the metal-semiconductor junction system.

The refraction coefficients T_{\uparrow} and T_{\downarrow} as a function of the incident angle θ_{i} for different α, β combinations are shown in Figs.3.3 (a) and (b) respectively at a particular Δ -value. We set E_{f} =15 meV, eV = 25 meV and ϵ_{q} = 20 meV for next few plots. Fig.3.3 (a) shows that for $\alpha \neq 0$, $\beta = 0$, the behaviour of θ_{i} with respect to θ_{i} =0 is almost symmetric except some kink like structures. For the θ_{i} <0 - region, as $|\theta_{i}|$ increases, T_{\uparrow} increases from a finite value at θ_{i} =0, reaches a small maximum and then decreases to zero after going through a kink structure. In the θ_{i} >0 region, save for the kink structure, T_{\uparrow} exhibits the same behaviour leading to the formation of a dip at θ_{i} =0. One may notice that DSOI enhances the refractivity and the peakstructure becomes much more prominent in the case of $\alpha = 0$, $\beta \neq 0$. For all the cases i. e., $\alpha > \beta$, $\alpha < \beta$ and $\alpha = \beta$, T_{\uparrow} behaves qualitatively in a similar way with respect to θ_{i} . T_{\uparrow} shows a clear maximum at some value of $|\theta_{i}|$ in the range $-a < \theta_{i} < a$, where a is a positive number and falls off to zero as θ_{i} increases on either side of normal incidence. For a set of set of (α, β) , T_{\uparrow} is higher for $\alpha < \beta$ than for $\alpha > \beta$. This can be concluded from the

figure by comparing the curve for α =3 meV-nm and β =5 meV-nm with that for α =5 meV-nm and β =3 meV-nm. It is also evident that the α = β - curve lies in between α > β and α < β - curves. One may also notice that the variation of T_{\uparrow} is not fully symmetric with respect to θ_i =0 except for the α = β - case.

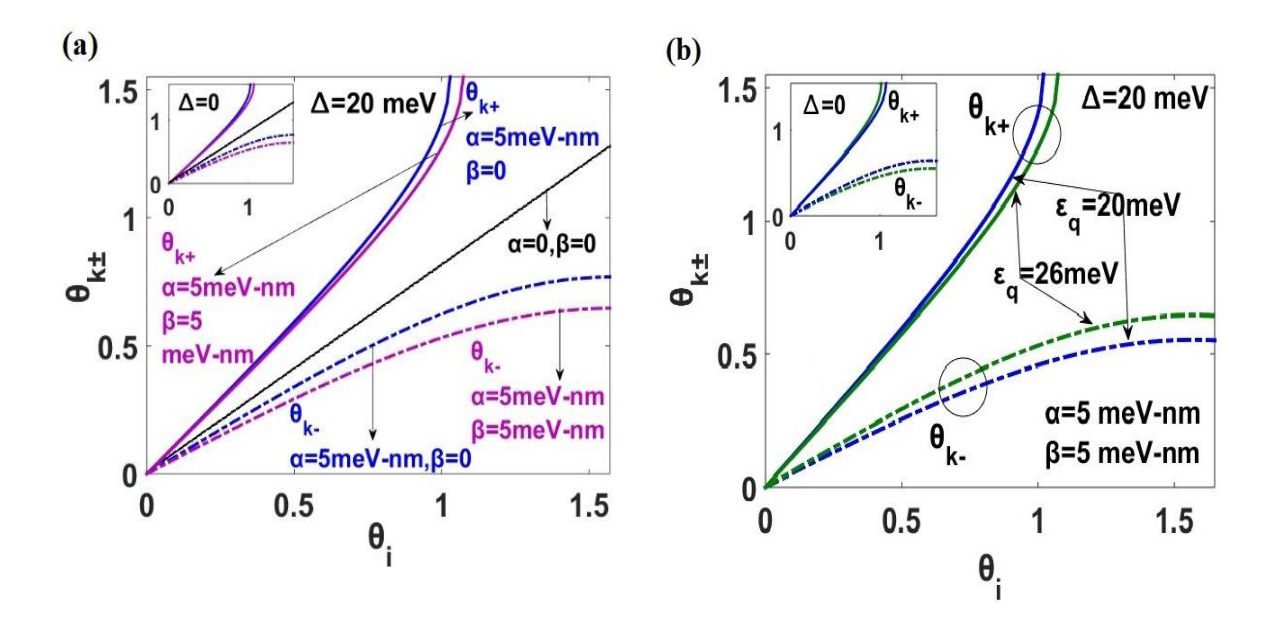


Fig.3.2 (a) $\theta_{k^{\pm}}$ as a function of θ_{i} for different α, β combinations at Δ = 20 meV. Inset: at Δ = 0. (b) $\theta_{k^{\pm}}$ as a function of θ_{i} for ϵ_{q} = 20 meV and ϵ_{q} = 26 meV at α =β =5 mev-nm. Inset: at Δ = 0.

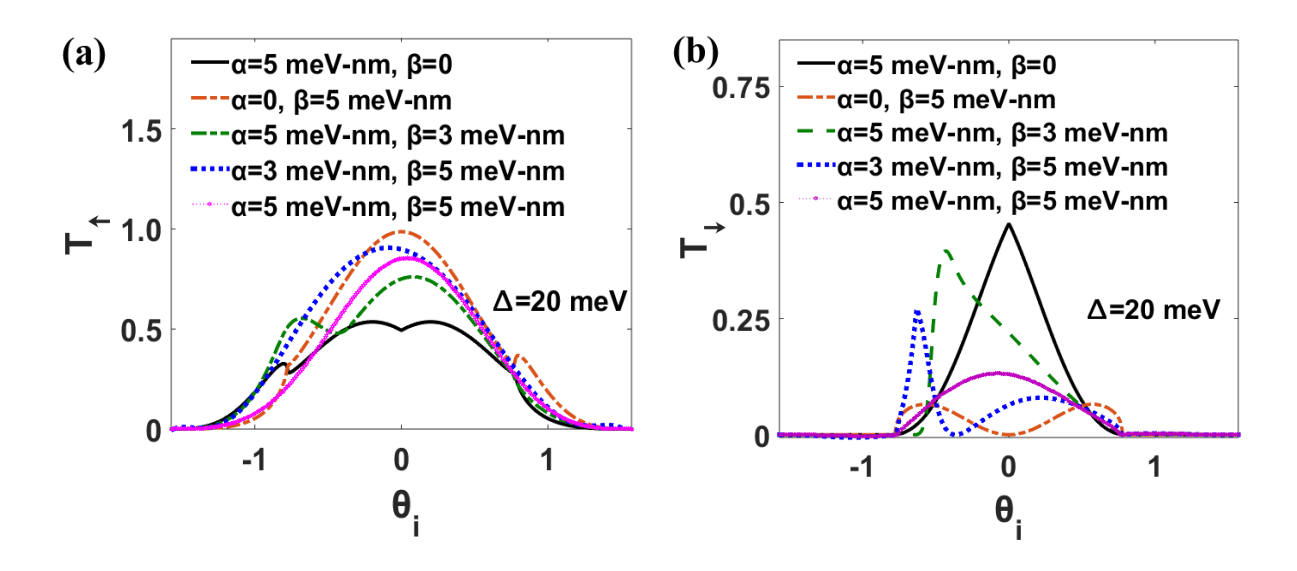


Fig.3.3 (a) T_{\uparrow} (b) T_{\downarrow} as a function of θ_{i} for different α , β combinations at $\Delta = 20$ meV.

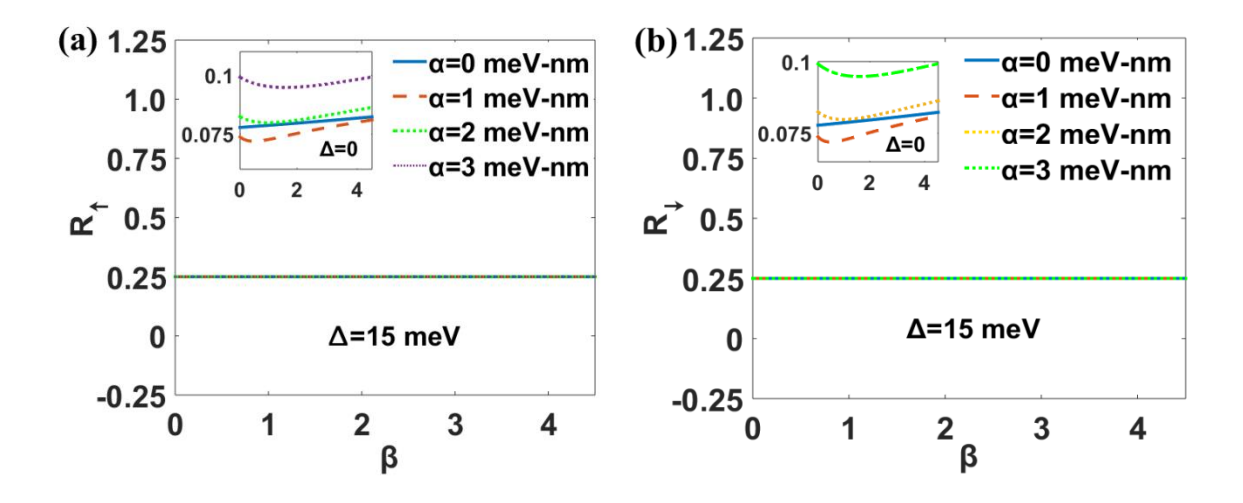


Fig.3.4 (a) R_{\uparrow} (b) R_{\downarrow} as a function of β for different α values at $\Delta=15$ meV. Insets: at $\Delta=0$ meV.

In Fig.3.3(b), we show T_{\downarrow} as a function of θ_i for the same set of values of α, β and Δ . Interestingly, for $\alpha \neq 0$, and $\beta = 0$, T_{\downarrow} decreases rapidly, essentially in a linearly way on both sides of $\theta_i = 0$ as $|\theta_i|$ increases from zero giving rise to a sharp kink-like peak at $\theta_i = 0$. T_{\downarrow} finally becomes zero as $|\theta_i|$ attains a certain value. The peak height in T_{\downarrow} for the case of $\alpha \neq 0$ and $\beta = 0$ is almost equal to the corresponding peak for T_{\uparrow} . Also, for T_{\downarrow} as a function of θ_i , the peak in the case of $\alpha \neq 0$, $\beta = 0$ is higher than that for other combinations of α and β . As we can see, the Gaussian-like pattern of the T_1 - θ_i -variation turns into a triangular structure in T_{\downarrow} plots for $\alpha > \beta$ and $\alpha < \beta$. In the case of T_{\downarrow} , there exists a region: $|\theta_i| \le \theta_*$, θ_* being close to 1, where the variations are symmetric for $\alpha \neq 0$, $\beta = 0$, $\alpha = 0$, $\beta \neq 0$ and $\alpha = \beta$. Beyond that region i.e., $|\theta_i| \ge \theta_*$, the refractivities die out to zero. For $\alpha = 0, \beta \ne 0$, T_{\downarrow} develops a double-peak structure symmetrically within the $|\theta_i| \leq \theta_*$ – region, whereas for $\alpha = \beta - \text{case}$, T_{\downarrow} shows a single peak. It can be seen that DSOI alone decreases T_{\downarrow} . Here also, $\alpha = \beta$ curve lies between $\alpha > \beta$ and $\alpha < \beta$ curves, but the $\alpha > \beta$ - curves lie higher than the $\alpha < \beta$ - curves which is an opposite behaviour compared to the case of T_{\uparrow} for the same set of α , β values. Therefore, the effect of RSOI and DSOI on T_{\uparrow} and T_{\downarrow} are opposite in nature. One can see for example, $T_{\uparrow,max} > T_{\downarrow,max}$ for $\alpha > \beta$, $\alpha < \beta$, $\alpha = \beta$ and $\alpha = 0$, $\beta \neq 0$, but for $\alpha \neq 0$ $0, \beta=0, T_{\uparrow,max} \approx T_{\downarrow,max}$. Thus, in the presence of a finite Δ , the variations of T_{\uparrow} and T_{\downarrow} are very much different from those for $\Delta = 0$ considered by Kalla et al. [35].

To see the effect of SOIs on reflection coefficients of spin-polarized electrons we plot R_{\uparrow} and R_{\downarrow} in Fig.3.4(a) and Fig.3.4(b) respectively with β for different values of α and a non-zero value of Δ . The $\Delta=0$ results are shown in the insets. The insets show that if we consider the non-zero α -cases, both R_{\uparrow} and R_{\downarrow} increase as α increases and the behaviour of R_{\uparrow} and R_{\downarrow} are also qualitatively the same. For non-zero α values, both R_{\uparrow} and R_{\downarrow} initially decrease with

increasing β , go through a dip and then increase β is further increased. But for $\alpha=0$, they monotonically increase with β essentially in a linear way. One can notice clearly that at a finite Δ value, R_{\uparrow} and R_{\downarrow} are independent of both α and β . We find that the variations of $R_{\uparrow,\downarrow}$ with α are similar to that with β (not shown here). Next, we study in Fig. 3.5, the effect of SOIs on the refraction coefficients T_{\uparrow} and T_{\downarrow} . The $\Delta=0$ – cases are shown in insets. Fig. 3.5(a) shows that at $\Delta\neq 0$, T_{\uparrow} has a finite discontinuity at a certain α (α_c) for small values of β . At large β , however, it decreases monotonically with α . Also, the $\beta=0$ – behaviour is qualitatively different from the $\beta\neq 0$ - behaviour for $\alpha<\alpha_c$.

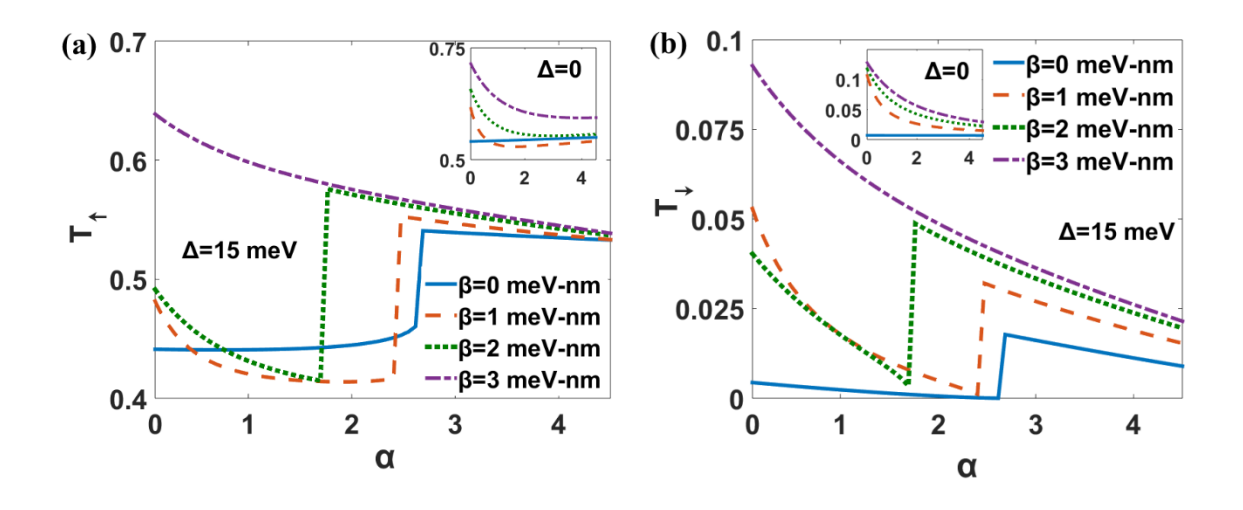


Fig.3.5 (a) T_{\uparrow} (b) T_{\downarrow} as a function of α for different β values at $\Delta = 15$ meV. Insets: at $\Delta = 0$ meV.

Another point to be observed is that α_c decreases as β increases. At $\Delta=0$ (inset), T_\uparrow decreases monotonically as α increases for all β except for $\beta=0$ for which it shows a slow but linearly increasing behaviour over the entire α -range. Thus, the discontinuity in T_\uparrow (which is completely absent at $\Delta=0$) appears to be directly related to the presence of the deltapotential at the metal-semiconductor junction. One can also see that the magnitude of T_\uparrow increases with increasing β , though $\beta=0$ curve lies on top of the $\beta=1$ and $\beta=2$ meV-nm curves for the intermediate range of α . Fig.3.5(b) shows a similar behaviour of T_\downarrow as a function of α for different values of β . Here also a discontinuity exits at $\Delta\neq0$. But in the case of T_\downarrow , it always increases with increasing β . Overall, the value of T_\uparrow is greater than that of T_\downarrow for the same range of α and β . Interestingly enough, T_\uparrow and T_\downarrow do not show any discontinuity for $\Delta\neq0$ when we plot them with β for different values of α . Also, the behaviour is qualitatively similar for both $\Delta=0$ and $\Delta\neq0$. We have not shown these plots here as they are well explained by Kalla et al. [35] for $\Delta=0$. It is evident from Fig.4 and Fig.5 that for plots at $\alpha=\beta=0$ and $\Delta=15$ meV, the refraction $(T_{\uparrow,\downarrow})$ and reflection $(R_{\uparrow,\downarrow})$ coefficients satisfy:

 $T_{\uparrow} + T_{\downarrow} + R_{\uparrow} + R_{\downarrow} \approx 1$ which is precisely Eq. (3.27). Also, for the other combinations of α and β , $T_{\uparrow,\downarrow}$ and $R_{\uparrow,\downarrow}$ satisfy Eq. (3.26) for which one has to solve k^{\pm} self consistently to get $\theta_{k^{\pm}}$ and hence $\varphi_{k^{\pm}}$.

As spin-resolved current densities are directly dependent on refraction coefficients, we plot spin-up current (J_{\uparrow}) and spin-down current (J_{\downarrow}) as a function of α for several values of β in Fig.3.6 (a) and (b) respectively at a finite value of Δ . J_0 stands for the normalization constant which is given by: $J_0 = el^2q_f/2\pi h$. As expected, J_{\uparrow} (J_{\downarrow}) behaves with α qualitatively almost in a similar way as T_{\uparrow} (T_{\downarrow}) . Of course, quantitatively, they differ by orders of magnitudes. The plots of J_{\uparrow} , and J_{\downarrow} exhibit the same signature of discontinuity at a particular α -value for $\Delta \neq 0$, which clearly has its genesis in the infinite scattering potential at the metal-semiconductor junction. $\Delta = 0$ variations are shown in the insets where, as expected, we do not see any discontinuity.

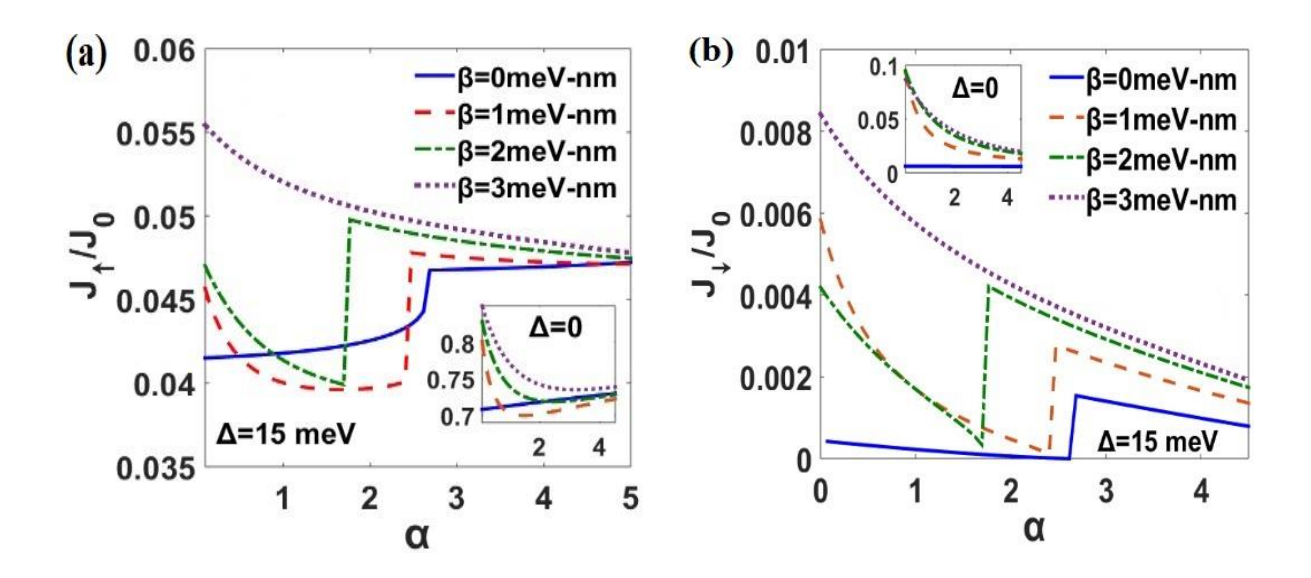


Fig.3.6 (a) J_{\uparrow} (b) J_{\downarrow} as a function of α for different β values at $\Delta = 15$ meV. Insets: at $\Delta = 0$ meV.

We show the variation of J_{\uparrow} and J_{\downarrow} with β for different values of α in Fig.3.7(a) and (b) respectively. As discussed earlier in the case of T_{\uparrow} and T_{\downarrow} , J_{\uparrow} and J_{\downarrow} do not exhibit any discontinuity when drawn as a function of β . In Fig.3.7(a), one can see that for $\alpha=0$, J_{\uparrow} shows a linear monotonic increase with β . However, for $\alpha\neq 0$, the behaviour is different. As β increases from zero, J_{\uparrow} first decreases, goes through a minimum and then increases with further increase in β . For $\alpha\neq 0$, J_{\uparrow} increases with increasing α in the weak- β regime while, for higher values of β , J_{\uparrow} decreases as α increases. Fig.3.7(b) displays J_{\downarrow} as a function of β for the same set of α values. It can be seen that for $\alpha\neq 0$, J_{\downarrow} initially increases with β but finally saturates as β becomes large. However, for $\alpha=0$, J_{\downarrow} shows a slow, linear and monotonically

decreasing behaviour with β . For $\alpha \neq 0$, J_{\downarrow} shows a decreasing behaviour with increasing α for the entire range of β . Comparison with the insets shows that the $\Delta=0$ variations that are qualitatively similar to the $\Delta\neq 0$ curves. Quantitatively, however, that the magnitudes of the current densities at $\Delta\neq 0$ are much smaller compared to those at $\Delta=0$. Thus, one can conclude that the presence of a delta-potential scattering potential at the interface reduces the transmission current.

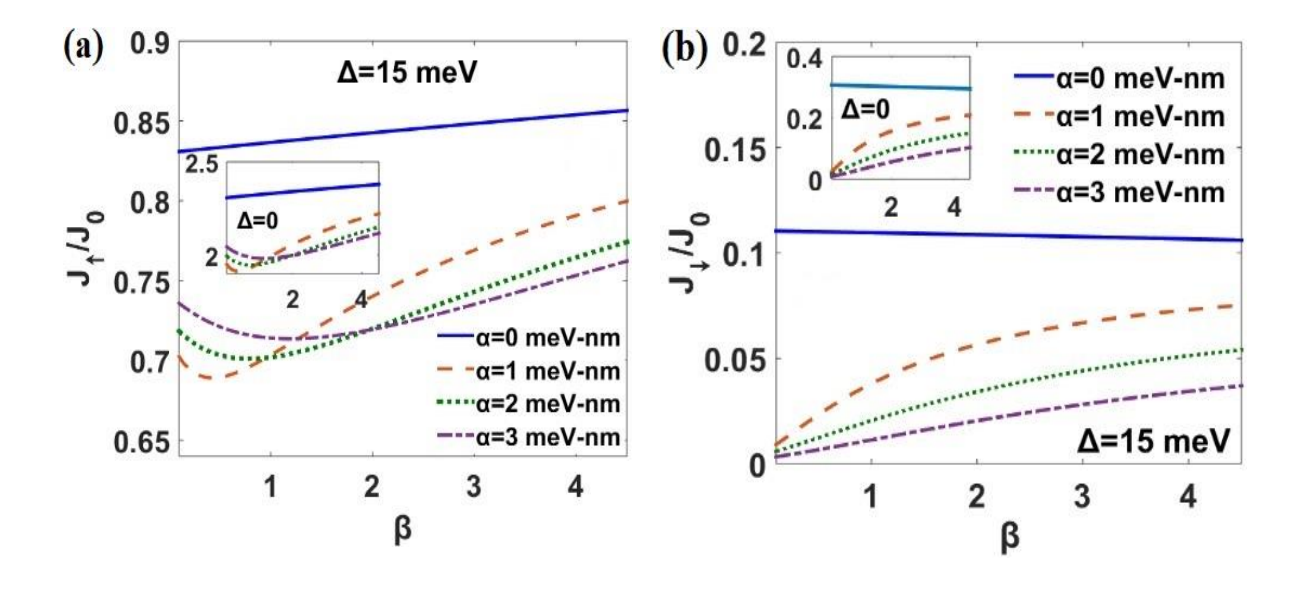


Fig.3.7 (a) J_{\uparrow} (b) J_{\downarrow} as a function of β for different α values at $\Delta = 15$ meV. Insets: at $\Delta = 0$ meV.

Next, we wish to study in Figs.3.8 and 3.9, the variations of J_{\uparrow} and J_{\downarrow} with respect to the applied voltage V for different α , β combinations at a certain Fermi energy E_f (=15 meV) and incident energy ϵ_q (= 20 meV). Figs.3.8 (a-c) suggest that for all combinations of α and β , J_{\uparrow} increases in a similar fashion with increasing V. In Fig.3.8(a), we can see that the presence of DSOI alone, J_{\uparrow} is much larger than in the presence of RSOI alone at a finite Δ . This effect is completely opposite to the Δ =0 case studied by Kalla et al. [35]. Fig.3.8(b) shows that J_{\uparrow} components for $\alpha > \beta$, are much higher than those for $\alpha < \beta$ at a particular Δ -value. Therefore, RSOI dominates over DSOI when both the SOIs are present. In Fig.3.8(c), we show the variations of J_{\uparrow} for equal strengths of RSOI and DSOI. In this case, J_{\uparrow} increases much faster than the case for $\alpha < \beta$. So, RSOI enhances J_{\uparrow} more compared to DSOI when both the interactions are present and are of equal strengths. Fig.3.9(a) suggests that when considered separately, RSOI increases J_{\downarrow} more than DSOI at a particular Δ , which is quite opposite to the observations shown in Fig.3.8(a). Fig.3.9 (b) and (c) also reveal the same effect at a finite value of Δ . It is clear from both the Figs.3.8 and 3.9 that the presence of Δ reduces J_{\uparrow} and J_{\downarrow} significantly for any combination of α and β .

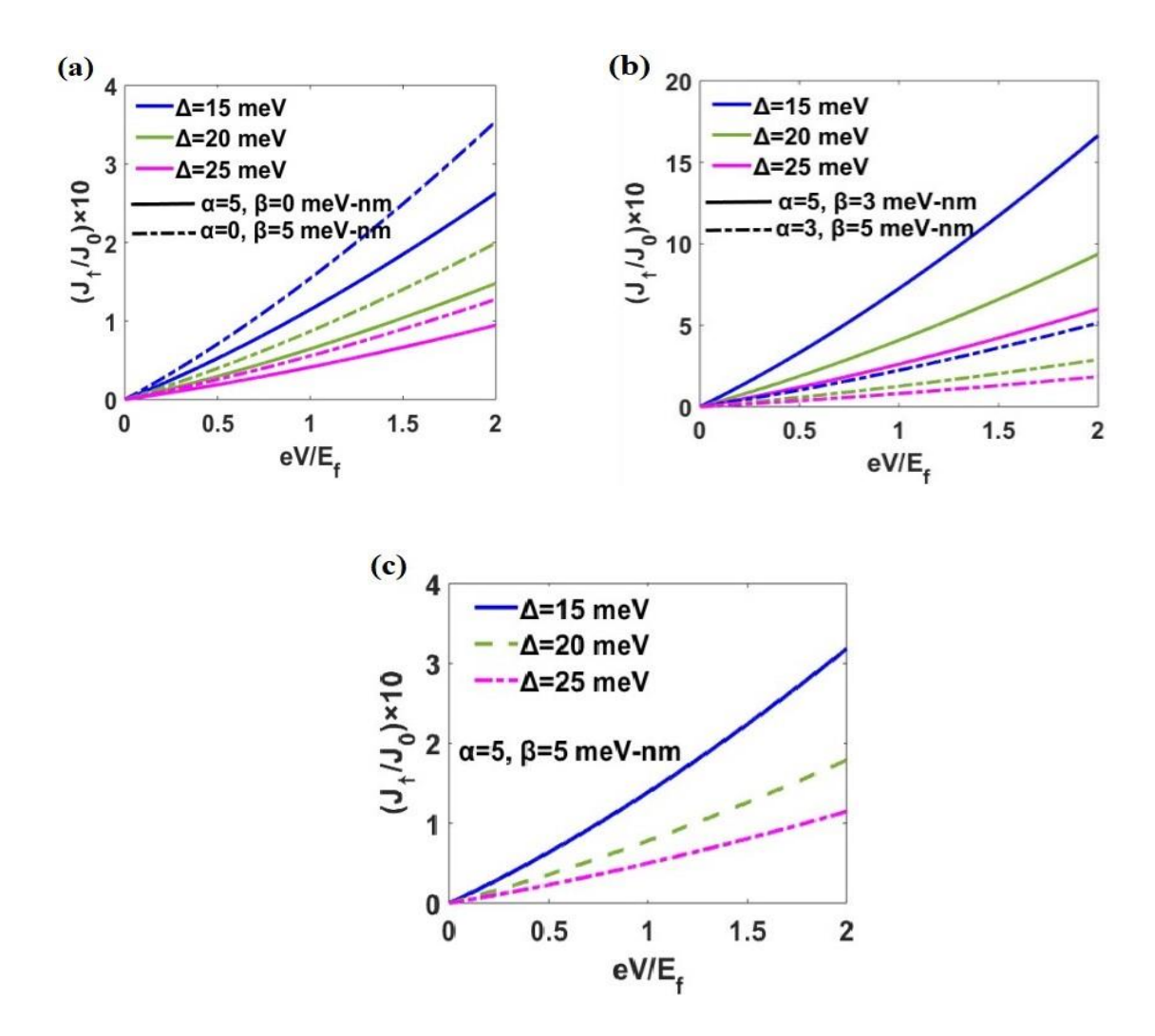
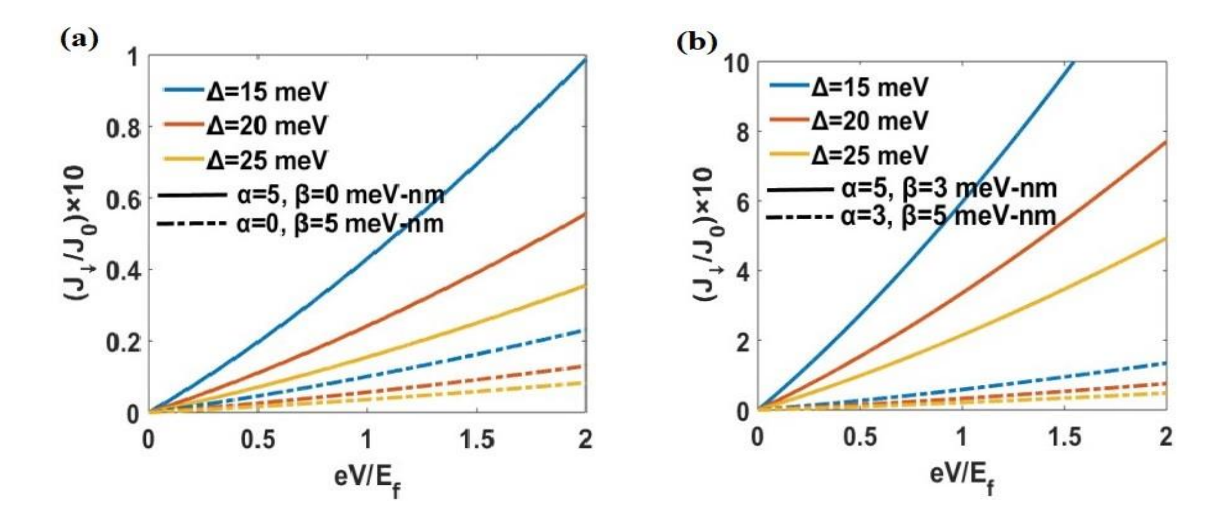


Fig.3.8 J_{\uparrow} as a function of eV/E_f for different Δ values with different α , β combinations: (a) $\alpha \neq 0$, $\beta = 0$; $\alpha = 0$, $\beta \neq 0$, (b) $\alpha > \beta$; $\alpha < \beta$, (c) $\alpha = \beta$.



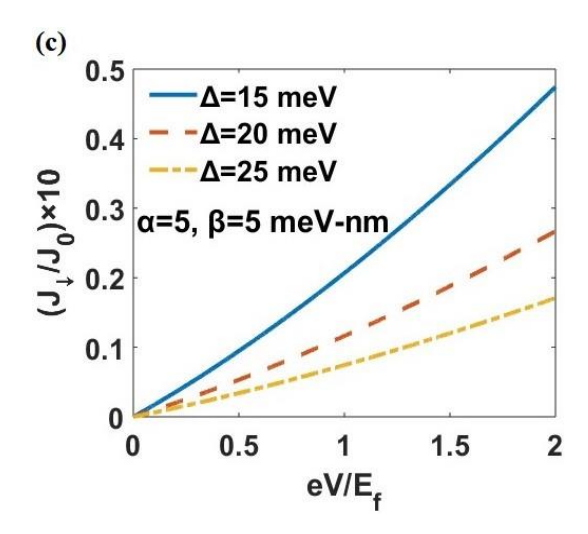


Fig.3.9 J_{\downarrow} as a function of eV/E_f for different Δ values with different α , β combinations: (a) $\alpha \neq 0$, $\beta = 0$; $\alpha = 0$, $\beta \neq 0$, (b) $\alpha > \beta$; $\alpha < \beta$, (c) $\alpha = \beta$.

Figs.3.10 and 3.11 display the variations of spin polarized differential conductance G_↑ and G_{\downarrow} respectively as a function of Fermi energy E_f for different combinations of α and β at a fixed applied voltage eV= 25 meV. We plot G_{\uparrow} and G_{\downarrow} in units of G_0 which is given by G_0 = $e^2l^2q_f/2\pi h$. Fig.3.10(a) shows that G_{\uparrow} decreases rapidly as we increase E_f and saturates after a certain E_f . Here also we can see that at a finite Δ , when considered separately, G_{\uparrow} is increased more by DSOI than by RSOI. This observation is completely opposite to $\Delta = 0$ case studied by Kalla et al. [35] where they have shown G_{\uparrow} is enhanced more by RSOI than by DSOI. Fig.3. 10(b) shows the same pattern of G_{\uparrow} with E_f/eV , but now G_{\uparrow} is found to be much larger for $\alpha > \beta$ than for $\alpha < \beta$ at a fixed Δ . This feature is similar to that observed in Fig.3.8(b). Interestingly, G_{\uparrow} for $\alpha = 3$ and $\beta = 5$ at $\Delta = 20$ meV has the same value as G_{\uparrow} for $\alpha = 5$, $\beta = 3$ at $\Delta = 30$ meV over the entire range of E_f/eV. We wish to mention that for a particular set of E_f and Δ , G_{\uparrow} -values are higher for the case of : $\alpha > \beta$ than for: $\alpha \neq 0$, $\beta = 0$, while they are lower for the case of $\alpha < \beta$ case than for: $\alpha = 0, \beta \neq 0$. The same conclusion can also be drawn from Figs.3.8(a-b). Thus, we can conclude that when both the SOIs are considered together, the RSOI dominates over DSOI in increasing G_{\uparrow} at a fixed value of Δ . Fig.3.10(c) shows the G_1 -variations for the equal strength of α and β for different values of Δ . In this case, the decrease in conductance with increasing E_f is slower in comparison with the case of $\alpha \neq 0$, $\beta = 0$, but is faster compared to the case of $\alpha = 0$, $\beta \neq 0$. As expected, the presence of Δ decreases conductance significantly for all the aforementioned cases. Figs. 3.11 (a-c) reveal that with E_f , G_{\downarrow} decreases qualitatively in a similar way as G_{\uparrow} , though the quantitative behaviour is different from G_{\uparrow} (shown in Fig.3.10). Fig.3.11(a) shows that when considered separately, G1 is enhanced more by RSOI than by DSOI. According to

Fig.3.11(b), G_{\downarrow} , as a function of E_f , increases more in the case of $\alpha > \beta$ than in the case of $\alpha < \beta$. This is consistent with Fig.3.9. The other observations in Fig.3.11 can also be easily understood from Fig.3.9. For example, Δ suppresses G_{\downarrow} quite significantly. At a fixed Δ , the values of J_{\downarrow} and G_{\downarrow} are much lower than those of J_{\uparrow} and G_{\uparrow} for a particular combination of α and β .

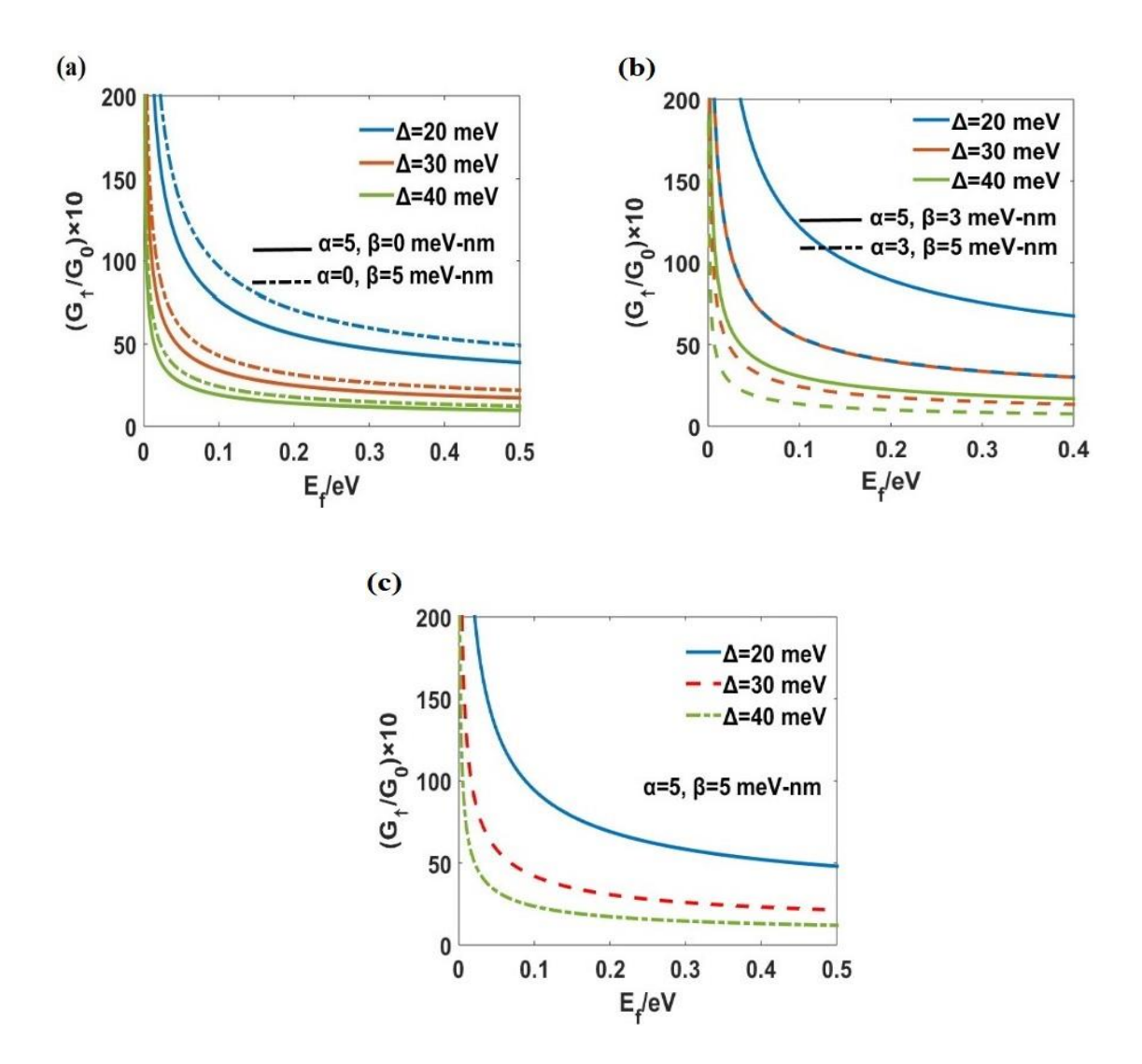


Fig.3.10 G_{\uparrow} as a function of E_f/eV for different Δ values with different α, β combinations: (a) α ≠ 0, β = 0; α = 0, β ≠ 0, (b) α > β; α < β, (c) α = β.

In Figs.3.12 and 3.13, we study the effect of SOIs directly on G_{\uparrow} and G_{\downarrow} at a fixed value of Δ (=15 meV). We set henceforth E_f =15 meV, eV = 25 meV and ϵ_q = 20 meV. Fig.3.12(a) shows that for certain values of β , G_{\uparrow} increases with α , though it can have a non-smooth behaviour at several values of α . This non-smooth behaviour in G_{\uparrow} reduces as β increases and G_{\uparrow} becomes essentially smooth. Interestingly, in the case of β = 0, G_{\uparrow} becomes completely

smooth and increases monotonically with α in a linear way. One can see from Fig.3.12(b) that for non-zero values of β , G_{\downarrow} also exhibits a non-smooth behaviour at several values of α . In fact, G_{\downarrow} has more non-smoothness than G_{\uparrow} . For β =0, G_{\downarrow} is also found to increase monotonically with α in a linear way. It is important to mention that unlike G_{\uparrow} -curves, the non-smoothness in G_{\downarrow} does not go away as β increases, especially for lower β values. However, if β increases further, this non-smoothness in G_{\downarrow} also disappears slowly (not shown here). Thus, the non-smooth behaviour in G_{\uparrow} and G_{\downarrow} arises at a non-zero Δ in the presence of reasonable values of SOIs.

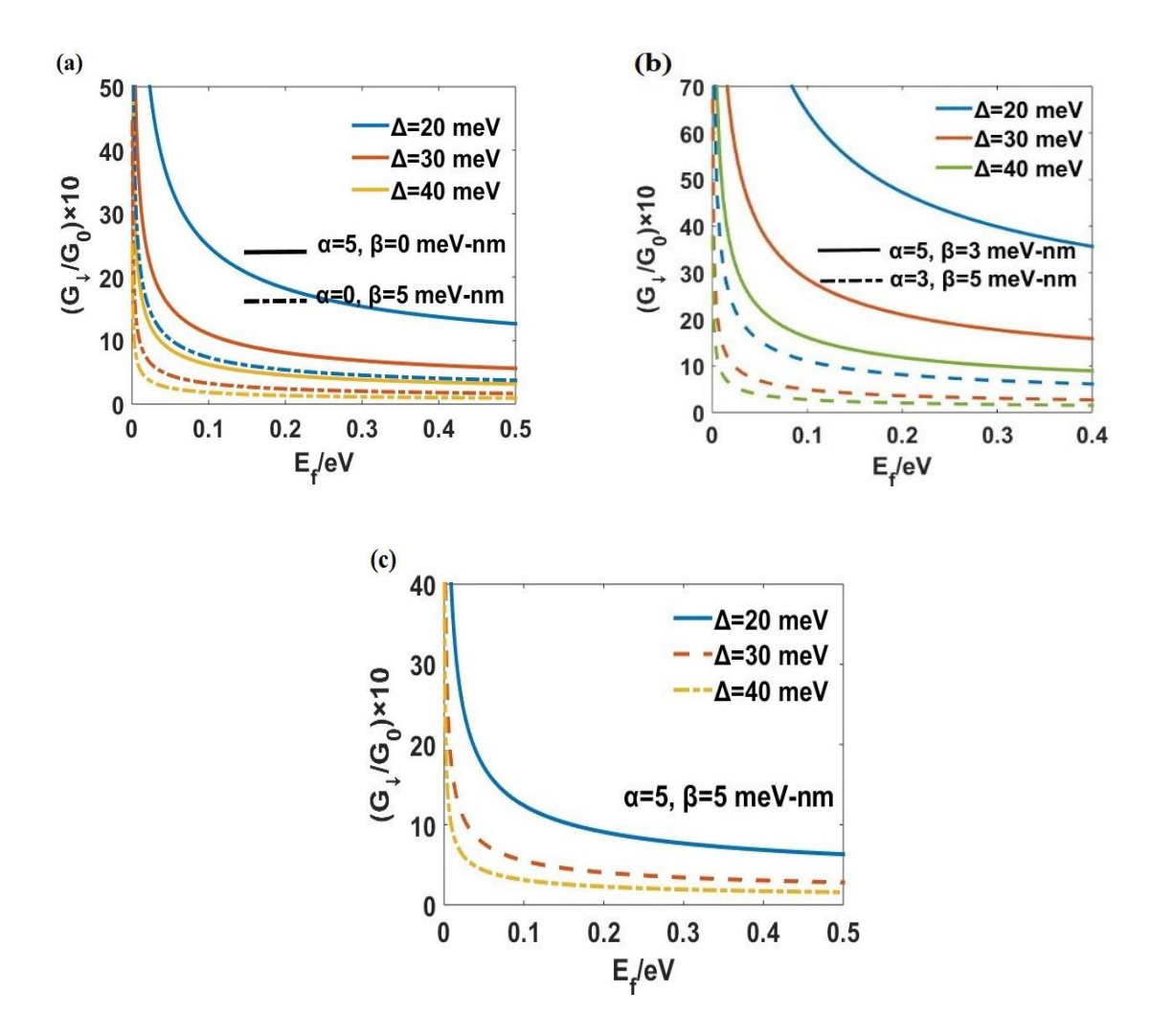


Fig.3.11 G_{\downarrow} as a function of E_f/eV for different Δ values with different α , β combinations: (a) $\alpha \neq 0$, $\beta = 0$; $\alpha = 0$, $\beta \neq 0$, (b) $\alpha > \beta$; $\alpha < \beta$, (c) $\alpha = \beta$.

Figs.3.13(a) and 3.13(b) respectively show the dependence of G_{\uparrow} and G_{\downarrow} on β for different values of α . It is seen that G_{\uparrow} and G_{\downarrow} increase with β as β increases from zero, show a bending at a certain β and finally appear to saturate as β increases further. How the increase

in G_{\uparrow} and G_{\downarrow} is only discernible at lower values of β . The figure also shows that G_{\uparrow} increases with increasing value of α . For $\alpha=0$, G_{\uparrow} decreases extremely slowly with increasing β . G_{\uparrow} —curve also shows some non-smoothness with respect to β at higher values of α . The observations in Fig.3.13(b) are similar to Fig.3.13(a) except for the $\alpha=0$ case, where G_{\downarrow} , unlike G_{\uparrow} , increases monotonically with β . From Figs.3.13(a) and 3.13(b), we can also conclude that the magnitudes of G_{\downarrow} components are smaller than those of the G_{\uparrow} components.

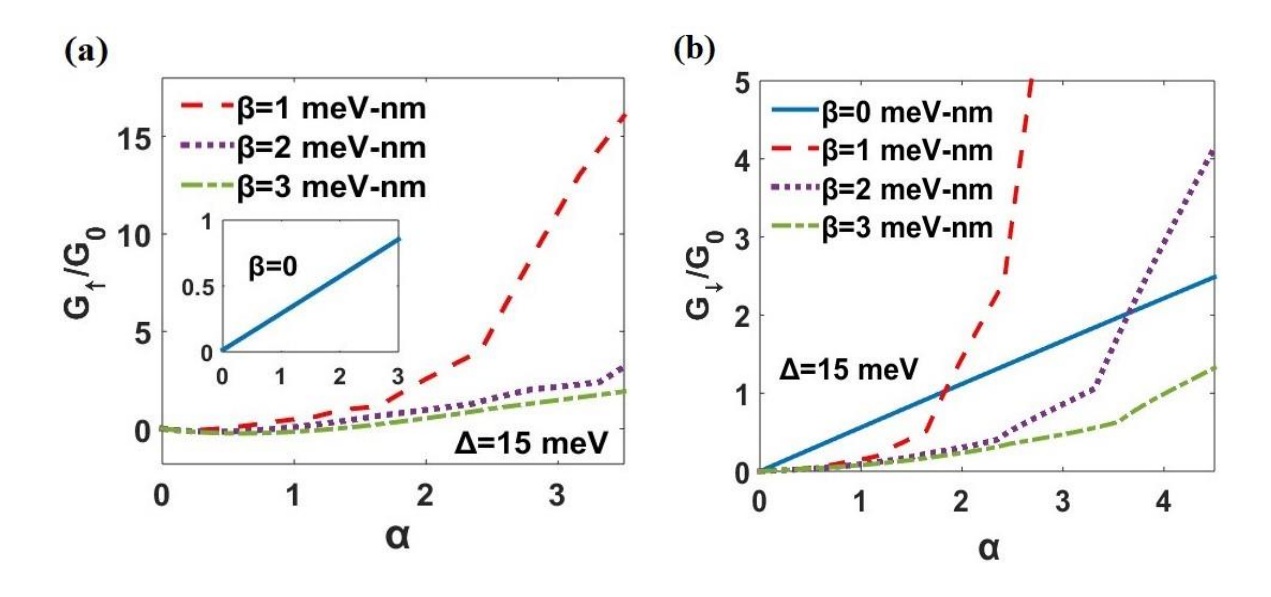


Fig.3.12 (a) G_{\uparrow} (b) G_{\downarrow} as a function of α for different β values at $\Delta = 15$ meV.

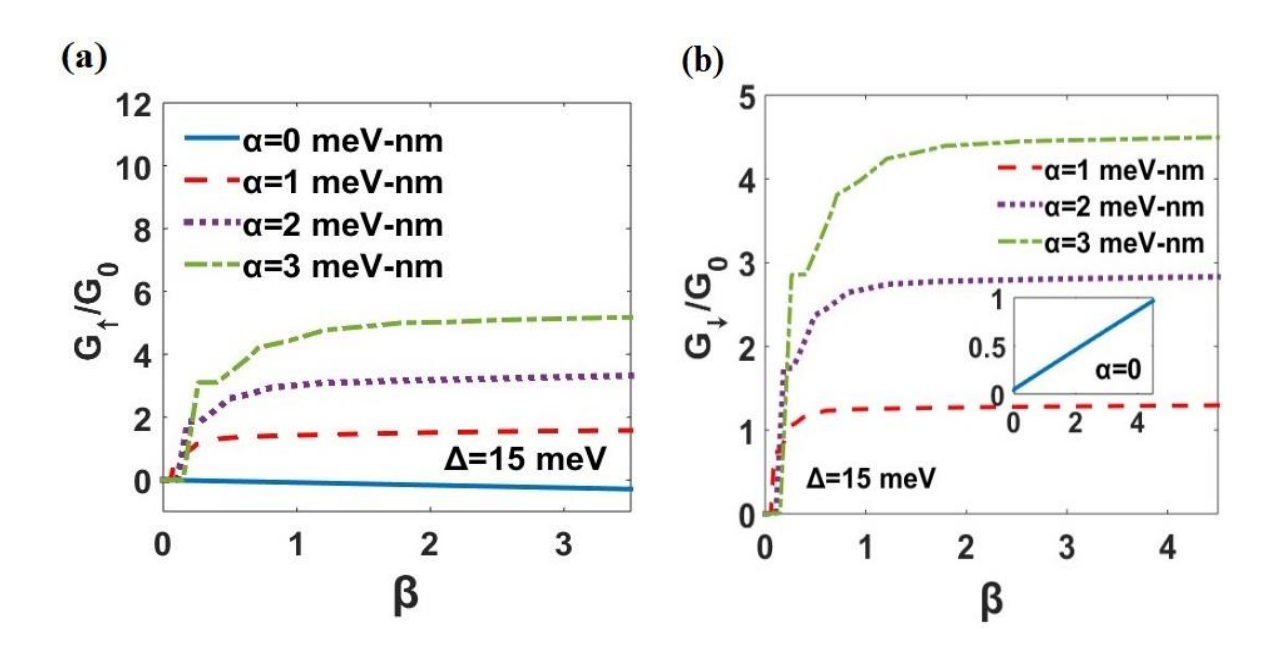


Fig.3.13 (a) G_{\uparrow} and (b) G_{\downarrow} as a function of β for different α values at $\Delta = 15$ meV.

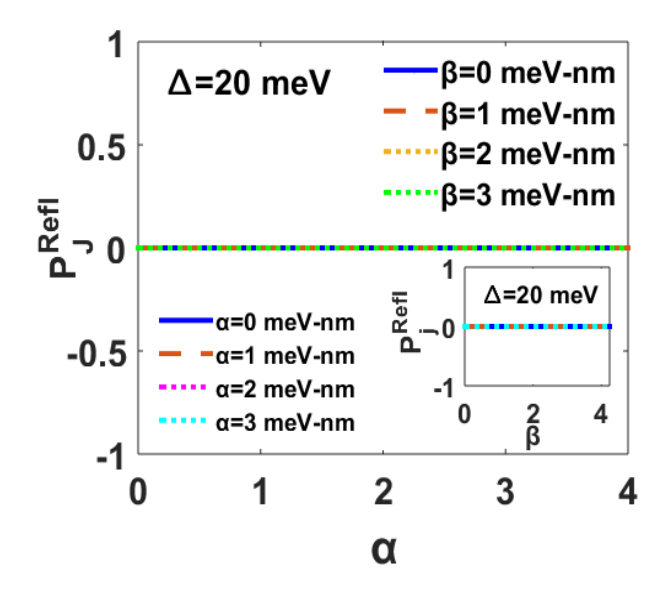


Fig.3.14 Reflected spin polarization P_J^{Refl} as a function of α for different values of β at $\Delta = 20$ meV. Inset: P_I^{Refl} as a function of β for different values of α at $\Delta = 20$ meV.

As the spin-polarization is an important quantity in the context of spin-filtering, we plot reflected spin-polarization (P_J^{Refl}) and refracted spin-polarization (P_J^{Refr}) with α and β in Figs. 3.14 and 3.15 respectively. We can clearly see that at a finite Δ , P_J^{Refl} remains zero over the entire α -axis for any value of β . The inset shows P_J^{Refl} remains zero also over the entire β -axis for any value of α . This can be understood from Fig.3.4 where the spin-up and spin—down reflection coefficients are constant with respect to SOIs in the presence of a finite Δ and hence, the spin-polarization becomes zero for any values of SOIs. Fig.3.15(a) shows that P_J^{Refr} increases as α increases at a finite Δ (Δ = 20) meV and the behaviour is slightly nonlinear for non-zero values of β . Comparison with the inset suggests that the nonlinearity is more for the case of Δ = 0. Fig.3.15(b) shows that for α ≠ 0, P_J^{Refr} initially decreases with increasing β , makes a broad valley in the intermediate region of β and then increases again as β increases. For α = 0, however, P_J^{Refr} is a monotonically increasing function of β , though at small β , the variation is rather slow. Therefore, the effects of RSOI and DSOI on P_J^{Refr} are opposite to each other. The presence of Δ appears to cause a constant shift in P_I^{Refr} with respect to SOIs.

Figs.3.16 and 3.17 display the contour plots of refracted spin polarization P_J^{Refr} . In Fig.3.16, we show the contour of P_J^{Refr} in α - β space at a finite value of Δ . Light yellow colour denotes the maximum value of P_J^{Refr} . We notice that P_J^{Refr} remains maximum over a finite region of α ($2 \le \alpha \le 5.2$) and in a small region close to $\alpha = 0$, but decreases along the

β-axis. It decreases significantly if we decrease α below α = 2, though the variations of P_J^{Refr} are different in different α-β regimes. For example, when α is close to zero, we find a small region where P_J^{Refr} is maximum for small a but non-zero value of β (i.e., for α = 0, β ≠ 0 case). For the case of α < β, as α approaches to α = 2, it is seen that P_J^{Refr} becomes maximum (light yellow colour) at a higher value of β(≈ 5) and P_J^{Refr} takes intermediate values for 1 ≤ α ≤ 2 and 4 ≤ β ≤ 5.2. P_J^{Refr} attains a minimum (deep blue colour) at sufficiently small values of α and with β in the intermediate range (1 ≤ β ≤ 4) and with β beyond 5.2. For α > β, P_J^{Refr} increases as α increases, develops a maximum in the range 2 ≤ α ≤ 5.2, but drops beyond α = 5.2. Therefore, for $\Delta \neq 0$, when both the SOIs are present, either of the two should be higher than the other but restricted to a particular window to lead to maximum P_J^{Refr} . However, interestingly, DSOI alone can make P_J^{Refr} significantly large, when RSOI is almost zero.

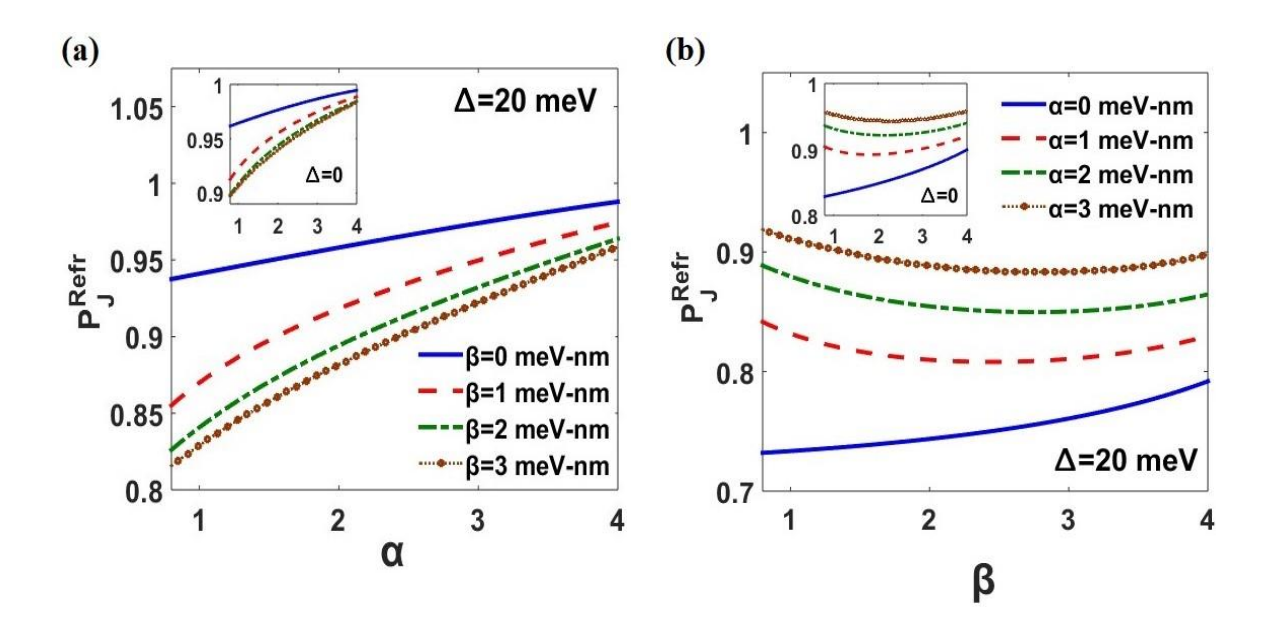


Fig.3.15 (a) Refracted spin polarization P_J^{Refr} as a function of α for different values of β at $\Delta = 20$ meV. (b) P_I^{Refr} as a function of β for different values of α at $\Delta = 20$ meV.

We plot P_J^{Refr} in $\Delta - \beta$ space for a particular value of α in Fig.3.17(a), and the same in Fig.3.17(b) in Δ - α astronomical for a particular value β . In these plots, one can notice that P_J^{Refr} shows a constant shift in its value as we increase Δ and furthermore, it decreases along the increasing value of β . It acquires a maximum in a narrow region around $\beta = 4$ meV-nm at a certain α -value. The same behaviour with respect to Δ is also visible in Fig.3.17(b). Here, however, P_I^{Refr} decreases along the decreasing α value, but it remains maximum over a

broader regime of α at a certain finite β -value. Thus, the effects of RSOI and DSOI on P_J^{Refr} are opposite and the presence of infinite delta-scatterer makes a change in the magnitude of P_J^{Refr} . The present results for the maxima in P_J^{Refr} for $\Delta \neq 0$ may be useful for the determination of the values of α and β .

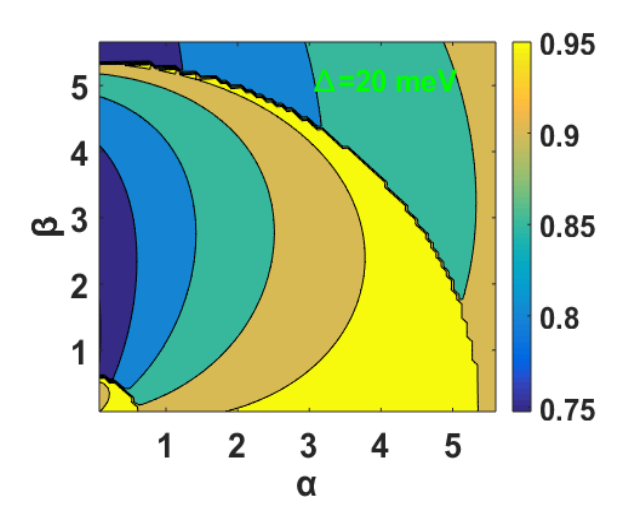


Fig.3.16 Contour plot of P_I^{Refr} in α - β space at Δ = 20 meV.

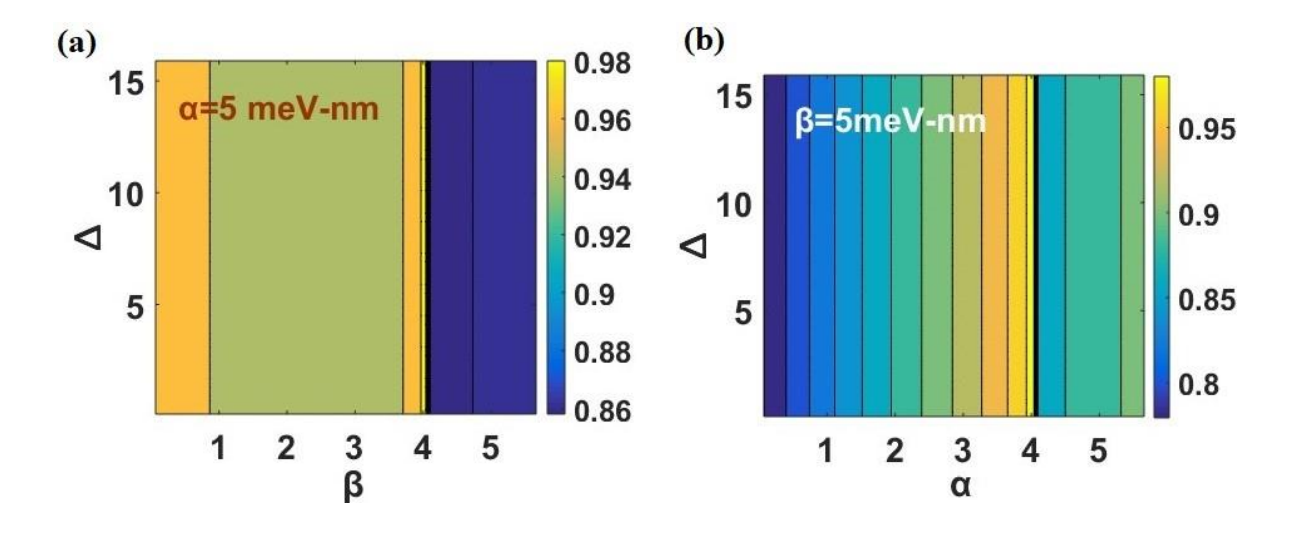


Fig.3.17 Contour plot of $P_J^{\,\mathrm{Refr}}$ in (a) Δ - β space at $\alpha=5$ meV-nm (b) Δ - α space at $\beta=5$ meV-nm.

3.4 CONCLUSIONS

In conclusion, we have studied the effect of both RSOI and DSOI on the electron transport across a metal-semiconductor junction with a delta-function interface potential by calculating the reflection and transmission coefficients and the experimentally measurable quantities like

spin-polarized current densities and differential conductance using discontinuous boundary conditions. In the presence of both SOIs, DSOI reduces the angle of refraction of the spin-up and spin-down electrons while RSOI increases the same, but the reduction due to DSOI is much larger than the increase due to RSOI and hence the spin-splitting angle increases in the presence of DSOI. We have shown that the increase in the incident electron energy decreases the angle of refraction of the spin-up electrons, while it increases that of the spin-down electrons which is completely opposite to the $\Delta = 0$ case. The effect of delta-scatterer becomes particularly important when we consider the spin-up refraction coefficients T₁ and T_{\downarrow} with respect to incident angle θ_i and the coefficients α and β . The variations of T_{\uparrow} and T_{\downarrow} with respect to α show some discontinuities at non-zero Δ and at lower values of β and this discontinuity effect also reflects in the variations of J_{\uparrow} and J_{\downarrow} at finite Δ . The presence of the finite jumps in the refracted coefficients and currents is a direct consequence of the infinite potential at the metal-semiconductor interface, as these discontinuities are completely absent for $\Delta = 0$. Interestingly, the discontinuities disappear when J_{\uparrow} and J_{\downarrow} are plotted with respect to β . Also, the qualitative behaviour of J_{\uparrow} and J_{\downarrow} with respect β for $\Delta \neq 0$ turns out to be the same as in the case of $\Delta = 0$. As expected, the presence of Δ decreases T_{\uparrow} , T_{\downarrow} , J_{\uparrow} and J_{\downarrow} significantly. Next, we have studied the variations of J_{\uparrow} , J_{\downarrow} and G_{\uparrow} , G_{\downarrow} with respect to the Fermi energy (E_f) and applied voltage (V) for different combinations of α and β at a finite Δ . It is observed that the current densities and hence the conductances increase as a function of V and decrease as a function of E_f. As observed with respect to E_f and V, the current density and differential conductance show qualitatively a similar behaviour, though they differ in their quantitative values. We have shown that spin-up current and conductance with respect to E_f and V are increased more by DSOI than by RSOI for $\Delta \neq 0$. Here also, the infinite interface potential causes a significant reduction in the current and conductance. G_{\uparrow} and G_{\downarrow} increase as α increases, but the presence of β suppresses them. The non-smooth behaviour of G_{\uparrow} and G_{\downarrow} are seen at low β and high α when $\Delta \neq 0$. It is important to mention that in the presence of delta-potential, the reflection coefficients R_{\uparrow} and R_{\downarrow} become constant independent of α and β and consequently, reflected spin polarization $P_I^{\,Refr}\,$ becomes zero as a function of SOIs. The refracted spin polarization $P_J^{\,\mathrm{Refr}}$, however, has a strong dependence on SOIs at finite Δ . We have shown that in the presence of both SOIs, $P_I^{\,Refr}$ is considerably large at large α and small β . One of the important observations of this investigation is that the presence of delta potential does not have any effect in changing the path of the refracted waves of the two different spin orientations, though it makes a constant shift in the P_I Refr spectrum with respect to SOIs. Also, in the case of $\Delta \neq 0$, $P_I^{\,Refr}$ develops maxima in a narrow window of α , β . This result may be useful for the determination of the SOI strengths.

REFERENCES

- 1. S. A. Wolf et al., Science **294**, 1488 (2001).
- 2. I. Žutić, J. Fabian, S. D. Sarma, Rev. Mod. Phys. **76**, 323 (2004).
- 3. S. Datta, B. Das, Appl. Phys. Lett. **56**, 665 (1990).
- 4. J. Schliemann, D. Loss, Phys. Rev. B 68, 165311 (2003).
- 5. J. Schliemann, M. Lee, J. C. Egues, D. Loss, Phys. Rev. Lett. 90, 146801 (2003).
- 6. P. Pietilainen, T. Chakraborty, Phys. Rev. B 73, 155315 (2006).
- 7. S. M. Badalyan, A. M. Abiague, G. Vignale, J. Fabian, Phys. Rev. B **79**, 205305 (2009).
- 8. H. Tamura, T. Ando, Phys. Rev. B **44**, 4, 1792-1800 (1991).
- 9. H. K. Sharma, S. Sil, A. Chatterjee, J. Magn. Magn. Mater. 500, 166329 (2013).
- 10. A. Boda, B. Boyacioglu, U. Erkaslan, A. Chatterjee, Physica B 498, 43 (2016).
- 11. P. J. Monisha, I.V. Sankar, S. Sil, A. Chatterjee, Sci. Rep. 6, 20056 (2016).
- 12. A. Chatterjee, M. O. Smolkina, I. Y. Popov, Nanosystems: Phys. Chem. Math. **50**, 10 (1), 50-62 (2019).
- 13. P. Saini, A. Boda, A. Chatterjee, J. Magn. Magn. Mater. 485, 407-412 (2019).
- 14. K. Bhattacharyya, D. Debnath, A. Chatterjee, J. Magn. Magn Mater. **506**, 166745 (2020).
- 15. Y. Khoshbakht, R. Khordad, H. R. Sedehi, J. Low Temp. Phys. 202, 202:59-70 (2021).
- 16. T. Schäpers, J. Nitta, H. B. Heersche, H. Takayanagi, Phys. Rev. B 64, 125314 (2001).
- 17. J. C. Egues, Phys. Rev. Lett. 80, 20, 4578(4) (1998).
- 18. A. Dyrdał, J. Barnaś, Phys. Rev. B **92**, 165404 (2015).
- 19. E. L. Wolf, *Principles of Electron Tunneling*, Oxford University Press, Oxford, England (1985).
- S. D. Franceschi, F. Giazotto, F. Beltram, L. Sorba, M. Lazzarino, A. Franciosi, Appl. Phys. Lett. 73, 26, 3890-3892 (1998).
- 21. V. M. Ramaglia, D. Bercioux, V. Cataudella, G. D. Filippis, C. A. Perroni, J. Phys. Condens. Matter **16**, 9143-9154 (2004).
- 22. T. Yokoyama, Y. Tanaka, J. Inoue, Phys. Rev. B 74, 035318 (2006).
- 23. J. C. Egues, C. Gould, G. Richter, L.W. Molenkamp, Phys. Rev. B 64, 195319 (2001).
- 24. F. Meier, D. Loss, Phys. Rev. Lett. 90, 16, 167204(4) (2003).
- 25. K. C. Hall, W. H. Lau, K. Gündoğdu, M. E. Flatté, T. F. Boggess, Appl. Phys. Lett. **83**, 14, 2937-2939 (2003).

- 26. A. Slobodskyy, C. Grould, T. Slobodskyy, C. Becker, G. Schmidt, W. Molenkamp, Phys. Rev. Lett. **90**, 24, 246601(4) (2003).
- 27. I. Žutić, S. D. Sarma, Phys. Rev. B 60, 24, 16322(4) (1999).
- 28. U. Zülicke, C. Schroll, Phys. Rev. Lett. 88, 2, 029701(1) (2001).
- 29. J.-Q. Lu, Y. Guo, F. Zhai, B.-L. Gu, J.-Z. Yu, Y. Kawazoe, Phys. Letts. A **299**, 616–621 (2002).
- 30. T. Koga, J. Nitta, H. Takayanagi, S. Datta, Phys. Rev. Lett. 88, 12, 126601(4) (2002).
- 31. B. Srisongmuang, P. Pairor, M. Berciu, Phys. Rev. B 78, 155317 (2008).
- 32. S. Bandyopadhyay, M. Cahay, J. Ludwick, Phys. Scr. 96, 065806 (2021).
- 33. S. Shee, R. Fabiha, M. Cahay, S. Bandyopadhyay, Magnetism 2, 117–129 (2022).
- 34. M. Khodas, A. Shekhter, A. M. Finkel'stein, Phys. Rev. Lett. 92, 8, 086602(4) (2004).
- 35. M. Kalla, D. S. Kumar, S. Sil, A. Chatterjee, Superlattices Microstruct. **156**, 106951 (2021).

CHAPTER 4

PERSISTENT CURRENTS IN A CORRELATED MESOSCOPIC HOLSTEIN-HUBBARD RING IN THE PRESENCE OF BULK INVERSION ASYMMETRY

ABSTRACT

The effect of e-p coupling, onsite repulsive Coulomb interaction and temperature on the PC in a quantum ring is studied in the presence of DSOI. The 1D QR threaded by the A-B flux is modelled by the Holstein-Hubbard-Dresselhaus Hamiltonian. The e-p interaction and DSOI are decoupled by respectively employing the standard Lang-Firsov coherent transformation and a unitary transformation. Thereafter, a mean-field-Hartree-Fock-self-consistent diagonalization technique is performed numerically to obtain the effective electronic energy and current. It is shown that the intrinsic DSOI enhances the persistent charge and spin currents significantly. On the other hand, the PC is effectively reduced by the onsite and nearest-neighbour e-p interaction and Coulomb interaction. The behaviour of the currents gets modified by temperature. The spin-splitting of persistent spin current is enhanced considerably by DSOI and this splitting is tuneable in different regimes of magnetic flux, temperature, chemical potential and the interactions present in the system.

4.1 Introduction

The study of the A-B effect in a mesoscopic ring has been in the focus of attention over the past few decades. There exists a PC in the QR which is generated by a magnetic flux Φ piercing through the ring. This novel phenomenon was first addressed by Büttiker et al. [1] and then several theoretical [2-8] and experimental [9-15] studies have come up to confirm the existence of PC in LDS. People have investigated the effect of e-e interaction on PC in a QR under the framework of the well-known HM [16-21]. But, to our knowledge, most of the studies have been performed in the absence of e-p interaction which can be crucial in mesoscopic systems. The effect of this interaction on PC is often dealt with using the Holstein-Hubbard (H-H) model. Recently, Monisha et al. [22] have studied the PC in an H-H ring under the influence of the RSOI. They have shown an enhancement of PC due to RSOI and investigated the effect of e-p interaction, onsite Coulomb repulsion and chemical potential on PC. In another study, Chatterjee et al. have studied the behaviour of PC in a chain of two H-H rings in the presence of the RSOI [23].

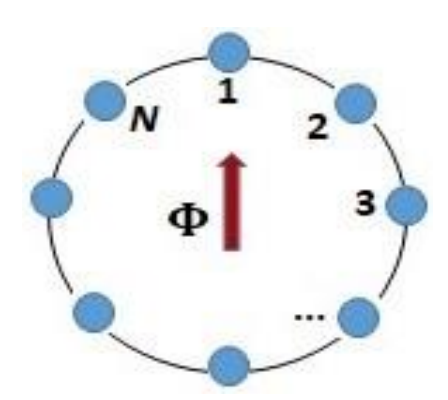


Fig.4.1 Schematic representation of a quantum ring threaded by an A-B flux Φ .

We present in Fig. 1, a schematic diagram of a mesoscopic ring threaded by a magnetic flux Φ . The A-B effect is a quantum mechanical phenomenon which causes a phase shift by $\theta =$ $2\pi\Phi/N\Phi_0$ in the wavefunctions of the electrons lying on the circumference of the ring. It is observed that the energy spectrum and thus the PC are periodic in Φ with period $\Phi_0 = hc/e$ which is the magnetic flux quantum. Since the DSOI is an intrinsic phenomenon for the materials having zinc blende structure that lacks inversion symmetry, it may be intriguing to study the effect of this interaction on PC in a ring-shaped nano-structure. Therefore, in this paper, we wish to study the behaviour of PC in a correlated QR in the presence of the onsite and NN e-p interaction, onsite e-e Coulomb interaction and DSOI. As the temperature very much affects the distributions of the electronic energy levels, we also wish to investigate the role of temperature on the system considered.

4.2 Analytical model and formulation

The model Hamiltonian for an H-H ring pierced through an A-B flux Φ in the presence of DSOI can be written as

$$H = H_e + H_{ph} + H_{e-ph} + H_{so}, (4.1)$$

where H_e represents the electronic Hamiltonian, H_p refers to the unperturbed phonon Hamiltonian, H_{e-ph} describes the e-p interaction and H_{so} denotes the SOI. H_e is given by

$$H_e = \epsilon_0 \sum_{i\sigma} c_{i\sigma}^{\dagger} c_{i\sigma} - t \sum_{\langle ij \rangle \sigma} (c_{i\sigma}^{\dagger} c_{j\sigma} e^{i\theta_{\sigma}} + h.c.) + U \sum_{i} n_{i\uparrow} n_{i\downarrow}, \qquad (4.2)$$

where ϵ_0 is the single-electron energy per site, $c_{i\sigma}^{\dagger}(c_{i\sigma})$ is the electron's creation(annihilation) operator at the i^{th} site with the spin-index σ , i=1,2,3,...N, N being the total number of identical sites in the system and $c_i = \binom{c_{i\uparrow}}{c_{i\downarrow}}$, t is the NN hopping integral, $e^{i\theta_{\sigma}}$ is the Peierls phase factor originating from the A-B flux, U measures the onsite e-e repulsive Coulomb correlation and $n_{i\sigma}$ ($c_{i\sigma}^{\dagger}c_{i\sigma}$) is the electron's number operator at site i with spin σ . In general, the phase $e^{i\theta_{\sigma}}$ can be represented by the spin-dependent magnetic vector potential A_{σ} [24] as: $\theta_{\sigma} = \int_{i}^{i+1} \overrightarrow{A_{\sigma}} \cdot \overrightarrow{dl} = 2\pi\Phi_{\sigma}$ /N Φ_{0} , where Φ_{σ} is the spin-dependent A-B flux [20, 21]. H_{ph} is given by

$$H_{ph} = \hbar\omega_0 \sum_{i} \left(b_i^{\dagger} b_i + \frac{1}{2} \right), \tag{4.3}$$

where $b_i^{\dagger}(b_i)$ is the creation (annihilation) operator for a phonon at the i^{th} site with a dispersionless frequency ω_0 . H_{e-ph} is given by

$$H_{e-ph} = g_1 \sum_{i\sigma} n_{i\sigma} (b_i + b_i^{\dagger}) + g_2 \sum_{\langle ij \rangle \sigma} n_{i\sigma} (b_j + b_j^{\dagger}),$$
 (4.4)

where g_1 denotes the strength of the onsite e-p interaction and g_2 denotes that at the NN sites. The e-p interactions beyond NN are considered small and therefore neglected. H_{so} is given by

$$H_{so} = -\sum_{\langle ij \rangle \sigma} t_{so} \left(c_{i\sigma}^{\dagger} c_{j\sigma} e^{i\theta_{\sigma}} + h.c. \right), \tag{4.5}$$

where t_{so} can be written, in general, as

$$t_{so} = i\alpha \left(\sigma_x \cos \varphi_{ij} + \sigma_y \sin \varphi_{ij}\right) - i\beta \left(\sigma_y \cos \varphi_{ij} + \sigma_x \sin \varphi_{ij}\right), \tag{4.6}$$

with α and β being the RSOI and DSOI strength respectively, σ_x and σ_y being the Pauli spin matrices, φ the azimuthal coordinate of the ring: $\varphi_{ij} = (\varphi_i + \varphi_j)/2 = 2\pi(i-1/2)/N$, where $\varphi_i = 2\pi(i-1)/N$. In this work, we consider the effect of DSOI only and therefore we keep $\alpha = 0$.

First, we perform the celebrated LFT, e^S where S is the generator of the transformation:

$$S = \frac{1}{\hbar\omega_0} \left[g_1 \sum_{i\sigma} n_{i\sigma} (b_i^{\dagger} - b_i) + g_2 \sum_{i\delta\sigma} n_{i\sigma} (b_{i+\delta}^{\dagger} - b_{i+\delta}) \right]. \tag{4.7}$$

This is essentially a coherent state transformation which eliminates the phonons from the system and gives an effective electronic Hamiltonian. We next employ a unitary transformation U_l given by

$$U_{l} = \frac{1}{\sqrt{2}} \begin{bmatrix} 1 & -1 \\ e^{-\frac{2\pi i \left(l - \frac{1}{2}\right)}{N}} & e^{-\frac{2\pi i \left(l - \frac{1}{2}\right)}{N}} \end{bmatrix}, \tag{4.8}$$

with site index l, to diagonalize the spin degrees of freedom. These two transformations together transform the Hamiltonian H to H_{eff} .

$$H_{eff} = \epsilon_0^{eff} \sum_{i\sigma} \tilde{n}_{i\sigma} - \sum_{\langle ij \rangle \sigma} \left[\tilde{c}_{i\sigma}^{\dagger} \left\{ t_{eff} \mathcal{F} + i\beta_{eff} \mathcal{G} \right\} \tilde{c}_{j\sigma} e^{i \left(\theta_{\sigma} + \frac{\pi}{N}\right)} + h.c. \right]$$

$$+ U_{eff} \sum_{i} \left[\tilde{n}_{i\uparrow} \tilde{n}_{i\downarrow} + \frac{\tilde{n}_{i}}{4} \left(\tilde{c}_{i\uparrow}^{\dagger} \tilde{c}_{i\downarrow} + \tilde{c}_{i\downarrow}^{\dagger} \tilde{c}_{i\uparrow} \right) - \left(\tilde{c}_{i\uparrow}^{\dagger} \tilde{c}_{i\downarrow} + \tilde{c}_{i\downarrow}^{\dagger} \tilde{c}_{i\uparrow} \right) \frac{\tilde{n}_{i}}{4} \right], \quad (4.9)$$

where,

$$\epsilon_0^{eff} = \epsilon_0 - \frac{1}{\hbar\omega_0} (g_1^2 + zg_2^2), \quad [z = \text{No. of NNs}] \quad (4.10)$$

$$t_{eff} = t e^{-\frac{1}{(\hbar\omega_0)^2} [(g_1 - g_2)^2 + (z - 1)g_2^2]},$$
(4.11)

$$\beta_{eff} = \beta e^{-\frac{1}{(\hbar\omega_0)^2} [(g_1 - g_2)^2 + (z - 1)g_2^2]},$$
(4.12)

$$U_{eff} = U - \frac{2}{\hbar\omega_0} (g_1^2 + zg_2^2). \tag{4.13}$$

$$\mathcal{F} = \begin{pmatrix} \cos\left(\frac{\pi}{N}\right) & -i\sin\left(\frac{\pi}{N}\right) \\ -i\sin\left(\frac{\pi}{N}\right) & \cos\left(\frac{\pi}{N}\right) \end{pmatrix},\tag{4.14}$$

$$g = \begin{pmatrix} \sin\left(\frac{\pi}{N}\right) & i\cos\left(\frac{\pi}{N}\right) \\ -i\cos\left(\frac{\pi}{N}\right) & -\sin\left(\frac{\pi}{N}\right) \end{pmatrix}. \tag{4.15}$$

To deal with the e-e interaction we now apply Hartree-Fock mean-field approximation (HF-MFA) which works well in the weak-coupling regime. The resulting Hamiltonian reads

$$H_{eff}^{M} = \sum_{i=1}^{N} \tilde{c}_{i}^{\dagger} \left[\mathbb{P} + (-1)^{j} \mathbb{Q} \right] \tilde{c}_{i} - \left[e^{i \left(\theta_{\sigma} + \frac{\pi}{N}\right)} \sum_{\langle ij \rangle}^{N} \tilde{c}_{i}^{\dagger} \left\{ t_{eff} \mathcal{F} + i \beta_{eff} \mathcal{G} \right\} \tilde{c}_{j} + h.c. \right] + K , (4.16)$$

where we have divided the total number of sites N (which, for simplicity, is considered as an even number) into even-numbered sites (A sub-system) and odd-numbered sites (B sub-system) and introduced the charge density n, CDW parameter c and SDW parameter s respectively as

$$n = \frac{1}{2} [(n_{A\uparrow} + n_{A\downarrow}) + (n_{B\uparrow} + n_{B\downarrow})], \qquad (4.17)$$

$$c = \frac{1}{2}[(n_{A\uparrow} + n_{A\downarrow}) - (n_{B\uparrow} + n_{B\downarrow})], \tag{4.18}$$

$$s = \frac{1}{2} [(n_{A\uparrow} - n_{A\downarrow}) - (n_{B\uparrow} - n_{B\downarrow})]. \tag{4.19}$$

and the notations \mathbb{P} , \mathbb{Q} as

$$\mathbb{P} = \begin{pmatrix} \frac{\epsilon_{A\uparrow} + \epsilon_{B\uparrow}}{2} & 0\\ 0 & \frac{\epsilon_{A\downarrow} + \epsilon_{B\downarrow}}{2} \end{pmatrix}, \tag{4.20}$$

$$\mathbb{Q} = \begin{pmatrix} \frac{\epsilon_{A\uparrow} - \epsilon_{B\uparrow}}{2} & 0\\ 0 & \frac{\epsilon_{A\downarrow} - \epsilon_{B\downarrow}}{2} \end{pmatrix}, \tag{4.21}$$

where,

$$\epsilon_{A\uparrow} = \epsilon_0^{eff} + \frac{U_{eff}}{2} (c - s), \tag{4.22}$$

$$\epsilon_{B\uparrow} = \epsilon_0^{eff} - \frac{U_{eff}}{2} (c - s), \tag{4.23}$$

$$\epsilon_{A\downarrow} = \epsilon_0^{eff} + \frac{U_{eff}}{2} (c+s),$$
 (4.24)

$$\epsilon_{B\downarrow} = \epsilon_0^{eff} - \frac{U_{eff}}{2} (c+s),$$
 (4.25)

$$K = \frac{U_{eff}}{4}N(n^2 - c^2 + s^2). \tag{4.26}$$

Next, we perform Fourier transformation: $\tilde{c}_l = \frac{1}{\sqrt{N}} \sum_k e^{ikla} \tilde{c}_k$, a being the lattice constant and obtain after some algebra, the following Hamiltonian in the momentum space:

$$H_{eff}^{M} = \sum_{k=-\pi/a}^{\pi/a} c_{k}^{\dagger} \mathbb{R} c_{k}^{\dagger} + \sum_{k=-\pi/a}^{\pi/a} c_{k}^{\dagger} \mathbb{Q} c_{k+\pi/a}^{\dagger} + K, \tag{4.27}$$

where \tilde{c}^{\dagger} (\tilde{c}) are redefined as c^{\dagger} (c) and the matrix \mathbb{R} is obtained as

$$\mathbb{R} = \begin{pmatrix} \frac{\epsilon_{A\uparrow} + \epsilon_{B\uparrow}}{2} + \alpha_{11}(k) & \alpha_{12}(k) \\ \alpha_{21}(k) & \frac{\epsilon_{A\downarrow} + \epsilon_{B\downarrow}}{2} + \alpha_{22}(k) \end{pmatrix}, \tag{4.28}$$

where α_{mn} (m, n = 1,2) are given by

$$\alpha_{11}(k) = -2t_{eff}\cos\left(ka + \theta_{\sigma} - \frac{\pi}{N}\right)\cos\left(\frac{\pi}{N}\right) + 2\beta_{eff}\sin\left(ka + \theta_{\sigma} - \frac{\pi}{N}\right)\sin\left(\frac{\pi}{N}\right), (4.29)$$

$$\alpha_{12}(k) = -2t_{eff}\sin\left(ka + \theta_{\sigma} - \frac{\pi}{N}\right)\sin\left(\frac{\pi}{N}\right) + 2\beta_{eff}\cos\left(ka + \theta_{\sigma} - \frac{\pi}{N}\right)\cos\left(\frac{\pi}{N}\right), (4.30)$$

$$\alpha_{12}(k) = -2t_{eff}\sin\left(ka + \theta_{\sigma} - \frac{\pi}{N}\right)\sin\left(\frac{\pi}{N}\right) - 2\beta_{eff}\cos\left(ka + \theta_{\sigma} - \frac{\pi}{N}\right)\cos\left(\frac{\pi}{N}\right), (4.31)$$

$$\alpha_{22}(k) = -2t_{eff}\cos\left(ka + \theta_{\sigma} - \frac{\pi}{N}\right)\cos\left(\frac{\pi}{N}\right) - 2\beta_{eff}\sin\left(ka + \theta_{\sigma} - \frac{\pi}{N}\right)\sin\left(\frac{\pi}{N}\right). (4.32)$$

Our calculation is performed in the reduced Brillouin zone (RBZ) i.e., k lies in the range: $-\pi/2a \le k \le +\pi/2a$ and α satisfies the relation: $\alpha_{ij} (k + \pi/a) = -\alpha_{ij} (k)$. Therefore, the effective MF Hamiltonian in the RBZ can be written as

$$H_{eff}^{M} = \sum_{k=0}^{\pi/a} \left[\begin{pmatrix} c_{k\uparrow}^{\dagger} & c_{k\downarrow}^{\dagger} & c_{k+\frac{\pi}{a},\uparrow}^{\dagger} & c_{k+\frac{\pi}{a},\downarrow}^{\dagger} \end{pmatrix} \mathbb{W} \begin{pmatrix} c_{k\uparrow} \\ c_{k\downarrow} \\ c_{k+\frac{\pi}{a},\uparrow}^{\dagger} \\ c_{k+\frac{\pi}{a},\downarrow}^{\dagger} \end{pmatrix} \right] + K , \quad (4.33)$$

where the matrix W is given by

$$\mathbb{W} = \begin{pmatrix}
\frac{\epsilon_{A\uparrow} + \epsilon_{B\uparrow}}{2} + \alpha_{11}(k) & \alpha_{12}(k) & \frac{\epsilon_{A\uparrow} - \epsilon_{B\uparrow}}{2} & 0 \\
\alpha_{21}(k) & \frac{\epsilon_{A\downarrow} + \epsilon_{B\downarrow}}{2} + \alpha_{22}(k) & 0 & \frac{\epsilon_{A\downarrow} - \epsilon_{B\downarrow}}{2} \\
\frac{\epsilon_{A\uparrow} - \epsilon_{B\uparrow}}{2} & 0 & \frac{\epsilon_{A\uparrow} + \epsilon_{B\uparrow}}{2} - \alpha_{11}(k) & -\alpha_{12}(k) \\
0 & \frac{\epsilon_{A\downarrow} - \epsilon_{B\downarrow}}{2} & -\alpha_{21}(k) & \frac{\epsilon_{A\downarrow} + \epsilon_{B\downarrow}}{2} - \alpha_{22}(k)
\end{pmatrix} \tag{4.34}$$

To calculate the GS energy of the system, we perform a self-consistent numerical diagonalization technique which generates the energy spectrum E_i with the corresponding Fermi distribution function: $f(E_i) = \left[e^{(E_i - \mu)/k_B T}\right]^{-1}$, μ being the chemical potential, k_B the Boltzman's constant and T the temperature. Thus, the GS energy can be expressed as

$$E_{GS} = \sum_{i} E_{i} f(E_{i}) + K, \tag{4.35}$$

and following Ref. [20], the persistent charge current (PCC), I_{PC} can be computed from the relation

$$I_{PC} = -\frac{1}{2\pi} \left(\frac{\partial E_{GS}}{\partial \Phi_{\sigma}} \right)$$
, where, $\Phi_{\uparrow} = \Phi_{\downarrow} = \Phi$. (4.36)

As there exist two types of particles namely, the spin-up and spin-down particles, we can also calculate persistent spin current (PSC), I_{PC}^{σ} for two different spin-orientations in the 1/2-spin current unit [20]. I_{PC}^{σ} is given by

$$I_{PC}^{\sigma} = -\frac{1}{2\pi} \frac{\partial E_{GS}}{\partial \Phi_{\sigma}}$$
, where, $\Phi_{\uparrow} = -\Phi_{\downarrow} = \Phi$, (4.37)

which can equivalently be expressed as

$$I_{PC}^{\sigma} = -\frac{1}{2\pi} \left(\frac{\partial E_{GS}}{\partial \Phi} \right) \sigma. \tag{4.38}$$

4.3 Numerical results and discussions

For convenience, we scale all energies in units of $\hbar\omega_0$ and set t=1. We discuss the numerical results of PCC and PSC in following sections.

4.3.1 Results for persistent charge current

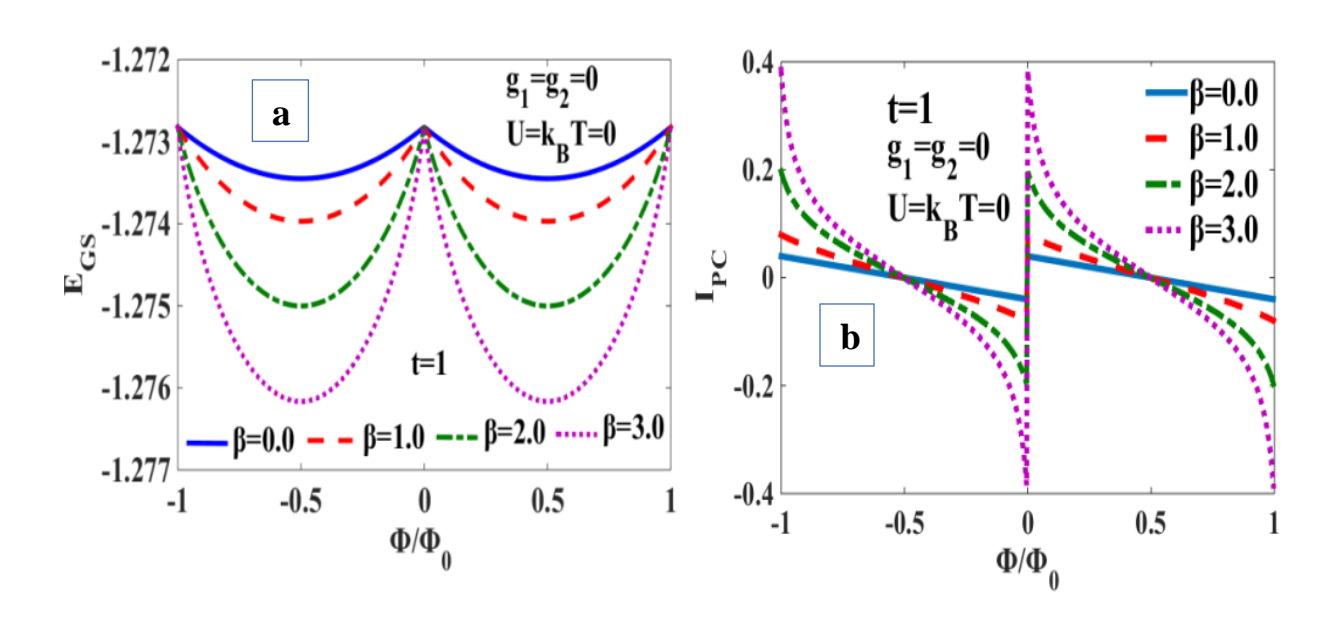


Fig.4.2 (a) GS energy and (b) PCC as a function of magnetic flux Φ/Φ_0 for different values of DSOI strength β at $U = g_1 = g_2 = k_B T = \mu = 0$.

In Fig.4.2a and 4.2b we plot respectively the GS energy (E_{GS}) and PCC (I_{PC}) as a function of magnetic flux Φ which is an integral multiple of magnetic flux quantum $\Phi_0 = hc/2e$. The periodicity with Φ in both the figures is clearly visible. Fig.4.2a shows the variation of GS energy for different values of the DSOI strength β and we can see that E_{GS} increases with β when all other interactions are absent. In general, the value of β cannot be changed for a particular material as it originated from the internal BIA of the material. Therefore, our results are applicable to different materials whose β lies in the range considered here. Fig.4.2b shows that PCC increases with increasing DSOI, but the shape of the variation gets altered after a critical β ($\beta_c = 1$), though remains symmetrical with respect to $\Phi = 0$. Monisha et al. [22] have studied the same in the presence of RSOI alone. We would like to mention that DSOI can give rise to a greater enhancement of PCC compared to RSOI (not shown here).

To see the variation with β explicitly, we have plotted Fig.4.3 both for zero and non-zero temperature. We observe that I_{PC} increases monotonically with β and the effect of temperature is significant for higher values of β .

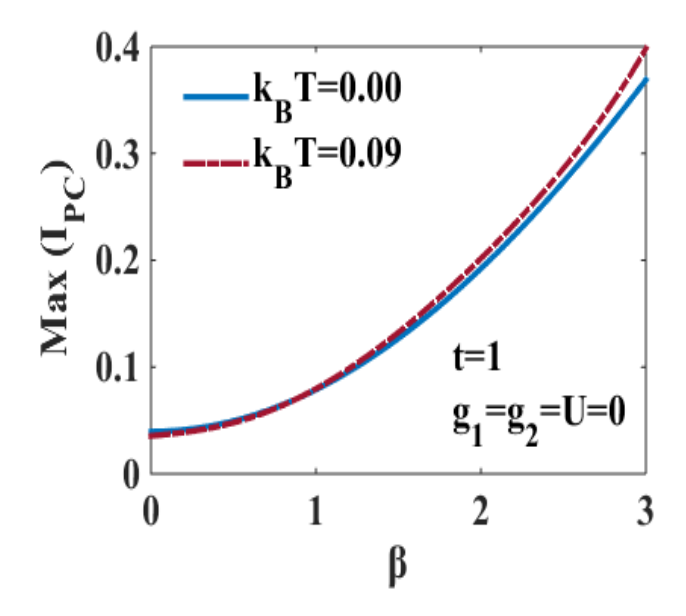


Fig.4.3 PCC vs. β for $k_BT = 0$ & $k_BT = 0.09$ at $U = g_1 = g_2 = \mu = 0$.

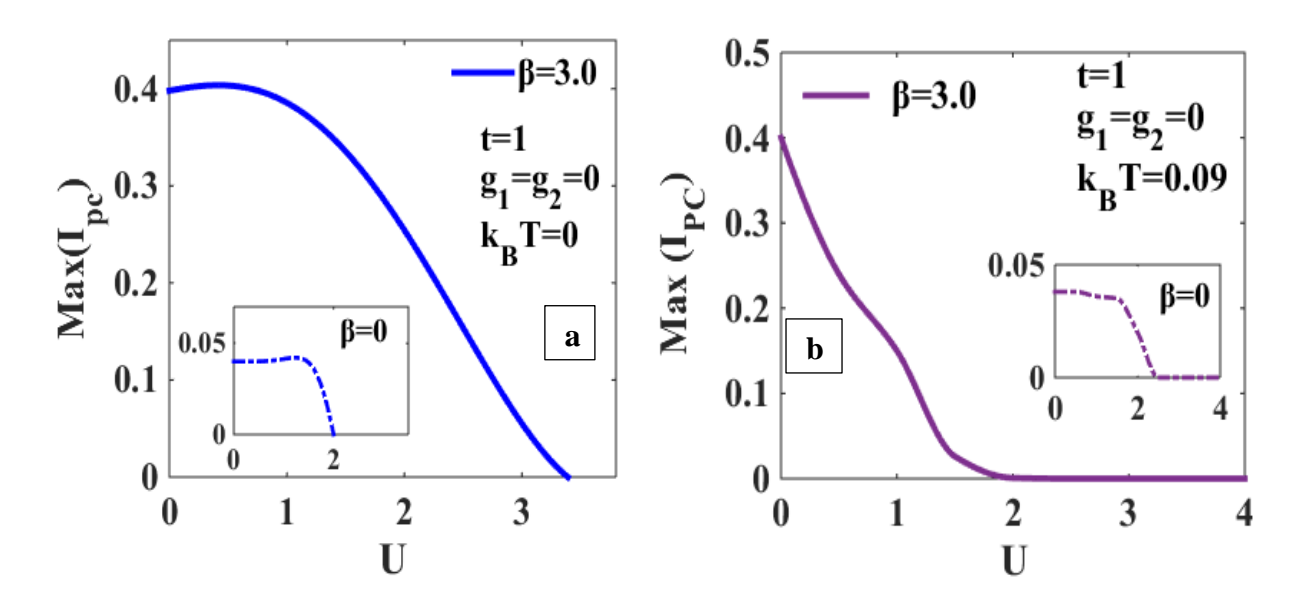


Fig.4.4 PCC vs. onsite e-e interaction U for $\beta=0$ (inset) and $\beta=3$ at $g_1=g_2=\mu=0$ for (a) $k_BT=0$ and (b) $k_BT=0.09$.

Fig.4.4a shows the variation of I_{PC} with onsite Coulomb interaction strength U with and without DSOI at T=0. In the chosen energy scale $\hbar\omega_0=1$, the range of U ($0 \le U \le 4$) provides a weak-coupling regime where MFA is considered to be a plausible approximation.

The inset is drawn for $\beta=0$. There exists a qualitative difference between $\beta=0$ and $\beta\neq 0$ plots. For $\beta=0$, the behaviour of PCC is primarily constant up to a certain value of U and after that it falls sharply and becomes zero at U=2. The reason can be explained simply by the competition between hopping, t and onsite repulsion due to Coulomb interaction, U. The electron can go from one site to the other unless U reaches a critical limit $U_c=1.3$ which prevents further hopping. Beyond U_c , U reduces PCC extremely rapidly. However, the notion of critical U is not so prominent for U at a finite temperature of U (inset) and U and U in a smooth fashion. In Fig.4.4b the effect of temperature is displayed for both U (inset) and U in a smooth U at a finite temperature for U in a smooth of PCC reduces much faster with U at a finite temperature for U in a smooth respective U at U at a finite temperature for U in a smooth respective U at a finite temperature for U in a smooth respective U at a finite temperature for U in a smooth respective U at a finite temperature for U in a smooth respective U at a finite temperature for U in the presence of temperature.

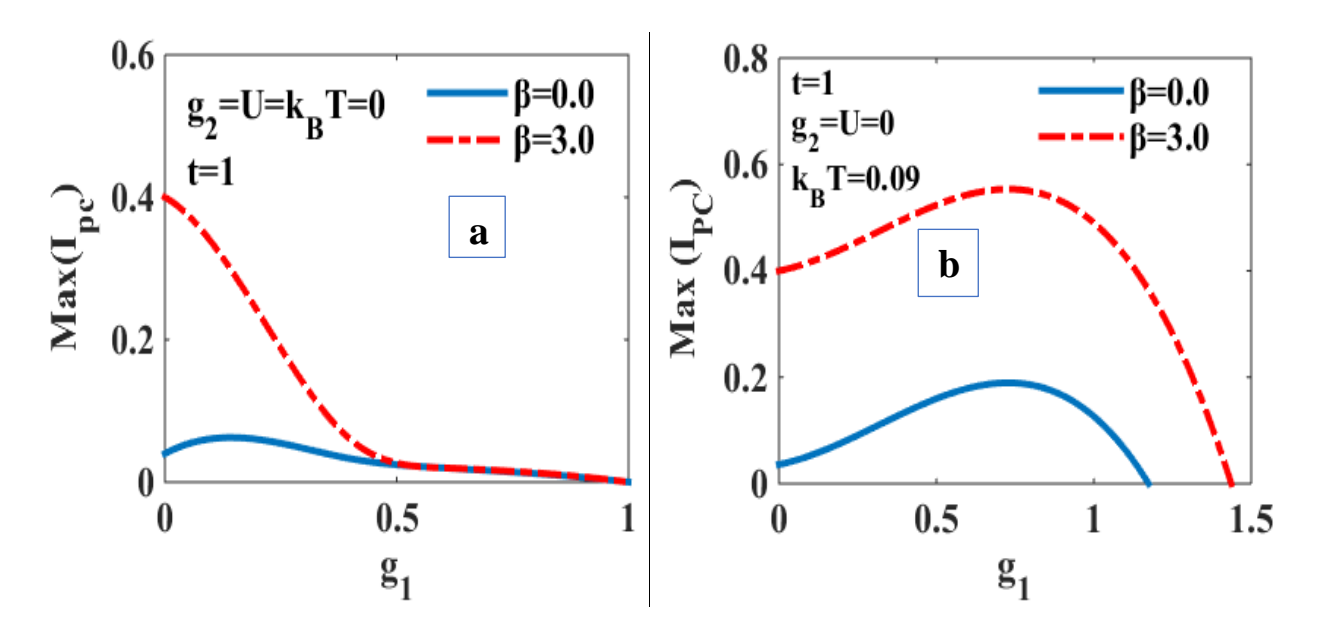


Fig.4.5 The effect of onsite e-p interaction, g_1 on PCC at $U = g_2 = \mu = 0$ for $k_B T = 0$ and (b) $k_B T = 0.09$.

To see the effect of onsite e-p interaction we plot I_{PC} as a function g_1 in Fig.4.5. We look into the effect of temperature on I_{PC} vs. g_1 behaviour in Fig.4.5b while in 4.5a, we consider the zero-temperature behaviour. In Fig.4.5a, one may notice that PCC drops as g_1 increases. This happens because of the polaronic effect. As g_1 increases, the e-p interaction distorts the lattice more giving rise to a deeper polarization potential in which the electron gets self-trapped or localized at that particular site [24-26]. This causes a reduction in mobility of the electron and as a result PCC decreases. It is obvious that the variation is enhanced for $\beta = 3$ which is also suggested by Fig.4.3. Fig.4.5b gives the behaviour at finite temperature (which

is more realistic). It is evident from the figure that at a finite temperature, PCC increases initially with g_1 , attains a peak, then declines and becomes zero as g_1 increases. The behaviour is same for $\beta=0$ and $\beta=3$.

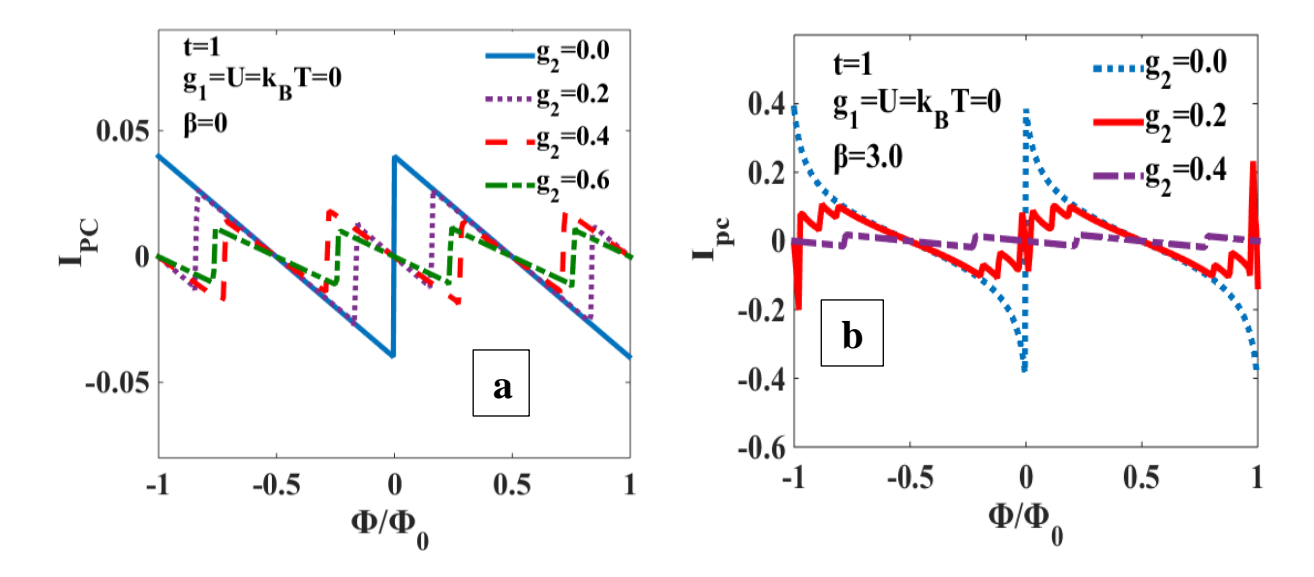


Fig.4.6 I_{PC} as a function of Φ at $U = g_1 = k_B T = \mu = 0$ for different values of g_2 at (a) $\beta = 0$ and (b) $\beta = 3$.

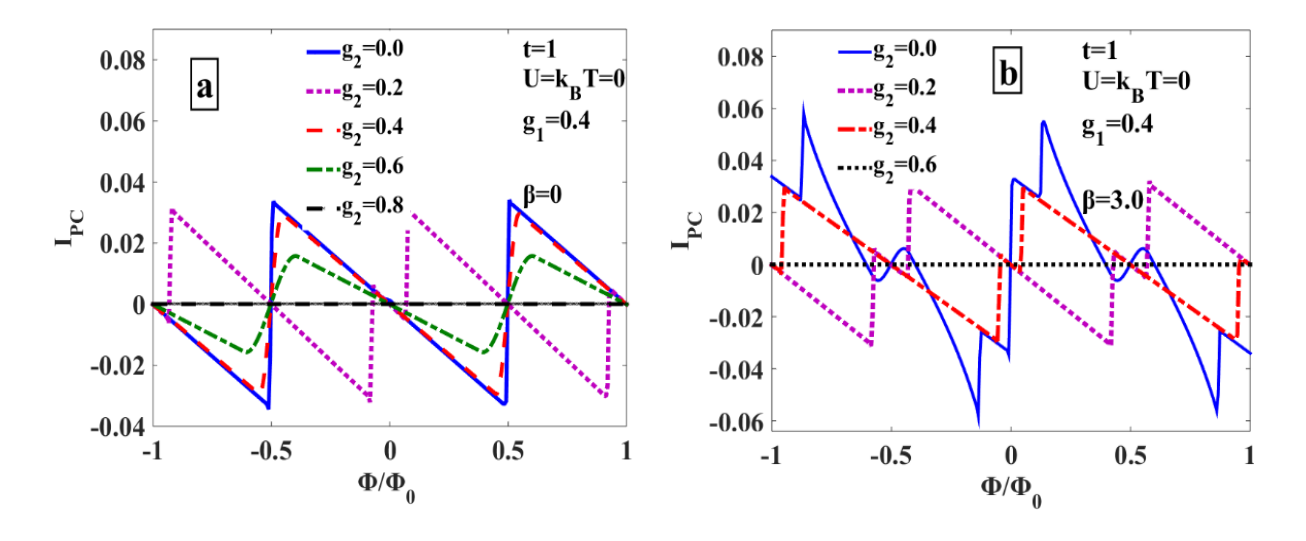


Fig.4.7 I_{PC} as a function of Φ at $U=k_BT=\mu=0$, $g_1=0.4$ for different g_2 values at (a) $\beta=0$ and (b) $\beta=3$.

We study in Fig.4.6, the effect of NN e-p interaction (g_2) on the Φ -dependence of I_{PC} with $g_1 = 0$. In Fig. 4.6a, we consider $\beta = 0$ while $\beta = 3$ -case is studied in Fig. 4.6b. The figures clearly display that PCC gets reduced as g_2 increases, though the magnitude of I_{PC} gets increased when $\beta \neq 0$ (Fig.4.6b). Next, in Figs.4.7, we study the effect of NN e-p interaction (g_2) on the I_{PC} versus Φ – curves in the presence of onsite e-p interaction. It is

evident from Figs.4.7a and 4.7b that the reduction of PC due to polaronic effect is more significant when $g_1 \neq 0$. Interestingly, it can be seen in Figs.4.7 that I_{PC} vanishes completely at a particular combination of g_1 and g_2 .

In Figs.4.8a and 4.8b it is explicitly shown how PCC declines as g_2 increases. The insets are drawn for $\beta=0$. Comparison of Fig. 4.8 with 4.5 shows that PCC dies out faster with g_2 than with g_1 This is understandable from the effective hopping term, $t_{eff} \sim e^{-[(g_1-g_2)^2+(z-1)g_2^2]/(\hbar\omega_0)^2}$. In t_{eff} , there is an additional contribution in the exponent entirely dependent on g_2 which sets off a more pronounced reduction in PCC than due to g_1 alone. The effect of temperature on I_{PC} with g_2 is plotted in Fig.4.8b. Here also, PCC exhibits a peak-like structure, but again the suppression of PCC is stronger in the case of g_2 . One may also notice that the resistive effect on PCC due to e-p interaction is much more prominent than due to e-e interaction.

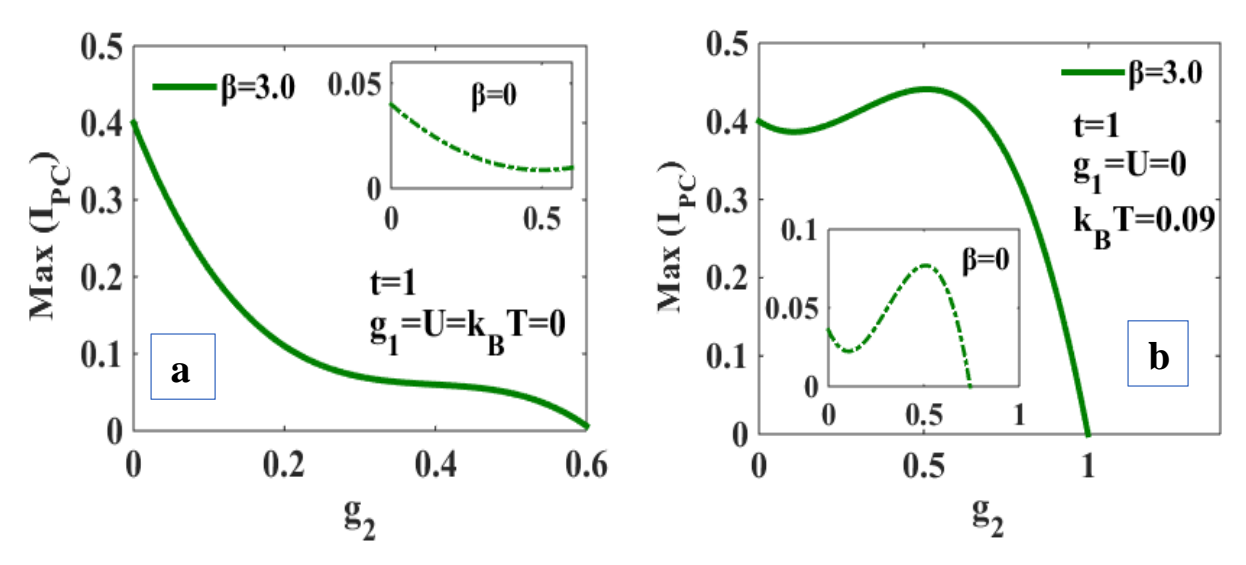


Fig.4.8 Effect of N-N e-p interaction, g_2 on I_{PC} as a function of Φ at $U = g_1 = \mu = 0$ for (a) $k_B T = 0$ and (b) $k_B T = 0.09$.

To show the impact of temperature, we plot PCC directly with k_BT in Figs. 4.9(a-c) for different combinations of g_1 and g_2 and $\beta = 3$. Fig.4.9a is shown for $g_1 = g_2 = 0$. (The $\beta = 0$ case is shown in the inset). Fig.4.9b and 4.9c are plotted for $g_1 = 0.5 \& g_2 = 0$ and $g_1 = 0 \& g_2 = 0.5$ respectively. The PCC not only reduces with increasing temperature (as was suggested by Büttiker et al. [28]), but it also exhibits peak at a low temperature. In the presence of g_1 or g_2 , PCC starts from zero at T = 0, whereas it starts from a finite value at T = 0 when both g_1 and g_2 are zero. The peak-like pattern is more noticeable when either g_1 or g_2 is nonzero.

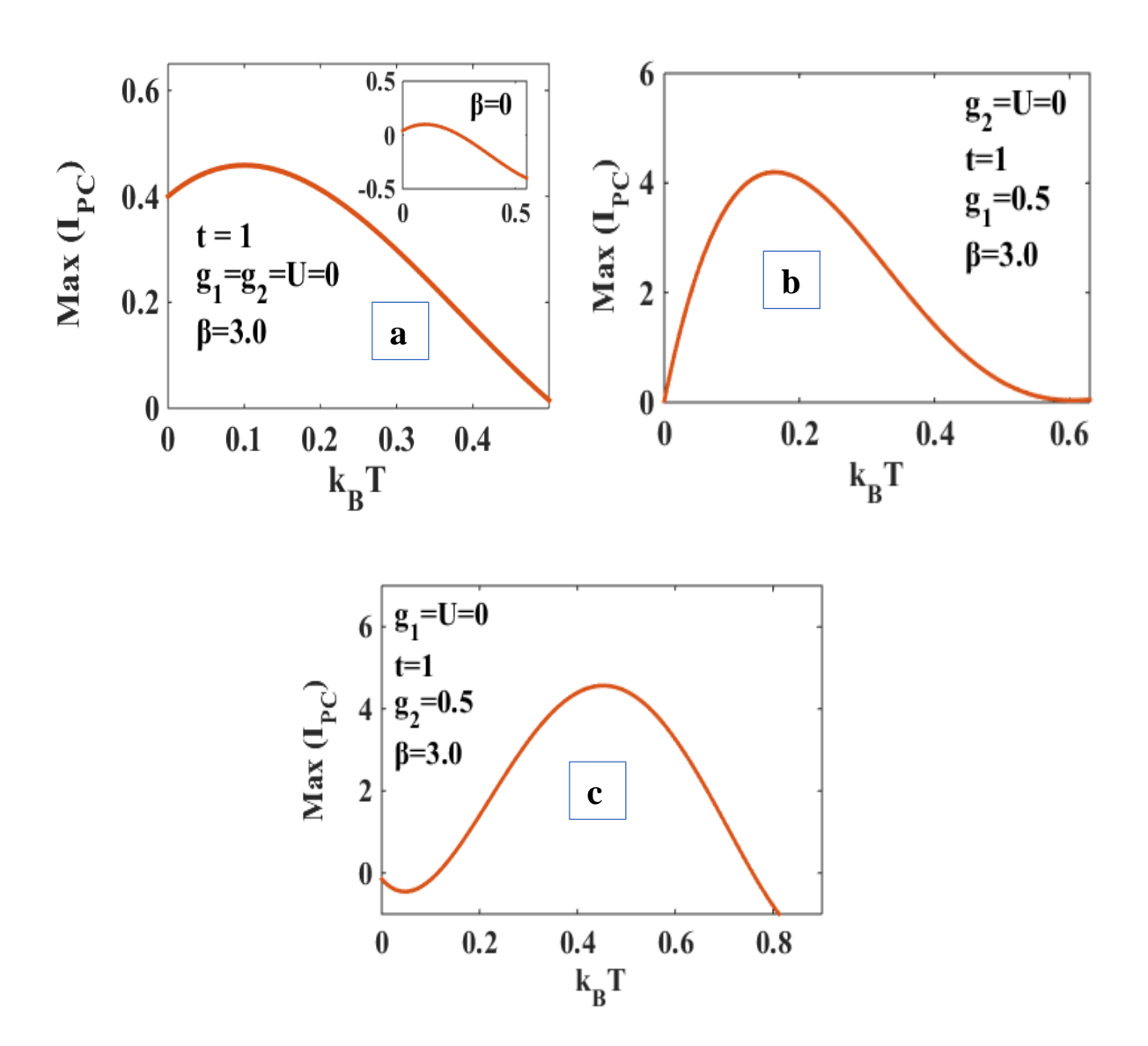


Fig.4.9 Effect of temperature, T on PCC at $\beta = 3.0$, $U = \mu = 0$ for: (a) $g_1 = g_2 = 0$; (b) $g_1 = 0.5 \& g_2 = 0$; (c) $g_2 = 0.5 \& g_1 = 0$.

As the change of number of particles may have some effect on PCC, we also study the variation of PCC with chemical potential μ . In Fig.4.10a, we plot I_{PC} versus Φ for several values of μ at $\beta=0$ with other interactions switched off. Fig.4.10b shows the explicit dependence of I_{PC} on μ for $\beta\neq0$ and $\beta=0$ (inset). These two plots are at T=0. We can notice clearly that PCC decreases monotonically with increasing μ at T=0. Interestingly, in Fig.4.9c it is seen that PCC increases with μ at a finite temperature.

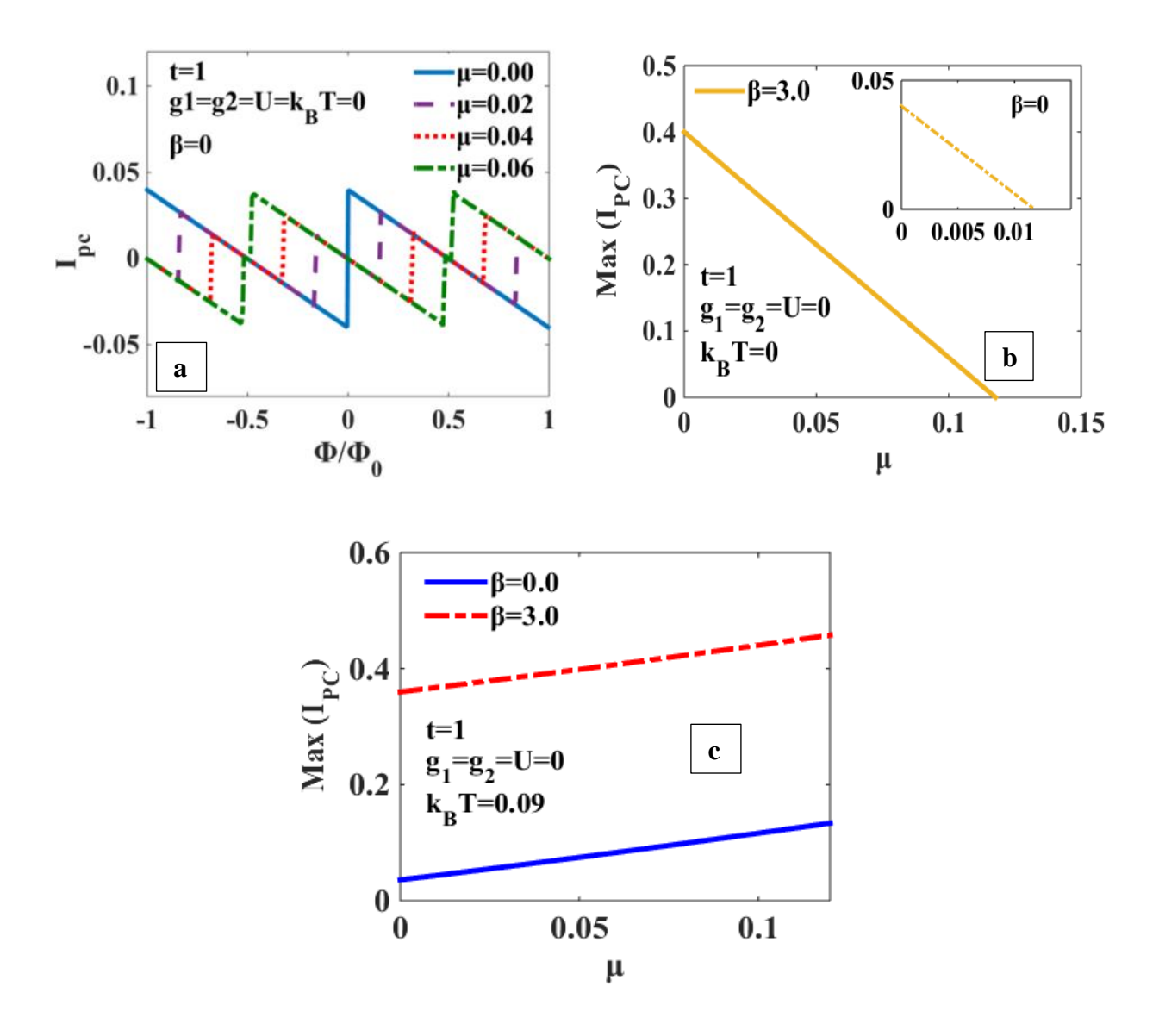


Fig.4.10 (a) I_{PC} vs. Φ/Φ_0 for different values of μ at $U = g_1 = g_2 = k_B T = \beta = 0$. PC vs. μ for different β values at $g_1 = g_2 = U = 0$ for (b) $k_B T = 0$ & (c) $k_B T = 0.09$.

4.3.2 Results for persistent spin current

Here we wish to investigate PSC (I_{PC}^{σ}) in the A-B ring. In Fig. 4.11(a), we plot I_{PC}^{σ} as a function of A-B flux Φ for a fixed DSOI strength β when all the other interactions and temperature have been taken equal to zero. The blue solid curve represents PSC for spin-up electrons and the red dotted curve denotes the same for the spin-down electrons. We can clearly see that the variations of spin-up PC, I_{PC}^{\uparrow} and spin-down PC, I_{PC}^{\downarrow} are completely opposite with respect to Φ/Φ_0 . They represent two circulating spin-currents moving in opposite directions in the A-B ring. Both I_{PC}^{\uparrow} and I_{PC}^{\downarrow} are periodic in Φ/Φ_0 with period 1 i.e., π . Interestingly, I_{PC}^{\uparrow} and I_{PC}^{\downarrow} meet each other at $\Phi/\Phi_0 = 0, \pm 0.5$. But for these values of

 Φ/Φ_0 , there exists clear separation between I_{PC}^{\uparrow} and I_{PC}^{\downarrow} which demonstrates a spin-current splitting at a fixed value of Φ/Φ_0 . One should notice that this splitting between two spin currents is an effective splitting arising from the combined effect of A-B flux Φ/Φ_0 and DSOI. The inset represents the PSCs in the absence of DSOI i.e., for $\beta = 0$. Here, the splitting in spin-currents is solely determined by magnetic flux Φ . It can be seen that PSC not only changes qualitatively, but it also reduces significantly at $\beta = 0$ and hence one can expect that the splitting reduces as β reduces. As mentioned earlier, both I_{PC}^{\uparrow} and I_{PC}^{\downarrow} equally exhibit a sharp discontinuity at $\Phi/\Phi_0 = 0$ when all other interactions are zero. To see the polaronic effects on I_{PC}^{σ} , we plot I_{PC}^{σ} as a function of Φ/Φ_0 for different combinations of g_1 and g_2 in Fig.4.11(b) for $\beta = 3$ and $U = k_B T = \mu = 0$. We observe that the qualitative behaviour of I_{PC}^{σ} changes with respect to Φ/Φ_0 in the presence of e-p interaction, although the periodicity of I_{PC}^{σ} is still preserved. Furthermore, I_{PC}^{\uparrow} and I_{PC}^{\downarrow} have an opposite behaviour with respect to Φ/Φ_0 . In $g_1 = 0.2$, $g_2 = 0$ case, we notice that unlike Fig.4.11(a), the sharp discontinuity at $\Phi/\Phi_0 = 0$ vanishes. As expected, the onsite e-p interaction reduces I_{PC}^{σ} . For $g_1 = 0$, $g_2 = 0.2$ case (inset(i)), the pattern of I_{PC}^{σ} changes and it reduces by the presence of g₂. Interestingly, I_{PC}^{\uparrow} and I_{PC}^{\downarrow} coincide also at $\Phi/\Phi_0 = \pm 1$ in addition to at $\Phi/\Phi_0 = 0, \pm 0.5$ points when either of g₁ and g₂ is non-zero. Therefore, one would expect spin-current splitting becoming zero at half-integral multiples of Φ/Φ_0 if g_1 or g_2 is non-zero. The existence of these additional crossing points is entirely caused by e-p interaction. Surprisingly, the degeneracy at $\Phi/\Phi_0=\pm 1$ is lifted again when $g_1=g_2=0.2$ (inset (ii))

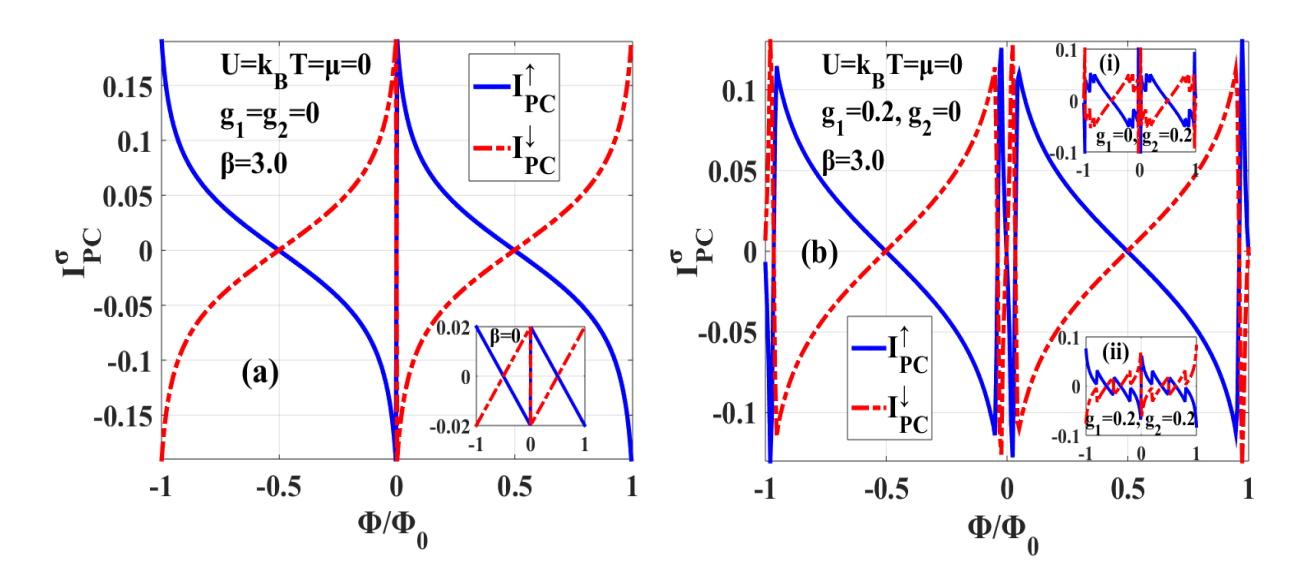


Fig.4.11 PSC I_{PC}^{σ} vs. A-B flux Φ/Φ_0 for $\beta = 3.0$, $U = k_B T = \mu = 0$ at (a) $g_1 = g_2 = 0$. (Inset: at $\beta = 0$), (b) $g_1 = 0.2$, $g_2 = 0$. (Insets: (i) $g_1 = 0$, $g_2 = 0.2$, (ii) $g_1 = g_2 = 0.2$).

resembling the observation in Fig.4.11(a), although the behaviour is very much different now. Hence, the splitting does not go to zero at $\Phi/\Phi_0 = \pm 1$ when g_1 and g_2 become equal. Another point to be observed in the inset (ii) is that the sharp discontinuity reappears at $\Phi/\Phi_0 = 0$ when g_1 equals g_2 .

To see how the spin-current splitting varies for different DSOI and e-p interaction strengths explicitly, we show splitting gap ΔI_{PC}^{σ} as a function of A-B flux Φ/Φ_0 in Fig.4.12 in the absence of other interactions. Here we define the spin-current splitting gap as: $\Delta I_{PC}^{\sigma} = I_{PC}^{\uparrow}$ I_{PC}^{\downarrow} . Essentially, it gives the total PSC, I_S . However, in Fig.4.12 we show the modulus of ΔI_{PC}^{σ} i.e., $|\Delta I_{PC}^{\sigma}|$ as we want to study the splitting gap with respect to Φ/Φ_0 . In Fig.4.12(a), it is shown that periodicity of $|\Delta I_{PC}^{\sigma}|$ with Φ/Φ_0 remains intact which is expected. More interestingly, $|\Delta I_{PC}^{\sigma}|$ additionally shows a symmetric behaviour. However, $|\Delta I_{PC}^{\sigma}|$ changes considerably with Φ and β . Thus, one can tune the splitting gap by changing the flux and the SOI parameters. One may notice that $|\Delta I_{PC}^{\sigma}|$ can be enhanced significantly by increasing DSOI strength, β . This is also expected as β enhances individual spin-currents shown in Fig.4.11(a). We want to mention that $|\Delta I_{PC}^{\sigma}|$ becomes zero at $\Phi/\Phi_0 = \pm 0.5$. At $\Phi/\Phi_0 = 0$, it becomes maximum suggesting a large splitting at zero A-B flux caused entirely due to DSOI. One can evaluate the strength of DSOI experimentally by measuring the zero-flux splitting. This zero-flux splitting arises due to the discontinuity of I_{PC}^{σ} at $\Phi/\Phi_0 = 0$. We can see that the extrema of $|\Delta I_{PC}^{\sigma}|$ occur at half-integral multiples of Φ/Φ_0 as suggested by Fig.4.11(a) when $U = g_1 = g_2 = 0$. Fig.4.12(b) displays $|\Delta I_{PC}^{\sigma}|$ as a function of Φ/Φ_0 for different combinations of g_1 and g_2 . Here also, $|\Delta I_{PC}^{\sigma}|$ is periodic with respect to Φ/Φ_0 even in the presence of e-p interaction as suggested by Fig.4.11(b), showing more oscillations especially when $g_2 \neq 0$. It is important to mention that the maximum of splitting gap $|\Delta I_{PC}^{\sigma}|$ decreases substantially as we turn on g_1 or g_2 or both. This can be understood from the resistive effect of polaronic interaction on I_{PC}^{σ} which reduces I_{PC}^{\uparrow} and I_{PC}^{\downarrow} individually and hence $|\Delta I_{PC}^{\sigma}|$ reduces as e-p interaction increases. It can be seen that unlike in Fig.4.12(a), when either g₁ (blue solid curve) or g_2 (red dotted curve) is present, $|\Delta I_{PC}^{\sigma}|$ becomes almost zero at $\Phi/\Phi_0 =$ ± 1 and at $\Phi/\Phi_0 = 0$ it reaches its minimum (but not exactly zero). However, $|\Delta I_{PC}^{\sigma}|$ is nonzero and finite at $\Phi/\Phi_0 = 0$, ± 1 when $g_1 = g_2$ and U = 0 as suggested by Fig.4.11. Due to the combined effect of g_1 and g_2 , the curve for $g_1 = g_2 = 0.2$ is much lower than that for the case of $g_1 = g_2 = 0$. But in all cases, $|\Delta I_{PC}^{\sigma}|$ vanishes at $\Phi/\Phi_0 = \pm 0.5$. Thus, spin-splitting gap is very much dependent on different regimes of A-B flux and e-p interaction strengths. These findings also follow from Fig.4.11(b).

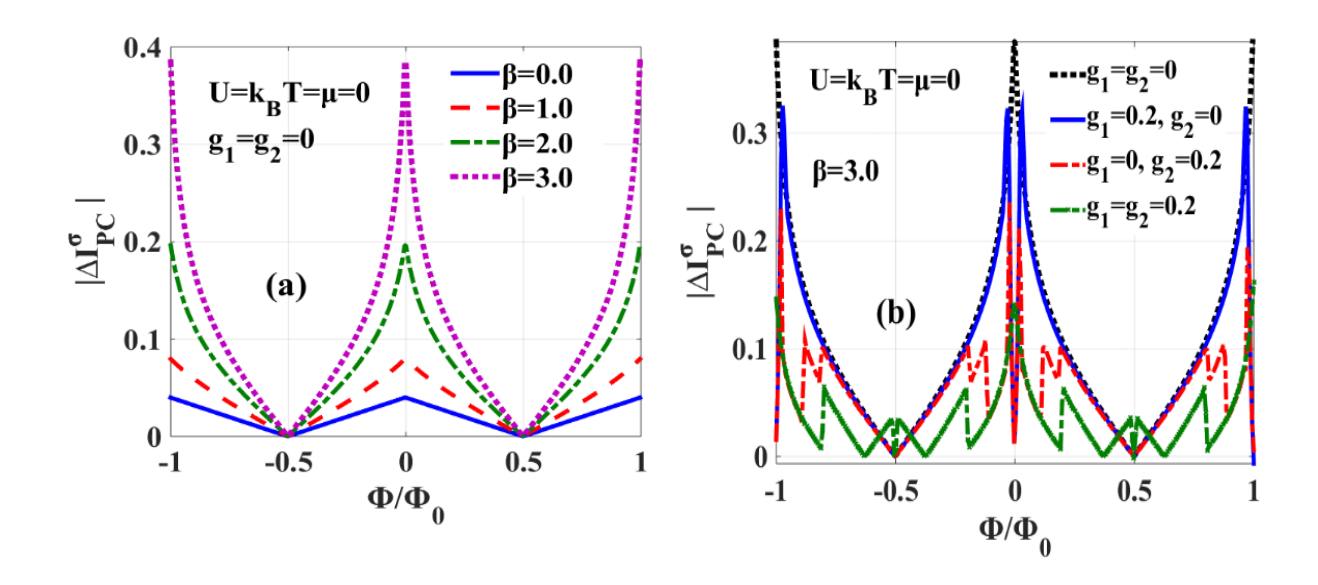


Fig.4.12 Absolute spin-current splitting gap $|\Delta I_{PC}^{\sigma}|$ vs. Φ/Φ_0 at $U=k_BT=\mu=0$ for (a) different values of at $g_1=g_2=0$, (b) different g_1 and g_2 combinations at $\beta=3$.

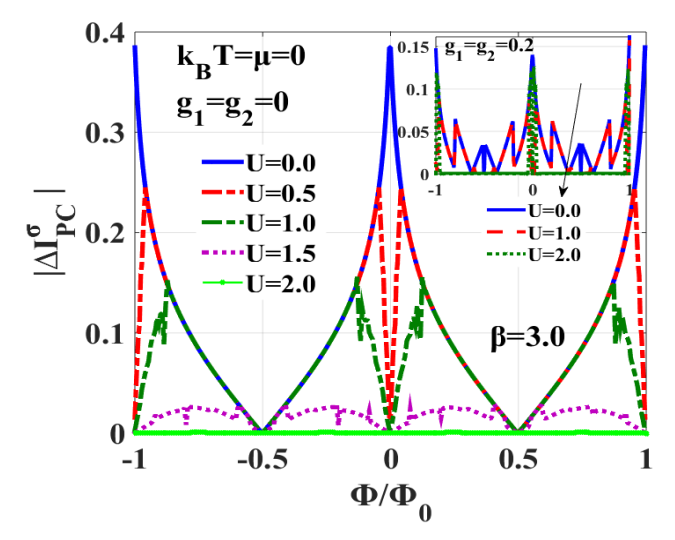


Fig.4.13 $|\Delta I_{PC}^{\sigma}|$ vs. Φ/Φ_0 for different *U*-values at $k_BT=\mu=g_1=g_2=0$ for $\beta=3$. Inset: at $g_1=g_2=0.2$.

Fig.4.13 shows the variation of the magnitude of the spin-splitting gap $|\Delta I_{PC}^{\sigma}|$ as a function of Φ/Φ_0 for different values of Coulomb strength U with a fixed β -value and $g_1=0=g_2$, whereas, the inset shows the same nonzero g_1 and g_2 . It is clearly shown that the shape and the value of $|\Delta I_{PC}^{\sigma}|$ change very much as we switch on U, but $|\Delta I_{PC}^{\sigma}|$ maintains periodicity and symmetry over the entire range of Φ/Φ_0 for any value of U. One can observe that U reduces the maximum of splitting-gap, $|\Delta I_{PC}^{\sigma}|$ because of the resistive effect produced by the Coulomb interaction. Also, it is interesting to mention that at equal intervals of half-flux, $|\Delta I_{PC}^{\sigma}|$ reaches zero giving rise to zero splitting for a finite U, whereas, at U=0, $|\Delta I_{PC}^{\sigma}|$ becomes zero only at $\Phi/\Phi_0=\pm 0.5$. These additional zero-splitting points at a finite U occur

purely due to Coulomb correlation as we have set other interactions as zero. However, $|\Delta I_{PC}^{\sigma}|$ remains zero over entire Φ -range beyond a particular U. Here, we can see this feature at U=2. To study the interplay of Coulomb and e-p interactions, we plot $|\Delta I_{PC}^{\sigma}|$ in the inset at $g_1=g_2=0.2$. We can notice that at a non-zero U, $|\Delta I_{PC}^{\sigma}|$ reduces further because of the combined resistive effects of both the interactions. Interestingly, for a given U-value, $|\Delta I_{PC}^{\sigma}|$ also becomes zero at $\Phi/\Phi_0=0,\pm 1$ even when $g_1=g_2=0.2$ which is completely opposite to what we observe in Fig.4.12(b) for the $g_1=g_2$ case. Hence, U makes the splitting zero at half-integral multiples of A-B flux including $\Phi/\Phi_0=0$ point for any combinations of g_1 and g_2 . At U=2 and $g_1=g_2=0.2$, $|\Delta I_{PC}^{\sigma}|$ remains zero throughout the Φ -axis, but it shows some spikes at $\Phi/\Phi_0=0,\pm 1$ unlike in the $g_1=g_2=0$ case. From Fig.4.12 and 4.13 we can comment that the interactions present in the system generate a greater number of crossing points for spin-up and spin-down currents where spin-current splitting gap becomes zero even in the presence of DSOI.

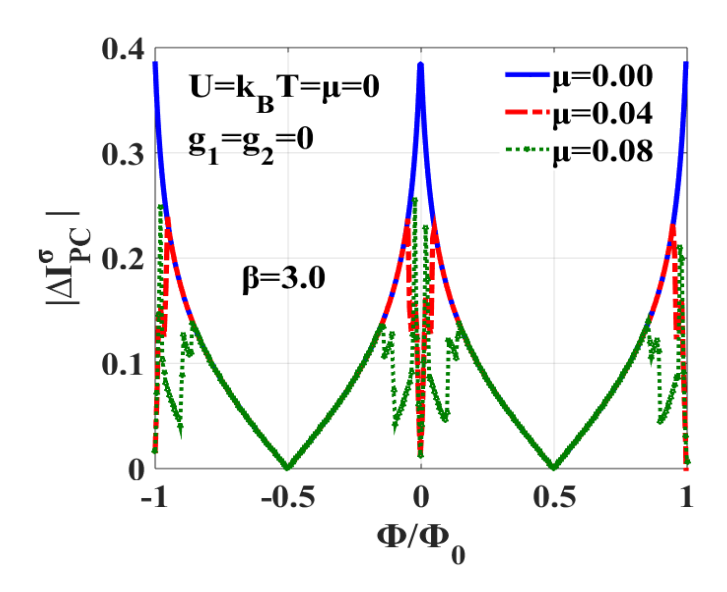


Fig.4.14 $|\Delta I_{PC}^{\sigma}|$ vs. Φ/Φ_0 for different μ -values for $\beta=3$ at $U=k_BT=g_1=g_2=0$.

In Fig. 14, we study the variation of $|\Delta I_{PC}^{\sigma}|$ with Φ for a fixed value of β and for different values of chemical potential μ at T=0 and in the absence of all other interactions. As the number of particles influences the current in the ring, this study should be important. We observe that the maximum of $|\Delta I_{PC}^{\sigma}|$ decreases with increasing μ . $|\Delta I_{PC}^{\sigma}|$ shows more oscillations at around $\Phi/\Phi_0=0,\pm 1$. It appears that $|\Delta I_{PC}^{\sigma}|$ may approach zero at large μ .

Finally, in Fig.4.15, we plot $|\Delta I_{PC}^{\sigma}|$ versus Φ for different values of T with $\beta=3$ in the absence of all other interactions. β . The periodicity and symmetry of $|\Delta I_{PC}^{\sigma}|$ are well-maintained even at a finite T, but both the qualitative and quantitative variations get affected.

The central peak of $|\Delta I_{PC}^{\sigma}|$ at $\Phi/\Phi_0=0$ splits into two less sharp peaks located at around $\Phi/\Phi_0=\pm 0.25$ for a non-zero T and other peaks appear close to $\Phi/\Phi_0=\pm 0.75$ values. More importantly, $|\Delta I_{PC}^{\sigma}|$ becomes zero at $\Phi/\Phi_0=0,\pm 1$ in the presence of T. Hence $|\Delta I_{PC}^{\sigma}|$ exhibits alternate minima and maxima at half-integral multiples of Φ/Φ_0 . It is worth mentioning that $|\Delta I_{PC}^{\sigma}|$ decreases significantly as T increases and becomes vanishingly small after a certain T-value.

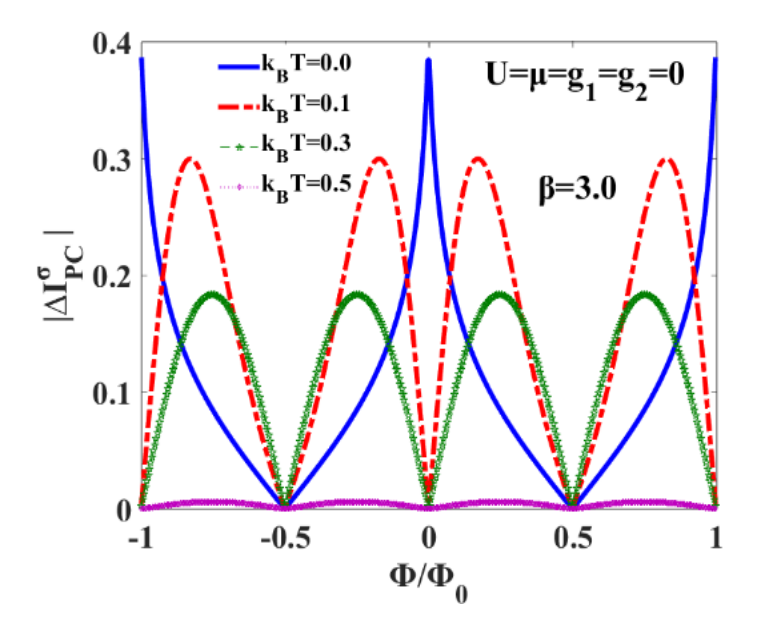


Fig.4.15 $|\Delta I_{PC}^{\sigma}|$ vs. Φ/Φ_0 for different *T*-values for $\beta=3$ at $U=k_BT=\mu=g_1=g_2=0$.

4.4 CONCLUSIONS

In conclusion, we have studied the behaviour of PCs in a mesoscopic QR threaded by an externally applied A-B flux in the presence of e-p interaction, onsite Coulomb interaction and DSOI. We have performed LFT to eliminate the e-p coupling and then applied a unitary transformation to treat the SOI. Finally, to treat the onsite e-e interaction, we have employed HF-MFA on the effective electronic Hamiltonian and performed a self-consistent numerical diagonalization method to calculate the GS energy and PCC. It is shown that the periodicity with the magnetic flux is obeyed both in the GS energy and in PCC. PCC is enhanced significantly by the DSOI. For large values of DSOI strength, the PCC changes its pattern. Both the e-e and e-p interactions reduce PCC significantly leading to a resistive effect. But the e-p interaction inhibits the conduction process more than e-e interaction. In the presence of temperature, the PCC falls more rapidly with e-e interaction. We have furthermore shown that PCC is suppressed more by the NN e-p interaction compared to the onsite e-p interaction.

At a finite temperature, PCC as a function of e-p interaction exhibits a peak. For nonzero g_1 or g_2 , a prominent peak in the low-to-intermediate temperature regime occurs, though in the absence of e-p interactions, PCC decreases with temperature. We have also shown that PCC decreases monotonically with increasing μ at zero temperature, but the behaviour is quite opposite at finite temperature.

We have also studied PSC in the A-B ring where two oppositely directed periodic spin currents for two different spin orientations are generated both in the absence and presence of DSOI. DSOI enhances spin-up and spin-down currents much more than the A-B flux does. In the presence of e-p interaction, a considerable change in the pattern and magnitude of spin-currents occur. The spin-current splitting gap (ΔI_{PC}^{σ}) is increases very much by DSOI. At U=0, the up and down PSCs cross over at every half-integral multiples of A-B flux excluding $\Phi/\Phi_0=0$, leading to zero spin-current splitting even in the presence of DSOI when either of g_1 is g_2 is present, whereas splitting becomes zero only at $\Phi/\Phi_0=\pm 0.5$ when $g_1=g_2$. However, at $U\neq 0$, ΔI_{PC}^{σ} turns out to be zero precisely at every half-integral multiples of Φ including $\Phi/\Phi_0=0$. Therefore, number of zero-splitting points increases as we turn on the interactions. A notable reduction in ΔI_{PC}^{σ} happens in the presence of all the interactions, chemical potential and temperature. The interesting fact is that the spin-splitting is highly tunable by DSOI, A-B flux, temperature and all the other interactions present in the system. We can also determine the value of DSOI strength experimentally by measuring the splitting ΔI_{PC}^{σ} at $\Phi=0$.

REFERENCES

- 1. M. Büttiker, Y. Imry, R. Landauer, Phys. Lett. A **96**, 365–367 (1983).
- 2. A. Schmid, Phys. Rev. Lett., 66, 80 (1991).
- 3. F. von Oppen, E. K. Riedel, Phys. Rev. Lett. 66, 84–87 (1991).
- 4. B. L. Altshuler, Y. Gefen, Y. Imry, Phys. Rev. Lett. 66, 88–91 (1991).
- 5. L. K Castelano., G.-Q Hai, B. Partoens, F. M. Peeters, Phys. Rev. B **78**, 195315 (2008).
- 6. P. A. Orellana, M. Pacheco, Phys. Rev. B 71, 235330 (2005).
- 7. S. K. Maiti, M. Dey, S. Sil, A. Chakrabarti, S. N. Karmakar, Eur. Phys. Lett. **95**, 57008 (2011).
- 8. M. Patra, S. K. Maiti, Ann. of Phys. **375**, 337-350 (2016).
- 9. G. Timp et al. Phys. Rev. B **39**, 6227–6230 (1989).
- 10. L. P. Levy, G. Dolan, J. Dunsmuir, H. Bouchait, Phys. Rev. Lett. 64, 2074 (1990).

- 11. V. Chandrasekhar, R. A Webb, M. J. Brady, M. B. Ketchen, W. J. Gallagher, A. Kleinsasser, Phys. Rev. Lett. **67**, 3578 (1991).
- 12. D. Mailly, C. Chapelier, A. Benoit, Phys. Rev. Lett. 70, 2020 (1993).
- 13. E. M. Q. Jariwala, P. Mohanty, M. B. Ketchen, R. A. Webb, Phys. Rev. Lett. **86**, 1594–1597 (2001).
- 14. R. Deblock, R. Bel, B. Reulet, H. Bouchiat, D. Mailly, Phys. Rev. Lett. **89**, 206803 (2002).
- H. Bluhm, N. C. Koshnick, J.A. Bert, M.E. Huber, K. A. Moler, Phys. Rev. Lett. 102, 136802 (2009).
- 16. M. Abraham, R. Berkovits, Phys. Rev. Lett. **70**, 1509–1512 (1993).
- 17. T. Giamarchi, B. S. Shastry, Phys. Rev. B 5, 10915–10922 (1995).
- 18. S. Gupta, S. Sil, B. Bhattacharyya, Phys. Lett. A **324**, 494-500 (2004).
- 19. S. K. Maiti, Solid State Commun. **150**, 2212–2217 (2010).
- 20. B. B. Wei, S.-J. Gu, H.-Q. Lin, J. Phys: Condens. Matter 20, 395209 (2008).
- 21. N. M. R Peres, P. D Sacramento and J. M. P. Carmelo, J. Phys: Condens. Matter **13**, 5135-5157 (2001).
- 22. P. J. Monisha, I. V. Sankar, S. Sil, A. Chatterjee, Sci. Rep. 6, 20056 (2016).
- 23. A. Chatterjee, M. O. Smolkina, I. Y. Popov, Nanosystems: Phys., Chem., Maths. **10** (1), 50-62 (2019).
- 24. S.-Q Shen, AAPPS Bulletin 18, 5 (2008).
- 25. R. P. M. Krishna, S. Mukhopadhyay, A. Chatterjee, Phys. Letts. A **327**, 67–72 (2004).
- 26. I. V. Sankar, S. Mukhopadhyay, A. Chatterjee, Physica C 480, 55–60 (2012).
- 27. D. Debnath, M. Z. Malik, A. Chatterjee, Sci. Rep. 11, 12305 (2021).
- 28. M. Büttiker, Phys. Rev. B **32**, 1846–1849 (1985).

CHAPTER 5

TEMPERATURE DEPENDENT NONEQUILIBRIUM MAGNETO-TRANSPORT IN A CORRELATED POLAR SINGLE MOLECULAR TRANSISTOR WITH QUANTUM DISSIPATION

ABSTRACT

Quantum magneto-transport in a dissipative SMT is investigated at finite temperature in the presence of electron correlation and electron-phonon interaction within the framework of the Anderson-Holstein-Caldeira-Leggett Hamiltonian. The e-p interaction and dissipation are dealt with by canonical transformations and the Coulomb correlation is treated at the mean-field level. The transport properties such as spectral function, tunnelling current, differential conductance and spin polarization are determined using the Keldysh method.

5.1 Introduction

Lately, the subject of nano-electronics has emerged as a promising area of research for technological advancement. In this context, Molecular electronics or moletronics [1-2] has received particular attention. The first molecular transistor device was fabricated by Aviram et al. [3]. Recently, a large number of investigations have been carried out on SMT [4-7] which essentially consists of a QD or a nano-molecule that is placed in the middle region of the device and connected on either side to two conducting electrodes, one acting as the source and the other drain. Park et al. [8] were the first to configure such a device with C_{60} as the central transistor. Subsequently, several investigations followed because of the potential applications of these devices [1,2,4-7,9-11]. Several groups have also studied low temperature transport through an SMT system which incorporates correlation effects, for example, Coulomb blockade [12] and Kondo effect [13-16]. In the presence of e-e and e-p interactions, the transport in SMT devices is found to exhibit quantum features [17-23].

The effect of a magnetic field and e-p interaction on the transport properties of an SMT device have been investigated by Chen et al. [24]. They have calculated the spectral function (SF), tunneling current and differential conductance employing the non-equilibrium Green function (NEGF) technique due to Keldysh and observed that the e-p interaction generates side bands in the spectral density. It has also been revealed that the polaronic effect causes a considerable decrease in the tunneling current and differential conductance. Recently, Raju and Chatterjee (RC) [25] have analyzed the role of e-p coupling on electron transport in an SMT device placed on a substrate that can be considered as a phonon reservoir. The local phonon of QD can in this case interact with the substrate phonons giving rise to quantum dissipation. RC have incorporated this dissipation effect using the Caldeira-Leggett (CL) model in the presence of both e-p coupling and Coulomb correlation and used the Anderson-Holstein-Caldeira-Leggett (AHCL) model to describe the whole system and studied the effect of all interactions with the help of the Keldysh method. As expected, the polaron formation has been found to diminish the tunneling current and the differential conductance, while the substrate-induced damping effect has been found to enhance the tunneling current. Later, Kalla et al. [26] have investigated the external magnetic field-induced non-equilibrium transport in the same SMT system and have shown that the applied field breaks the spin degeneracy of the strongly coupled QD-electron energy level leading to a spin filtering effect. The effect of temperature on the SMT devices has been studied experimentally in recent

times [27, 28], but to our knowledge, theoretical investigations on this aspect have been rather scarce [29]. Kalla et al. [30] have examined the temperature effect on the tunneling current density in an SMT device. Very recently, Kalla et al. have studied the transient dynamics in a dissipative SMT with e-p and e-e interactions [31]. In the present work, we shall consider the combined effect of both temperature and magnetic field on the current in a dissipative SMT device. We include the Coulomb correlation between the QD electrons and consider the polaronic interactions in the Holstein regime. We model the system by the AHCL Hamiltonian and use the Keldysh finite-temperature Green function formalism to examine the interplay of temperature and magnetic field on the transport mechanisms.

5.2 Analytical Model and Formulation

A schematic diagram of the SMT device is shown in Fig.5.1. The figure shows that a central non-magnetic polar semiconducting QD is connected to the source (S) and drain (D) and a bias voltage, V_b and a gate voltage, V_g are applied to the leads and the QD respectively. One can control the transport through the SMT channel by tuning V_g [32,33]. B denotes the externally applied magnetic field. The whole arrangement is placed on an insulating substrate that plays the role of a bath of phonons. The model Hamiltonian is given by

$$H = H_{S,D} + H_{QD} + H_T + H_V , (5.1)$$

Here, the Hamiltonian H_{S,D} describes S and D and can be written as

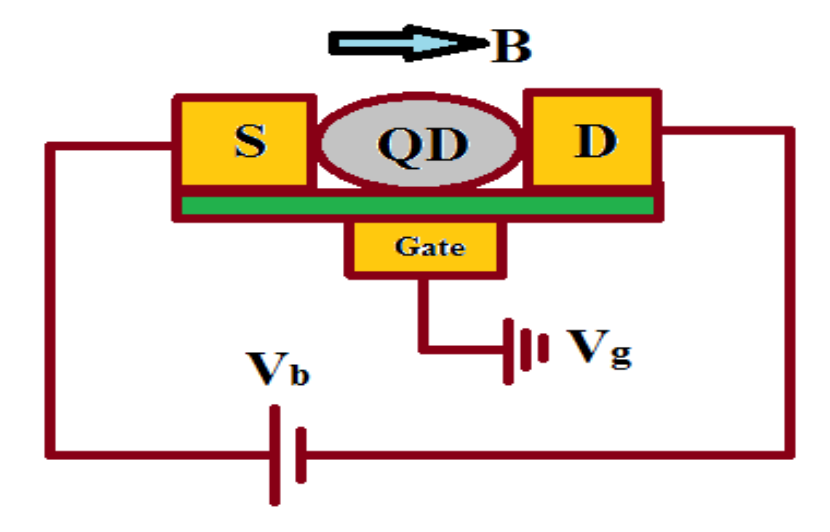


Fig.5.1 Schematic representation of an SMT device

$$H_{S,D} = \sum_{k\sigma \in S,D} \varepsilon_k \, n_{k\sigma} \,, \tag{5.2}$$

where $n_{\mathbf{k}\sigma}(=c_{\mathbf{k}\sigma}^{\dagger}c_{\mathbf{k}\sigma})$ denotes the number operator for free electrons in S and D with momentum \mathbf{k} and spin σ . H_{OD} is the Hamiltonian of the QD and is given by

$$H_{QD} = \sum_{\sigma} (\varepsilon_d - eV_g) n_{d\sigma} + U n_{d,\sigma} n_{d,-\sigma} - g^* \mu_B B S_d^z + \left(\frac{p_0^2}{2m_0} + \frac{1}{2} m_0 \omega_0^2 x_0^2\right) + g \sum_{\sigma} n_{d\sigma} x_0,$$
(5.3)

where $n_{d\sigma}(=c_{d\sigma}^{\dagger}c_{d\sigma})$ is the number operator for the QD electrons in the single localized energy level ϵ_d , $c_{d\sigma}^{\dagger}$ and $c_{d\sigma}$ denote respectively the creation and annihilation operator of the QD electrons, U refers to the onsite correlation energy, $\mathbf{B}(0,0,B)$ is the magnetic field applied along $\hat{\mathbf{z}}$, S_d^z is the z-component of the total spin of the QD electrons which can be written as $S_d^z = \frac{\hbar}{2} \sum_{d\sigma} \sigma c_{d\sigma}^{\dagger} c_{d\sigma}$, g^* is the gyromagnetic ratio and μ_B is the Bohr magneton. The fourth term of H_{QD} is the Hamiltonian for the local lattice mode of QD, where (x_0, p_0) are the coordinate and the corresponding canonical momentum of the QD oscillator with mass m_0 and frequency ω_0 which are respectively given by $x_0 = (\hbar/2m_0\omega_0)^{1/2}(b^{\dagger} + b)$ and $p_0 = i(\hbar m_0\omega_0/2)^{1/2}(b^{\dagger} - b)$. The fifth term represents the e-p coupling of the QD, where g gives the strength of the coupling between the electrons and phonon of the QD. The quantum tunneling of electrons from S to QD and QD to D can be described by the Hamiltonian

$$H_T = \sum_{k\sigma\in S,D} (V_k c_{k\sigma}^{\dagger} c_{d\sigma} + h.c), \tag{5.4}$$

where V_k refers to the strength of the coupling between the QD and the leads.

The Hamiltonian H_V is the vibrational part of the SMT system and comprises two pieces, H_{BO} and H_{Vib-B} , where H_{BO} describes the Hamiltonian for the bath oscillators and is given by

$$H_{BO} = \sum_{i=1}^{N} \left[\frac{p_i^2}{2m_i} + \frac{m_i}{2} \omega_i^2 x_i^2 \right], \tag{5.5}$$

where x_i , p_i , m_i and ω_i denote respectively the position, momentum, mass and the i^{th} bath-oscillator frequency and H_{vib-B} stands for the coupling between the QD phonon and the bath phonons which we describe by the C-L Hamiltonian [34]

$$H_{vib-B} = \sum_{i=1}^{N} \beta_i \, x_i x_0 \,, \tag{5.6}$$

where x_0 refers to the QD oscillator position, x_i refers to i^{th} bath-oscillator position and β_i gives the measure of coupling strength between the QD phonon and the bath phonon. This interaction causes the dissipation effect in the QD phonon dynamics.

First of all, we partially eliminate the interaction between the QD oscillator and the substrate oscillators by applying a canonical transformation [25, 26]:

$$\tilde{x}_i = \left[x_i + \left(\frac{\beta_i}{m_i \omega_i^2} \right) x_0 \right], \tag{5.7}$$

$$\tilde{p}_i = -i\hbar \left(\frac{\partial}{\partial \tilde{x}_i}\right). \tag{5.8}$$

which incorporates the most important aspect of the effect of the bath phonons which is dissipation. This renormalizes the frequency ω_0 of the local QD phonon to $\widetilde{\omega}_0 = (\omega_0^2 - \Delta \omega^2)^{1/2}$, where $\Delta \omega^2$ is given by

$$\Delta\omega^{2} = \sum_{i=1}^{N} \frac{\beta_{i}^{2}}{m_{0}m_{i}\,\omega_{i}^{2}},\tag{5.9}$$

For large N, $\Delta\omega^2$ can be written in an integral form over ω as

$$\Delta\omega^2 = 2\int_0^\infty \frac{I(\omega)}{m_0\omega} d\omega, \tag{5.10}$$

where $I(\omega)$ stands for the spectral density of the phonon bath which is given by

$$I(\omega) = \sum_{i=1}^{N} \frac{\beta_i^2}{2m_i \omega_i} \delta(\omega - \omega_i), \tag{5.11}$$

which can be taken in the Lorentz-Drude model as

$$I(\omega) = \frac{2m_0\gamma\omega}{\left[1 + \left(\frac{\omega}{\omega_c}\right)^2\right]},\tag{5.12}$$

where γ denotes the dissipation rate and ω_c is the cut-off frequency. As ω_c is considerably larger than other SMT frequencies, the deviation in the QD phonon frequency essentially becomes

$$\Delta\omega^2 = 2\pi\gamma\omega_c \,. \tag{5.13}$$

After the canonical transformations (7, 8), the transformed Hamiltonian reads

$$H = H_{S,D} + \sum_{\sigma} (\varepsilon_d - eV_g - \frac{1}{2}g^*\mu_B B\sigma_z)n_{d\sigma} + Un_{d,\sigma}n_{d,-\sigma} + \hbar\widetilde{\omega}_0 b^{\dagger}b$$

$$+\sum_{i=1}^{N} \left(\frac{\tilde{p}_{i}^{2}}{2m_{i}} + \frac{m_{i}}{2} \omega_{i}^{2} \tilde{x}_{i}^{2} \right) + \lambda \hbar \tilde{\omega}_{0} (b^{\dagger} + b) \sum_{\sigma} n_{d\sigma} + H_{T}, \quad (5.14)$$

where g and all the multiplicative factors are clubbed into $\lambda = g(1/2m_0\hbar\omega_0\tilde{\omega}_0^2)^{1/2}$ which we can call as renormalized e-p interaction coefficient.

Next, we tackle the e-p interaction term of QD by performing the well-known LFT: $e^S = e^{\lambda(b^{\dagger}-b)\sum_{\sigma}n_{d\sigma}}$ [35]. After this transformation, the effective Hamiltonian $\widetilde{H}(\equiv e^{-S}He^S)$ reads

$$\widetilde{H} = \sum_{k\sigma\in S,D} \varepsilon_k \, n_{k\sigma} + \sum_{\sigma} \widetilde{\varepsilon}_{d\sigma} n_{d\sigma} + \, \widetilde{U} n_{d,\sigma} n_{d,-\sigma} + \hbar \widetilde{\omega}_0 b^{\dagger} b + \sum_{k\sigma\in S,D} (\widetilde{V}_k \, c_{k\sigma}^{\dagger} c_{d\sigma} + h. \, c), (5.15)$$

with

$$\tilde{\varepsilon}_{d\sigma} = \varepsilon_d - eV_q - \sigma\mu_B B - \lambda^2 \hbar \widetilde{\omega}_0 , \qquad (5.16)$$

$$\widetilde{U} = U - 2\lambda^2 \hbar \widetilde{\omega}_0 \,, \tag{5.17}$$

$$\widetilde{V}_k = e^{-\lambda(b^{\dagger} - b)} V_k = \widehat{\chi} V_k \,, \tag{5.18}$$

where $\tilde{\epsilon}_{d\sigma}$ is the effective energy of the QD, \widetilde{U} is the modified Coulomb strength and \widetilde{V}_k is the renormalized hybridization strength.

5.2.1 The Keldysh formalism: spectral function, tunneling current and differential conductance

The tunneling current [36-38] through QD connected to two leads is given by

$$J = \frac{e}{2h} \int [(f_S \Gamma_S - f_D \Gamma_D) A(\omega) + (\Gamma_S - \Gamma_D) G^{<}(\omega)] d\omega.$$
 (5.19)

Here $f_S(\epsilon)$ and $f_D(\epsilon)$ refer to the source (S) and the drain (D) Fermi distributions which can be written as

$$f_{S,D}(\varepsilon) = \left[e^{\left(\frac{\mu_{S,D} - \varepsilon}{k_B T}\right)} + 1 \right]^{-1}, \tag{5.20}$$

where μ_S and μ_D are respectively the chemical potentials of S and D which are connected to the mid-voltage V_m and the bias voltage, V_b by the relations

$$eV_b = \mu_S - \mu_D; \ eV_m = \frac{\mu_S + \mu_D}{2},$$
 (5.21)

 Γ_S and Γ_D are defined as

$$\Gamma_{S,D}(\varepsilon_i) = 2\pi \rho_{S,D}(\varepsilon_i) \bar{\tilde{V}}_k V_k^*, \tag{5.22}$$

where $\overline{\widetilde{V}}_k$ is the expectation value of \widetilde{V}_k with respect to the relevant phonon state, ρ_S and ρ_D are the density of states of S and D respectively and $A(\omega)$ represents the SF which describes the excitations and is given by

$$A(\omega) = i[G_{dd}^{r}(\omega) - G_{dd}^{a}(\omega)] = i[G_{dd}^{>}(\omega) - G_{dd}^{<}(\omega)], \tag{5.23}$$

where $G^r_{dd}(\omega)$ and $G^a_{dd}(\omega)$ denote the retarded and advanced Green functions of the QD electrons which are obtained by taking the Fourier transform (FT) of $G^{r(a)}_{dd}(\tau=t-t')$ defined by

$$G_{dd}^{r(a)}(\tau = t - t') = \mp i \,\theta(\pm t \mp t')\langle 0 | \{\tilde{c}_{d\sigma}(t), \tilde{c}_{d\sigma}^{\dagger}(t')\} | 0 \rangle, \tag{5.24}$$

and $G_{dd}^{<}(\omega)$ and $G_{dd}^{>}(\omega)$ are the lesser and greater Keldysh Green functions for the QD electrons in the energy space which can be obtained by taking the FT of the corresponding time-dependent Keldysh Green functions $G_{dd}^{<}(\tau)$ and $G_{dd}^{>}(\tau)$ [39] which are given by

$$G_{dd}^{<}(\tau) = i\langle 0|\tilde{c}_{d\sigma}^{\dagger}(0)\tilde{c}_{d\sigma}(\tau)|0\rangle, \tag{5.25}$$

and

$$G_{dd}^{>}(\tau) = -i\langle 0|\tilde{c}_{d\sigma}(\tau)\,\tilde{c}_{d\sigma}^{\dagger}(0)|0\rangle. \tag{5.26}$$

where,

$$c_{d\sigma}(t) = e^{-i\tilde{H}_{el}t}c_{d\sigma}e^{i\tilde{H}_{el}t}, \qquad (5.27)$$

$$\tilde{c}_{d\sigma}(t) = \hat{\chi} c_{d\sigma}(t), \tag{5.28}$$

and $|0\rangle$ refers to the actual ground state of SMT i.e.,

$$|0\rangle = |0\rangle_{el}|0\rangle_{ph}. \tag{5.29}$$

For mathematical simplicity, we consider the interaction of QD with S and D to be symmetric which implies

$$\Gamma(\omega) = \frac{1}{2} [\Gamma_{S}(\omega) + \Gamma_{D}(\omega)], \qquad (5.30)$$

which after the n-phonon averaging becomes

$$\Gamma_{S,D} = 2\pi\rho(0)|V_k|^2 e^{\left[-\lambda^2 \left(f_{ph} + \frac{1}{2}\right)\right]},$$
(5.31)

f_{ph} being the phonon distribution function given by

$$f_{ph} = \left[e^{\hbar \widetilde{\omega}_0 / k_B T} - 1 \right]^{-1}. \tag{5.32}$$

Thus, the tunneling current for a symmetric SMT simplifies to

$$J = \frac{e}{2h} \Gamma \int (f_s - f_D) A(\omega) d\omega, \qquad (5.33)$$

where $A(\omega)$ can be obtained by substituting the expressions of $G^r_{dd}(\omega)$ and $G^a_{dd}(\omega)$ in Eq. (5.23) which can be calculated by taking FT of $G^{r(a)}_{dd}(t,t')$ which can be written as

$$G_{dd}^{r(a)}(t,t') = \left[\tilde{G}_{dd}^{r(a)}(t,t')\right]_{el} \langle \hat{\chi}(t)\hat{\chi}^{\dagger}(t')\rangle_{ph} = \left[\tilde{G}_{dd}^{r(a)}(t,t')\right]_{el} e^{-\varphi(\tau)}, \tag{5.34}$$

where $\,\widetilde{G}^{r(a)}_{dd}(t,t')$ is defined as

$$\left[\tilde{G}_{dd}^{r(a)}(t,t')\right]_{el} = \mp i \,\theta(\pm t \mp t')\langle 0|\left\{c_{d\sigma}(t),c_{d\sigma}^{\dagger}(t')\right\}|0\rangle,\tag{5.35}$$

and $\langle \hat{\chi}(t) \hat{\chi}^{\dagger}(t') \rangle_{ph}$ is calculated as

$$\langle \widehat{\chi}(t) \widehat{\chi}^{\dagger}(t') \rangle_{ph} = \langle e^{-i\widetilde{H}_{ph}t} \widehat{\chi} e^{i\widetilde{H}_{ph}t} e^{-i\widetilde{H}_{ph}t'} \widehat{\chi}^{\dagger} e^{i\widetilde{H}_{ph}t'} \rangle_{ph} = e^{-\varphi(\tau)}, \quad (5.36)$$

with

$$\varphi(\tau) = \lambda^{2} \left[2f_{ph} + 1 - 2\{f_{ph}(1 + f_{ph})\}^{1/2} \cos(\hbar \widetilde{\omega}_{0}(\tau + i\beta/2)) \right], \quad (5.37)$$

where f_{ph} is the phonon distribution function given by Eq. (5.32). After some algebraic manipulation, we obtain

$$\varphi(\tau) = -\ln\left[\sum_{n=-\infty}^{\infty} L_n(z) e^{-in\hbar\tilde{\omega}_0 \tau}\right],\tag{5.38}$$

where L_n is the spectral weight of the n^{th} phonon side band [24] and is given by

$$L_n(z) = exp\left[-\lambda^2 \left(2f_{ph} + 1\right) + \left(\frac{n\hbar\widetilde{\omega}_0}{2k_B T}\right)\right] I_n(z), \tag{5.39}$$

where, $z = 2\lambda^2 [f_{ph}(1 + f_{ph})]^{\frac{1}{2}}$, n is the number of phonons and I_n is the Modified Bessel function of second kind.

 $G_{dd}^{r(a)}(\omega)$ can be written in the ω -space as

$$G_{dd}^{r(a)}(\omega) = \sum_{n=-\infty}^{\infty} L_n(z) \left[\tilde{G}_{dd}^{r(a)}(\omega - n\hbar \tilde{\omega}_0) \right]_{el}, \qquad (5.40)$$

where the Green functions $\left[\tilde{G}_{dd}^{r,a}(\omega)\right]_{el}$ are the FTs of $\left[\tilde{G}_{dd}^{r(a)}(t,t')\right]_{el}$ in the ω – space.

 $\widetilde{G}_{dd}^{r(a)}(\omega)$ is calculated by the equation of motion approach [39] and is given by the following expression in ω – space as

$$\tilde{G}_{dd}^{r(a)}(\omega \mp n\hbar \tilde{\omega}_0) = \frac{1}{\omega \mp n\hbar \tilde{\omega}_0 - \tilde{\varepsilon}_{d\sigma} - \tilde{U}\langle n_{d,-\sigma} \rangle - \tilde{\Sigma}^{r(a)}(\omega)}, \quad (5.41)$$

where n is the phonon number, $\langle n_{d,-\sigma} \rangle$ is the mean electron occupancy in QD and $\widetilde{\Sigma}^{r(a)}(\omega)$ is the retarded (advanced) self-energy which can be expressed as

$$\widetilde{\Sigma}^{r(a)}(\omega) = \lim_{\eta \to 0} \sum_{k \in S, D} \left(\frac{\left| < \widetilde{V}_k > \right|^2}{\left(\omega \mp n\hbar \widetilde{\omega}_0 - \varepsilon_k \pm i\eta \right)} \right) = \widetilde{\Lambda}(\omega) \mp i\widetilde{\Gamma}(\omega), \tag{5.42}$$

where the real part of $\tilde{\Sigma}^{r(a)}(\omega)$ can be clubbed with the QD energy and the imaginary part assumes the following expression

$$\tilde{\Gamma} = \Gamma e^{-\lambda^2 \left(f_{ph} + \frac{1}{2} \right)}. \tag{5.43}$$

Substituting Eqs. (5.40) and (5.41) in Eq. (5.23), SF can be obtained as

$$A(\omega) = \sum_{n=-\infty}^{\infty} i L_n(z) \left[\tilde{G}_{dd}^r(\omega \mp n\hbar \tilde{\omega}_0) - \tilde{G}_{dd}^a(\omega \mp n\hbar \tilde{\omega}_0) \right]$$

$$=\sum_{n=-\infty}^{\infty} \frac{2\tilde{\Gamma} L_n(z)}{\left(\omega \mp n\hbar \tilde{\omega}_0 - \tilde{\varepsilon}_{d\sigma} - \tilde{U} \langle n_{d,-\sigma} \rangle\right)^2 + \tilde{\Gamma}^2},\tag{5.44}$$

The mean electron occupancy in QD is given by

$$\langle n_{d,\sigma} \rangle = \int d\omega \, \frac{(f_s + f_D)}{2\pi} \, A(\omega).$$
 (5.45)

Eqs. (5.44) and (5.45) can be solved self consistently to obtain $A(\omega)$ and hence the tunneling current can be calculated.

The expression of $A(\omega)$ can also be obtained by calculating the lesser and greater Keldysh Green functions which assume, after some algebraic manipulations, the following expressions

$$G_{dd}^{\leq}(\tau) = i \langle 0 | c_d^{\dagger}(0) c_d(\tau) | 0 \rangle_{el} \langle \hat{\chi}^{\dagger}(0) \hat{\chi}(\tau) \rangle_{ph} = \tilde{G}_{dd}^{\leq}(\tau)_{el} \sum_{n=-\infty}^{\infty} L_n e^{in\hbar \tilde{\omega}_0 \tau}, \qquad (5.46)$$

$$G_{dd}^{>}(\tau) = -i \langle 0 | c_d(\tau) c_d^{\dagger}(0) | 0 \rangle_{el} \langle \hat{\chi}(\tau) \hat{\chi}^{\dagger}(0) \rangle_{ph} = \tilde{G}_{dd}^{>}(\tau)_{el} \sum_{n=-\infty}^{\infty} L_n e^{-in\hbar \tilde{\omega}_0 \tau}, \quad (5.47)$$

where

$$\tilde{G}_{dd}^{<}(\tau) = i \left\langle 0 \left| c_d^{\dagger}(0) c_d(\tau) \right| 0 \right\rangle_{el} = i \left\langle 0 \left| c_d^{\dagger}(0) e^{-i \tilde{H}_{el} \tau} c_d e^{i \tilde{H}_{el} \tau} \right| 0 \right\rangle_{el}, \tag{5.48}$$

$$\tilde{G}_{dd}^{>}(\tau) = -i \langle 0 | c_d(\tau) c_d^{\dagger}(0) | 0 \rangle_{el} = -i \langle 0 | e^{-i\tilde{H}_{el}\tau} c_d e^{i\tilde{H}_{el}\tau} c_d^{\dagger}(0) | 0 \rangle_{el}, \tag{5.49}$$

and

$$\langle \hat{\chi}^{\dagger}(0)\hat{\chi}(\tau)\rangle_{ph} = \langle \hat{\chi}^{\dagger}(0)e^{-i\tilde{H}_{ph}\tau}\hat{\chi}e^{i\tilde{H}_{ph}\tau}\rangle_{ph} = \sum_{n=-\infty}^{\infty} L_n e^{in\hbar\tilde{\omega}_0\tau}, \qquad (5.50)$$

$$\langle \hat{\chi}(\tau) \hat{\chi}^{\dagger}(0) \rangle_{ph} = \langle e^{-i\tilde{H}_{ph}\tau} \hat{\chi} e^{i\tilde{H}_{ph}\tau} \hat{\chi}^{\dagger}(0) \rangle_{ph} = \sum_{n=-\infty}^{\infty} L_n e^{-in\hbar\tilde{\omega}_0 \tau}, \qquad (5.51)$$

 $G_{dd}^{<}(\omega)$ and $G_{dd}^{>}(\omega)$ are now obtained as

$$G_{dd}^{\leq}(\omega) = \sum_{n=-\infty}^{\infty} L_n \, \tilde{G}_{dd}^{\leq}(\omega + n\hbar \tilde{\omega}_0), \tag{5.52}$$

$$G_{dd}^{>}(\omega) = \sum_{n=-\infty}^{\infty} L_n \, \tilde{G}_{dd}^{>}(\omega - n\hbar \tilde{\omega}_0). \tag{5.53}$$

where $\tilde{G}_{dd}^{<}(\omega)$ and $\tilde{G}_{dd}^{>}(\omega)$ are the FTs of $\tilde{G}_{dd}^{<}(\tau)$ and $\tilde{G}_{dd}^{>}(\tau)$ respectively, in the ω – space. Thus, in the Fourier space (ω), the SF of the SMT system reads

$$A(\omega) = \sum_{n=-\infty}^{\infty} iL_n(z) \big[\tilde{G}^{>}(\omega - n\hbar \tilde{\omega}_0) - \tilde{G}^{<}(\omega + n\hbar \tilde{\omega}_0) \big]. \tag{5.54}$$

Applying the Langreth's analytical continuation rule to the Dyson equations for $\ \widetilde{G}^{>(<)}(\omega)$, we obtain

$$\tilde{G}^{>(<)}(\omega) = \tilde{G}^{r}_{dd}(\omega) \, \tilde{\Sigma}^{>(<)}(\omega) \, \tilde{G}^{a}_{dd}(\omega), \tag{5.55}$$

where $\tilde{\Sigma}^{<(>)}(\omega)$ can be written as

$$\tilde{\Sigma}^{<}(\omega) = i \, \tilde{\Gamma}[f_S(\omega) + f_D(\omega)], \tag{5.56}$$

$$\tilde{\Sigma}^{>}(\omega) = -i\,\tilde{I}\left[2 - (f_S(\omega) + f_D(\omega))\right]. \tag{5.57}$$

Substituting the expressions of $\widetilde{G}_{dd}^{r(a)}$ from Eq. (5.41) and the expressions of $\widetilde{\Sigma}^{>(<)}(\omega)$ from (5.56) and (5.57) in Eq. (5.55), we can obtain the lesser and greater Keldysh Green functions $\widetilde{G}^{>(<)}$ and hence the SF and the tunneling current.

To obtain the Differential conductance, we calculate dJ/dV_b which gives

$$G = \frac{dJ}{dV_b} = \frac{e^2 \Gamma}{2h} \sum_{n=-\infty}^{\infty} L_n \int_{-\infty}^{\infty} d\omega F_n(\omega) A(\omega - n\hbar \widetilde{\omega}_0), \qquad (5.58)$$

where $F_n(\omega)$ is given by

$$F_{n}(\omega) = \frac{1}{2k_{B}T} \{f_{S}(\omega)[1 - f_{S}(\omega)] + f_{D}(\omega)[1 - f_{D}(\omega)]\} \left\{ 1 + \frac{1}{2} \left(e^{-\frac{n\hbar\widetilde{\omega}_{0}}{k_{B}T}} - 1 \right) (X_{S} + X_{D}) \right\} + \frac{1}{4k_{B}T} \left(e^{-\frac{n\hbar\widetilde{\omega}_{0}}{k_{B}T}} - 1 \right) \left(f_{S}(\omega) - f_{D}(\omega) \right) \{X_{S}(1 - X_{S}) - X_{D}(1 - X_{D})\}, \quad (5.59)$$

where,

$$X_S = f_S(\omega - n\hbar\widetilde{\omega}_0)$$
 ; $X_D = f_D(\omega - n\hbar\widetilde{\omega}_0)$. (5.60)

Finally, we determine the spin polarization from the relation:

$$P_{\sigma,-\sigma} = \frac{J_{\sigma} - J_{-\sigma}}{J_{\sigma} + J_{-\sigma}}.$$
(5.61)

5.3 NUMERICAL RESULTS AND DISCUSSIONS

We choose the phonon energy, $\hbar\omega_0=1$ to set the energy scale of the system and take $\Gamma=0.2,\ eV_g=0,\ \epsilon_d=0.$ We also consider the electronic density of states for the conduction electrons in S and D are constant (independent of energy). For concreteness, we consider $eV_b=0.1, eV_m=0.5$ and U=5 and evaluate the normalized spectral density A/A_0 , normalized tunneling current J/J_0 , differential conductance G/G_0 and spin polarization $P_{\sigma,-\sigma}$ as functions of different parameters of the SMT system at different temperature (T) and external magnetic field (B).

In Fig.5.2(a) we show the behavior of the normalized spectral function A with energy (ω) incorporating the effects of e-e interaction U, e-p interaction λ and dissipation (measured by the coefficient y) at different temperature T, while in Fig.5.2(b) we display the same for different values of the magnetic field B. Here we choose other parameters of the system as $eV_b = 0.5$, $eV_m = 0.1$, U = 5, $\lambda = 0.6$, $\gamma = 0.02$. A is calculated in the units of $A_0 = 2/\Gamma$. We observe interesting peak structure in these plots. Fig.5.2(a) reveals that at constant B, as T increases, these peaks decrease in height and shift to the right, while Fig.5.2(b) shows that at constant (finite) T, the peaks increase in height with increasing B. Both the plots exhibit side bands which arise because of emission or absorption of phonons by the tunneling electron due to the polaronic effect. At T = 0, as higher-order phonon scattering becomes less probable, the heights of the side-band peaks reduce with increasing ω , while as T increases, the overall spectrum shifts towards right and the side-peaks diminish as temperature has a debilitating effect on the side bands. The inset (a) of Fig.5.2(a) shows that the distance between the peaks increases as B increases. This spin separation is completely absent at B = 0 (Inset (b) of Fig.5.2(a)). We notice from Fig.5.2(b) that as B increases, two spin-resolved peaks appear, the heights and the separation between them increasing with B. The left peak refers to the up-spin electrons and the right peak the down-spin electrons. This happens because of the breaking of spin-degeneracy in the QD energy spectrum. This character is also visible in Fig.5.2(a), though it becomes less prominent in the presence of temperature which impedes this effect. The inset of Fig.5.2(b) shows that at a higher temperature, the peaks shift

towards right and splitting of the peaks reduces.

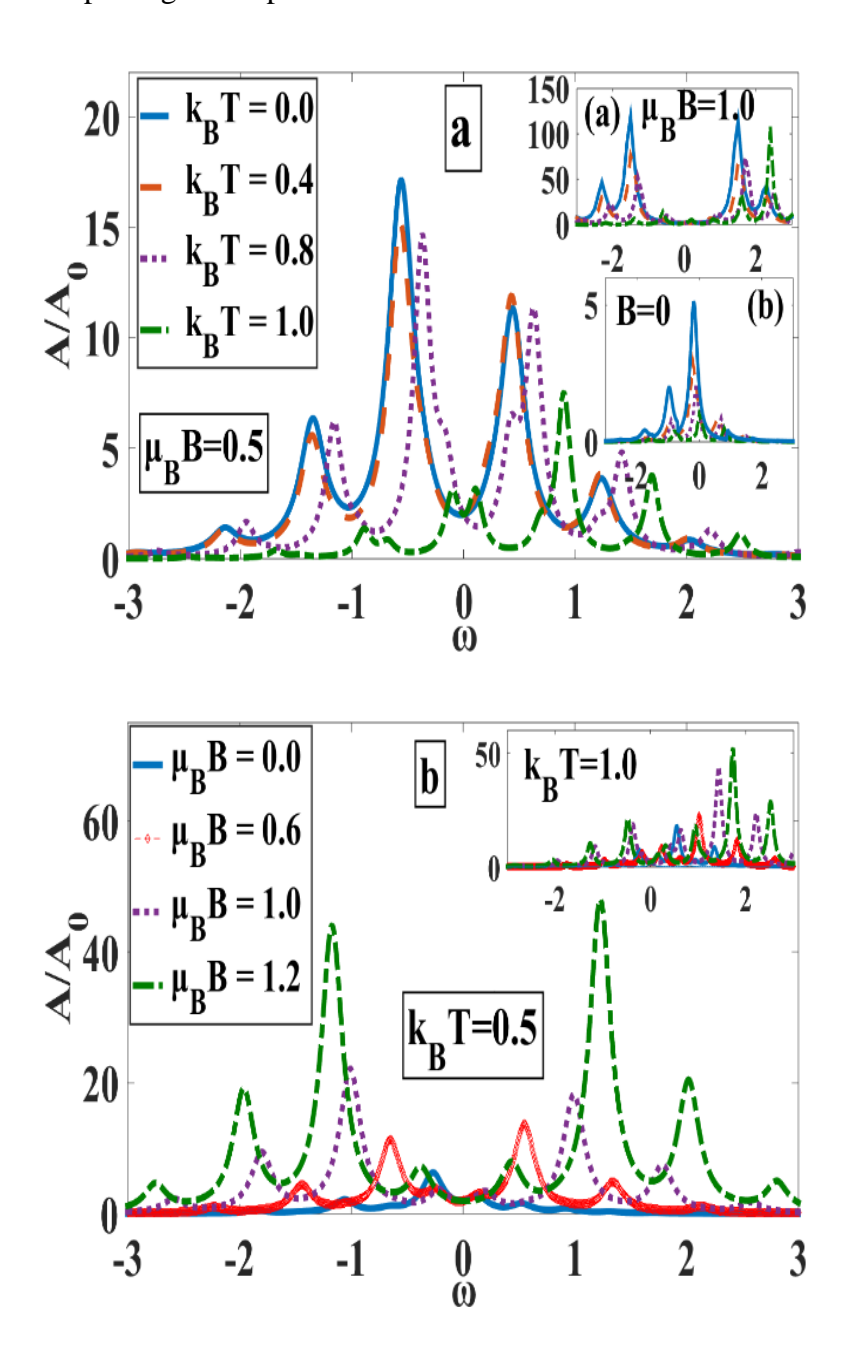
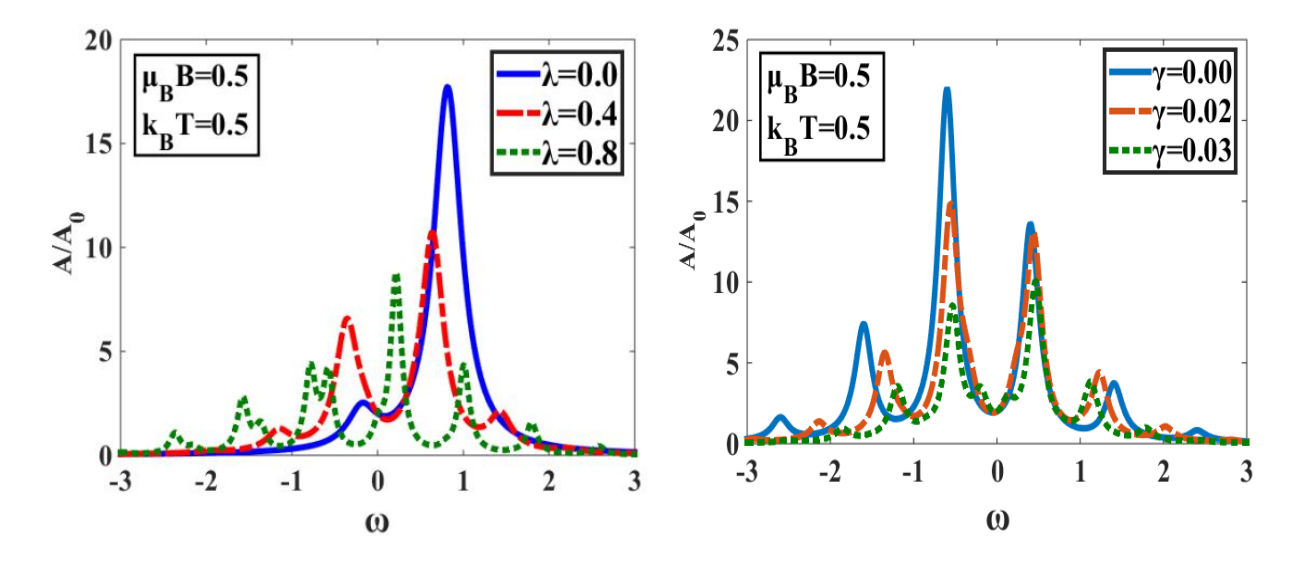


Fig.5.2 A/A₀ as a function of ω (a) for different values of k_BT at $\mu_BB=0.5$ (Insets: at $\mu_BB=1.0$ & B=0.0) and (b) for different μ_BB values at $k_BT=0.5$ (Inset: at $k_BT=1.0$).

To understand the effects of polaronic interaction and dissipation, we study the variation of the spectral density as a function of ω for different values of e-p coupling constant λ and dissipation factor γ in Fig.5.3 and Fig.5.4 respectively. Fig.5.3 demonstrates that as we increase λ , the central peak reduces in height and starts developing side bands. We have also observed (not shown here) that with increasing λ , peaks become shorter in height and shift to the left if $\mu_B B > k_B T$, while for $k_B T > \mu_B B$, the heights and the number of peaks increase.

When both T and B are equally large, the peaks get sharper and taller in height with increasing λ and they shift toward right. Fig. 5.4 exhibits that at low B and T, the peaks of the spectral function diminish and get more stretched with increasing y reducing the occupancy of phonon side bands, but it sharply increases with increasing γ for $\mu_B B > k_B T$, $k_B T > \mu_B B$ or at high µ_BB & k_BT (not shown here). This signifies a stronger correlation between QD and bath phonons at higher temperature or magnetic field.



 $\mu_B B \; = \; k_B T = 0.5 \,, \;\; eV_b = 0.5 \,, \; eV_m = 0.1 \,, \;\; U = \quad \mu_B B \; = \; k_B T = 0.5 \;, \quad eV_b = 0.5 \;, \;\; eV_m = 0.1 \;, \label{eq:mu_BB}$ $5, \gamma = 0.02.$

Fig.5.3 A/A $_0$ vs. ω for different λ values with Fig.5.4 A/A $_0$ vs. ω for different γ values with $U = 5, \lambda = 0.6.$

Next, we wish to understand the response of the tunnelling current J to magnetic field, e-p interaction and damping at different temperature. J is measured in the units of $J_0 = e/2h$. Fig. 5.5 displays the variation of current density J with V_b at different T and B respectively. For comparison, we also show the plots for zero (lower bunch) and nonzero (upper bunch) B. We observe that J initially increases linearly with V_b showing an Ohmic nature and then saturates. The explanation goes as follows. On application of V_b, the Fermi level of S shifts up and that of the right lead goes down. Due to this non-uniform alignment of the Fermi levels electrons enter from S-lead into QD giving rise to a nonzero tunnelling current. But as the QD is able to accommodate only a limited number of electrons, the current gets saturated if V_b is raised beyond a certain value. In the B \neq 0 case, the spin degeneracy of QD's energy level is lifted and as result, the spin-up level moves up and spin-down level moves down. Now either of the two levels can be much closer to the Fermi level of the leads which causes a hike in the current for $B \neq 0$ (upper bunch). However, it is clear from Fig.5.5 that J decreases with increasing T for given values of B and the SMT parameters. The inset shows

the scenario for T=0. The response of J at low temperatures is not so significant unless the bias voltage is sufficiently high to match the spin levels with the Fermi levels of S and D leads.

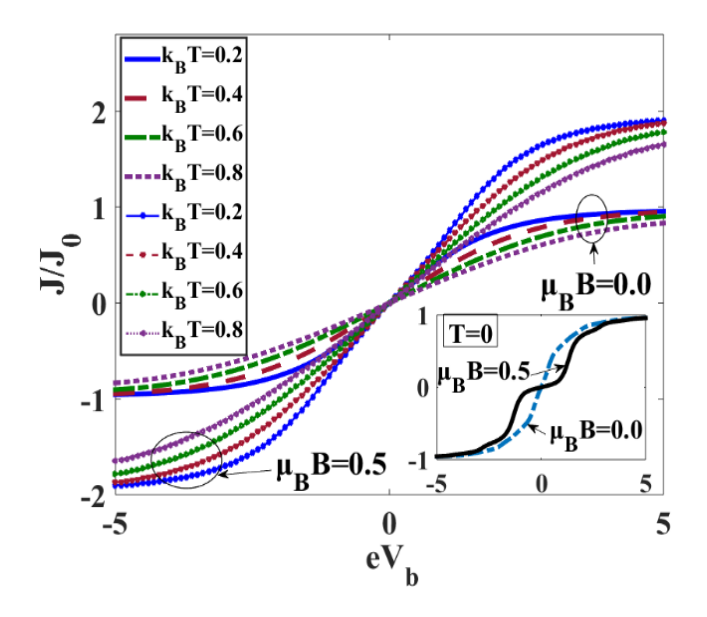


Fig.5.5 J/J₀ vs. eV_b for different values of k_BT at $\lambda=0.6$, $eV_m0.1$, $\gamma=0.02$ for $\mu_BB=0$ & $\mu_BB=0.5$. Inset: Results at T=0.

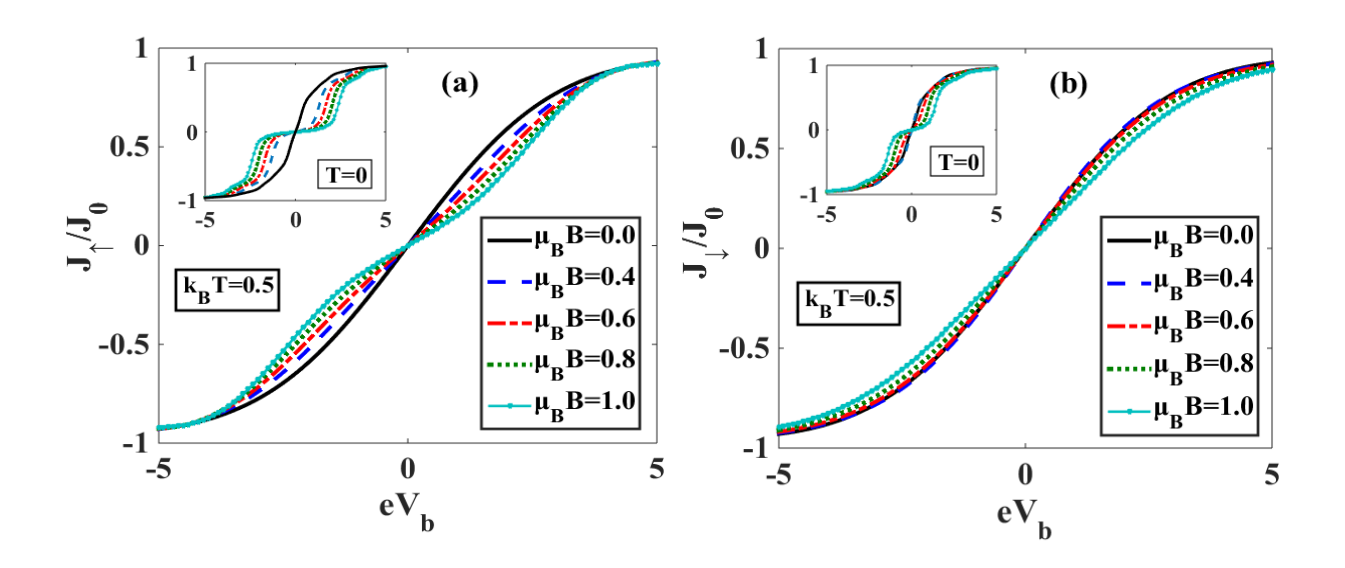


Fig.5.6 (a) J_{\uparrow}/J_0 and (b) J_{\downarrow}/J_0 vs. eV_b for different B values at $\lambda=0.6$, $eV_m=0.1$, $\gamma=0.02$ for $k_BT=0.5$. Insets: Results at T=0.

To see the effect separately in up and down-spin current densities, we draw in Fig.5.6, J versus V_b at a finite T for several B values. The insets in Fig.5.6 give the zero-temperature behaviour. One may notice from the figures that at finite temperature, both J_{\uparrow} and J_{\downarrow} grow in

the Ohmic fashion from $V_b = 0$ (unlike in the case of T = 0) till some finite V_b beyond which they grow at a slower rate and finally reach saturation values. Also, the behviour of J_{\uparrow} at large B is non-ohmic. At finite temperature, J_{\uparrow} and J_{\downarrow} become smaller than their corresponding zero-temperature values. This is consistent with Fig.5.5. We also see that the current decreases on increasing B. The decrease in the spin-up current is more than that in the spin-down current. This happens because the spin-splitting becomes stronger as B increases and as a result, the spin-up level shifts down more resulting in a lesser tunnelling probability through QD to D. Interestingly, the staircase-like behavior observed at T = 0 disappears as T is increased. The behavior of J_{\uparrow} and J_{\downarrow} with respect to V_b at T = 0 has been explained by Kalla et al. [26].

The combined effect of magnetic field and polaronic interaction on J_{\uparrow} and J_{\downarrow} is studied in Fig. 5.7 for a non-zero value of T and a set of λ values. One may notice from Fig. 5.7(a) that at nonzero T and a very small value of λ , the spin-up current density J_{\uparrow} first rises with B and quickly reaches a maximum and then decreases as B increases further. For larger λ values, J_{\uparrow} however reduces monotonically as B rises. The behavior of down-spin current J_{\downarrow} is however more interesting. The effect of λ is also interesting here. At a finite temperature, e-p interaction reduces J₁ for the entire range of B. This is because the polaronic interactions restrict the flow of current. In the case of J_{\downarrow} , for not too small λ , J_{\downarrow} first rises with B, reaches a maximum and then monotonically decreases as B increases further. Interestingly, at low B, J_k decreases with increasing λ while at high B, it increases with λ . This gives rise to a crossing behaviour and the crossover point is right shifted as we increase λ . This can be explained by the help of Fig.5.6. The external field splits the spin-degenerate electron states, the spin-down state being shifted above the Fermi level and the spin-down state below the Fermi level. As the spin-up state is lowered in energy, it becomes more difficult for an electron in this state to leave QD. Thus J₁ may decrease because of lesser availability of tunneling electrons through the channel. On the other hand, the down-spin state is raised and this favours the flow of tunneling electrons from QD causing an enhancement in current for low and intermediate value of B. Above a certain value of B, however, two effects may come into play. First, the availability of unoccupied states in QD may become less or probability of having tunneling electrons through QD channel becomes small and as a result J₁ reduces. This scenario holds good even at a higher T (insets). It is important to note that the peaks occurring in the current densities at T = 0 (inset (i)) for small values of λ become much flatter and also smaller in height as temperature increases. The plot of $J_{\uparrow,\downarrow}$ vs. λ clearly shows this (not shown here).

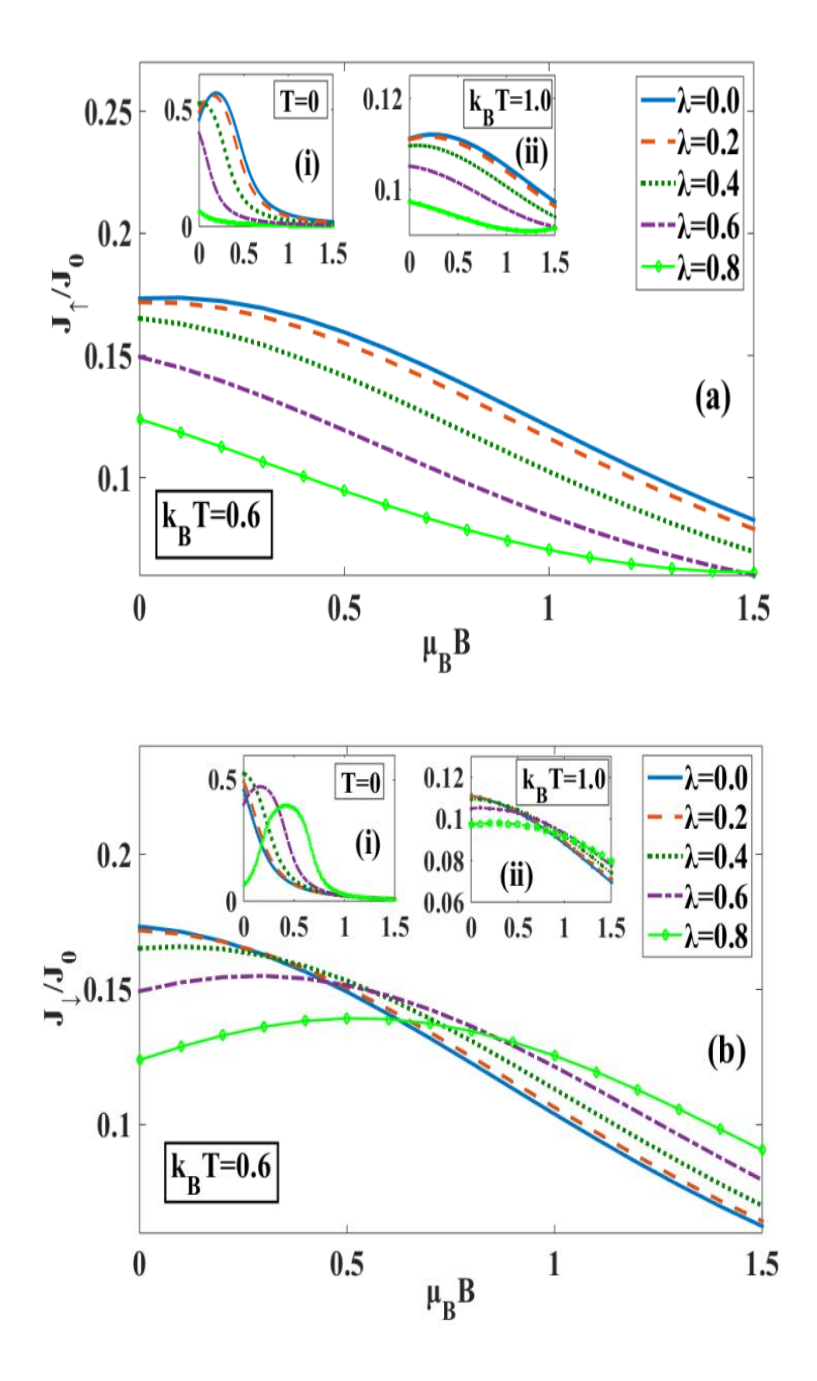


Fig.5.7 (a) J_{\uparrow}/J_{0} (b) J_{\downarrow}/J_{0} vs. $\mu_{B}B$ for a few λ values at $eV_{b}=0.5$, $eV_{m}=0.1$, $\gamma=0.02$ for $k_{B}T=0.6$ & $k_{B}T=1.0$. Insets: Results at (i) T=0, (ii) T=1.0.

In Fig.5.8, we plot J_{\uparrow} and J_{\downarrow} as a function of B for different values γ at a finite value of T. The insets display the variations at T=0. Fig.5.8(a) reveals that J_{\uparrow} dies out monotonically as B increases while it increases with γ . Here we have considered $\lambda=0.6$, because of which J_{\uparrow} decreases from the beginning itself i.e., from B=0. Interestingly, Fig.5.8(b) suggests that initially J_{\downarrow} increases with B and also gets enhanced by dissipation but then beyond a critical B it falls off monotonically. In this range it also decreases due to damping. This gives rise to a crossing behaviour which however disappears as T is increased. At these temperatures, J_{\downarrow} is

always enhanced by dissipation, though changes are marginal for the considered parameters. It is also clear that the current densities are lower at higher T values at small magnetic field. At large magnetic field, however, the T-dependence becomes more complicated giving rise to some interesting crossing behaviour. Also, the rate of decrease in $J_{\uparrow,\downarrow}$ with B slows down as T increases.

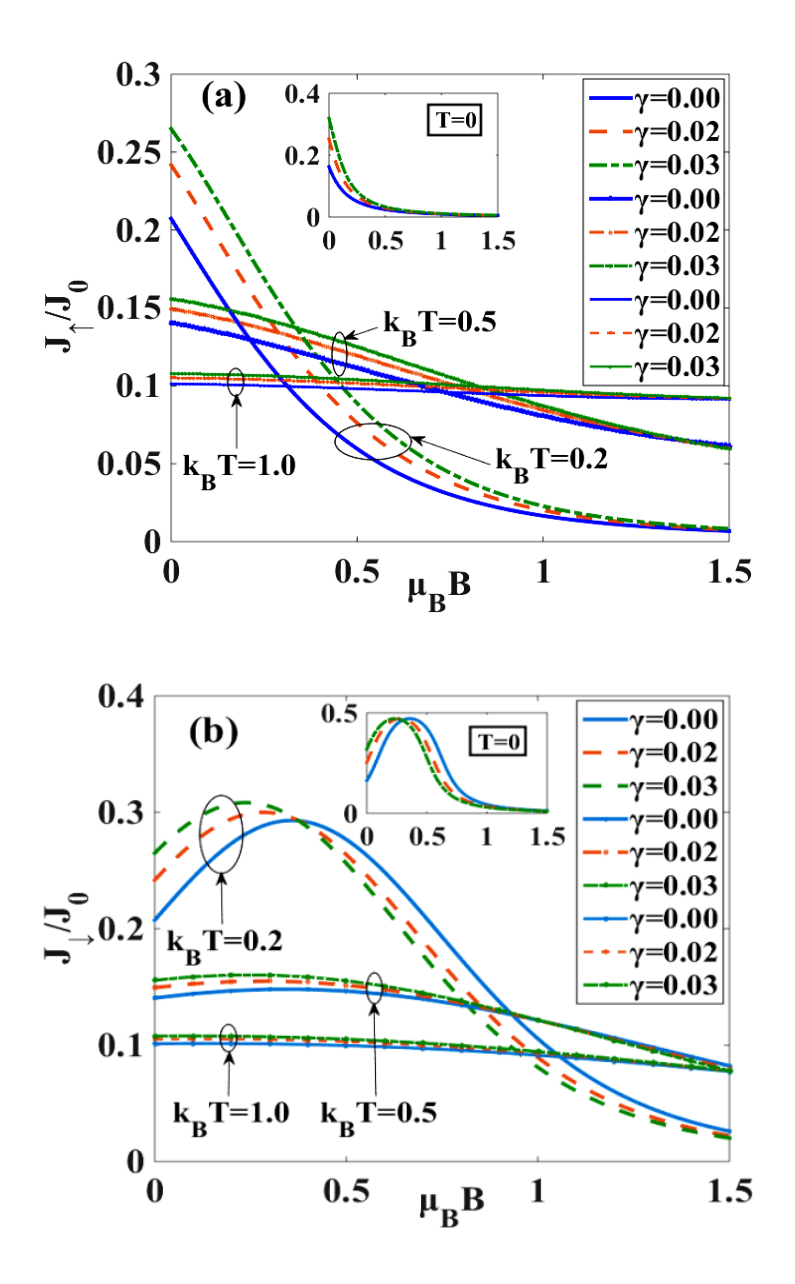


Fig.5.8 (a) J_{\uparrow}/J_0 (b) J_{\downarrow}/J_0 vs. $\mu_B B$ for several γ values at $eV_b=0.5$, $eV_m=0.1$, $\lambda=0.6$ for $k_B T=0.2$, 5 & 1.0 . Insets: at T=0.

The contrasting nature of both J_{\downarrow} and J_{\uparrow} at high B values with respect to λ and γ is noticeable in Fig.5.7 and Fig.5.8. This can be understood from the effective QD-energy: $\tilde{\varepsilon}_{d\sigma} = \varepsilon_d - eV_g - \sigma\mu_B B - \lambda^2 \hbar \widetilde{\omega}_0$. For up-spin case, the energy looks like $\tilde{\varepsilon}_{d,+} = \varepsilon_d - eV_g - eV_g$

 $\mu_B B - \lambda^2 \hbar \widetilde{\omega}_0$ while for the down-spin case, the same becomes: $\widetilde{\varepsilon}_{d,-} = \varepsilon_d - eV_g + \mu_B B - \lambda^2 \hbar \widetilde{\omega}_0$. Thus, for the down-spin case, there exists a competition between the relative strengths of the B and λ or γ -terms leading to the crossover behaviour.

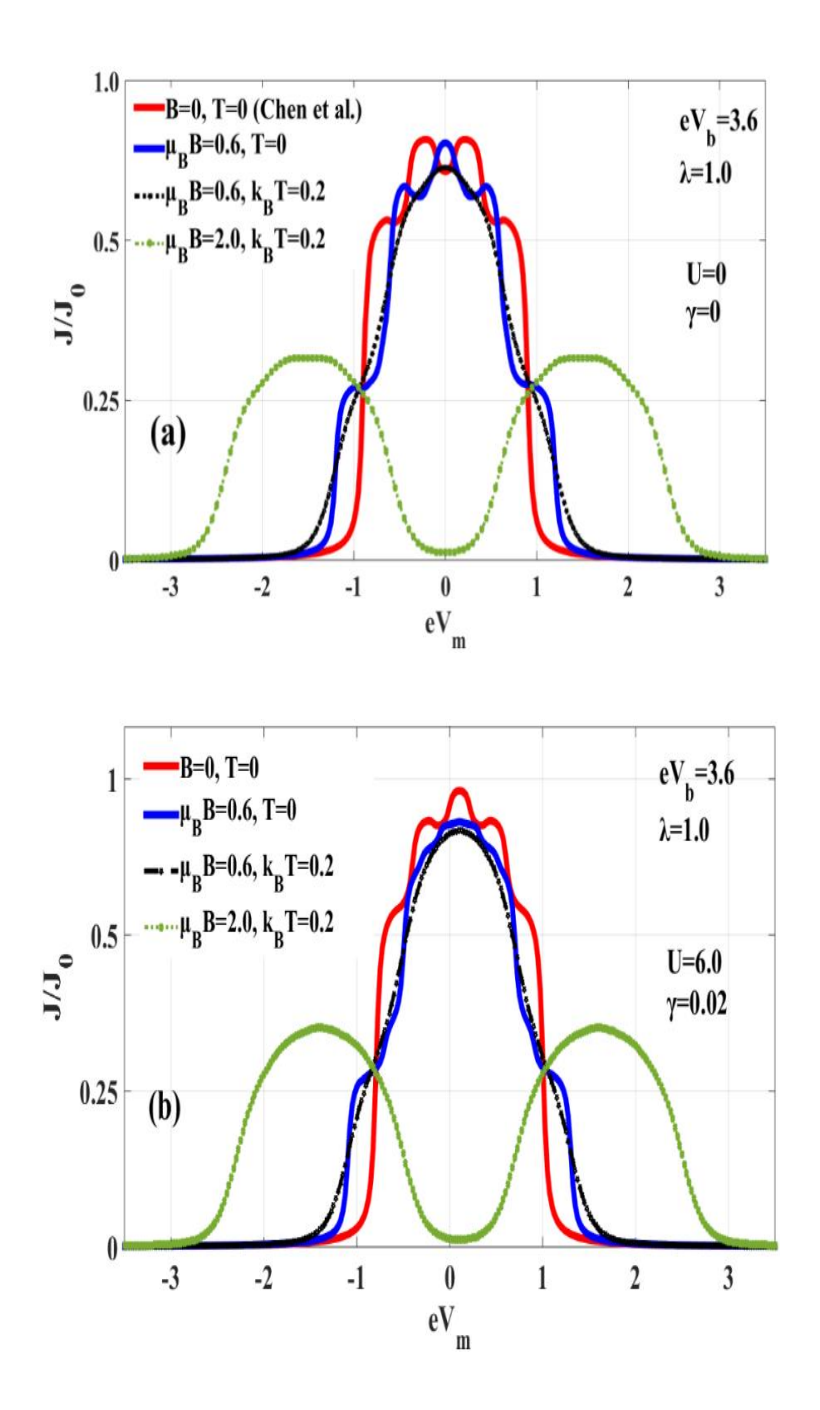
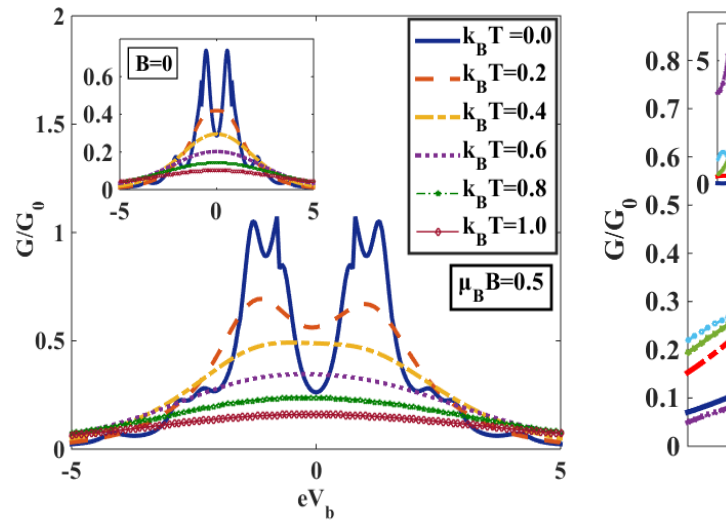
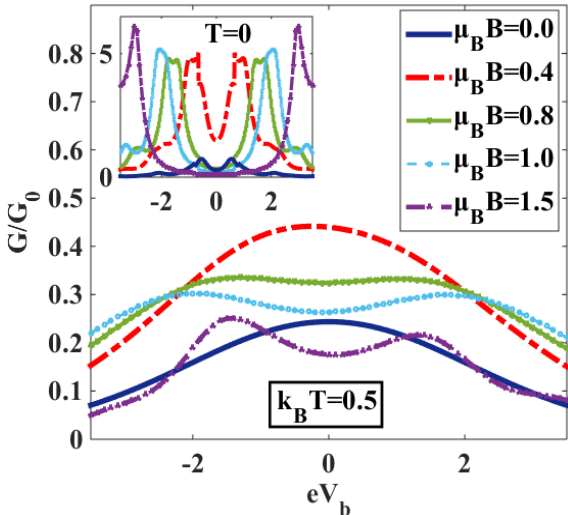


Fig.5.9 J/J₀ vs. eV_m for a few values of T and B at $eV_b = 3.6$, $\lambda = 1.0$: (a) $U=0, \gamma = 0$ (b) $U=6, \gamma = 0.02$.

Fig.5.9 shows the nature of J as a function of mid-voltage, V_m for different k_BT and μ_BB combinations at a fixed λ and eV_b for $\gamma = U = 0$ and $\gamma = 0.02$, U = 6 in Fig.5.9(a) and Fig.5.9(b) respectively. The behaviour in Fig.5.9(a) turns out to be symmetric with respect to $V_m = 0$ at $\gamma = U = 0$. In this plot we notice that for B = 0, T = 0, as V_m increases from the

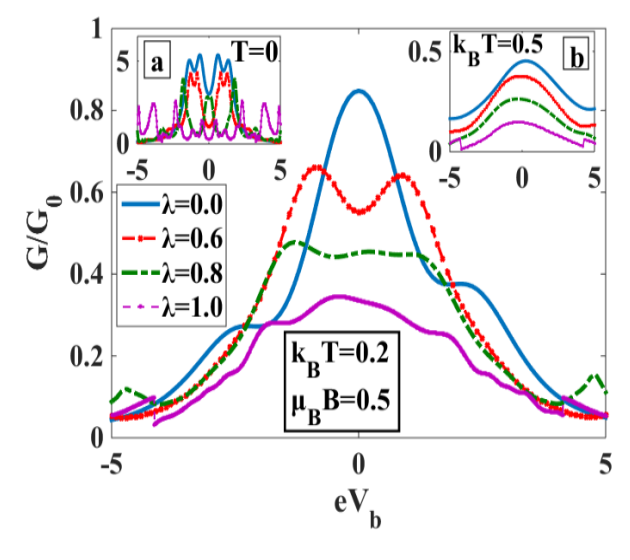
negative side, initially J increases with V_m and later exhibits a symmetric structure of shoulder, peak and valley and finally falls off very rapidly at as $V_{\rm m}$ increases further. This behaviour has also been observed by Chen et al. [24] (red solid curve) who suggest that this pattern corresponds to the phonon-assisted conduction peaks. Now as we turn on the magnetic field (blue solid curve), some of the shoulders also turn into peaks increasing the total number of conduction peaks, but the height of the peaks decreases. Our figure however shows that at a finite temperature (black dotted curve), the shoulders disappear making it more like a Gaussian curve. It is also shown that at this low temperature if we increase magnetic field to sufficiently high value, a clear double peak structure with less peak-height and a valley at around $V_m = 0$ appears corresponding to two spin-resolved (up-down) conduction peaks, but multiple peak-valley structure seems to disappear. Here, the spinresolved current peaks show a broad maximum. This suggests that although the magnetic field reduces current, but the spin-splitting is favourable at large B and low T. In Fig. 5.9(b), we show the effect of U and y with the same set of other parameters. It can be seen that the presence of y enhances the current. Here the variations in the presence of U and y become slightly right-shifted with respect to $V_m = 0$. However, the qualitative behaviour of the variations is almost same as Fig.5.9(a). Fig.5.10 displays how the normalized differential conductance, G/G₀ changes with V_b at different T value.G conductance is computed in units of $G_0 = e^2/2h$. The double-peak structure was already observed in [30] at T=0 in the absence of a magnetic field. An introduction of a magnetic field brings about a splitting in the peaks. This was observed in [26]. As the temperature is increased in the $B \neq 0$ case, the splitting in the peaks disappears and the peaks also come down in value. As the temperature is further increased, the double-peak configuration vanishes and in place of it, a single wide maximum appears. Thus, at a high temperature, the behaviour in the case of $B \neq 0$ is qualitatively same as in the case of B = 0. The behaviour at B = 0 is shown in the inset. Fig.5.11 shows the nature of G versus V_b at a finite T for a few values of B. The behaviour at T = 0 is shown in the inset. At B = 0, G displays a peak structure. As B is increased from zero (to say $\mu_B B$ = 0.4), the peak structure continues to show up, but the value of G increases for the range of V_b considered and consequently, the peak value of G also becomes higher. This increase at a nonzero B is suggested by Fig.5.5. As B is increased beyond a certain value, G starts decreasing because of the localizing effect of B. Also, it is evident that the double-peak structure occurring in G at T = 0 due to spin-splitting (shown in the inset) vanishes at finite T as expected until B is made sufficiently strong ($\mu_B B \ge 0.8$) when the double-peak structure reappears.

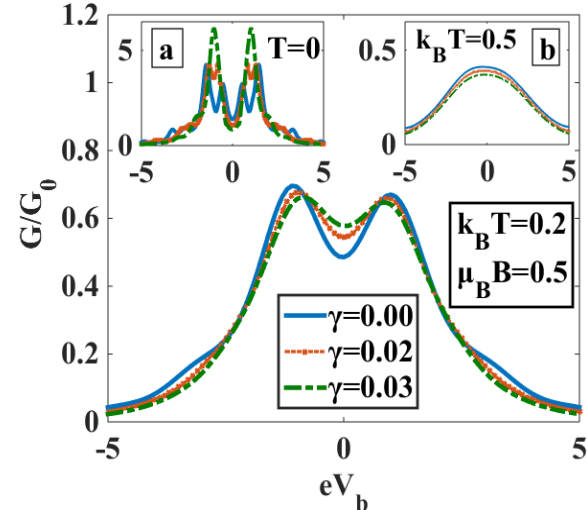




Inset: Results at B = 0.

Fig.5.10 G/G_0 vs. eV_b for several T values at Fig.5.11 G/G_0 vs. eV_b for several B values at $\lambda = 0.6, \ eV_m = 0.1, \\ \gamma = 0.02 \ \ {\rm for} \quad \mu_B B = 0.5 \ . \quad \lambda = 0.6, \ eV_m = 0.1, \\ \gamma = 0.02 \ \ {\rm for} \quad k_B T \ = 0.5 \ . \ \$ Inset: Results at T = 0.





 $\textbf{Fig.5.12} \ \text{G/G}_0 \ \text{vs.} \ V_b \ \text{for several} \ \lambda \quad \text{values at} \quad \textbf{Fig.5.13} \ \text{G/G}_0 \ \text{vs.} \ V_b \ \text{for several} \quad \gamma \ \text{values at}$ $eV_{m} = 0.1 \ , \quad \textit{U} = 5 \ , \qquad \gamma = 0.02 , \ k_{B}T = 0.2 , \quad eV_{m} = 0.1 \, , \ U = 5 , \ \lambda = 0.6 \, , \ k_{B}T = 0.2 \, , \ \mu_{B}B = 0.1 \, , \ \lambda = 0.6 \, , \ k_{B}T = 0.2 \, , \ \mu_{B}B = 0.1 \, , \ \lambda = 0.1 \, , \$ $\mu_B B = 0.5. \; \text{Inset:} \; G \; \; \text{at (a)} \; T = 0, \; \; \mu_B B = 0.5; \; \; \text{(b)} \quad \; 0.5 \; . \; \; \text{Insets:} \; \; G \; \; \text{at (a)} \; \; T = 0, \; \; \mu_B B = 0.5 \; ; \; \; \text{(b)}$ $k_BT = 0.5$, $\mu_BB = 0.5$.

 $k_BT = 0.5, \mu_BB = 0.5.$

In Fig.5.12, we show the effect of e-p interaction (λ) on the (G – V_b) – plots at a fixed temperature $k_BT = 0.2$ and magnetic field $\mu_BB = 0.5$. Insets (a) and (b) show the behaviour for $\mu_B B = 0.5$ at T = 0 and T = 0.5 respectively. The main plot shows that for $\lambda = 0$ (central blue curve), as V_b is increased from zero, G decreases till V_b acquires some critical value where it develops a shoulder. After this G again decreases with the further increase in V_b . The figure shows a bit of asymmetry around $V_b=0$. Interestingly, at $\lambda=0.6$, the central peak of G splits into a double-peak structure with a little asymmetry around $V_b=0$. At higher values of λ ($\lambda=0.8,\ 1.0$), G shows more structures. Thus, the splitting also depends on the strength of the e-p interaction. Interestingly, at low values of T and high values of λ , small side peaks are fund to occur in G. Of course, as expected, G is reduced by e-p interaction. The double-peak structure due to B at T=0 is shown in the inset (a). Inset (b) shows that both the double-peak structure and the side peaks observed in G at low temperature due to polaron formation disappear at higher temperature. This is because at high temperature, real phonons are excited which impede the polaron formation. One can see that the reduction in G by e-p interaction is pronounced only at a lower T. Also, the temperature in general reduces the peak height of G making them more Lorentzian-like.

Fig.5.13 shows how damping (γ) influences the G vs. V_b – behaviour at a non-zero temperature ($k_BT=0.2$) and in the presence of both e-p interaction ($\lambda=0.6$) and an external magnetic field ($\mu_BB=0.5$). The zero-temperature effect is shown in inset (a) and the effect at high temperature ($k_BT=0.5$) is shown in inset (b). One can see a double-peak structure, the minimum occurring at $V_b=0$. As V_b increases, G falls off to zero. At T=0 (inset (a)), a sharp double-peak structure is seen (at $\lambda=0.6$) and the peak values are higher for larger values of γ . But we notice that as T increases, the sharpness in the peaks decreases and above a certain value of T, the double-peak nature of G vanishes completely and G exhibits a solitary wide maximum which looks like a Lorentzian (inset (b)). We can see that G has only a marginal dependence of γ at finite temperature. Also, at low T, the dependence is different in different ranges of V_b . Therefore, we conclude that the behavior of G at a fixed B with respect to λ and γ changes qualitatively in different temperature regimes.

As the interactions affect the spin-resolved conductivities differently, we plot G_{\uparrow} and G_{\downarrow} separately with λ $T \neq 0$ and $B \neq 0$ in Fig.5.14. The insets in Fig.5.14(a) and Fig.5.14(b) show the behaviour at T = 0, and B = 0. Both G_{\uparrow} and G_{\downarrow} show almost a similar behaviour. They first decrease as λ increases from zero and then exhibit a shoulder-like feature and finally again decrease to zero. As temperature is increased, the shoulder disappears and $G_{\uparrow,\downarrow}$ monotonically decreases to zero. Fig.5.14(a) shows that for $B \neq 0$, G_{\uparrow} dies out quite rapidly with increasing λ . As we increase T, still T0 decreases with increasing T1 becomes slower with increasing T2. As can be seen from Fig.5.14(b), the behaviour of T3 with respect to T4 is more interesting for T5. At T6 and T7 in the case of T8 develops a peak at a certain T8 and a shorter side-peak at a higher T8 value. At temperature rises, this peak-structures disappear and T8 shows a broad maximum and on further increase in T8, shows a monotonic decrease.

This can be explained as follows. As mentioned earlier, the magnetic field and the e-p interaction have competing effects on the spin-down component and this gives rise to a non-monotonic behaviour at a low temperature. The polaronic effect is mainly controlled by $\lambda^2 e^{-\lambda^2}$. Therefore, in the small- λ regime, the behavior is dominated by λ^2 while in the large- λ regime, the behaviour is Gaussian resulting into peaks at T=0. Higher temperature minimizes this effect.

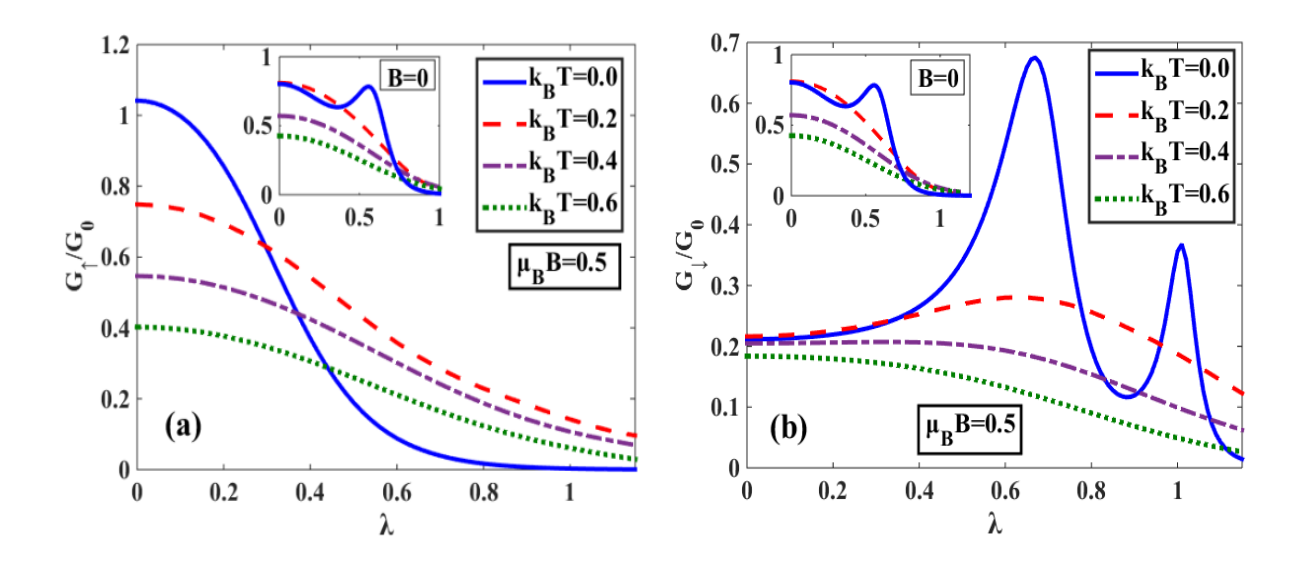
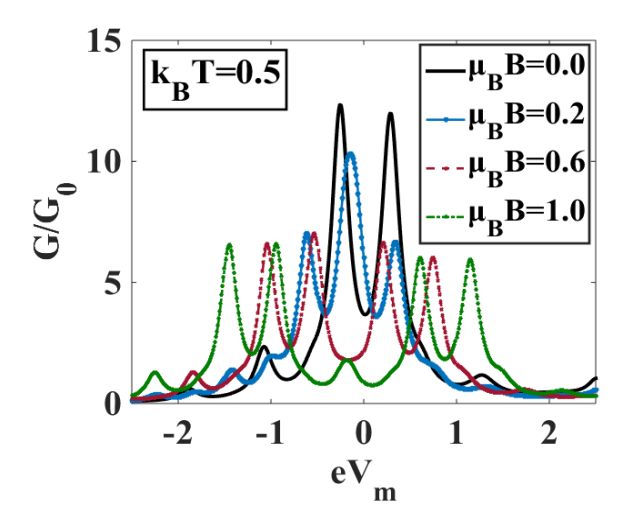


Fig.5.14 (a) G_{\uparrow}/G_0 (b) G_{\downarrow}/G_0 vs. λ for a few T values at $eV_b = 0.5$, $eV_m = 0.1$, $\gamma = 0.02$ for $\mu_B B = 0.5$. (Inset: B = 0).

Fig.5.15 describes the variation of G with V_m for a few values of B at $k_BT = 0.6$ with $\lambda = 0.6$ and $\gamma = 0.02$. Multiple peaks appear in G due to e-p interaction and these peaks are spread equally over $\pm V_m$ axis. Also, the peak heights reduce with increasing B. One may notice that at a certain temperature, each peak splits into two as a magnetic field is switched on. Similarly, in Fig.5.16 also, one can see the spin-splitting at a nonzero B. Also, we see that at nonzero T and B, the heights of the peak in G decrease as λ increases.

Fig.5.17 displays the variation of the spin polarization $P_{\uparrow\downarrow}$ with V_b at few values of T and B. $P_{\uparrow\downarrow}$ decreases with increasing V_b at all T except at T=0, where it initially rises with V_b , shows a peak and finally falls sharply with additional increase in V_b . It is also visible from Fig.5.17 that at nonzero T, $P_{\uparrow\downarrow}$ decreases with increasing T. This is however the behaviour at low B ($\mu_B B = 0.5$). At a comparatively higher B ($\mu_B B = 2.5$) (inset), $P_{\uparrow\downarrow}$ is generally large at low T and reaches maximum polarization ($P_{\uparrow\downarrow,max} = 1.0$) at a certain critical value of V_b . At higher T, $P_{\uparrow\downarrow}$ remains negligibly small up to a certain V_b above which it sharply rises with V_b and reaches a saturation. In general, high B ($\mu_B B \ge 2.5$) and low T ($k_B T = 0.5$) may be

considered as the good criteria for a reasonably good spin-polarization for a given set of SMT constants. Fig.5.18 shows the effect of e-p interaction, λ on the variation of $P_{\uparrow\downarrow}$ with V_b at high B and low T. We can see that the phonon-induced spin-polarization increases with increasing λ even at a higher T (inset), although a relatively high T (inset) suppresses $P_{\uparrow\downarrow}$.



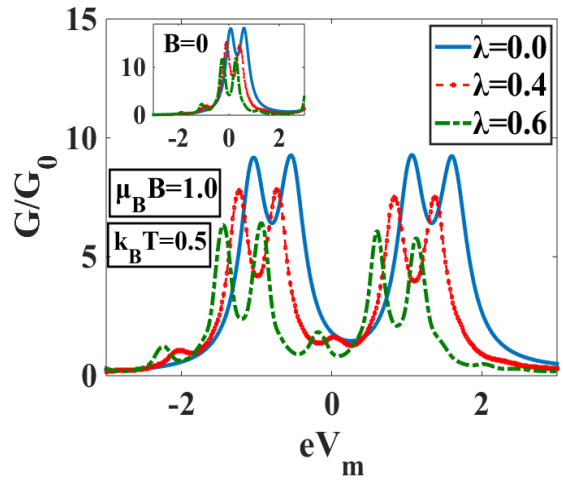


Fig.5.15 G/G $_0$ vs. eV $_m$ for a few B values at $\lambda =$ 0.6, eV $_b = 0.5$, $\gamma = 0.02$ for $k_BT = 0.6$.

Fig.5.16 G/G₀ vs. eV_m for a few λ values at $\mu_B B = 1.0$, $k_B T = 0.5$, $eV_b = 0.5$, $\gamma = 0.02$. Inset: Results at B = 0.

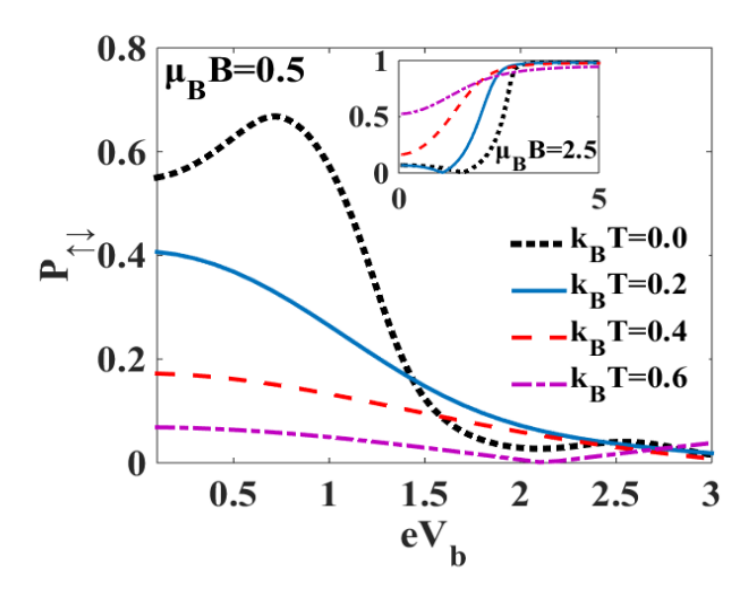


Fig.5.17 $P_{\uparrow\downarrow}$ vs. eV_b for a few T values at $\lambda=0.6$, $eV_m=0.1, \gamma=0.02$ for $\mu_B B=0.5$. Inset: Results at $\mu_B B=2.5$.

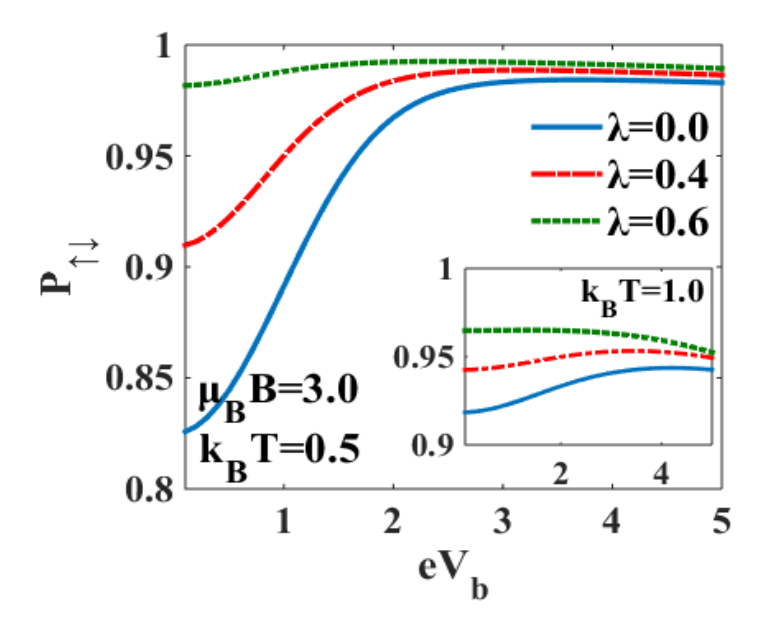


Fig.5.18 $P_{\uparrow\downarrow}$ vs. eV_b for a few λ values at $eV_m=0.1, \gamma=0.02$ for $\mu_B B=3.0, k_B T=0.5$. Inset: Results at $k_B T=1.0$.

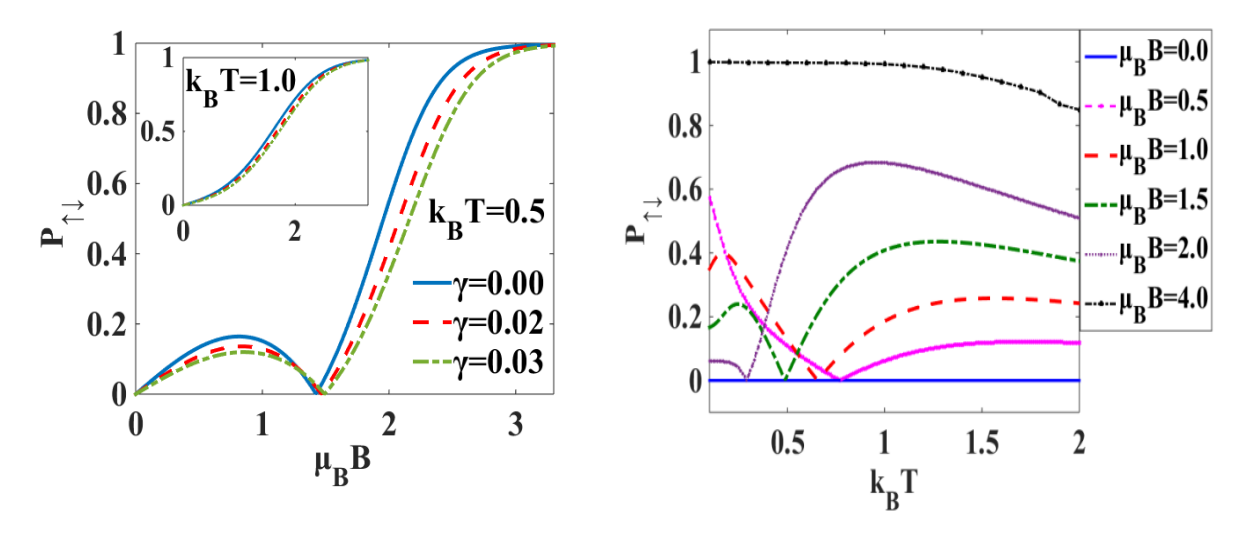


Fig.5.19 $P_{\uparrow\downarrow}$ vs. $\mu_B B$ for a few γ values at $eV_m=0.1$, $eV_b=0.5$, $\lambda=0.6$ for $k_B T=0.5$. Inset: at $k_B T=1.0$.

Fig.5.20 $P_{\uparrow\downarrow}$ vs. k_BT for a few B values at $eV_m=0.1$, $eV_b=0.5$, $\gamma=0.02$, $\lambda=0.6$.

In Fig.5.19, we describe the effect of damping, γ on the variation of $P_{\uparrow\downarrow}$ with B at a given T. Understandably, $P_{\uparrow\downarrow}$ is zero at B = 0 for all γ . As B increases from zero, $P_{\uparrow\downarrow}$ increases and reaches a maximum and then falls off to zero at around $\mu_B B = 1.5$. As B is further increased, $P_{\uparrow\downarrow}$ also increases and now the increase becomes more rapid. However, above a certain B, the growth in $P_{\uparrow\downarrow}$ slows down and finally $P_{\uparrow\downarrow}$ reaches saturation. We thus observe a structure resembling a swan-neck. At a higher value of T (see inset), however, the swan-structure

disappears and $P_{\uparrow\downarrow}$ shows a monotonic increase with B until it saturates at a critical B. With increase in γ , $P_{\uparrow\downarrow}$ gets reduced and right-shifted. Fig.5.20 shows the behavior of $P_{\uparrow\downarrow}$ directly with respect to T at different B. As expected, at B=0, $P_{\uparrow\downarrow}=0$ for all T. At a low magnetic field ($\mu_BB=0.5$), we observe that $P_{\uparrow\downarrow}$ first decreases monotonically with increasing T, reaches zero at some critical T and then grows with further rise in T and finally saturates. Here the neck-part develops a broad maximum and shows a down-turn or a saturation depending on the value of B. When B becomes sufficiently large, $P_{\uparrow\downarrow}$ becomes 1.0 in conformity with Fig.5.19 and continues to have this value till a certain T after which it falls slowly. This again shows that temperature causes lower polarization, but a magnetic field increases it.

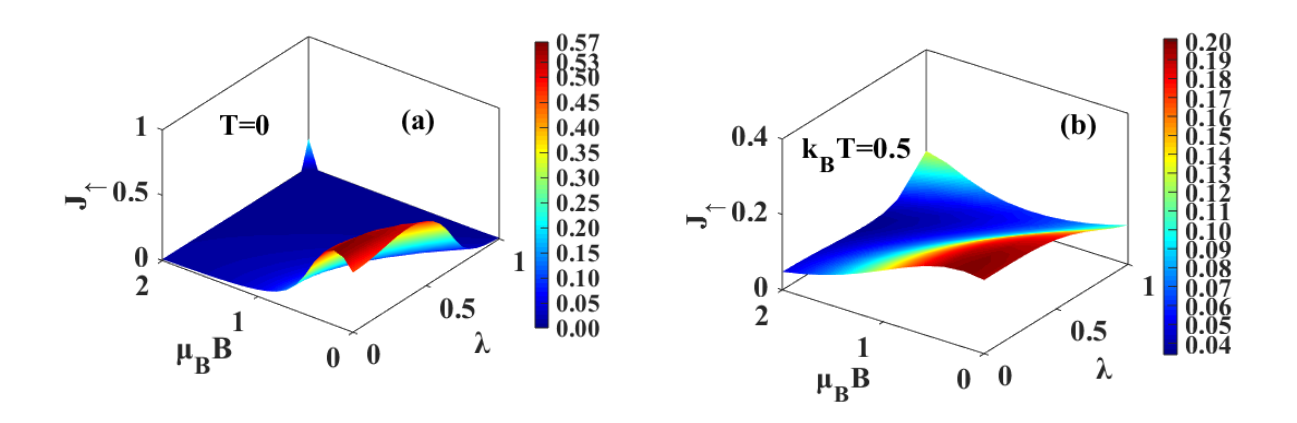


Fig.5.21 3D plots of J_{\uparrow} with respect to B and λ at $eV_m=0.1$, $eV_b=0.5$, U=5, $\gamma=0.02$ for (a) T=0, (b) $T\neq 0$.

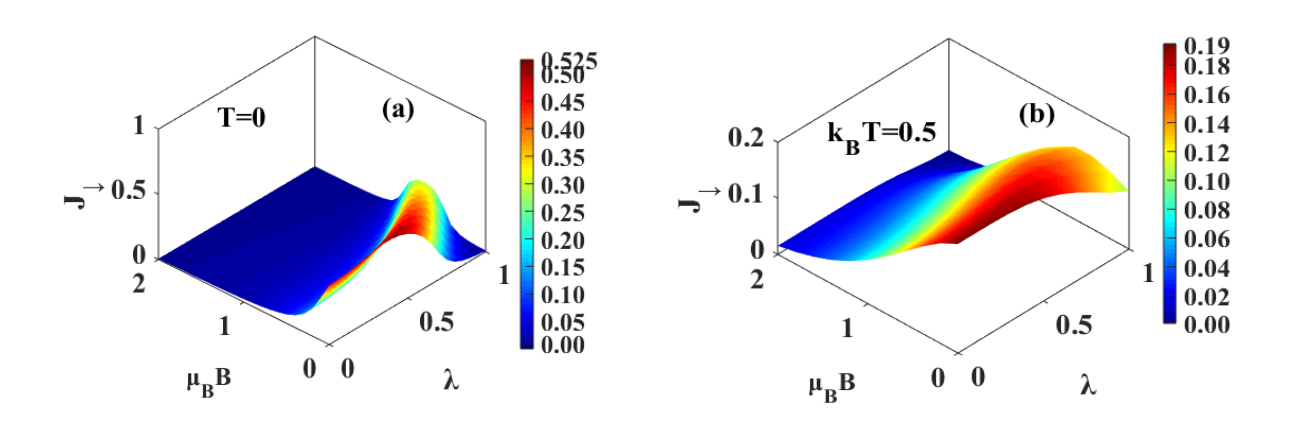


Fig.5.22 3D plots of J_{\downarrow} with respect to B and λ at $eV_m=0.1$, $eV_b=0.5$, U=5, $\gamma=0.02$ for (a) T=0, (b) $T\neq 0$.

In Figs.5.21-22, we display the nature of the surface plots of J_{\uparrow} and J_{\downarrow} in terms of B and λ for $k_BT=0$ and 0.5 and a set of SMT parameters. The dark red and the blue denote

respectively the maximum and minimum values of the current densities. We can see from Fig.5.21 that as T is increased from zero, J_{\uparrow} acquires the maximum at low values of λ and B and it decreases rather slowly as λ or B increases in contrast to what happens at T=0. The scenario is quite similar in the case of J_{\downarrow} , but the maximum of J_{\downarrow} is now found slightly shifted towards higher values of λ values. Thus, the e-p interaction acts differently upon J_{\uparrow} and J_{\downarrow} . This is in agreement with the observations in Fig.5.7. Similar plots can also be drawn for the conductance.

The surface plots of G are plotted in Fig.5.23 for a few values of B. One can see that as B is increased from zero to a small finite value, G does not drop to zero with increasing λ in contrast to its behaviour at B=0, while with increasing T, it drops faster and reduces to almost zero which is again a behaviour different from that at B=0. If B is increased more, the decrease of G with T again turns slower and it does not drop to zero.

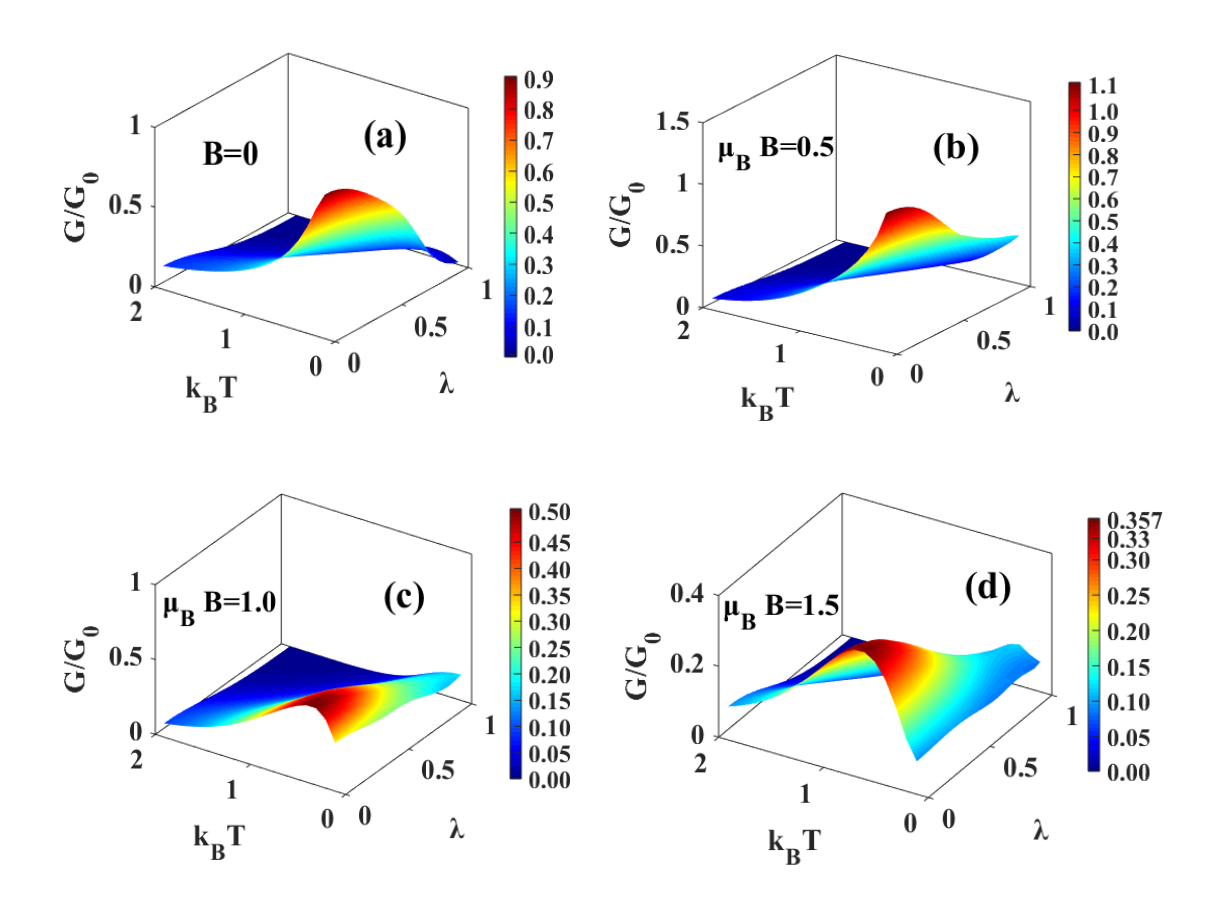


Fig.5.23 3D plots of G with respect to T and λ for a few B values with $eV_m = 0.1$, $eV_b = 0.5$, U = 5, $\gamma = 0.02$.

Figs.5.24-25 show the temperature effect on the contour maps of J and G in the $V_{\rm m}-V_{\rm b}$ plane for a given set of SMT parameters and a fixed magnetic field. In Fig.5.24, the darker

red and the darker blue represent the higher values of J_{\uparrow} and J_{\downarrow} respectively in upper and lower halves of the graphs. One can notice that in the presence of an external magnetic field, the behaviour of the spin-up current turns out to be opposite to that of the sin-down one and both of them get reduced and smoothened on increasing T. The colours fade as V_b approaches zero indicating that the current densities decrease as V_b decreases. The differential conductance G also shows the similar nature. Here also the darker red represents the higher G values, but darker blue represents the lower G values. We can see from Fig.5.25 that, at T=0, there exists two channels on each side with respect to V_m and V_b axes meeting at $V_m=V_b=0$. These channels represent two spin-resolved parts of G. This can also be seen from dark blue solid curve of Fig.5.10. One can see from Fig.5.25 (b-c) that as T increases, the channels become broader indicating the suppression of spin splitting. This can be understood from Fig.5.10 as well. It is also shown that at a non-zero T and B the G values are higher at lower V_m-V_b values.

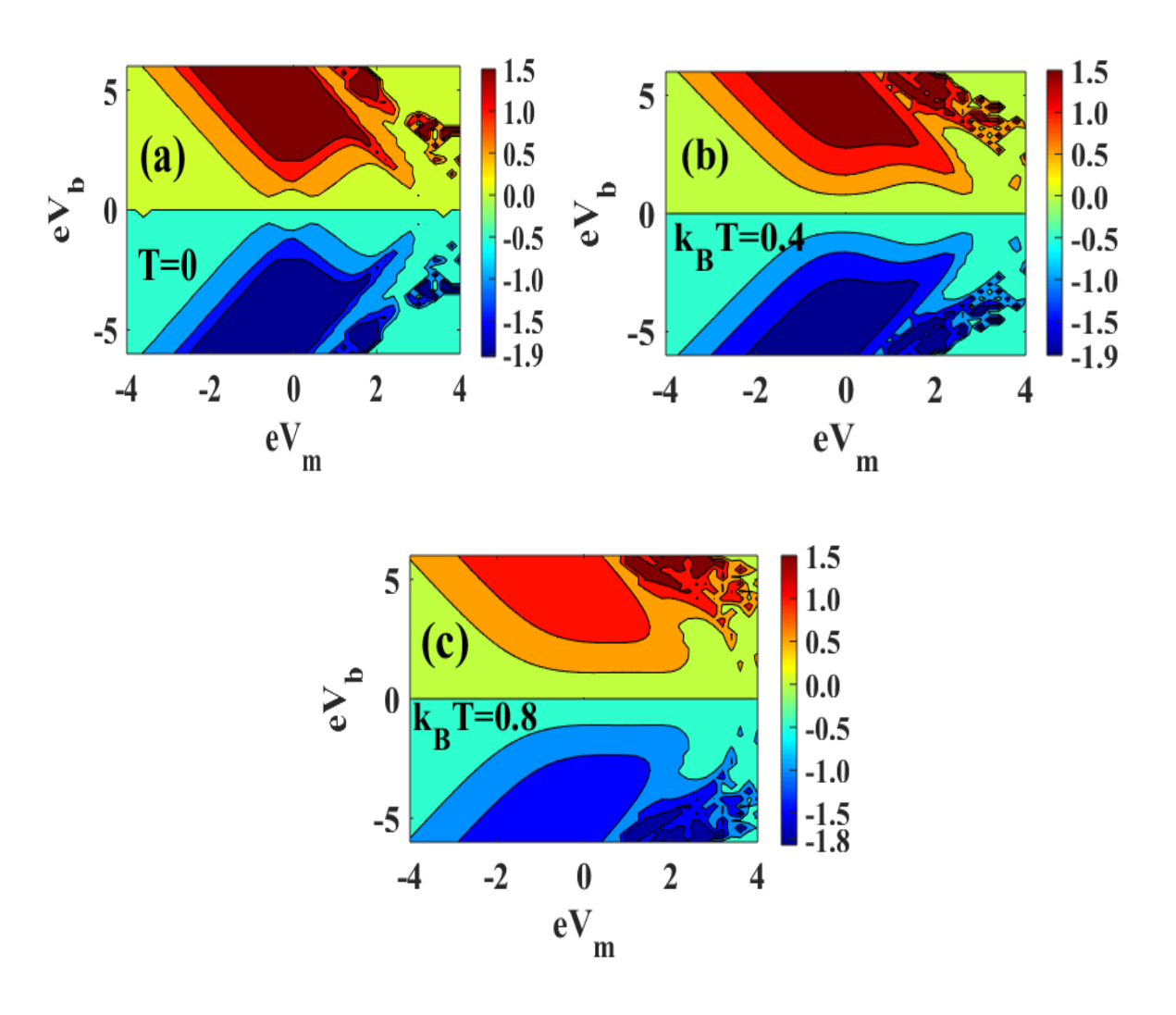


Fig.5.24 Contour plots of J in V_m-V_b plain at $\lambda=0.6$, U=5, $\gamma=0.02$, $\mu_BB=0.5$ for (a) T=0,(b) $k_BT=0.4$, (c) $k_BT=0.8$.

In Figs.5.26-27 we depict the dependence of the contour plot of J and G on λ and U in the V_m-V_b plane for finite T and B and a given set of SMT parameters. The presence of Coulomb correlation, U modifies the variation of both J and G at finite T and B in the V_m-V_b space. From Fig.5.26, the spin splitting with respect to $V_b=0$ in the J-plots is clearly visible at U=0 even at a finite T. As the onsite Coulomb repulsion opposes a further flow of conduction electrons from the S-lead, U reduces both the spin-resolved components of J and makes them chaotic for large values of V_m . One can see that the higher values of J_{\uparrow} and J_{\downarrow} lie in the higher V_m and V_b regions denoted by dark red and dark blue colours. This can be explained as follows. At low temperature, we can write: $(f_S-f_D)\approx \left(\exp\left(-\frac{\mu_S}{k_BT}\right)-\exp\left(-\frac{\mu_D}{k_BT}\right)\right)$, where $\mu_S=e\left(V_m+\frac{1}{2}V_b\right)$, $\mu_D=e\left(V_m-\frac{1}{2}V_b\right)$ and thus $|(f_S-f_D)|$ increases with increasing V_m and V_b values and consequently the higher values of J lie in the high V_m-V_b ($V_b>V_m$) region. One can make the same observation for the variations of G from Fig.5.27.

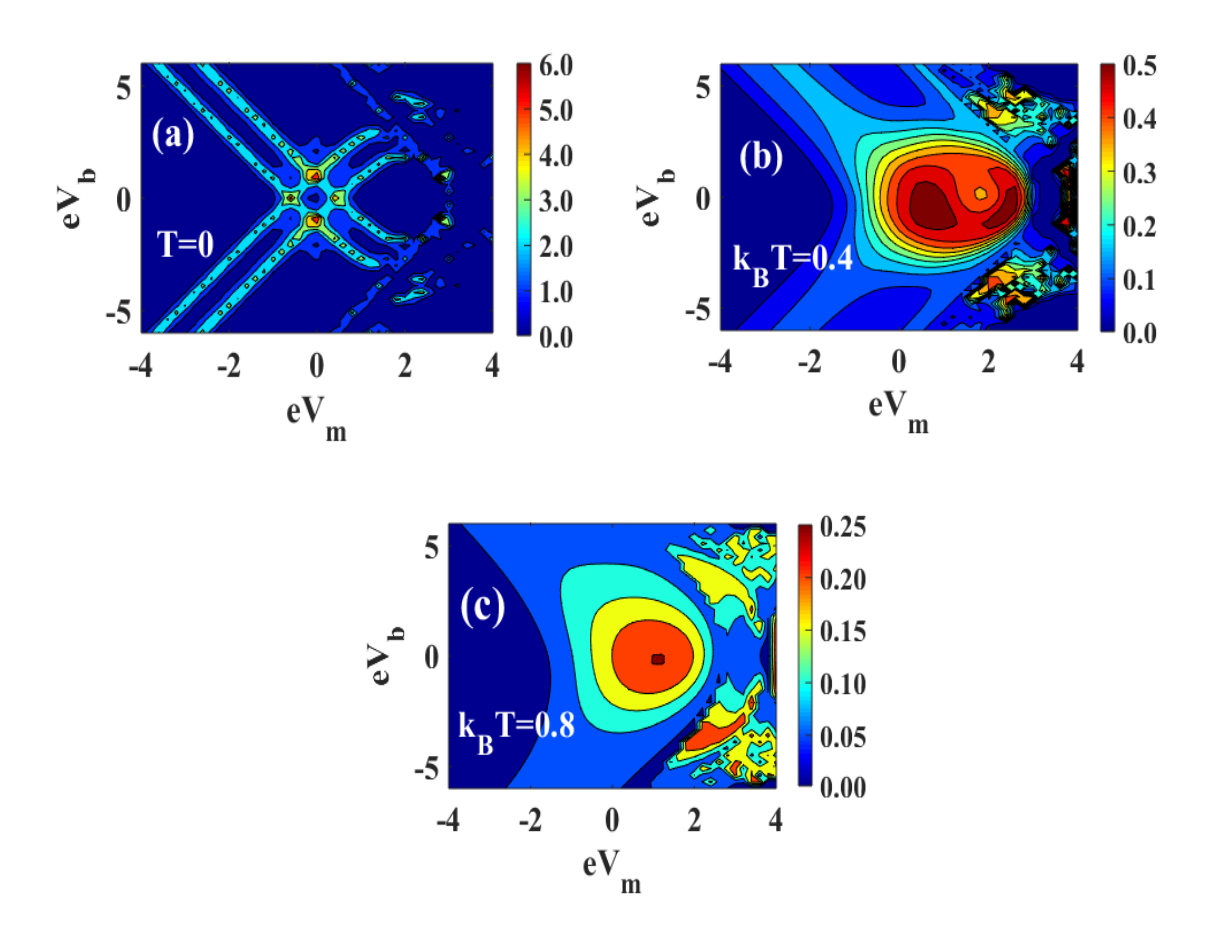


Fig.5.25 Contour plots of G in the V_m-V_b plain at $\lambda=0.6, U=5, \gamma=0.02$, $\mu_BB=0.5$ for (a) T=0 (b) $k_BT=0.4$ (c) $k_BT=0.8$.

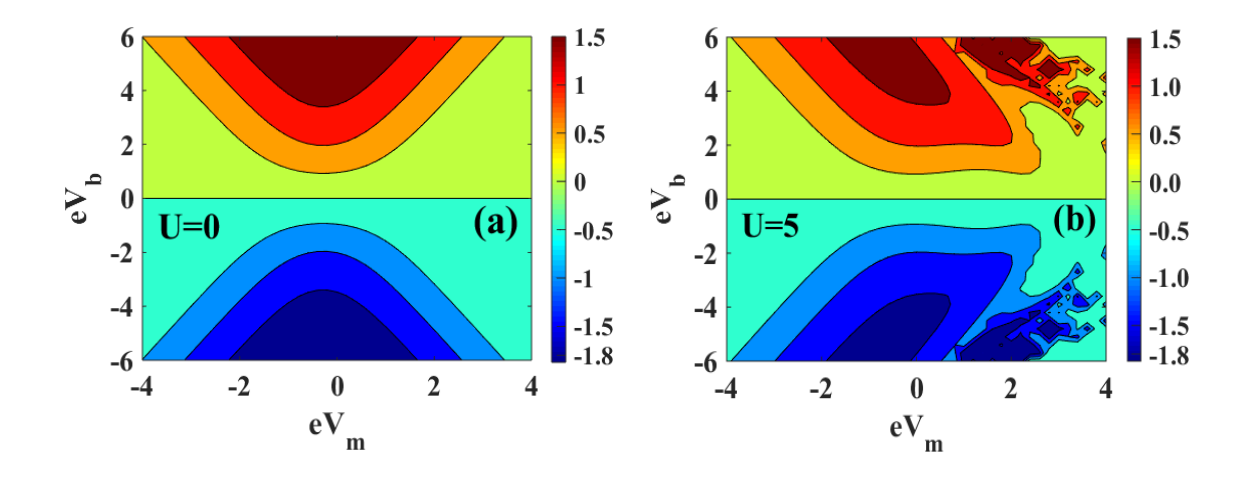


Fig.5.26 Contour plots of J in $V_m - V_b$ plain at $\lambda = 0.6$, $\gamma = 0.02$, $k_B T = 0.6$, $\mu_B B = 0.5$ for (a) U = 0 and (b) U = 5.

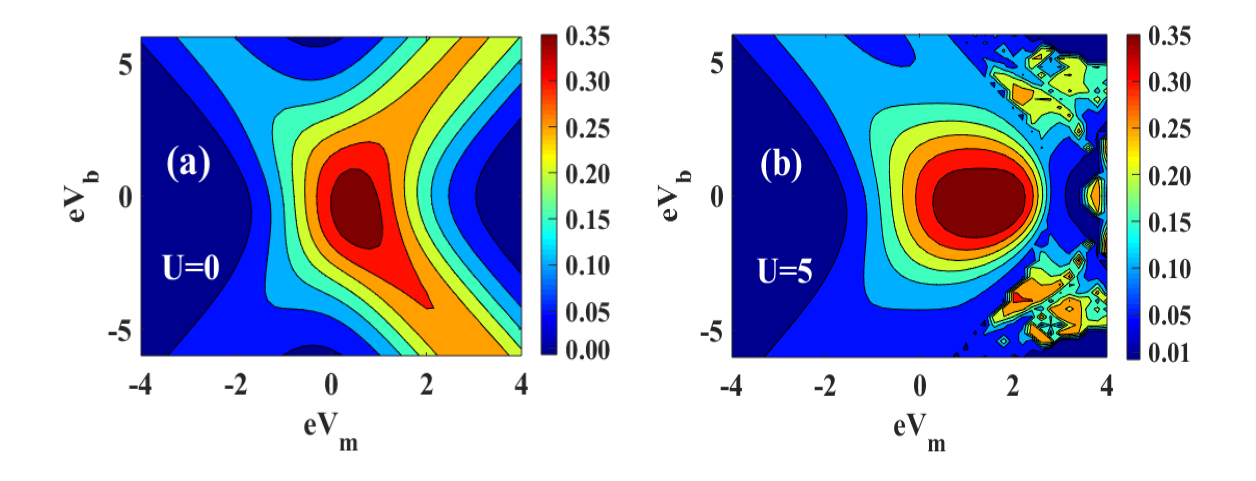


Fig.5.27 Contour plots of G in V_m-V_b space at $\lambda=0.6,~\gamma=0.02$, $k_BT=0.6,~\mu_BB=0.5$ for (a) U=0 and (b) U=5.

5.4 CONCLUSIONS

In conclusion, we have studied the combined effect of magnetic field B and temperature T on the quantum transport in SMT in the presence of e-p interaction, e-e correlation and dissipation. The interaction of the QD phonon and the substrate phonons which causes dissipation is incorporated by a linear model following Caldeira and Leggett and this interaction is treated approximately by a canonical transformation which introduces the main effect of the dissipation namely, the reduction in the frequency of the QD phonon which is precisely the damping effect. The e-p interaction is decoupled by the conventional Lang-Firsov approach and the onsite e-e interaction is treated by the Hartree-Fock mean-field approximation and finally the Keldysh method is used to investigate the effect of dissipation,

e-p interaction and e-e interaction on the spectral function, tunneling current and the differential conductance. We find that magnetic field and temperature have contrasting roles on current. Temperature not only reduces the spectral density, current and differential conductance but also decreases the spin splitting, while the magnetic field increases the height of the spectral function and broadens the separation between the spin-up and the spindown peaks. The magnetic field, of course, reduces the current and the conductance.

The effects of e-p coupling and dissipation on the transport properties are greatly influenced by magnetic field and temperature. Also, these effects depend on the range of T and B. We have shown that the spectral function is reduced by the e-p interaction and damping at low T and low B while at high T and high B, it is enhanced by polaronic interaction strength and damping. The spectral function peak is shifted by the magnetic field towards left on the V_{R} axis and towards right by the temperature. It is also shown that due to polaronic effect, side peaks develop in the spectral function which become shorter as T rises, but at high T and high B, they again reappear. At $T \neq 0$, the e-p interaction reduces the tunneling current much more in the presence of a magnetic field than in the absence of it. On the other hand, though the enhancement of the tunneling current by damping becomes more pronounced at a nonzero B, a sufficiently high field suppresses this effect. The differential conductance is reduced by damping and e-p coupling at $T \neq 0$ and $B \neq 0$. This reduction becomes more prominent at high temperature. The temperature and magnetic field have contrasting effects on spin resolved current densities, conductance and spin-polarization with respect to the interactions. It is important to mention that finally the temperature effect dominates over the magnetic field.

Finally, the spin-resolved current density and the conductance are studied as a function of different SMT parameters through surface and contour plots. This work can have potential application as a spin-filter which can be tuned by temperature and magnetic field.

REFERENCES

- 1. P. T. Mathew and F. Fang, Engineering 4, 760–771 (2018).
- 2. K. S. Kwok and J.C. Ellenbogen, Mater. Today 5, 2, 28-37 (2002).
- 3. A. Aviram and M. A. Ratner, Chem. Phys. Lett. **29**, 277 (1974).
- 4. K. Stokbro, J. Phys. Chem. C 114, 20461 (2010).
- 5. L.P. Mickael, B. Enrique, and H.S. J. van der Zant, Chem. Soc. Rev. 44, 902 (2015).
- 6. S. Datta, Electronic Transport in Mesoscopic Systems. (Cambridge University Press, 1997).

- 7. S. Datta, Quantum Transport: Atom to Transistor (Cambridge University Press, 2005).
- 8. H. Park, J. Park, A.K.L. Lim, E.H. Anderson, A.P. Alivisatos, and P.L. McEuen Nature **407**, 57 (2000).
- 9. T. A. Costi, Phys. Rev. B **64**, 241310(R) (2001).
- 10. L. Li, W. Y. Lo, Z. Cai, N. Zhang, and L. Yu, Chem. Sci. 7, 3137 (2016).
- 11. S. J. Ray, J. Appl. Phys. **118**, 034303 (2015).
- 12. U. V. Pipit, A. Yasuo, S. Masanori, T. Toshiharu, and M. Yutaka, Mater. Res. Express 4, 024004 (2017).
- 13. D. G.-Gordon, H. Shtrikman, D. Mahalu, D. A.-Magder, U. Meirav, and M. A. Kastner, Nature **391**, 156 (1998).
- 14. L. H. Yu and D. Natelson, Nano Lett. 4, 79 (2003).
- 15. W. Liang, M. P. Shores, M. Bockrath, J. R. Long, and H. Park, Nature 417, 725 (2002).
- 16. G. Gonzalez, M. N. Leuenberger, and E. R. Mucciolo, Phys. Rev. B 78, 054445 (2008).
- 17. Z. Z. Chen, H. Lü, R. Lu, and B. Zhu, J. Phys. Condens. Matter 18, 5435 (2006).
- 18. A. Khedri, T. A. Costi, and V. Meden, Phys. Rev. B 98, 195138 (2018).
- 19. H. Haiying, P. Ravindra, and P. K. Shashi, Nanotechnology 19, 50 (2008).
- 20. J. Loos, T. Koch, A. Alvermann, A. R. Bishop, and H. J. Fehske, Phys.:Conf, Ser. 220, 012014-9 (2010).
- 21. M. C. Luffe, J. Koch, and F. von Oppen, Phys. Rev. B 77, 125306–7 (2008).
- 22. J. Paaske and K. Flensberg, Phys. Rev. Lett. 94, 176801–4 (2005).
- 23. D. Bing and X. L. Lei, Phys. Rev. B **63**, 235306 (2001).
- 24. Z. Z. Chen, R. Lü, and B. F. Zhu, Phys, Rev. B 71, 165324 (2005).
- 25. C. N. Raju and A. Chatterjee Sci. Rep. 6, 18511 (2016).
- 26. M. Kalla, Ch. N. Raju, and A. Chatterjee, Sci. Rep. 9 16510 (2019).
- 27. M. Kamenetska, J. R. Widawsky, M. Dell'Angela, and M. Frei, V. Latha, J. Chem. Phys. **146**, 092311 (2017).
- 28. R. G. Alvar, W. Lejia, D. B. Enrique, and A. N. Christian, Nature. Comm. 7, 11595 (2016).
- 29. U. Lundin and R. H. McKenzie, Phys. Rev B 66, 075303 (2002).
- 30. M. Kalla, C. N. Raju, and A. Chatterjee, Sci. Rep. 11, 10458 (2021).
- 31. M. Kalla, C. N. Raju, and A. Chatterjee, Sci. Rep. 12, 9444 (2022).
- 32. J. T. Sander, R. M. Alwin, and D. V. Cees, Nature 393, 49 (1998).
- 33. Y. Makoto, A. Yasuo, S. Masanori, T. Toshilharu, I. Hisao, M. Yukata, and N. Yutaka, Sci. Rep. 7, 1589 (2017).
- 34. A. O. Caldeira and A. J. Leggett, Ann. of Phys. **149**, 374 (1983).

- 35. I. G. Lang and Y. A. Firsov, Sov. Phys. JETP 16, 1301 (1962).
- 36. Y. Meir, N. S. Wingreen, and P. A. Lee, Phys. Rev. Lett. 66, 3048 (1991).
- 37. A. P. Jauho and N. S. Wingreen, Y. Meir, Phys. Rev. B 50, 5528 (1994).
- 38. R. Świrkowicz, J. Barnaś, and M. Wilczyński, Phys. Rev. B 68, 195318 (2003).
- 39. L. V. Keldysh, Sov. Phys. JETP 20, 1018 (1965).

CHAPTER 6

SPIN-FILTERING BY RASHBA COUPLING IN A CORRELATED POLAR DISSIPATIVE MOLECULAR TRANSISTOR AT FINITE TEMPERATURE AND IN A MAGNETIC FIELD

ABSTRACT

The RSOI induced quantum transport through a QD embedded in a two-arm quantum loop of an SMT is studied at finite temperature in the presence of e-p and Hubbard interactions, an external magnetic field and quantum dissipation. The Anderson-Holstein-Caldeira-Leggett-Rashba model is used to describe the system and several unitary transformations are employed to decouple some of the interactions and the transport properties are calculated using the Keldysh technique. It is shown that RSOI alone separates the spin-up and spin-down currents causing zero-field spin-polarization. The gap between the up and down-spin currents and conductances can be changed by tuning the Rashba strength. In the absence of a field, the spin-up and spin-down currents show an opposite behaviour with respect to spin-orbit interaction phase. The spin-polarization increases with increasing e-p interaction at zero magnetic field. In the presence of a magnetic field, the tunneling conductance and spin-polarization change differently with the polaronic interaction, SOI and dissipation in different temperature regimes. This study predicts that for a given Rashba strength and magnetic field, the maximum spin-polarization in a single molecular device occurs at zero temperature.

6.1 Introduction

Spintronics has emerged in the last few decades as a very fascinating area of modern condensed matter physics due to its potential use in manipulating electron spin [1,2] to control spin current. The SOI which is one of the key elements of low-dimensional spintronics physics has been studied by many research groups [3-14]. These studies have been motivated by the pioneering work of Datta and Das on spin field-effect-transistor [14]. Molecular transistor is another branch which has received so much attention thanks to Aviram et al. [15] who fabricated the first model of SMT. A molecular junction transistor contains at its centre a molecule or a QD connected to two conducting leads which act as a source (S) and a drain (D). The S-QD-D system is placed on a substrate to which is attached gate. The electrons in S and D can be treated as free electrons with continuous momentum states. The central QD contains discrete energy levels and so the QD electrons are described by localized states. Because of the application of a bias voltage, electrons from S can travel to D through QD giving rise to a tunneling current which can also be controlled by the gate voltage. The tunneling of electrons from S to QD and QD to D and vice versa can be described by a hybridization term. Several transport properties have been studied in SMT systems [16-20] which show potential for promising applications in nano-devices. There have also been investigations on correlation effects in a SMT system namely, the Coulomb blockade and Kondo effect [21-25]. It has also been observed that the e-e and local e-p interactions play a crucial role on the non-equilibrium quantum transport through SMT structures [26-31]. The effect of e-p interaction on the transport properties in an SMT system has been studied by Chen et al [30]. They have shown that phonon-assisted conductance is reduced significantly in the presence of e-p coupling. Recently, Khedri et al. [31] have shown the phononic responses in the bias-voltage-dependent electric currents in a vibrating molecular transistor. The effect of quantum dissipation on the tunneling conductance of an SMT system has been investigated by RC [32]. They have assumed that QD contains a single localized lattice mode which interacts with the QD electrons through a coupling of Holstein type. They have further assumed that the insulating substrate contains a large number of uncoupled harmonic oscillator modes and thus acts as a phonon-reservoir. In the RC picture, the substrate phonons can interact with the local QD phonon through the linear CL interaction giving rise to dissipation. They have formulated the whole system by AHCL model and used the Keldysh NEGF technique to calculate the tunneling current and differential conductance. It has been shown that dissipation renormalizes the QD phonon frequency and consequently the polaronic effect decreases leading to an increase in the tunneling current. Later, Kalla et al. [33] have studied the transport properties of the same set-up in the presence of an external magnetic field. This work has useful applications for a spin-filtering device. The SOI is another important characteristic feature that can lead to spin-dependent transport [34-44]. Sun et al. [44] have given a derivation of the Rashba SO (RSO) interaction in second quantized notation and have shown how RSOI and magnetic flux together can polarize the transport properties of a QD in an A-B ring. Some experimental studies [45, 46] have shown that temperature can also play a significant role on the non-equilibrium transport. Kalla et al. have theoretically analysed the effect of between the source and the drain temperature in an SMT system [47]. Very recently, Kalla et al. have studied the transient dynamics in a dissipative SMT with e-p and e-e interaction [48].

In this study, we wish to investigate the effect of RSOI on the non-equilibrium quantum transport in a dissipative SMT device. We consider an SMT system in which a two-arm quantum loop containing a QD in one of its arms is sandwiched between the source and the drain (Fig.6.1(a)). Thus, the electrons from S can tunnel to D following two paths, one through the arm of the loop that contains the QD and the other through the arm of the loop that does not contain any QD. We assume that the QD electrons can interact with each other through a Hubbard-like interaction and with the local phonon through an e-p interaction of Holstein type. Following the approach of Sun et al. [44] we incorporate the RSOI-phase and model the system by AHCL Hamiltonian and employ the finite Keldysh NEGF technique [49] to calculate the phonon-induced magneto-transport properties in a correlated dissipative SMT structure in the presence of RSOI.

6.2 Analytical model and formulation

The standard model of an SMT with a QD embedded in a two-arm loop that is attached to two metallic leads namely Source (S) and Drain (D) is depicted in Fig.6.1(a) where the QD placed on one arm of the loop contains RSO, e-p and Hubbard interactions and the other arm (which does not contain RSOI) directly connects S and D with a coupling strength t_{SD} . A schematic diagram for the realization of the QD used in Fig.6.1(a) is shown in Fig.6.1(b). It is evident that the heterostructure geometry of Fig.6.1(b) would lead to a band-bending at the GaAs-AlGaAs interfaces giving rise to a structural inversion asymmetry (shown in Fig.6.1(c)) which produces the RSO coupling in the GaAs QD. The red part of Fig.6.1(b) is considered as the central GaAs QD which is attached to S on one side and to D on the other side. A given number of electrons can be accumulated in the QD by using the voltage V_0 . The whole system is mounted on an insulating substrate that contains non-interacting phonons behaving as a phonon-bath which can interact with the QD-phonon giving rise to a quantum

damping effect. The bias voltage V_b and the gate voltage V_g are applied as shown in the Fig. 6.1(a). Because of the bias voltage, electrons can travel from S to D by tunnelling through the QD and also by hopping through the other path. It may be noted that the current channel is in the x-direction and a magnetic field B(0,0,B) is applied in the z-direction. In general, a QD may have many discrete energy levels, but it may still behave like an SMT system at a sufficiently small size, as the higher energy levels in that case can be disregarded.

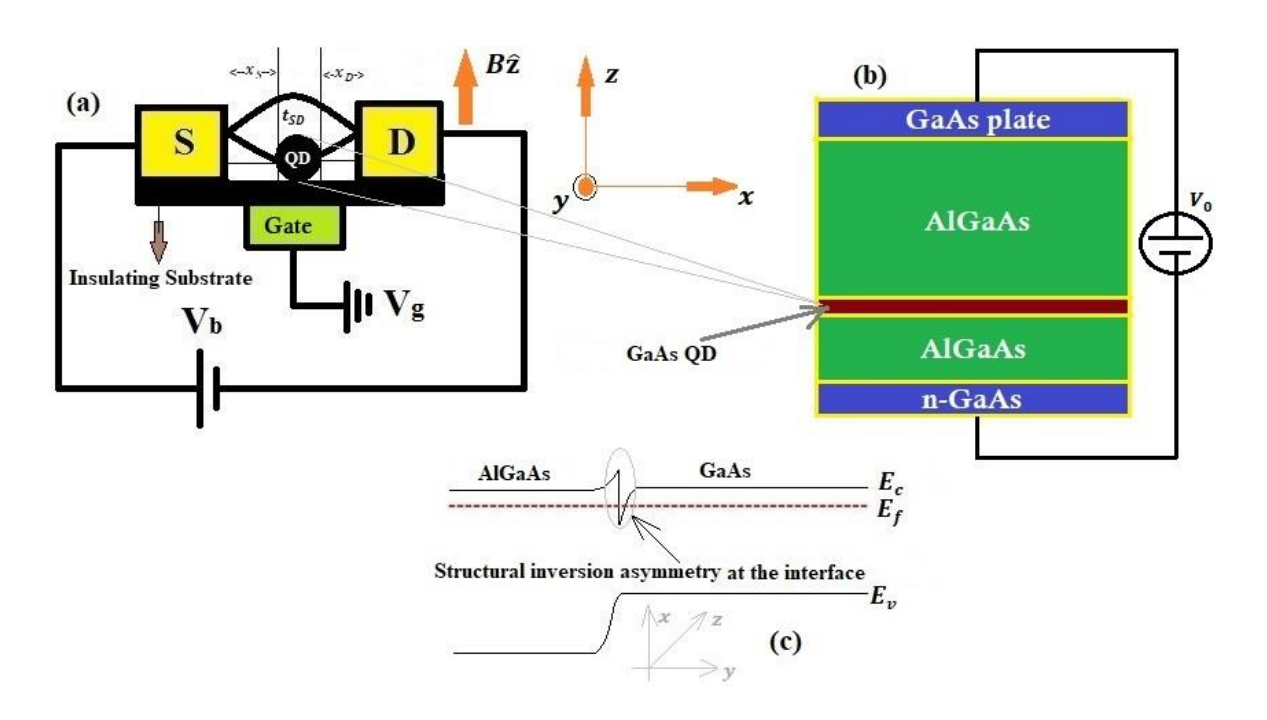


Fig.6.1 Schematic diagram (a) of an SMT device with a QD containing RSOI embedded in a two-arm loop; (b) for experimental realization of a QD; (c) showing structural inversion asymmetry at the GaAs-AlGaAs interface.

The system can be described, in general, by the following AHCL-RSO Hamiltonian

$$H = H_{S,D} + H_{QD} + H_T + H_V , (6.1)$$

where,

$$H_{S,D} = \sum_{k\sigma \in S,D} \varepsilon_k \left(c_{kS,\sigma}^{\dagger} c_{kS,\sigma} + c_{kD,\sigma}^{\dagger} c_{kD,\sigma} \right) + t_{SD} \sum_{k\sigma \in S,D} \left(c_{kS,\sigma}^{\dagger} c_{kD,\sigma} + h.c. \right) , \qquad (6.2)$$

$$H_{\rm QD} = \sum_{d\sigma} (\varepsilon_d - eV_g - \frac{1}{2}g^*\mu_B B\sigma_z) n_{d\sigma} + \sum_d U n_{d\uparrow} n_{d,\downarrow} + \left(\frac{p_0^2}{2m_0} + \frac{1}{2}m_0\omega_0^2 x_0^2\right) + g \sum_{d\sigma} n_{d\sigma} x_0 + H_R,$$
(6.3)

$$H_T = \sum_{kd\sigma} \left[V_k \left(c_{kS,\sigma}^{\dagger} c_{d\sigma} + c_{kD,\sigma}^{\dagger} c_{d\sigma} \right) + h.c \right], \tag{6.4}$$

$$H_V = H_{BO} + H_{QD-B} \equiv \sum_{i=1}^{N} \left[\frac{p_i^2}{2m_i} + \frac{1}{2} m_i \omega_i^2 x_i^2 \right] + \sum_{i=1}^{N} \beta_i x_i x_0.$$
 (6.5)

Eq. (6.2) represents the lead Hamiltonian $H_{S,D}$. The first term of $H_{S,D}$ gives the total energy of the conduction electros in S (D), where $n_{kS(D),\sigma}$ (= $c_{kS(D),\sigma}^{\dagger}c_{kS(D),\sigma}$) denotes the number operator for the S (D) electrons with momentum k and spin σ , $c_{kS(D),\sigma}^{\dagger}$ ($c_{kS(D),\sigma}$) being the corresponding creation (annihilation) operator and the second term of $H_{S,D}$ represents the coupling between the two leads with the hopping strength t_{SD} . Eq. (5.3) gives Hamiltonian $(H_{\rm QD})$ for the QD which in general can contain many localized energy levels d with energy ε_d . The first term of $H_{\rm QD}$ shows that the QD energy is modified by the gate voltage V_g and the magnetic field $B\hat{z}$, where $n_{d\sigma} \left(= c_{d\sigma}^{\dagger} c_{d\sigma} \right)$ denotes the number operator for the QD electrons, $c_{d\sigma}^{\dagger}(c_{d\sigma})$ being the corresponding creation (annihilation) operator of the dth energy level, σ_z is the z-component of the Pauli matrices σ , g^* is the gyromagnetic ratio and μ_B is the Bohr magneton. The second term of $H_{\rm QD}$ represents the Hubbard interaction with U as the Coulomb correlation strength. The third term of $H_{\rm OD}$ is the Hamiltonian for the local lattice mode of QD, where (x_0, p_0) are the coordinate and the corresponding canonical momentum of the QD oscillator with mass m_0 and frequency ω_0 . The fourth term of $H_{\rm QD}$ represents the interaction of the QD electrons with the local QD phonon with g giving the strength of the coupling. The fifth term of $H_{\rm OD}$ represents the RSOI which, in general, can be written in the x - z plane as

$$H_R = \hat{y}.\frac{\alpha_R}{\hbar} \left[\vec{\sigma} \times \left(\vec{p} + \frac{e\vec{A}}{c} \right) \right], \tag{6.6}$$

where α_R is the strength of RSOI. Choosing the Landau gauge: $\vec{A} = (0, Bx, 0)$, we can write H_R in the second quantized notation in the chosen basis $|d\sigma\rangle \equiv \varphi_d(\vec{r}) \begin{pmatrix} 1 \\ 0 \end{pmatrix}$ as

$$H_{R} = \frac{\alpha_{R}}{\hbar} \sum_{dd'} \left[t_{d'd}^{x} \left(c_{d'\sigma}^{\dagger} c_{d\sigma} - c_{d',-\sigma}^{\dagger} c_{d,-\sigma} \right) + t_{d'd}^{z} \left(c_{d',-\sigma}^{\dagger} c_{d\sigma} - c_{d,-\sigma}^{\dagger} c_{d'\sigma} \right) \right] + h.c., \quad (6.7)$$

where $t_{d'd}^{x(z)} = \int d\vec{r} \, \varphi_{d'}^*(\vec{r}) \, p_{x(z)} \, \varphi_d(\vec{r})$. The first term of Eq. (6.7) denotes the inter-level hopping between the same spin state and the second term denotes the between a spin-flip state. Eq. (6.4) represents the tunneling Hamiltonian H_T which describes the tunneling of electrons from S to D through the QD and that of the reverse process, V_k being the hybridization strength. Eq. (6.5) represents the substrate Hamiltonian H_V which contains two pieces, H_{BO} and H_{QD-B} . H_{BO} describes a collection of N uncoupled bath oscillators where (x_i, p_i) refer to the generalized coordinates and momenta of the i-th bath oscillator of mass m_i and frequency ω_i and H_{QD-B} gives the linear interaction between the QD-phonon and the i-th bath-phonon with the coupling strength β_i . H_{QD-B} is chosen in the spirit of the Caldeira-Leggett model [50].

To decouple SOI, we apply a transformation [44] to H by a unitary operator U_R so that H transforms to $\overline{H} = U_R^{\dagger} H U_R$. U_R is chosen as

$$U_{R} = \begin{cases} \frac{1}{\sqrt{2}} e^{-ik_{R}(x-x_{S})\sigma_{z}} & \text{for } x < x_{S}, \\ \frac{1}{\sqrt{2}} e^{-ik_{R}(x_{D}-x_{S})\sigma_{z}} & \text{for } x_{S} < x < x_{D}, \\ \frac{1}{\sqrt{2}} e^{-ik_{R}(x_{D}-x_{S})\sigma_{z}} & \text{for } x_{D} < x. \end{cases}$$
(6.8)

where, $k_R = (\alpha_R m^*/\hbar^2)$. Defining a new set of operators: $\bar{c} = U_R^{\dagger} c$ and $\bar{c}^{\dagger} = c^{\dagger} U_R$, we can express \bar{H} as

$$\begin{split} \overline{H} &= \sum_{k\sigma \in S,D} \varepsilon_k \left(\bar{c}_{kS,\sigma}^\dagger \bar{c}_{kS,\sigma} + \; \bar{c}_{kD,\sigma}^\dagger \bar{c}_{kD,\sigma} \right) + \; t_{SD} \sum_{k\sigma \in S,D} \left(\bar{c}_{kS,\sigma}^\dagger \bar{c}_{kD,\sigma} + h.\,c. \right) \\ &+ \sum_{d\sigma} \bar{\varepsilon}_d \; \bar{n}_{d\sigma} + \sum_{d} U \bar{n}_{d\uparrow} \bar{n}_{d\downarrow} + \left(\frac{p_0^2}{2m_0} + \frac{1}{2} m_0 \omega_0^2 x_0^2 \right) + \; g \sum_{d\sigma} \bar{n}_{d\sigma} \, x_0 \\ &+ \frac{\alpha_R}{\hbar} \sum_{dd'} \left[t_{d'd}^x \left(\bar{c}_{d'\sigma}^\dagger \bar{c}_{d\sigma} - \bar{c}_{d',-\sigma}^\dagger \bar{c}_{d,-\sigma} \right) + t_{d'd}^z \left(\bar{c}_{d',-\sigma}^\dagger \bar{c}_{d\sigma} - \bar{c}_{d,-\sigma}^\dagger \bar{c}_{d'\sigma} \right) \right] + h.\,c. \\ &+ \sum_{i=1}^N \left[\frac{p_i^2}{2m_i} + \frac{1}{2} m_i \omega_i^2 x_i^2 \right] + \sum_{i=1}^N \beta_i \, x_i x_0 \end{split}$$

$$+\sum_{kd\sigma} \left[V_k \left(\bar{c}_{kS,\sigma}^{\dagger} \bar{c}_{d\sigma} e^{-i\sigma k_R(x-x_S)} + \bar{c}_{kD,\sigma}^{\dagger} \bar{c}_{d\sigma} e^{-i\sigma k_R(x-x_D)} \right) + h.c \right], \tag{6.9}$$

where $\bar{\varepsilon}_d = \left(\varepsilon_d - eV_g - \frac{1}{2}g^*\mu_B B\sigma_z\right)$. For simplicity, we assume that the QD contains effectively a single localized level and a single lattice mode which allows us to neglect the terms involving inter-level hopping and spin-flip term in the transformed Hamiltonian (9). Also, we choose x = 0 and redefine: $e^{i\sigma k_R x_S} \bar{c}_{d\sigma}$ as $c_{d\sigma}$. The Hamiltonian \bar{H} then reads

$$H = H_{S,D} + \sum_{\sigma} \bar{\varepsilon}_{d} n_{d\sigma} + U n_{d\sigma} n_{d,-\sigma} + \left(\frac{p_{0}^{2}}{2m_{0}} + \frac{1}{2} m_{0} \omega_{0}^{2} x_{0}^{2} \right) + g \sum_{\sigma} n_{d\sigma} x_{0} + H_{V}$$

$$+ \sum_{k\sigma} \left[\left(V_{k} c_{kS,\sigma}^{\dagger} c_{d\sigma} + h.c \right) + \left(V_{k} c_{kD,\sigma}^{\dagger} c_{d\sigma} e^{-i\sigma\phi_{SO}} + h.c \right) \right], \tag{6.10}$$

which shows that the RSOI generates a spin-induced phase factor $-\sigma\phi_{SO}$ in the tunneling Hamiltonian for the (QD -D) - sector, where $\phi_{SO} \equiv k_R l = k_R (x_S - x_D)$, $l = (x_S - x_D)$ being the length scale over which α_R is non-zero and $\sigma = +1$ and $\sigma = -1$ correspond to spin-up and spin-down electrons respectively.

Next, we proceed to decouple the interaction between the QD phonon and the substrate phonons as we have done in Ch.5. After applying the canonical transformations (Eqs. (5.7) and (5.8)) and eliminating the substrate phonons partially followed by the algebra mentioned in Ch.5, the relevant SMT Hamiltonian reads

$$H = H_{S,D} + \sum_{\sigma} \bar{\varepsilon}_{d} n_{d\sigma} + U n_{d,\sigma} n_{d,-\sigma} + \hbar \tilde{\omega}_{0} b^{\dagger} b + \lambda \hbar \tilde{\omega}_{0} (b^{\dagger} + b) \sum_{\sigma} n_{d\sigma}$$
$$+ \sum_{k\sigma} \left[\left(V_{k} c_{kS,\sigma}^{\dagger} c_{d\sigma} + h.c \right) + \left(V_{k} c_{kD,\sigma}^{\dagger} c_{d\sigma} e^{-i\sigma\phi_{SO}} + h.c \right) \right], \tag{6.11}$$

where g together with all the multiplicative factors are clubbed into λ which we can refer to as the renormalized e-p interaction coefficient. The renormalized frequency is given as $\widetilde{\omega}_0 = (\omega_0^2 - \Delta \omega^2)^{1/2}$ and $\Delta \omega^2 = 2\pi \gamma \omega_c$ defined in Eq. (5.13) where γ is the dissipation coefficient.

The next interaction to be dealt with is the e-p interaction. The e-p coupling can be removed by the well-known LFT [51]: $e^S = exp\{\lambda \sum_{\sigma} n_{d\sigma} (b^{\dagger} - b)\}$. The transformed Hamiltonian can be expressed as

$$\begin{split} \widetilde{H} &= H_{S,D} + \sum_{\sigma} \widetilde{\varepsilon}_{d\sigma} n_{d\sigma} + \widetilde{U} n_{d,\sigma} n_{d,-\sigma} + \hbar \widetilde{\omega}_0 b^{\dagger} b \\ &+ \sum_{k\sigma} \left[(\widetilde{V}_k \, c_{kS,\sigma}^{\dagger} c_{d\sigma} + h.\, c) + (\widetilde{V}_k \, c_{kD,\sigma}^{\dagger} c_{d\sigma} e^{-i\sigma\phi_{SO}} + h.\, c) \right], \end{split} \tag{6.12}$$

where the phonon-mediated renormalized energy, modified Hubbard strength and the effective QD-lead coupling are respectively defined in Eqs. (5.16), (5.17) and (5.18).

6.2.1 RASHBA INDUCED SPIN-RESOLVED TUNNELING VIA KELDYSH METHOD

Following Refs. [28, 29], the tunneling current from S to D through the QD embedded in the ring can be written as

$$J_{S(D)} = -e \left\langle \frac{dN_{S(D)}}{dt} \right\rangle = -\frac{ie}{\hbar} \left\langle \left[\widetilde{H}, \sum_{k\sigma} c_{kS(D),\sigma}^{\dagger} c_{kS(D),\sigma} \right] \right\rangle, \tag{6.13}$$

where $c_{kS(D),\sigma}(t) = e^{-iHt}c_{kS(D),\sigma}e^{iHt}$ and the averaging is to be done with respect to the actual ground state of the system $|0\rangle$ which is defined as $|0\rangle = |0\rangle_{el}|0\rangle_{ph}$. In the steady state, $J = J_S = -J_D$ and after symmetrizing, we can write the tunneling current as

$$J_{\sigma} = \frac{J_{S} - J_{D}}{2} \equiv \frac{e}{\hbar} \operatorname{Re} \left\{ \sum_{k} \langle \tilde{V}_{k} \rangle G_{d\sigma,kS}^{<}(t,t) - \sum_{k} \langle \tilde{V}_{k}^{\sigma} \rangle G_{d\sigma,kD}^{<}(t,t) \right\}, \quad (6.14)$$

where \tilde{V}_k has been defined earlier, $\tilde{V}_k{}^\sigma = \tilde{V}_k e^{-i\sigma\phi_{SO}}$, $\langle ... \rangle$ denotes the expectation value of ... with respect to nth-phonon state i. e., $\langle \tilde{V}_k \rangle = \langle n | \tilde{V}_k | n \rangle$ and $\langle \tilde{V}_k{}^\sigma \rangle = \langle n | \tilde{V}_k{}^\sigma | n \rangle$ and $G^<_{d\sigma,kS(D)}(t,t')$ and $G^>_{d\sigma,kS(D)}(t,t')$ are respectively the lesser and the greater (tunneling) Keldysh Green functions defined as

$$G_{d\sigma,kS(D)}^{\leq}(t,t') = i\langle 0|c_{kS(D)}^{\dagger}(t')c_{d\sigma}(t)|0\rangle, \tag{6.15}$$

$$G_{d\sigma,kS(D)}^{>}(t,t') = -i\langle 0 | c_{d\sigma}(t') c_{kS(D)}^{\dagger}(t) | 0 \rangle. \tag{6.16}$$

Now, we define the retarded (r) and advanced (a) tunneling Green functions $G_{d\sigma,kS(D)}^{r(a)}(t,t')$ as

$$G_{d\sigma,kS(D)}^{r(a)}\left(t,t'\right) = \mp i\theta(\pm t \mp t')\langle 0 \left| \left\{ \tilde{c}_{d\sigma}(t),c_{kS,\sigma}^{\dagger}(t') \right\} \right| 0 \rangle, \tag{6.17}$$

where $c_{d\sigma}(t) = e^{-i\widetilde{H}_{el}t}c_{d\sigma}e^{i\widetilde{H}_{el}t}$ and $\widetilde{c}_{d\sigma}(t) = \widehat{\chi}\,c_{d\sigma}(t)$, Using the equation of motion of $G^{r(a)}_{d\sigma,kS(D)}(t,t')$ and applying the analytical continuation rule of Langreth, we get the expression for $G^{<}_{d\sigma,kS(D)}(t,t')$ as

$$G_{d\sigma,kS}^{\leq}(t,t') = \int \frac{d\omega}{2\pi} \left[V_k^* + V_k^{\sigma^*} t_{SD} \right] \left[G_{dd}^{\leq}(\omega) g_{kS}^a(\omega) + G_{dd}^r(\omega) g_{kS}^{\leq}(\omega) \right] e^{-i\omega(t-t')}, (6.18)$$

$$G_{d\sigma,kD}^{\leq}(t,t') = \int \frac{d\omega}{2\pi} \left[V_k^{\sigma^*} + V_k^* t_{SD} \right] \left[G_{dd}^{\leq}(\omega) g_{kD}^a(\omega) + G_{dd}^r(\omega) g_{kD}^{\leq}(\omega) \right] e^{-i\omega(t-t')}, (6.19)$$

where $g_{kS(D)}^{r(a)}(\omega)$ and $g_{kS(D)}^{<}(\omega)$ are the lead Green functions in the energy space which are related by Fourier transformation (FT) to the corresponding time-dependent Green functions $g_{kS(D)}^{r(a)}(t,t')$ and $g_{kS(D)}^{<}(t,t')$ defined by

$$g_{kS(D)}^{r(a)}(t,t') = \mp i\theta(\pm t \mp t')\langle 0|\left\{c_{kS(D),\sigma}(t), c_{kS(D),\sigma}^{\dagger}(t')\right\}|0\rangle, \tag{6.20}$$

$$g_{kS(D)}^{\leq}(t,t') = i \left\langle c_{kS(D),\sigma}^{\dagger}(t')c_{kS(D),\sigma}(t) \right\rangle, \tag{6.21}$$

 $G_{dd}^{r(a)}(\omega)$ and $G_{dd}^{<(>)}(\omega)$ are the energy-dependent retarded (advanced) and the Keldysh lesser(greater) Green functions of the QD which can be obtained by Fourier transforming the corresponding time-dependent Green functions $G_{dd}^{r(a)}(t,t')$ and $G_{dd}^{<(>)}(\tau=t-t')$ defined respectively by (5.24), (5.25) and (5.26).

Substituting Eqs. (6.18) and (6.19) together with (6.20) and (6.21) in Eq. (6.14), we get an expression of J_{σ} which after some algebraic manipulations becomes

$$J_{\sigma} = \frac{e}{2h} \Gamma \left[(1 + t_{SD} \cos(\sigma \phi_{SO})) \int \frac{d\omega}{2\pi} \left(f_{S}(\omega) - f_{D}(\omega) \right) A(\omega) \right]$$
$$-t_{SD} \sin(\sigma \phi_{SO}) \int \frac{d\omega}{2\pi} \left(f_{S}(\omega) + f_{D}(\omega) \right) \left(G_{dd}^{r}(\omega) + G_{dd}^{a}(\omega) \right)$$
$$-4t_{SD} \sin(\sigma \phi_{SO}) \int \frac{d\omega}{2\pi} \operatorname{Re} \left\{ G_{dd}^{\leq}(\omega) \right\} \right], \tag{6.22}$$

where $f_{S,D}(\varepsilon) = \left(\exp\left[(\mu_{S,D} - \varepsilon)/k_BT\right] + 1\right)^{-1}$ are the Fermi functions for S and D, $\mu_{S,D}$ being the corresponding chemical potentials which are related through V_b and V_m as: $eV_b = (\mu_S - \mu_D)$, $eV_m = (\mu_S + \mu_D)/2$, $\Gamma = (\Gamma_S + \Gamma_D)/2$, where Γ_S and Γ_D are defined as: $\Gamma_{S,D} = \Gamma = 2\pi\rho_{S,D}\langle \tilde{V}_k \rangle V_k^*$, $\rho_{S,D}$ being the density of states of leads and $A(\omega)$ is the spectral function (SF) of the SMT system which can be calculated by Eq. (5.23). We would like to mention that the derivations of Eqs. (6.18) and (6.19) are made under the assumptions: $\left[g_{kS(D)}^{r(a)}(t,t')\right]^2 \approx g_{kS(D)}^{r(a)}(t,t')$ and $t_{SD} \ll V_k$, so that the terms of order higher than $t_{SD}g_{kS(D)}^{r(a)}$ can be neglected. As we have already mentioned earlier, there exist two different paths for the metallic electrons to tunnel from S to D, one through a QD with SOI and the other directly by hopping from S to D. Thus, the SO phase ϕ_{SO} in Eq. (6.22) is essentially the phase difference between two paths.

To calculate SF $A(\omega)$ and hence spin-resolved current J_{σ} , we need to calculate $G_{dd}^{r(a)}(\omega)$ and $G_{dd}^{<(\gt)}(\omega)$. The derivation of $A(\omega)$ using $G_{dd}^{r(a)}(\omega)$ is not shown here as it is already calculated in detail in Ch.5. We would want the reader to follow Sec. (5.2) from Eqs. (5.34) to (5.45) to see the calculation of $A(\omega)$. To obtain J_{σ} , we also need to calculate $G_{dd}^{<(\gt)}(\omega)$. It is also calculated in Ch.5. One may follow the Eqs. (5.46) to (5.57) to see the calculation of $G_{dd}^{<(\gt)}(\omega)$.

We finally calculate the Rashba induced spin-resolved differential conductance G_{σ} and the spin-polarization $P_{\sigma,-\sigma}$ respectively by Eq. (5.58) and (5.61).

6.3 Numerical results and discussions

In this section, we calculate numerically the spin-resolved tunneling current, conductance and spin-polarization in the presence of e-p interaction, Coulomb interaction and quantum dissipation and show its behaviour as a function of a few tunable parameters. We normalize the energy scale of the system by the phonon-energy, $\hbar\omega_0$. For convenience, we set $\Gamma=0.2$, $eV_g=0$, $m^*=0.036m_e$, $eV_m=0.1$, U=5 and $\varepsilon_d=0$.

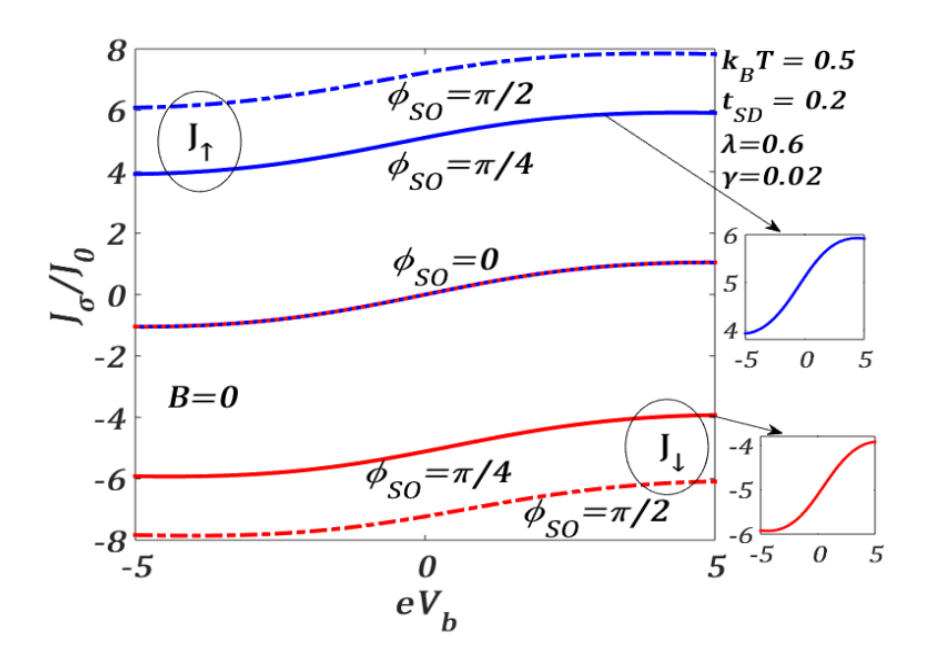


Fig.6.2 Spin-resolved current J_{σ}/J_0 vs. eV_b for different values of ϕ_{SO} for $k_BT=0.5$, $\lambda=0.6, t_{SD}=0.2, \gamma=0.02$ at B=0.

In Fig.6.2, we present the variation of the spin-resolved normalized tunneling current J_{σ} at finite temperature T as a function of the bias voltage V_b for a given set of SMT parameters and different RSOI strengths $\phi_{SO} = \alpha_R \frac{m^*}{h^2} l$. J_{σ} is measured in the units of $J_0 = e/2h$. One can observe that J_{σ} initially increases with increasing V_b in a nonlinear way, then shows an Ohmic nature in the middle region and finally saturates after a certain value of V_b . This can be explained as follows. On application of V_b, the Fermi level of S shifts up and that of the right lead goes down. This causes electrons to enter from the S-lead into QD giving rise to a nonzero tunneling current. But as the QD is able to accommodate only a limited number of electrons, the current gets saturated if V_b is raised beyond a certain value. One may notice that the tunneling is not significant unless V_b is high enough. As mentioned above, for a nonzero V_b , S- and D-Fermi levels shift respectively up and down equally and electrons from S-Fermi level jump into the spin-up (spin-down) level of the QD and then go to the D-Fermi level causing a non-zero spin-up (spin-down) current. So, a substantial strength of the bias voltage is required for this tunnelling to happen. However, the more interesting phenomenon here is the splitting of J_{σ} and $J_{-\sigma}$ for a nonzero value of ϕ_{SO} even at B=0. At $\phi_{SO}\neq 0$, the spin degeneracy is removed due to the RSOI and the single degenerate QD energy level splits

into spin-up and spin-down levels leading to the separation of the spin-up and spin-down currents J_{\uparrow} and J_{\downarrow} . As this separation between J_{\uparrow} and J_{\downarrow} is entirely due to RSOI, the graphs for J_{σ} and $J_{-\sigma}$ obviously merge with each other for $\phi_{SO}=0$ in the absence of B.

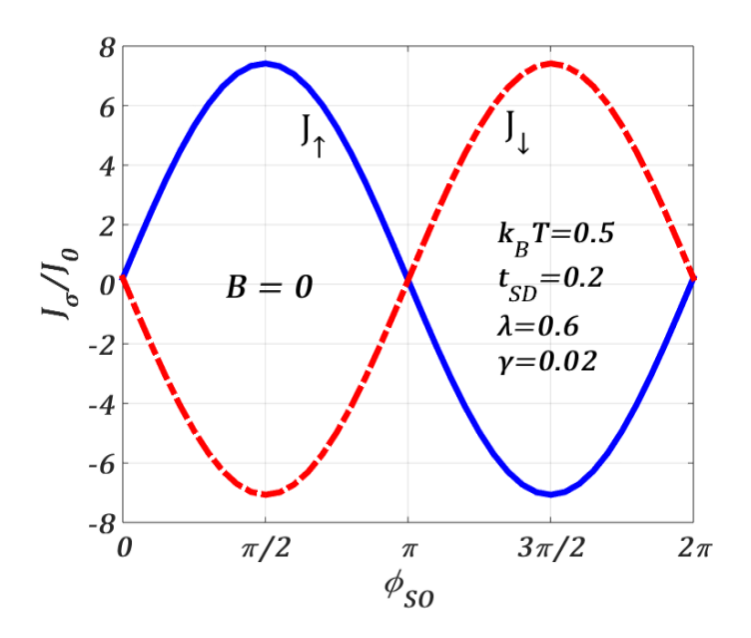


Fig.6.3 Spin-resolved current J_{σ}/J_0 vs. ϕ_{SO} for $k_BT = 0.5$, $\lambda = 0.6$, $t_{SD} = 0.2$, $\gamma = 0.02$, $eV_b = 0.5$ at B = 0.

To study the SOI-induced splitting more specifically, we plot J_{\uparrow} and J_{\downarrow} , in Fig.6.3, as a function of ϕ_{SO} at B=0 and $T\neq 0$. The periodic behaviour with a period 2π is clearly visible. At $\phi_{SO}=0$, J_{\uparrow} is zero and as ϕ_{SO} increases, J_{\uparrow} also increases and exhibits a maximum at $\phi_{SO}=\pi/2$, and then it continues to decrease with further increase in ϕ_{SO} and shows a minimum at $\phi_{SO}=3\pi/2$ after which it again rises and becomes zero at $\phi_{SO}=2\pi$. Though both J_{\uparrow} and J_{\downarrow} have the same period 2π , they have the opposite phase. This gives an interesting crossing behaviour in the J_{\uparrow} and J_{\downarrow} - curves. The crossing occurs at those values of ϕ_{SO} that are even multiples of $\pi/2$. Obviously, the phase difference between J_{\uparrow} and J_{\downarrow} in the case of B=0, is caused entirely due to the RSOI. It is important to mention that the spin gap $(J_{\uparrow}-J_{\downarrow})$ can be controlled by varying the RSOI parameter α_R which can be accomplished by tuning the gate voltage. The spin gap shows maxima at odd-integral multiple values of ϕ_{SO} and vanishes at even integral values of ϕ_{SO} including zero.

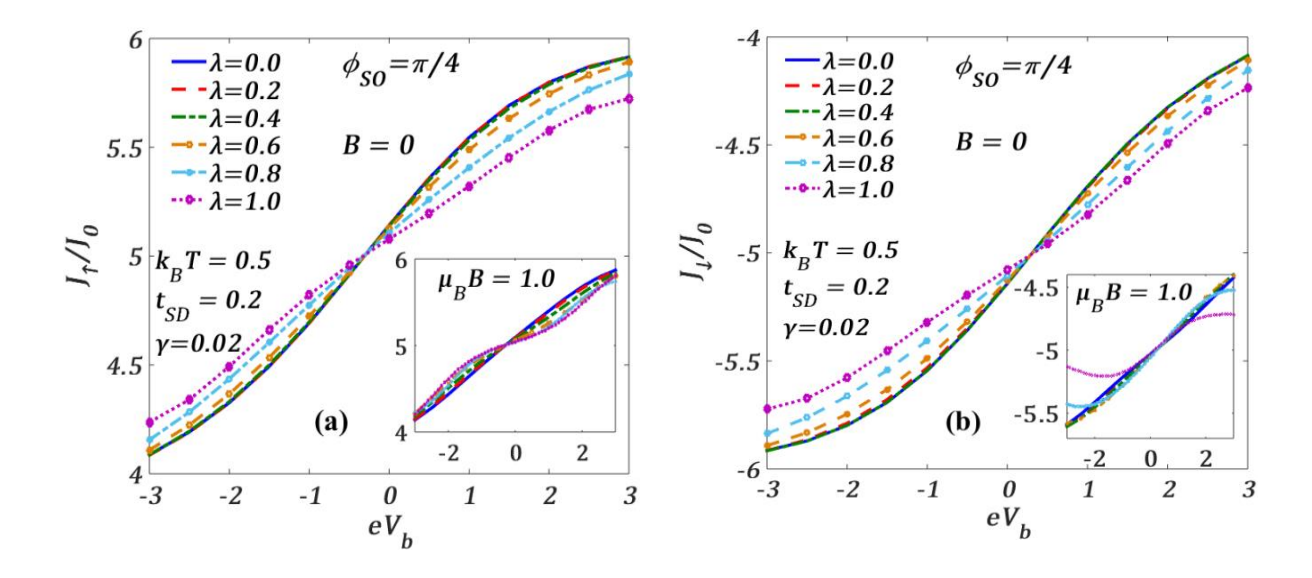


Fig.6.4 (a) J_{\uparrow}/J_0 and (b) J_{\downarrow}/J_0 vs. eV_b for different values of λ at a fixed ϕ_{SO} for $k_BT=0.5$ and B=0. Insets at $\mu_BB=1.0$.

In Fig.6.4, we plot J_{\uparrow} and J_{\downarrow} with respect to V_b for different values of λ at a finite T to see the effect of e-p interaction on J_{\uparrow} and J_{\downarrow} in the presence of RSOI. Fig.6.4(a) shows the behaviour of J_{\uparrow} while Fig.6.4(b) presents the behaviour of J_{\downarrow} . One may notice that for a given ϕ_{SO} , the qualitative behaviour of J_{\uparrow} and J_{\downarrow} is similar at B=0. Both J_{\uparrow} and J_{\downarrow} decrease with increasing λ for positive V_b . This can be understood from the mechanism of polaron formation which impedes the flow of the tunneling of conduction electrons. In the insets we show the variations at $\mu_B B=1.0$. These figures show that the qualitative variations of J_{\uparrow} and J_{\downarrow} at a finite value of the magnetic field are different, particularly for higher values of λ . This implies that, in the presence of a magnetic field, the effect of RSOI on J_{\uparrow} and J_{\downarrow} is qualitatively different. This can be explained from Eq. 20, which shows that the effective dotenergy $\tilde{\varepsilon}_{d\sigma}$ is different for spin-up and spin-down electrons. The expression of $\tilde{\varepsilon}_{d\sigma}$ also shows that for the spin-down electrons, there exists a competition between the polaronic energy and the magnetic energy, whereas no such competition exists for the spin-up electrons. One may also observe that the changes in current densities in the presence of magnetic field for lower values of λ are minimal for the chosen set of parameters.

Fig.6.5 describes the effect of quantum dissipation (parameterized by γ) on spin current densities in the presence of ϕ_{SO} at a finite value of T. It is evident that for positive V_b , J_{\uparrow} and J_{\downarrow} increase as γ increases. This can be explained as follows. The coupling of the bath phonons with the QD phonon reduces the frequency of the phonon ω_0 to $\widetilde{\omega}_0 = (\omega_0^2 - \Delta \omega^2)^{1/2}$ which apparently means that the QD lattice mode undergoes a frictional effect which is precisely the effect of dissipation. This effect reduces the e-p interaction and consequently increases the

tunneling current. Here, again the insets suggest that at finite B, the variations of J_{\uparrow} and J_{\downarrow} with γ are different, though γ enhances both J_{\uparrow} and J_{\downarrow} . At $B \neq 0$, the variations of J_{\downarrow} are much more prominent than those of J_{\uparrow} .

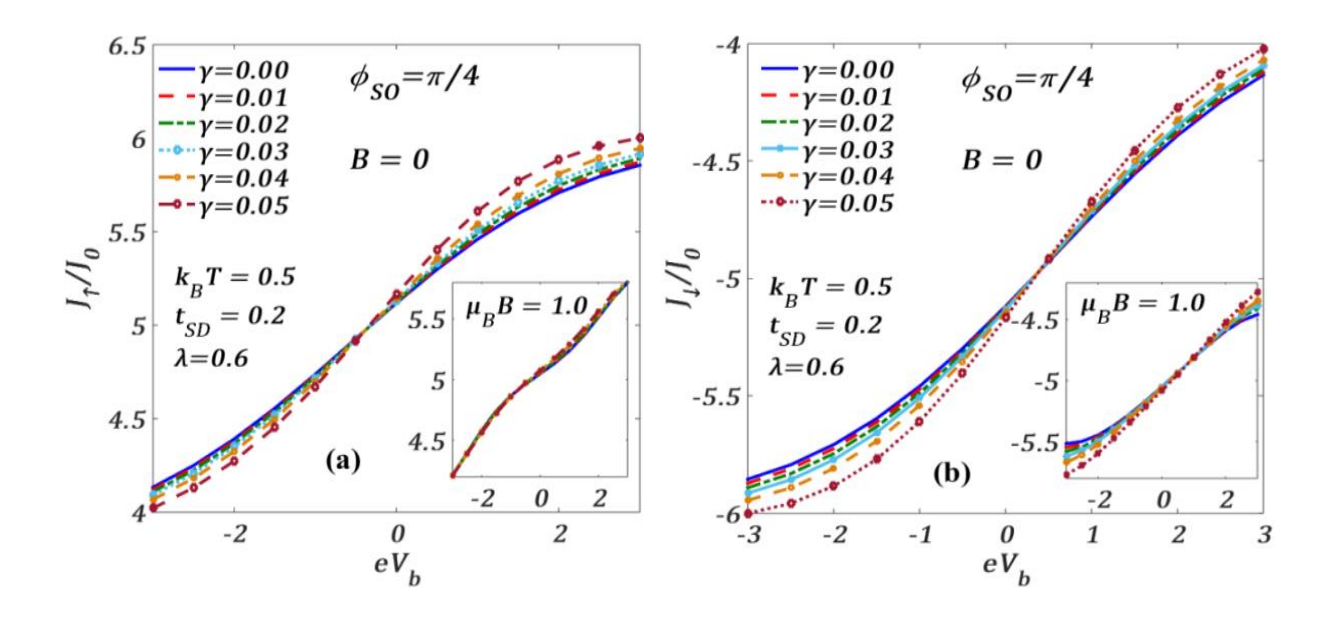


Fig.6.5 (a) J_{\uparrow}/J_0 and (b) J_{\downarrow}/J_0 vs. eV_b for different values of γ at a fixed ϕ_{SO} for $k_BT=0.5$ and B=0. Insets at $\mu_BB=1.0$.

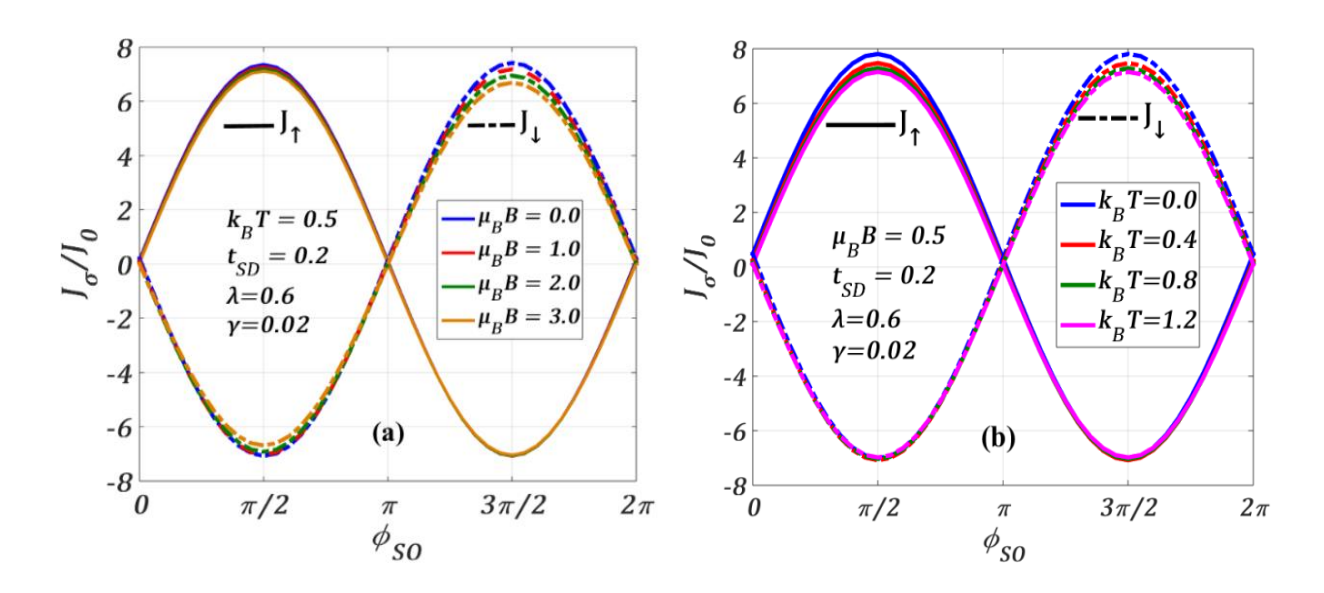


Fig.6.6 Spin-resolved current J_{σ}/J_0 vs. ϕ_{SO} at $\lambda=0.6$, $t_{SD}=0.2$, $\gamma=0.02$, $eV_b=0.5$ for different values of : (a) B at $k_BT=0.5$; (b) T at $\mu_BB=0.5$.

In Fig.6.6, we study how J_{σ} changes with ϕ_{SO} at different values of the magnetic field and temperature in a particular window of the SMT parameters. In Fig.6.6(a), we present the effect of the magnetic field and in Fig.6.6(b) the effect of temperature. We observe that, in

general, J_{σ} reduces with the increase in both T and B. From Fig.6.6(a), we see that though the change in J_{\uparrow} with B is only marginal, J_{\downarrow} exhibits a visible change with B, especially for higher values of SO coupling (for $\pi \le \phi_{SO} \le 2\pi$). This again suggests that because of the magnetic field, SOI effects in J_{\uparrow} and J_{\downarrow} become different. Mathematically, Eq. (35) shows that the change in J_{σ} is mostly dependent on $\tilde{G}_{dd}^{r(a)}$ and the denominator for J_{\uparrow} ($\sigma=+1$) is greater than that of J_{\downarrow} ($\sigma = -1$) for a given set of parameters. This makes the gap between the J_{\downarrow} curves for two values of B larger than that of the corresponding J_{\uparrow} curves. Thus, the localizing effect of B is stronger in the case of J_{\downarrow} than in the case of J_{\uparrow} . We can explain the reduction in the current densities with increasing B in the following way. The presence of Bgives rise to an additional spitting of the QD's energy level, the spin-down level rising up and the spin-up level shifting down. As B increases, the splitting also increases and for a given ϕ_{SO} , it may so happen that the rise in the spin-down level becomes more than the downshift in the spin-up level. This can cause a large mismatch between the S-Fermi level of the source and the spin-down of the QD giving rising to a lesser probability of S-electrons to tunnel and consequently J_{\downarrow} decreases with increasing field. Fig.6.6(b) shows the variation of J_{σ} with T. As the phonon excitations increase with increasing T, J_{σ} reduces as T increases, but unlike in the case of Fig.6.6(a), here J_{\uparrow} and J_{\downarrow} will be affected equally at a particular temperature.

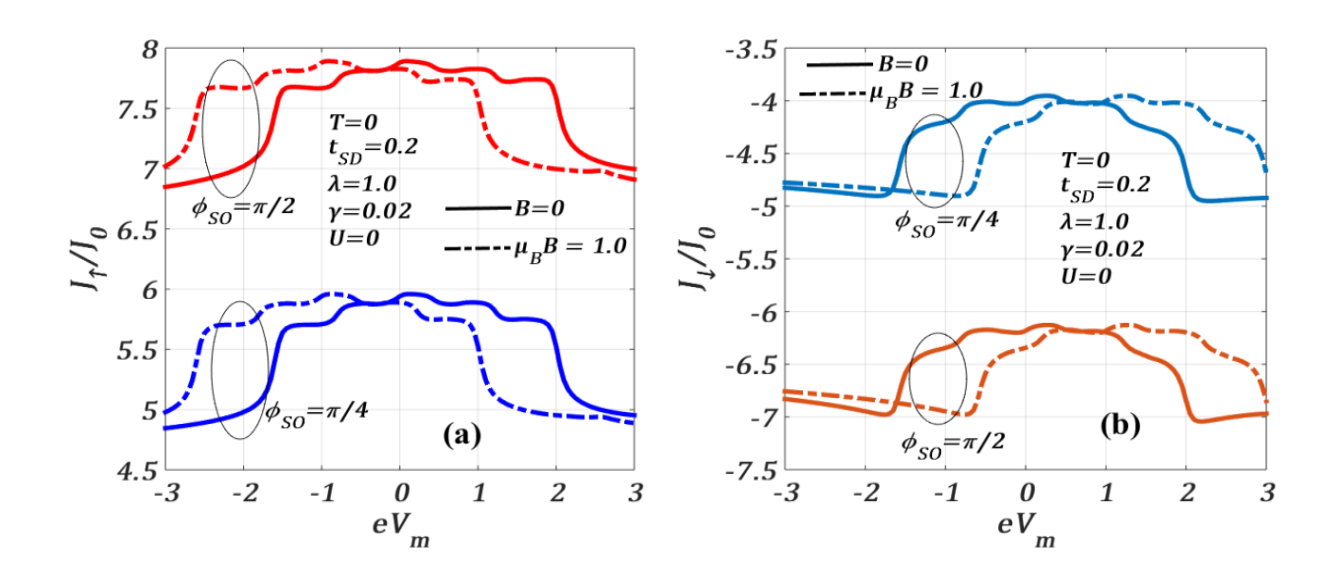


Fig.6.7 (a) J_{\uparrow}/J_0 and (b) J_{\downarrow}/J_0 vs. eV_m for different ϕ_{SO} at $T=0, \lambda=1.0, U=0, \gamma=0.02, eV_b=3.6$ for B=0 and $B\neq 0$.

In Fig.6.7, we study the variation of J_{σ} with respect to the mid-voltage V_m both for B=0 and $B \neq 0$ at T=0. One can notice that J_{σ} exhibits multiple plateaus and shows a maximum around $V_b=0$. Chen et al. [30] have studied this variation at zero temperature for $\lambda=0$ and

 $\lambda=1$ in the absence of a magnetic field, Coulomb correlation, SOI and dissipation and have obtained plateaus in the current density for $\lambda=1$. We observe similar plateaus in the presence of SOI and dissipation, although the value of the current density is much larger in our case. The figures also suggest that the current at $\phi_{SO}=\pi/2$ is larger than that at $\phi_{SO}=\pi/4$. Interestingly, at non-zero B, J_{\uparrow} undergoes a rigid shift towards left on the V_m axis while J_{\downarrow} shifts towards right.

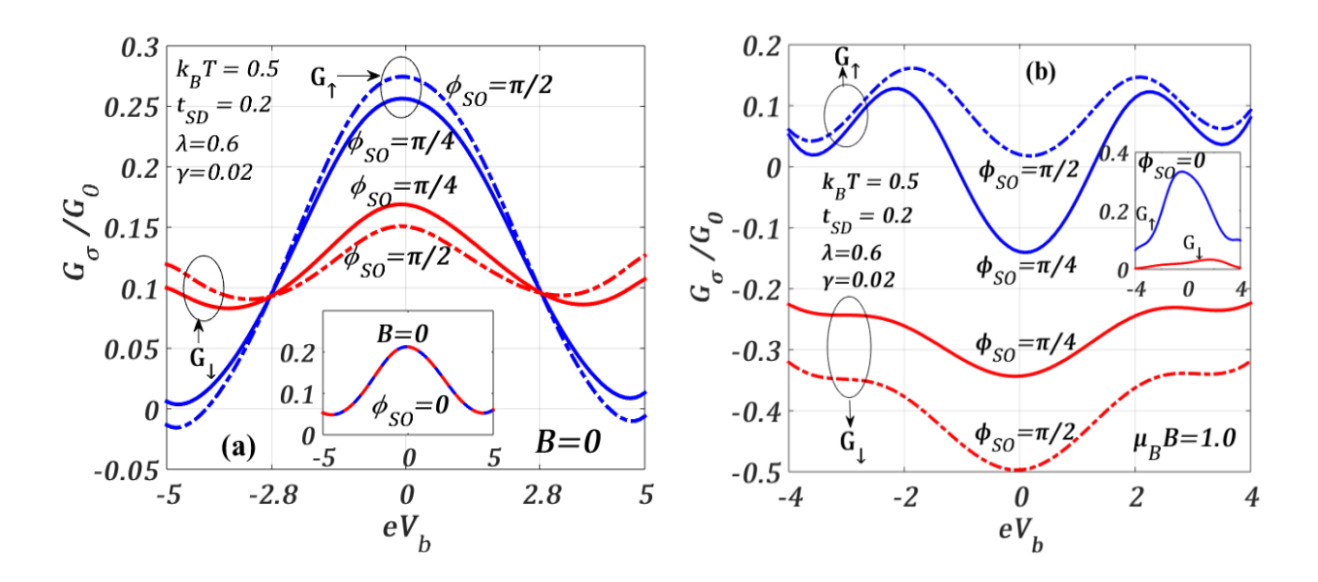


Fig.6.8 Spin-resolved differential conductance G_{σ}/G_0 vs. eV_b for different values of ϕ_{SO} at $k_BT=0.5$ (a) B=0, (b) $\mu_BB=1.0$.

Next, we numerically calculate the differential conductance in the presence of e-p interaction, Coulomb correlation and quantum dissipation. The conductance is calculated in units of $G_0 = e^2/2h$.

We investigate in Figs.6.8, the behaviour of the spin-resolved differential conductance G_{σ} as a function of the bias voltage V_b for different values of ϕ_{SO} and a set of SMT parameters both in the absence and presence of a magnetic field B. Fig.6.8(a) provides the results for B=0 while Fig.6.8(b) gives the results for $B\neq 0$. Fig.6.8(a) shows that variation of G_{σ} with V_b is Gaussian-like with a maximum $(G_{\sigma,max})$ at $V_b=0$. The variation is also symmetric with respect to $V_b=0$. As expected, G_{σ} splits into G_{\uparrow} and G_{\downarrow} as we switch on ϕ_{SO} at B=0. The solid lines describe the variations for $\phi_{SO}=\pi/4$ and the dotted lines for $\phi_{SO}=\pi/2$. The peak height of G_{\uparrow} is greater than that of G_{\downarrow} . It can be seen that for $|V_b| < 2.8$, $G_{\uparrow}(G_{\downarrow})$ is larger (smaller) for $\phi_{SO}=\pi/2$ than for $\phi_{SO}=\pi/4$, but for $|V_b| > 2.8$, the situation reverses. G_{\uparrow} and G_{\downarrow} cross each other at $V_b=\pm 2.8$. The inset shows no splitting at $\phi_{SO}=0$ which implies $G_{\uparrow}=G_{\downarrow}$ in this case. Fig.6.8(b) shows that the variations are a little different in the presence of a magnetic field. Interestingly, the graphs now exhibit a central minimum at

 $V_b=0$ with two more minima, one on each side of $V_b=0$, placed symmetrically at higher value of $|eV_b|$. The curves for G_\uparrow and G_\downarrow do not cross each other at any value of the bias voltage. It is clearly evident that the gap between the G_\uparrow and G_\downarrow - curves increase as ϕ_{SO} is changed from $\pi/4$ to $\pi/2$. The gap between $\phi_{SO}=\pi/2$ and $\phi_{SO}=\pi/4$ curves also increases in the case of $B\neq 0$. As mentioned earlier, this splitting between G_\uparrow and G_\downarrow caused by ϕ_{SO} can be manipulated by tuning the gate voltage which alters $\phi_{SO}(\propto \alpha_R)$. The inset shows that in the case of $\phi_{SO}=0$, splitting still occurs due to the magnetic field.

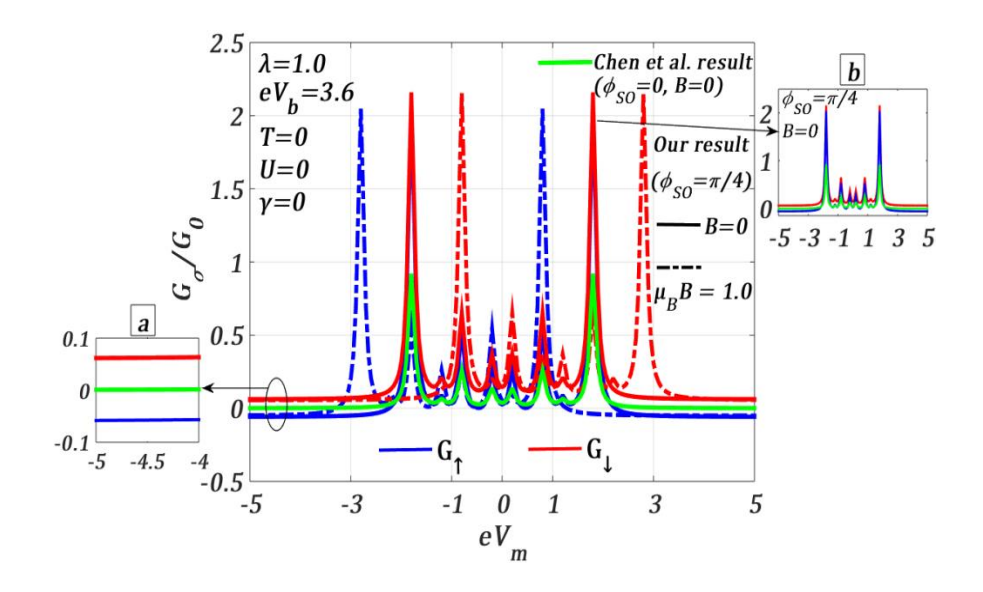


Fig.6.9 Spin-resolved differential conductance G_{σ}/G_0 vs. eV_m for $\phi_{SO} = \pi/4$ at $T = U = \gamma = 0$, $\lambda = 1.0$, $eV_b = 3.6$ for B = 0 and $B \neq 0$: comparison with the Chen et al. [30] result.

In Fig.6.9, we study the behaviour of the differential conductance G_{σ} as a function of midvoltage V_m in the presence of RSOI ϕ_{SO} for both B=0 and $B\neq 0$ with $\lambda=1.0$. We also compare our results with those of Chen et al. [30] who have studied the same in the absence of RSOI and magnetic field. They have observed a few satellite peaks in the conductance along with two zero-phonon peaks (taller peaks) symmetrically distributed (solid light green curve at $B=\phi_{SO}=0$) with respect to $V_m=0$ and suggested that these satellite peaks occur because of the phonon-assisted tunnelling. We like to see the effects of the RSOI and magnetic field on G_{σ} for the same parameter values considered by Chen et al. In the presence of RSOI ($\phi_{SO}=\pi/4$) alone, it can be clearly seen that the solid light green curve splits into two curves (shown in the inset (a)) corresponding to the up-spin (G_{\uparrow} , solid blue) and downspin (G_{\downarrow} , solid red) spin-resolved conductances respectively. One can also see that the zero-phonon peaks and the satellite peaks generated by the e-p interaction are symmetric with respect to $V_m=0$. We would like to mention that the conductance peak heights increase and

become sharper in the presence of RSOI, although the zero-phonon up and down-spin peaks merge at a particular V_m . The inset (b) shows that the G_{\downarrow} - peaks (solid blue) are higher than the G_{\uparrow} - peaks (solid blue). As we turn on B ($\mu_B B = 1.0$) in addition to RSOI, G_{\uparrow} undergoes a rigid shift towards left and G_{\downarrow} towards right equally and as a result the zero-phonon up-spin (dashed blue curve) and down-spin (dashed red curve) conductance peaks split, though the heights of the peaks remain the same as in the case of B = 0. Thus, the RSOI enhances the phonon-assisted conductance by increasing the peak heights and the magnetic field splits the peaks. This signature of the peak pattern in spin-resolved conductances can also be understood from Fig.6.7, where one can see the boundary lines before and after the plateaus associated with the phonon-mediated conductance peaks. The left-right shift at $B \neq 0$ can also be seen in Fig.6.7. Here we have shown results in the absence of quantum dissipation. Similar studies can also be carried out in the presence of dissipation.

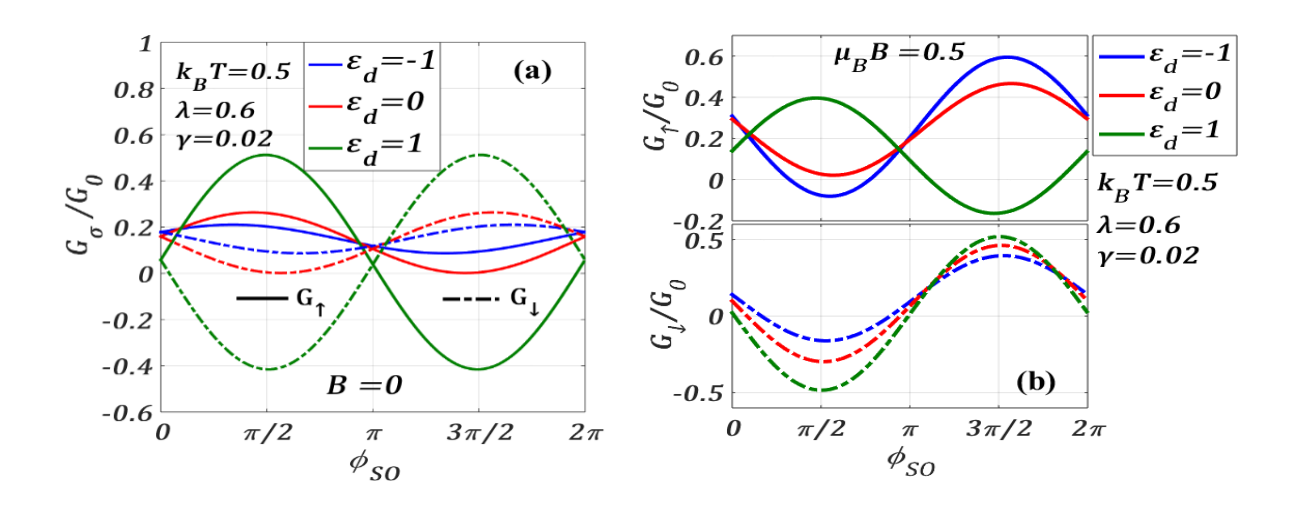
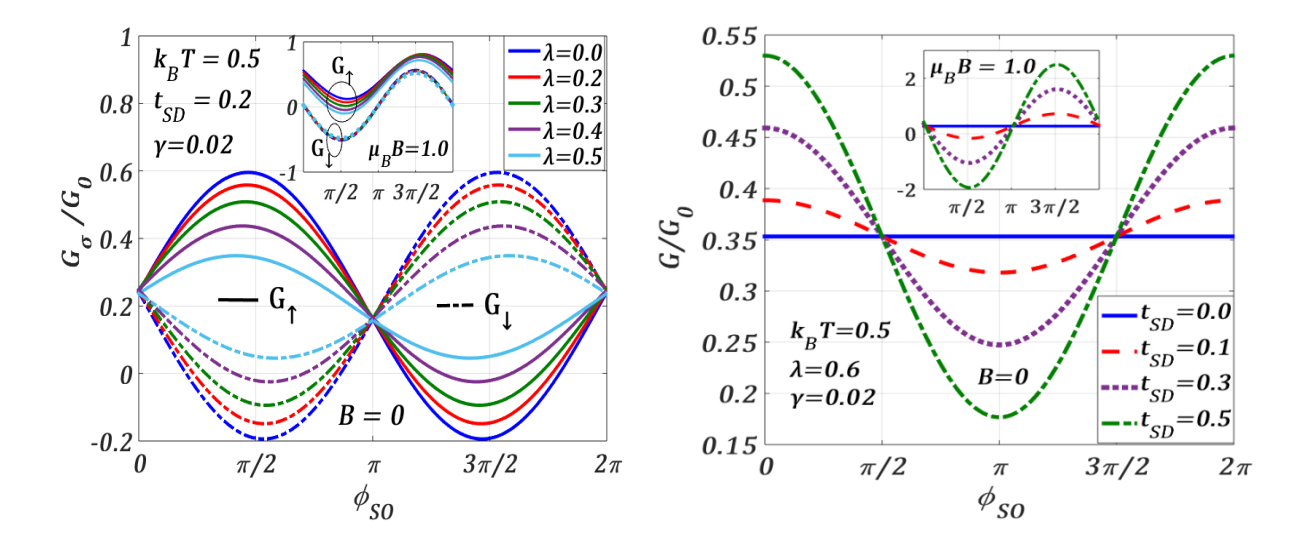


Fig.6.10 (a) Spin-resolved differential conductance G_{σ}/G_0 vs. ϕ_{SO} for different values of dot energy ε_d at $\lambda=0.6, t_{SD}=0.2, \gamma=0.02, eV_b=0.5$ (a) for B=0 (b) $\mu_B B=0.5$.

Fig.6.10 displays the nature of G_{σ} with respect to ϕ_{SO} for different values of dot energy. Fig.6.10(a) provides results for B=0 and Fig.6.10(b) gives results for non-zero values of B. From Fig.6.10(a), we see that the variation of G_{σ} with ϕ_{SO} is 2π -periodic, though G_{\uparrow} and G_{\downarrow} are out of phase by π in conformity with the plots of J_{σ} vs ϕ_{SO} shown in Figs.6.3 and 6.6. As the dot energy ε_d can be varied by tuning the gate voltage V_g , we consider three values of ε_d namely, $\varepsilon_d=-1$, $\varepsilon_d=0$ and $\varepsilon_d=1$. It is clear from Fig.6.10(a) that as ε_d increases, G_{\uparrow} increases in the range, $0 \le \phi_{SO} \le \pi$, and decreases in the range, $\pi \le \phi_{SO} \le 2\pi$, and shows extrema at $\phi_{SO}=p\pi/2$, p=0,1,2,.... The behaviour of G_{\downarrow} with ε_d is just the opposite to that of G_{\uparrow} versus ε_d and can be obtained from the results of G_{\uparrow} by giving a π shift. The quantitative difference between the results of G_{\uparrow} and G_{\downarrow} is particularly significant for positive

 ε_d . One can see in Fig.6.10(b) that in the case of $B \neq 0$, G_{\uparrow} and G_{\downarrow} behave differently from those at B=0 and the constant phase correlation between G_{\uparrow} and G_{\downarrow} is absent except for the case of $\varepsilon_d = 1$, where again G_{\uparrow} and G_{\downarrow} as a function of ϕ_{SO} have a phase difference of π .



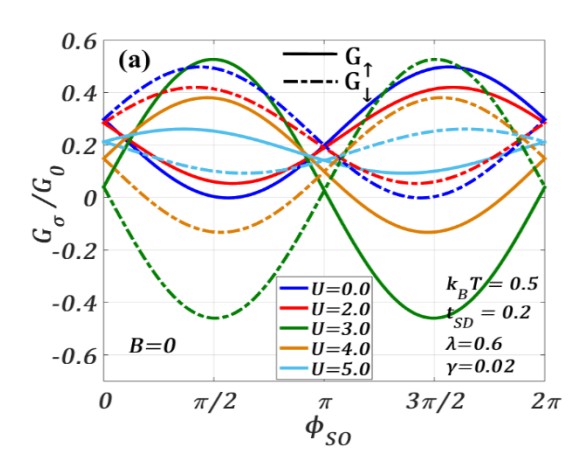
B = 0. Inset: at $\mu_B B = 0.5$.

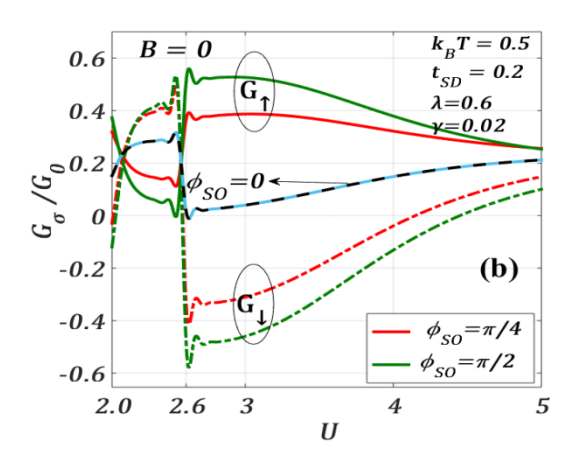
Fig.6.11 G_{σ}/G_0 vs. ϕ_{SO} for different λ values at **Fig.6.12** Total G vs. ϕ_{SO} for different t_{SD} values at $k_BT = 0.5$ $t_{SD} = 0.2, \gamma = 0.02, eV_b = 0.5$ for $k_BT = 0.5, \lambda = 0.6, \gamma = 0.02, eV_b = 0.5$ for $B = 0.5, \lambda = 0.6, \gamma = 0.02, eV_b = 0.5$ 0. Inset: at $\mu_B B = 1.0$.

To study the effects of polaronic interaction on spin-resolved conductance G_{σ} , we plot, in Fig.6.11, G_{σ} as a function of ϕ_{SO} for different values of e-p interaction strength λ at B=0for a given set of SMT parameters. As discussed above, G_{\uparrow} and G_{\downarrow} as a function of ϕ_{SO} are opposite in phase. For $0 \le \phi_{SO} \le \pi$, the peak-height of G_{\uparrow} decreases with increasing λ while that of G_{\downarrow} increases. The behaviour becomes just opposite in the region: $\pi \leq \phi_{SO} \leq 2\pi$. Thus, the e-p interaction which induces the formation of polarons, does not always reduce G_{σ} , rather the effect of e-p interaction also depends on the strength of ϕ_{SO} . This implies that there exists an interesting interplay between the Rashba and e-p interactions that has a significant and decisive effect on the transport process. The inset shows the variations at a finite B where the phase correlation between G_{\uparrow} and G_{\downarrow} disappears and the variations of G_{\uparrow} and G_{\downarrow} with respect to ϕ_{SO} become very different. As a magnetic field is switched on, the maxima and minima in G_{\uparrow} as a function of ϕ_{SO} exchange their positions. Interestingly, at $B \neq 0$, G_{\uparrow} always decreases with increasing λ , though the rate of decrease changes as ϕ_{SO} increases. However, the variation of G_{\downarrow} does not change much for the set of parameters used in this work. This can again be understood from the fact that in J_{\downarrow} , there exists a competition between the magnetic and polaronic energies which is however absent in J_{\uparrow} . As a result, J_{\uparrow} varies monotonically with λ for a given value of B, whereas for the same value of B, J_{\downarrow} may

not change much with λ and consequently, the variations of G_{\uparrow} and G_{\downarrow} become different. We wish to mention that as we turn on the magnetic field, one can see a clear separation between G_{\uparrow} and G_{\downarrow} curves vertically like the Zeeman splitting for a given ϕ_{SO} which can, of course, be tuneable. This can also be observed in Figs. 6.8(b) and 6.10(b).

As the SOI phase contains the hopping parameter t_{SD} , it would be interesting to study the behaviour of the total conductance $G(=\sum_{\sigma}dJ_{\sigma}/dV_{b})$ as a function of ϕ_{SO} for different values of t_{SD} . The results are presented in Fig.6.12. Let us first describe the results for B=0. The figure shows that for $t_{SD}=0$, G is independent of ϕ_{SO} . At a finite value of t_{SD} , as ϕ_{SO} increases from zero, G initially decreases, then forms a minimum at $\phi_{SO} = \pi$ and finally increases with the further increase in ϕ_{SO} . It is clear from the plot that G increases with increasing t_{SD} for $0 \le \phi_{SO} \le \pi/2$ and $3\pi/2 \le \phi_{SO} \le 2\pi$, while in the window $\pi/2 \le \pi/2$ $\phi_{SO} \leq 3\pi/2$, it decreases as t_{SD} increases. In the inset, we show the variations at $B \neq 0$, where one can notice that G reduces with increasing t_{SD} in the region $0 \le \phi_{SO} \le \pi$, while it decreases with t_{SD} in the other half i.e., in the region $\pi \le \phi_{SO} \le 2\pi$. Interestingly, for $t_{SD} =$ 0, G remains zero over the entire range of ϕ_{SO} .





 $0.6, eV_b = 0.5 \text{ for } B = 0.$

Fig.6.13 G_{σ}/G_0 vs. ϕ_{SO} for different U values **Fig.6.14** G_{σ}/G_0 vs. U for different ϕ_{SO} values at $k_BT = 0.5 \quad , \quad t_{SD} = 0.2, \\ \gamma = 0.02, \\ \lambda = \quad k_BT = 0.5 \quad , \quad t_{SD} = 0.2, \\ \gamma = 0.02, \\ \lambda = 0.6, \\ eV_b = 0.02, \\ \lambda = 0.02, \\ \lambda$ 0.5 for B = 0.

Fig.6.13 displays the variation of spin-polarized conductance G_{σ} with ϕ_{SO} for different values of U at B = 0. G_{σ} exhibits an interesting behaviour with respect to U. For U = 0 and 2, G_{\uparrow} has a minimum at around $\phi_{SO} = \pi/2$ and a maximum at around $\phi_{SO} = 3\pi/2$. However, for U > 2, G_{\uparrow} changes its phase by around π , showing maximum and minimum at $\phi_{SO} = \pi/2$ and $\phi_{SO} = 3\pi/2$ respectively. It is interesting to see that G_{\downarrow} and G_{\uparrow} are opposite in phase with respect to ϕ_{SO} for all values of U. Thus, there exists a critical value of U at which the phase of G_{σ} reverses with respect to ϕ_{SO} . To explore this critical behaviour, we plot G_{σ} as a function of U for different values of ϕ_{SO} at B=0 in Fig.6.14. As our main interest is to locate the transition point, we consider only a particular window of ϕ_{SO} . In particular, we choose $\phi_{SO}=0$, $\pi/4$ and $\pi/2$. One can clearly see that for both $\phi_{SO}=\pi/4$ and $\pi/2$, G_{\uparrow} and G_{\downarrow} have an inverted behaviour as a function of U. For $\phi_{SO}=0$, we find $G_{\uparrow}=G_{\downarrow}$ which is, of course, an expected result. At around $U_c=2.6$, G_{σ} has a discontinuity with respect to U and with respect to ϕ_{SO} , its sign reverses. To understand the discontinuity, we consider the second derivative of J_{σ} with respect to ϕ_{SO} .

$$\frac{\partial^2 J_{\uparrow}}{\partial \phi_{SO}^2} = \mathcal{F}_1(\phi_{SO})\mathcal{G}_1(\phi_{SO}, U) + \{\mathcal{F}_2(\phi_{SO})\mathcal{G}_2(\phi_{SO}, U) + \mathcal{F}_3(\phi_{SO})\mathcal{G}_3(\phi_{SO}, U)\},$$

$$\frac{\partial^2 J_{\downarrow}}{\partial \phi_{SO}^2} = \mathcal{F}_1(\phi_{SO})\mathcal{G}_1(\phi_{SO}, U) - \{\mathcal{F}_2(\phi_{SO})\mathcal{G}_2(\phi_{SO}, U) + \mathcal{F}_3(\phi_{SO})\mathcal{G}_3(\phi_{SO}, U)\},$$

where \mathcal{F}' s are periodic functions of ϕ_{SO} and \mathcal{G}' s are functions of Green's functions. It may be noted that the Green functions appearing in the above equations change sign at a critical value of $U(U_c)$ causing an overall change in both $\partial^2 J_{\uparrow}/\partial \phi_{SO}^2$ and $\partial^2 J_{\downarrow}/\partial \phi_{SO}^2$ at $U=U_c$. Also, at $U=U_c$, the positions of maxima and minima of J_{\uparrow} and J_{\downarrow} (with respect to ϕ_{SO}) interchange. Hence, the gap between J_{\uparrow} and J_{\downarrow} at $U=U_c$, becomes maximum. As G_{σ} is directly related to J_{σ} , the interchange of maxima and minima of J_{\uparrow} and J_{\downarrow} causes a discontinuity at U_c in the G_{σ} -spectrum.

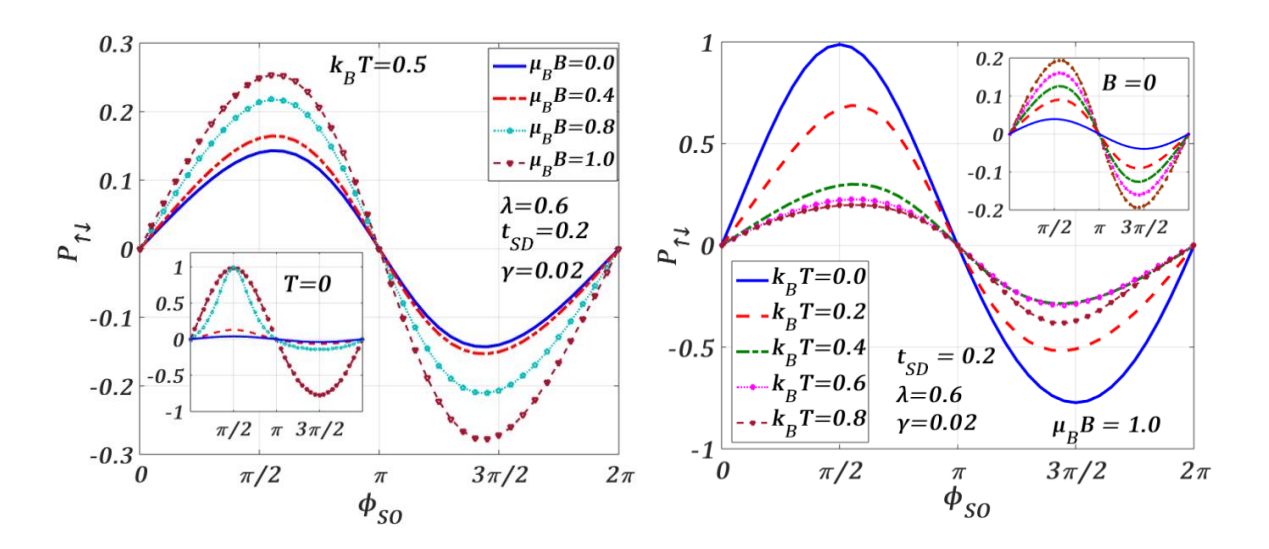


Fig.6.15 Spin-polarization $P_{\uparrow,\downarrow}$ vs. ϕ_{SO} for different $\mu_B B$ values for $\lambda = 0.6, t_{SD} = 0.2, \gamma = 0.02, eV_b = 0.5$ at $k_B T = 0.5$. Inset: at T = 0.

Fig.6.16 Spin-polarization $P_{\uparrow,\downarrow}$ vs. ϕ_{SO} for different k_BT values for $\lambda=0.6, t_{SD}=0.2, \gamma=0.02, eV_b=0.5$ at $\mu_BB=1.0$. Inset: at B=0.

We study in this section the behaviour of the spin-polarization $P_{\uparrow,\downarrow}$ (defined in Eq. 61) of a dissipative SMT system at finite temperature as a function of ϕ_{SO} in the presence of a magnetic field, e-p interaction, Coulomb correlation and quantum dissipation. $P_{\uparrow,\downarrow}$ gives a measure of the spin-filtering effect that originates owing to the RSOI.

Fig.6.15 describes the behaviour of $P_{\uparrow,\downarrow}$ as a function of ϕ_{SO} for different values of B with =0.6, $t_{SD}=0.2$, $\gamma=0.02$, $eV_b=0.5$, $k_BT=0.5$. $P_{\uparrow,\downarrow}$ shows a 2π -periodic pattern. $P_{\uparrow,\downarrow}$ is positive in the region, $0 \le \phi_{SO} \le \pi$ and negative in the region, $\pi \le \phi_{SO} \le 2\pi$ and is zero at $\phi_{SO}=0$, π and 2π . Furthermore, $|P_{\uparrow,\downarrow}|$ increases as magnetic field increases. Thus, the magnetic field favours spin-polarization. Also, the spin-polarization can be tuned by varying the strength of RSOI. At T=0 (see the inset), in the absence of the magnetic field, $P_{\uparrow,\downarrow}$ remains essentially constant with ϕ_{SO} . As B increases, however, $P_{\uparrow,\downarrow}$ does show a significant variation with ϕ_{SO} . The behaviour is again periodic, $P_{\uparrow,\downarrow}$ exhibiting a maximum at $\phi_{SO}=\pi/2$ ($P_{\uparrow,\downarrow,max}=1$ at $\mu_BB=1$) and a minimum at $\phi_{SO}=3\pi/2$ ($P_{\uparrow,\downarrow,min}=-1$ approximately at $\mu_BB=1$). Therefore, it is possible to achieve a fully-polarized spin transport at T=0 with the help of a sufficiently high field. Once the maximum polarization is achieved at a particular ϕ_{SO} , one can experimentally determine α_R for a given set of SMT parameters.

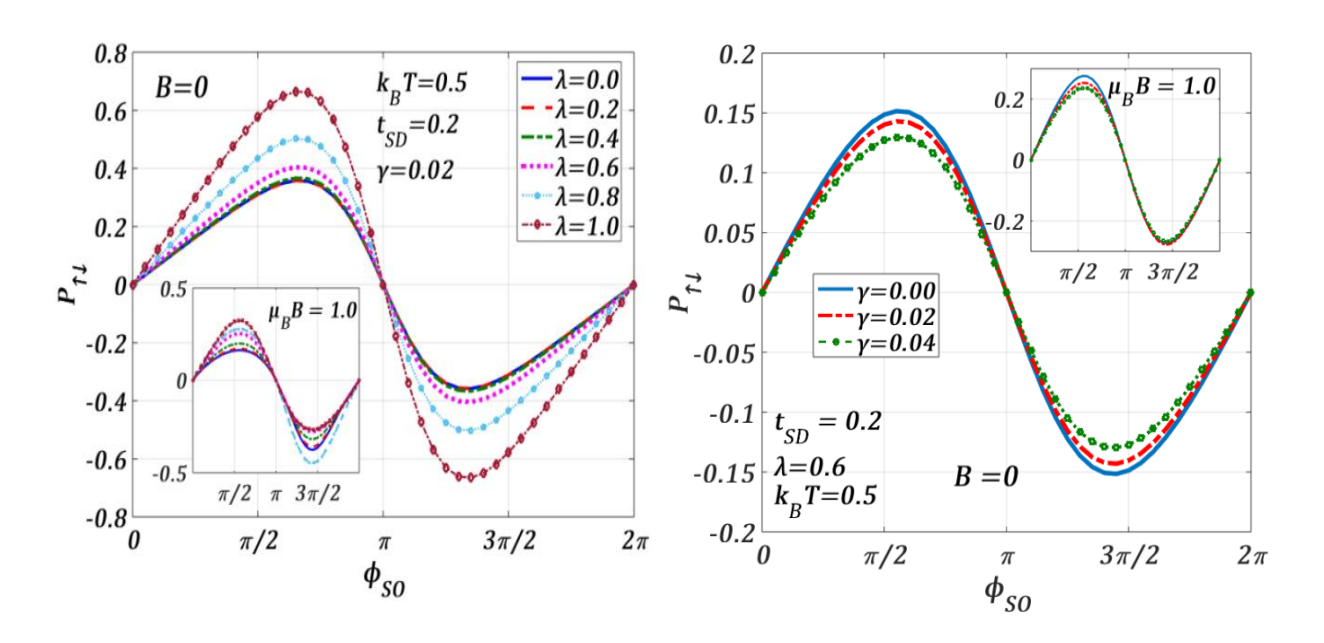


Fig.6.17 Spin-polarization $P_{\uparrow,\downarrow}$ vs. ϕ_{SO} for **Fig.6.18** Spin-polarization $P_{\uparrow,\downarrow}$ vs. ϕ_{SO} for different λ values at $k_BT=0.5$ $t_{SD}=0.2, \gamma=0.02, eV_b=0.5$ for B=0. Inset: at $\mu_BB=1.0$. 0.6, $eV_b=0.5$ for B=0. Inset: at $\mu_BB=1.0$.

In Fig.6.16, $P_{\uparrow,\downarrow}$ is varied with ϕ_{SO} at a finite magnetic field in the regions $0 \le \phi_{SO} \le \pi$ and $\pi \le \phi_{SO} \le 2\pi$ for different temperature values. In the region, $0 \le \phi_{SO} \le \pi$, the

polarization decreases with increasing temperature, while in the region $\pi \le \phi_{SO} \le 2\pi$, the magnitude of $P_{\uparrow,\downarrow}$ decreases with increasing T except for $k_BT=0.8$. Hence, a non-zero magnetic field can make the $P_{\uparrow,\downarrow}$ variations non-monotonic with respect to T for different ϕ_{SO} . The inset show the plots for B=0. It is clear that, with respect to ϕ_{SO} , $|P_{\uparrow,\downarrow}|$ has a 2π -periodic variation for different values of T and the behaviour is perfectly antisymmetric around $\phi_{SO}=\pi$. Interestingly, in contrast to $B\neq 0$, at B=0, temperature enhances $|P_{\uparrow,\downarrow}|$, though the values of $|P_{\uparrow,\downarrow}|$ are less than those at B. One may notice from the inset that $P_{\uparrow,\downarrow}=1$ cannot be achieved even at T=0 in the absence of the magnetic field. So, both the conditions of: $B\neq 0$ and T=0 are required to complete polarization.

In Fig.6.17, we study the effect of e-p interaction on $P_{\uparrow,\downarrow}$ both in the absence and presence of a magnetic field. It is observed that $P_{\uparrow,\downarrow}$ shows a periodic pattern with a period 2π It is important to point out that the polaronic interaction increases the spin-polarization. The inset shows the behaviour at $B \neq 0$. As mentioned earlier, the magnetic field influences the spin-up and spin-down oppositely and therefore, the contrast in the variations of $P_{\uparrow,\downarrow}$ is understandable. For completeness, we show the effect of dissipation on $P_{\uparrow,\downarrow}$ in Fig.6.18. Although γ increases the tunneling spin currents J_{\uparrow} and J_{\downarrow} , $P_{\uparrow,\downarrow}$ reduces with increasing γ in both the regions: $0 \leq \phi_{SO} \leq \pi$ and $\pi \leq \phi_{SO} \leq 2\pi$. The presence of a magnetic field (inset) makes the variations different both qualitatively and quantitatively. $|(P_{\uparrow,\downarrow})_{max}|$ becomes larger in both the regions: $0 \leq \phi_{SO} \leq \pi$ and $\pi \leq \phi_{SO} \leq 2\pi$. Though the nature of the variations in the region: $0 \leq \phi_{SO} \leq \pi$ remains essentially the same, in the region: $\pi \leq \phi_{SO} \leq 2\pi$, $\pi \leq 2\pi$, $\pi \leq 2\pi$, seems to be independent of $\pi \leq 2\pi$.

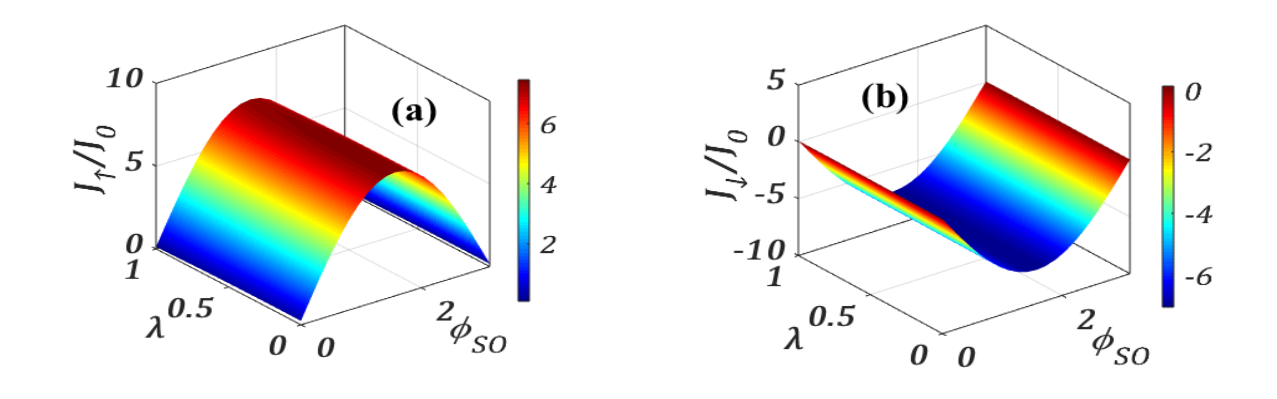


Fig.6.19 Surface plots of (a) J_{\uparrow}/J_0 (b) J_{\downarrow}/J_0 in $\lambda - \phi_{SO}$ plane at $eV_b = 0.5, t_{SD} = 0.2, \gamma = 0.02, \lambda = 0.6, k_B T = 0.5, U = 5 & B = 0.$

Fig.6.19 describes two-dimensional surface plots of spin-polarized current densities J_{\uparrow} and J_{\downarrow} in the $\lambda - \phi_{SO}$ plane at B = 0. Red (blue) and blue (red) colours denote the maxima and

minima of J_{\uparrow} (J_{\downarrow}) respectively. It is clearly visible that J_{σ} is zero at $\phi_{SO}=0$ and $\lambda=0$ and J_{\uparrow} (J_{\downarrow}) has a maximum (minimum) at a particular ϕ_{SO} value. The surface plots show more vividly that J_{\uparrow} and J_{\downarrow} are completely in opposite phase with respect to ϕ_{SO} which again confirms that J_{\uparrow} and J_{\downarrow} are separated entirely by RSOI at B=0.

We show in Fig.6.20, the contour plot of the total differential conductance G at a finite T and a fixed set of SMT parameters in the $(B - \phi_{SO})$ – plane in the absence and presence of e-p interaction. There exists a qualitative difference between the plots for $\lambda = 0$ and for $\lambda \neq 0$. For $\lambda = 0$ (Fig.6.20(a)), G_{max} (deep red) is concentrated at low ϕ_{SO} and low B and G starts decreasing as ϕ_{SO} and B increase showing a minimum (deep blue) at a particular region of ϕ_{SO} and B. Interestingly, Fig.6.20(b) suggests that for $\lambda \neq 0$, G goes from a positive to a negative value at a certain critical value of B. The figure also shows an approximately equal distribution of red and blue colours separated into two halves indicating two different spin-polarized conductances. However, the number of contour lines in the two halves are not equal, which again suggests that the external magnetic field acts on the spin-up and spin-down electron transport differently. The splitting between the spin-up and spin-down conductance becomes much more prominent in the presence of e-p interaction. This observation is supported by Fig.6.17 where we can see that the e-p interaction increases the spin-polarization.

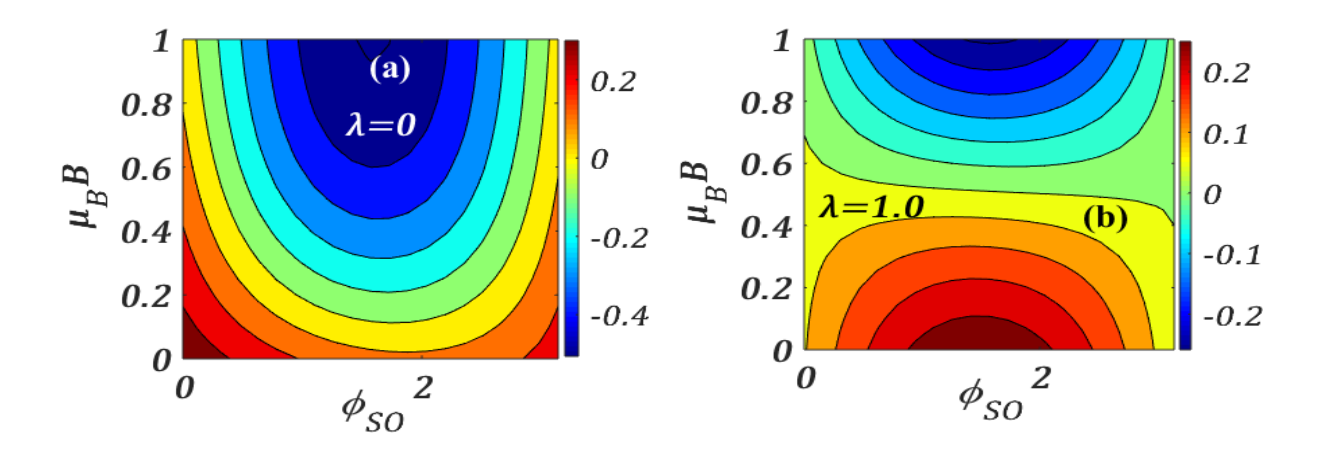


Fig.6.20 Contour plots of total differential conductance $G = \sum_{\sigma} dJ_{\sigma}/dV_b$ in $\mu_B B - \phi_{SO}$ space at $eV_b = 0.5, t_{SD} = 0.2, \gamma = 0.02, k_B T = 0.5, U = 5$ for (a) $\lambda = 0$ and (b) $\lambda = 1.0$.

Finally, the surface plots of spin-polarization $P_{\uparrow,\downarrow}$ are shown in the $\mu_B B - \phi_{SO}$ plane in Fig.6.21. Fig.6.21(a) gives results for $T \neq 0$ and 6.21(b) provides those for T = 0. We choose $k_B T = 0.5$ in Fig.6.21(a), as we have used this value for most of our graphs. The figure reveals that $P_{\uparrow,\downarrow}$ has a maximum at a particular set of ϕ_{SO} and B. Fig.6.21(b) shows that $P_{\uparrow,\downarrow}$ is more significant at T = 0. At T = 0, $P_{\uparrow,\downarrow}$ exhibits a sharp peak at a certain combination of

 ϕ_{SO} and B and the peak value is $P_{\uparrow,\downarrow,max} = 1$. This can be understood from the inset of Fig.6.15 where we observe the same behaviour at T = 0.

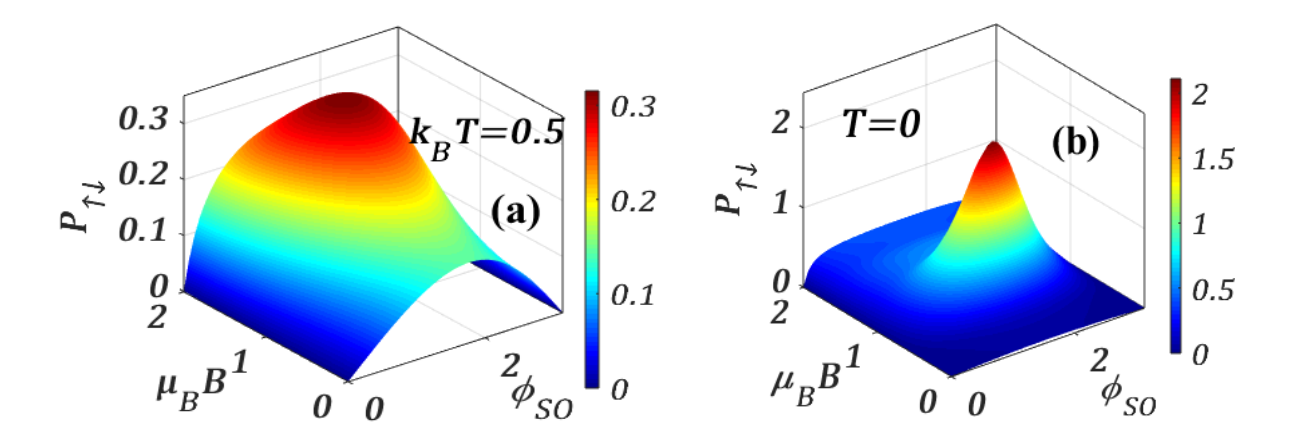


Fig.6.21 Surface plots of spin-polarization $P_{\uparrow,\downarrow}$ in $\mu_B B - \phi_{SO}$ plane at $eV_b = 0.5$, $t_{SD} = 0.2$, $\gamma = 0.02$, $\lambda = 0.6$, U = 5 (a) $k_B T = 0.5$ and (b) T = 0.

6.4 CONCLUSIONS

To summarize, we have studied the effects of RSOI (measured by ϕ_{SO}) on the nonequilibrium transport of a dissipative single molecular transistor system where a single-level QD is embedded in a closed loop connected to two metallic leads so that transport occurs through two paths, one of which contains the QD. We consider the QD electrons to have the Holstein-Hubbard interactions and also the Rashba coupling. To reduce the effect of e-p coupling we introduce a dissipation term which can arise from the interaction of the OD phonon with the substrate phonons. This coupling is modelled by the linear Caldeira-Leggett Hamiltonian and the whole system is modelled by the Anderson-Holstein-Caldeira-Leggett Hamiltonian together with the RSOI and transport properties are calculated at finite temperature by Keldysh method. It is shown that without any external field, tunneling current gets decoupled completely by RSOI into spin-up and spin-down currents that are opposite in phase with respect to RSOI strengths. They are also 2π -periodic with respect to ϕ_{SO} both in the absence and presence of the magnetic field. This SO interaction induced splitting between spin-up and spin-down currents and conductances can be tuned through the external gate voltage and a spatial magnetic field. We observe that the magnetic field influences the effects of e-p and RSO interactions on the spin-up and spin-down components differently. It also wipes out the phase correlation between the spin-up and spin-down conductances leading to complete separation of spin-up and spin-down spectra with no crossover. We also show that the dissipation originating from the QD-bath phonons interaction enhances the spin-resolved

current, but the spin-polarization with respect to RSOI decreases with increasing dissipation in the absence of an external magnetic field. However, the change in the variations of spin-polarization is not significant as we turn on the magnetic field for the given set of parameters.

Though the e-p interaction usually restricts the flow of conduction electron owing to polaron formation, in the presence of RSOI, the spin-polarized conductances (G_{\uparrow} and G_{\downarrow}) do not always decrease with increasing λ in the absence of the magnetic field. G_{\uparrow} (G_{\downarrow}) decreases (increases) with increasing λ in the window: $0 \le \phi_{SO} \le \pi$ and increases (decreases) with increasing λ in the window: $\pi \le \phi_{SO} \le 2\pi$. There exists a phase correlation between G_{\uparrow} and G_{\downarrow} at zero magnetic field. Interestingly, in the presence of a magnetic field, this phase correlation is broken and G_{\uparrow} reduces as λ increases for all values of RSOI, but G_{\downarrow} does not change much which again confirms that magnetic field acts differently on spin-up and spin-down components. This suggests that the effects of RSO and e-p interactions on spin-transport get correlated through the external magnetic field. The spin resolved conductance is also 2π -periodic with respect to ϕ_{SO} .

Finally, we have studied the variation of spin-polarization $P_{\uparrow,\downarrow}$ as a function of RSOI for different ranges of the magnetic field, temperature, and e-p interaction. Like currents and conductances, the spin-polarization is also 2π -periodic with respect to ϕ_{SO} . We have shown that $|P_{\uparrow,\downarrow}|$ increases with the external magnetic field at a finite temperature while it reduces with increasing temperature at a finite field. The polaronic interaction enhances the phenomenon of separation of up and down spins and consequently $|P_{\uparrow,\downarrow}|$ increases significantly in the presence of e-p interaction. Our study predicts that though RSOI alone can produce a spin-filtering effect (without any external field), a fully spin-polarized (i.e., $P_{\uparrow,\downarrow,max}=1$) transport can be achieved only at T=0 and a reasonably large magnetic field for a particular strength of RSOI. From the above conditions, one can determine experimentally the value of RSOI strength at which the maximum spin-polarization can occur.

Our results may find important applications in the fabrication of stronger spin-filtering devices in which the spin-filtering can be tuned by controlling the external magnetic field, RSOI and the e-p interaction in different temperature regimes.

REFERENCES

- 1. I. Žutić, J. Fabian, and S. D. Sarma, Rev. Mod. Phys. 76, 323 (2004).
- 2. S. A. Wolf et al., Science 294, 1488 (2001).

- 3. G. A. Prinz, *Science* **282**, 1660 (1998).
- 4. J. Schliemann, M. Lee, J.C. Egues and D. Loss, Phys. Rev. Lett. 90, 146801 (2003).
- 5. S. Murakami, N. Nagaosa, and S.-C. Zhang, Science 301, 1348 (2003).
- D. Culcer, J. Sinova, N. A. Sinitsyn, T. Jungwirth, A. H. Mac-Donald, and Q. Niu, *Phys. Rev. Lett.* 93, 046602 (2004).
- 7. L. P. Rokhinson, V. Larkina, Y. B. Lyanda-Geller, L. N. Pfeiffer, and K. W. West, *Phys. Rev. Lett.* **93**, 146601 (2004).
- 8. A. Boda and A. Chatterjee, *Physica E* **45**, 36 (2012).
- 9. P. J. Monisha, I.V. Sankar, S. Sil and A. Chatterjee, Sci. Rep. 6, 20056 (2016).
- 10. K. Bhattacharyya, D. Debnath, A. Chatterjee, *J. Magn. Magn Mater.* **506**, 166745 (2020).
- 11. E. I. Eashba and AI. L. Efros, Phys. Rev. Lett. 91, 126405 (2003).
- 12. N. Hatano, R. Shirasaki, and Hiroaki Nakamura, Phys. Rev. A 75, 032107 (2007).
- 13. S. M. Badalyan, A. M. Abiague, G. Vignale, J. Fabian, *Phys. Rev. B* **79**, 205305 (2009).
- 14. S. Datta and B. Das, Appl. Phys. Lett. 56, 665 (1990).
- 15. A. Aviram, M. A. Ratner, *Chem. Phys. Lett.* **29**, 277(1974).
- 16. S. Datta, *Electronic Transport in Mesoscopic Systems*. (Cambridge University Press, 1997).
- 17. S. Datta, *Quantum Transport: Atom to Transistor* (Cambridge University Press, 2005).
- 18. L. P. Mickael, B. Enrique and Herre S. J. van der Zant, Chem. Soc. Rev. 44, 902 (2015).
- 19. L. Li, W. Y. Lo, Z. Cai, N. Zhang, L. Yu, Chem. Sci. 7, 3137 (2016).
- 20. S. J. Ray, J. Appl. Phys. 118, 034303 (2015).
- 21. J.C Cuevas and E. Scheer, Ch.15 Single-molecule transistors: Coulomb blockade and Kondo physics, *Molecular Electronics: An Introduction to Theory and Experiment*, (World Scientific, 2017).
- 22. J. Park et al., *Nature* **417**, **p.** 722-725 (2002).
- 23. D. G. Gordon et al., Nature 391, 156 (1998).
- 24. W. Liang, M. P. Shores, M. Bockrath, J. R. Long, and H. Park, *Nature* **417**, 725 (2002).
- 25. G. Gonzalez, M. N. Leuenberger, E. R. Mucciolo, *Phys. Rev. B* **78**, 054445 (2008).
- 26. D. Bing, X. L. Lei, *Phys. Rev. B* **63**, 235306 (2001).
- 27. M. C. Luffe, J. Koch, F. von Oppen, *Phys. Rev. B* 77, 125306–7 (2008).
- 28. Y. Meir, N. S. Wingreen, P. A. Lee, *Phys. Rev. Lett.* **66**, 3048 (1992).
- 29. A. P. Jauho, N. S. Wingreen. Y. Meir, *Phys. Rev. B* **50**, 5528 (1994).

- 30. Z. Z. Chen, R. Lü, B. F. Zhu, *Phys, Rev. B* **71**, 165324 (2005).
- 31. A. Khedri, T. A. Costi, V. Meden, *Phys. Rev. B* **98**, 195138 (2018).
- 32. Ch. N. Raju and A. Chatterjee Sci. Rep. 6, 18511 (2016).
- 33. M. Kalla, Ch. N. Raju, A. Chatterjee, Sci. Rep. 9, 16510 (2019).
- 34. F. Mireles and G. Kirczenow, *Phys. Rev. B* **66**, 024426 (2001).
- 35. M. H. Larsen, A. M. Lunde, and K. Flensberg, Phys. Rev. B 66, 033304 (2002).
- 36. M. Cahay and S. Bandyopadhyay, *Phys. Rev. B* **68**, 115316 (2003).
- 37. M. Cahay and S. Bandyopadhyay, *Phys. Rev. B* **69**, 045303 (2004).
- 38. S. Bandyopadhyay and M. Cahay, *Introduction to Spintronics* (2nd edition, CRC press, 2015).
- 39. M. Zarea, S. E. Ulloa, and N. Sandler, Phys. Rev. Lett. 108, 046601 (2012).
- 40. J. Moser, A. Matos-Abiague, D. Schuh, W. Wegscheider, J. Fabian, and D. Weiss, *Phys. Rev. Lett.* **99**, 056601 (2007).
- 41. M. W. Wu, J. Zhou, and Q. W. Shi, Appl. Phys. Lett. 85, 6 (2004).
- 42. F. Mahfouzi, N. Nagaosa, and B. K. Nikolic', Phys. Rev. Lett. 109, 166602 (2012).
- 43. J. R. Petta, S. K. Slater, and D. C. Ralph, *Phys. Rev. Lett.* **93**, 13 (2004).
- 44. Q-feng Sun, J. Wang and H. Guo, Phys. Rev. B 71, 165310 (2005).
- 45. M. Kamenetska, J. R. Widawsky, M. Dell'Angela, M. Frei, V. Latha, *J. Chem. Phys.* **146**, 092311 (2017).
- 46. R. G. Alvar, W. Lejia, D. B. Enrique, A. N. Christian, *Nature. Comm*, **7**, **11595** (2016).
- 47. M. Kalla, Ch. Narasimha Raju, A. Chatterjee, Sci. Rep. 11, 10458 (2021).
- 48. M. Kalla, Ch. Narasimha Raju, A. Chatterjee, Sci. Rep. 12, 9444 (2022).
- 49. L. V. Keldysh, Sov. Phys. JETP 20, 1018 (1965).
- 50. A. O. Caldeira, A. J. Leggett, Ann. of phys. 149, 374 (1983).
- 51. I. G. Lang, Yu. A. Firsov, Sov. Phys. JETP 16, 1301 (1962).

CHAPTER 7

SUMMARY AND CONCLUSIONS

To summarize, we have studied in this thesis, the effects of e-e, e-p and SO interactions in different LDS such as QDs, QR, Metal-Semiconductor interface and SMT.

In **Chapter 1**, we have introduced the basic concepts relevant to the studies undertaken in the thesis and also different models used in our work. For example, we have discussed the subject of LDS, polarons, the Fröhlich and Holstein models, Persistent current in LDS, e-e interaction and the Hubbard model, the Rashba and Dresselhaus spin-orbit interactions and SMT.

In Chapter 2, we have studied the effect of RSOI on the polaron self-energy corrections for the GS and the first ESs of a 2D polar PQD with an arbitrary size using an all-coupling variational theory. It is observed that the two-fold spin degeneracy of the first ESs is substantially lifted by RSOI in the absence of a magnetic field (B). However, the GS does not show any such splitting. Similar results are also seen for the bound polaron problem. Application of our theory to a GaAs QD suggests that the self-energies of both free and bound polarons and spin-splitting are considerably large for small QDs making them a pure quantum effect. However, polaronic self-energies remain unaffected by RSOI. To study the interplay of RSOI and e-p interaction, we next studied the same system in the presence of a magnetic field B and obtained the polaronic corrections for GS and the first ESs using the 2nd-order RSPT. In contrast to the B=0 case, we see a strong influence of RSOI on the polaronic corrections in a sufficiently high magnetic field. In GaAs and CdS QDs, it is found that the effects of e-p interaction and RSOI on Zeeman splitting (ZS) are opposite and both are size-dependent. While the e-p interaction suppresses ZS, RSOI enhances it. Although, the enhancement of ZS by RSOI is much small for the chosen set of parameters, but it can be enhanced by increasing the RSOI strength through a gate voltage. Thus, in summary, RSOI prevents the suppression of ZS caused by e-p interaction in a polar QD. Our theory can be applied to magneto-optical experiments to observe some interesting effects.

In **Chapter 3**, we have studied the electron transport across a metal-semiconductor junction with a delta-function interface potential $(\Delta\delta(x))$ in the presence of both RSOI and DSOI. We have calculated the reflection and transmission coefficients and the experimentally measurable quantities like spin-polarized current densities and differential conductance using

discontinuous boundary conditions. In the presence of both SOIs, DSOI reduces the angle of refraction of the spin-up and spin-down electrons while RSOI increases the same, but the reduction due to DSOI is much larger than the increase due to RSOI and hence the spinsplitting angle increases in the presence of DSOI. We have shown that the increase in the incident electron energy decreases the angle of refraction of the spin-up electrons, while it increases that of the spin-down electrons which is completely opposite to the $\Delta = 0$ case. In the $\Delta \neq 0$ case, the variations of spin-up (T_{\uparrow}) and spin-down (T_{\downarrow}) refraction coefficients and correspondingly the currents J_{\uparrow} and J_{\downarrow} with respect to RSOI show some discontinuities at lower values of DSOI which are absent at Δ = 0. RSOI and DSOI have contrasting effects on G_{\uparrow} and G_{\downarrow} ; while RSOI increases G_{\uparrow} and G_{\downarrow} , DSOI suppresses them. The presence of the infinite interface potential causes a significant reduction in T_{\uparrow} , T_{\downarrow} , J_{\uparrow} , J_{\downarrow} , G_{\uparrow} and G_{\downarrow} . It is important to mention that in the presence of delta-potential, the reflection coefficients R_{\uparrow} and R_{\downarrow} become independent of α and β and consequently, reflected spin polarization P_{I}^{Refr} becomes zero as a function of SOIs. The refracted spin polarization P_I^{Refr} , however, has a strong dependence on SOIs at a finite Δ . We have shown that in the presence of both SOIs, P_I^{Refr} is considerably large at large α and small β . One of the important observations of this study is that the presence of delta potential does not have any effect on the magnitude of spin filtering.

In Chapter 4, the role of DSOI on the PCs in a mesoscopic QR threaded by an externally applied A-B flux in the presence of the e-p interaction and onsite Coulomb interaction has been studied. It is shown that both the GS and PCC (I_{PC}) are periodic with respect to A-B flux. PCC is enhanced significantly by DSOI. Both the e-e interaction and e-p interaction participate in reducing PCC leading to a resistive effect. But the e-p interaction inhibits the conduction more strongly than the e-e interaction. In the presence of temperature T, the PCC falls more rapidly with e-e interaction than at T = 0. We have also shown that the suppression of PCC by the NN e-p interaction is stronger than that by the onsite e-p interaction. The PCC exhibits as a function of e-p interaction (g1 or g2) a peak at a finite temperature. In the case of PSC (I_{PC}^{σ}) , DSOI enhances spin-up and spin-down currents and the hence the spin-current splitting gap (ΔI_{PC}^{σ}) considerably. The spin currents change both quantitatively and qualitatively in the presence of interactions. Interestingly, as we turn on the interactions and temperature, ΔI_{PC}^{σ} reduces and number of zero-splitting points increases. However, the spin-splitting can be enhanced in a material with large DSOI strength and can be tuned by the A-B flux, temperature and all the other interactions present in the system.

In Chapter 5, the combined effect of magnetic field (B) and temperature (T) on the quantum transport in an SMT system has been investigated by the Keldysh method in the presence of e-p interaction, e-e correlation and dissipation. It is found that magnetic field (B) and temperature (T) have contrasting roles on transport properties. While the magnetic field increases the height of the spectral function and broadens the separation between the spin-up and the spin-down peaks, temperature reduces the spectral density and the spin splitting. Both B and T reduce the current and the conductance as expected. The e-p coupling and dissipation have interesting effects on the transport properties in different regimes of the magnetic field and temperature. Interestingly, the spectral function is reduced by the e-p interaction and damping at low T and low B while at high T and high B, it is enhanced by polaronic interaction and damping. It is also shown that due to polaronic effect, side peaks develop in the spectral function which become shorter as T rises, although at high T and high B, they again reappear. At $T \neq 0$, the e-p interaction reduces the tunneling current and conductance much more in the presence of a magnetic field than in the absence of it. Although the enhancement of the tunneling current by damping becomes more pronounced at a non-zero B, a sufficiently high field suppresses this effect. The differential conductance is reduced by damping at $T \neq 0$ (more prominently at high T) and $B \neq 0$. It is also shown that e-p interaction increases the spin-polarization up to a certain T. In general, magnetic field favours the spin-polarization and temperature reduces it. It is important to mention that the temperature effect dominates over the magnetic field. This work can have potential application as a spin-filter which can be tuned by temperature and magnetic field.

In Chapter 6, we have extended our work of Chapter 5 by incorporating RSOI to study the zero-field spin-filtering effect in SMT. Instead of considering a linear metal-QD-metal structure, we have considered a closed loop in which QD is embedded in one path of the loop and the other path is directly connected to the other metallic leads. The QD electrons experience the Holstein-Hubbard interactions and RSOI. The metallic electrons travel through two different paths and give rise to a RSOI-phase ϕ_{SO} while going through the QD. We have shown that the tunneling current gets decoupled by RSOI into spin-up (I_{\uparrow}) and spindown (I_{\perp}) currents even in the absence of any external magnetic field. The currents are opposite and 2π -periodic with respect to ϕ_{SO} both in the absence and presence of the magnetic field. We have also shown that the dissipation originating from the interaction between the QD phonon and the bath phonons enhances both J_{\uparrow} and J_{\downarrow} . It is observed that the magnetic field influences the effects of e-p and RSO interactions on the spin-up and spindown components differently and also wipes out the phase correlation between the spin-up (G_1) and spin-down (G_1) conductances leading to complete separation of spin-up and spindown conductance with no crossover. Though the e-p interaction usually restricts the flow of conduction electron owing to polaron formation, in the presence of RSOI, the spin-polarized conductances do not always decrease with increasing λ in the absence of the magnetic field.

Interestingly, in the presence of a magnetic field, G_{\uparrow} reduces as λ increases for all values of RSOI, but G_{\downarrow} does not change much which again confirms that magnetic field acts differently on spin-up and spin-down components. This suggests that the effects of RSO and e-p interactions on spin-transport get correlated through the external magnetic field. The SOI induced splitting between spin-up and spin-down currents and conductances can be tuned through the external gate voltage and magnetic field. Like currents and conductances, the spin-polarization $P_{\uparrow,\downarrow}$ is also 2π -periodic with respect to ϕ_{SO} . We have shown that $|P_{\uparrow,\downarrow}|$ increases with the external magnetic field at a finite temperature while it reduces with increasing temperature at a finite field. The polaronic interaction enhances $|P_{\uparrow,\downarrow}|$ significantly. Our study predicts that although RSOI alone can produce a spin-filtering effect (without any external field), a fully spin-polarized (i.e., $P_{\uparrow,\downarrow,max} = 1$) transport can be achieved only at T =0 and a reasonably large magnetic field for a particular strength of RSOI. From the above conditions, one can determine experimentally the value of RSOI strength at which the maximum spin-polarization can occur. Our results may find important applications in the fabrication of stronger spin-filtering devices in which the spin-filtering can be tuned by controlling the external magnetic field, RSOI and the e-p interaction in different temperature regimes.



"Ever Tried.
Ever Failed.
No matter.
Try again.
Fail again.
Fail better."

Samuel Beckett



Effects of electron-electron, electron-phonon and spin-orbit interactions in low-dimensional systems

by Kuntal Bhattacharyya

Submission date: 30-Dec-2022 09:27AM (UTC+0530)

Submission ID: 1987396297

File name: Thesis-Kuntal_Bhattacharyya-16PHPH03.pdf (6.95M)

Word count: 47559 Character count: 219384

Effects of electron-electron, electron-phonon and spin-orbit interactions in low-dimensional systems

ORIGINALITY REPORT

SIMILARITY INDEX

INTERNET SOURCES

PUBLICATIONS

STUDENT PAPERS

PRIMARY SOURCES

Internet Source This similarity percentage is from candidate's own publication available as a preprint

4%

Kuntal Bhattacharyya, Manasa Kalla, Ashok Chatterjee. "Temperature dependent nonequilibrium magneto-transport in a correlated polar single molecular transistor with quantum dissipation", Journal of Applied Physics, 2022

Publication

Kuntal Bhattacharyya, Debika Debnath, Ashok Chatterjee. "Role of Rashba spin-orbit interaction on polaron Zeeman effect in a two-dimensional quantum dot with parabolic confinement", Journal of Magnetism and Magnetic Materials, 2020 **Publication**

SCHOOL OF PHYSICS SCHOOL OF HYDERABAD UNIVERSITY OF HYDERABAD LIYDERABAD - 500 046. INDIA

Prof. ASKOK CHATTERJEE SCHOOL OF PHYSICS UNIVERSITY OF HYDERABAD TIYDERABAD - 500 046. INDIA

Kuntal Bhattacharyya, Debika Debnath, Ashok Chatterjee. "Role of Rashba Spin-orbit Interaction on Polaron Zeeman Effect in a Two-dimensional Quantum Dot with Parabolic

The total similarity inder is

SCHOOL OF PHYSICS UNIVERSITY OF HYDERABAD

Confinement", Journal of Magnetism and Magnetic Materials, 2020

Publication

5	www.ncbi.nlm.nih.gov Internet Source	1%
6	Submitted to University of Hyderabad, Hyderabad Student Paper	1 %
7	mafiadoc.com Internet Source	1 %
8	Manasa Kalla, Narasimha Raju Chebrolu, Ashok Chatterjee. "Quantum transport in a single molecular transistor at finite temperature", Scientific Reports, 2021	<1%
9	link.springer.com Internet Source	<1%
10	Manasa Kalla, D. Sanjeev Kumar, Shreekantha Sil, Ashok Chatterjee. "Double refraction of electron spin across a metal-semiconductor junction with Rashba and Dresselhaus spinorbit interactions: A stronger spin-filtering effect", Superlattices and Microstructures, 2021 Publication	<1%
11	Anastassakis, E M, and J D Joannopoulous. "The Physics of Semiconductors: 20th	<1%

"The Physics of Semiconductors: 20th

International Conference", The Physics of Semiconductors, 1990.

Publication

12	es.scribd.com Internet Source	<1%
13	P. J. Monisha, I. V. Sankar, Shreekantha Sil, Ashok Chatterjee. "Persistent current in a correlated quantum ring with electron- phonon interaction in the presence of Rashba interaction and Aharonov-Bohm flux", Scientific Reports, 2016 Publication	<1%
14	"Introduction to the Physics of Diluted Magnetic Semiconductors", Springer Science and Business Media LLC, 2010 Publication	<1%
15	"Spin Physics in Semiconductors", Springer Science and Business Media LLC, 2017 Publication	<1%
16	Handbook of Spintronics, 2016. Publication	<1%
17	Submitted to University of Sydney Student Paper	<1%
18	Wu, M.W "Spin dynamics in semiconductors", Physics Reports, 201008 Publication	<1%

- Miodrag L. Kulić. "Interplay of electronphonon interaction and strong correlations: the possible way to high-temperature superconductivity", Physics Reports, 2000
- <1%

dokumen.pub

<1%

Debika Debnath, Kuntal Bhattacharyya, Ashok Chatterjee. "A semi-exact study of self-trapping transition in a one-dimensional Holstein-Hubbard model", Physica B:

Condensed Matter, 2022

Prof. ACHOOL OF MINSICS

Debika Debnath, M. Zahid Malik, Ashok Chatterjee. "A semi exact solution for a metallic phase in a Holstein-Hubbard chain at half filling with Gaussian anharmonic phonons", Scientific Reports, 2021

<1%

SOMA MUKHOPADHYAY, ASHOK CHATTERJEE.
"PHONON INDUCED SUPPRESSION OF THE
ZEEMAN SPLITTING IN POLAR
SEMICONDUCTOR QUANTUM DOTS: A
QUANTUM SIZE EFFECT", International Journal
of Modern Physics B, 2012

<1%

Publication

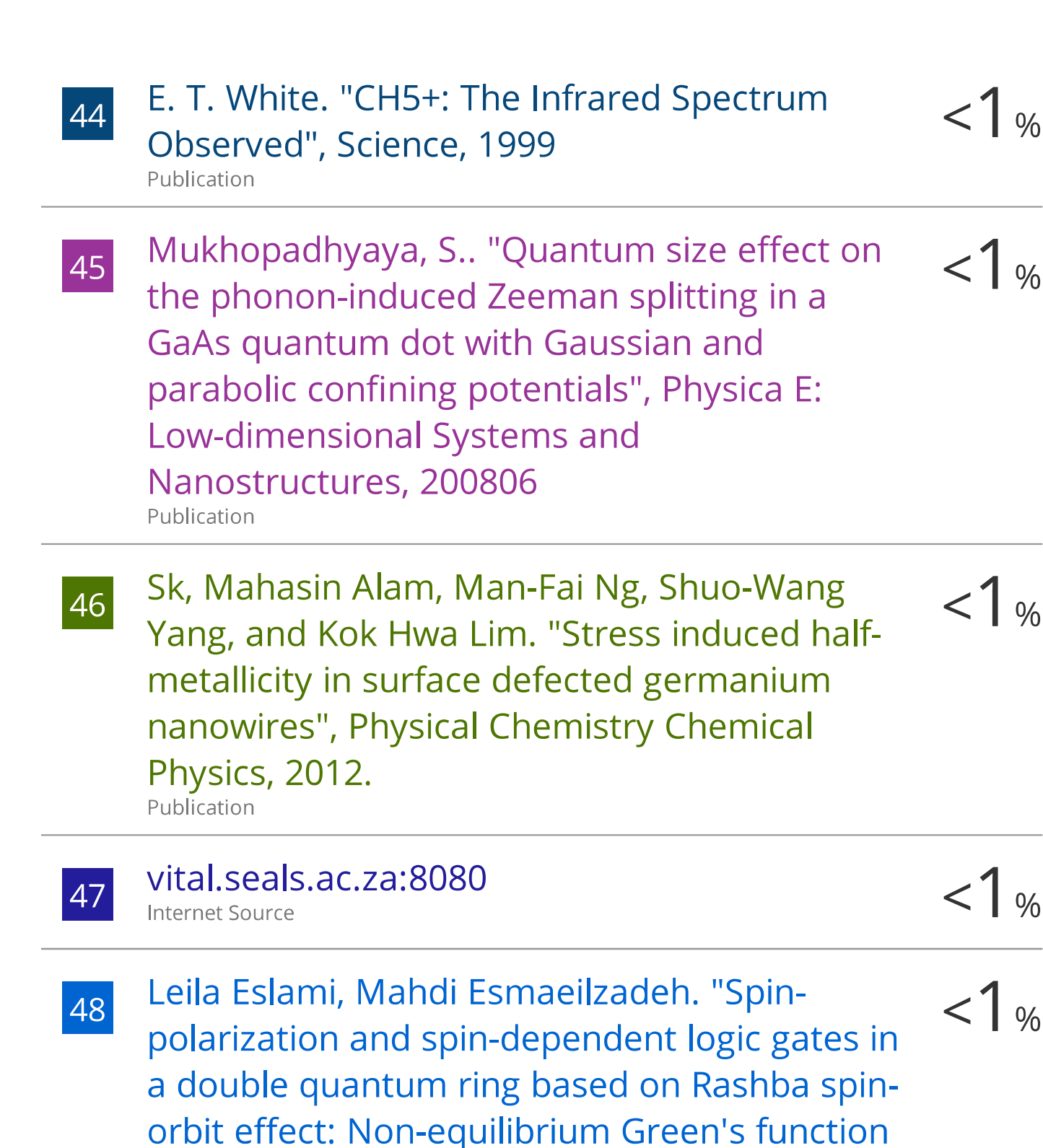
idr.nitk.ac.in

Internet Source

36

Igor Žutić. "Spintronics: Fundamentals and <1% 31 applications", Reviews of Modern Physics, 04/2004 Publication Manasa Kalla, Narasimha Raju Chebrolu, <1% 32 Ashok Chatterjee. "Transient dynamics of a single molecular transistor in the presence of local electron-phonon and electron-electron interactions and quantum dissipation", Scientific Reports, 2022 Publication I.V. Sankar, P J Monisha, Shreekantha Sil, <1% 33 Ashok Chatterjee. "Persistent current and the existence of a metallic phase flanked by two insulating phases in a quantum ring with both electron-electron and electron-phonon interactions", Physica E: Low-dimensional Systems and Nanostructures, 2015 Publication chineseinwhiterock.drillionnet.com <1% Internet Source Luca Chirolli, Guido Burkard. "Decoherence in 35 solid-state qubits", Advances in Physics, 2008 Publication

37	Soma Mukhopadhyay. Journal of Physics Condensed Matter, 03/08/1999 Publication	<1 %
38	Foundations of Engineering Mechanics, 2016. Publication	<1%
39	Phani Murali Krishna, R.P.M "Effect of electron-phonon interaction on the electronic properties of an axially symmetric polar semiconductor quantum wire with transverse parabolic confinement", Physica B: Physics of Condensed Matter, 20050415 Publication	<1%
40	modis.marine.usf.edu Internet Source	<1%
41	www.scribd.com Internet Source	<1%
42	Cao, X "An alternative mechanism for current-induced antisymmetric lateral edge spin accumulations in ballistic two-dimensional electron gases", Physics Letters A, 20080303 Publication	<1 %
43	D. S. L. Abergel. "Properties of graphene: a theoretical perspective", Advances In Physics, 07/2010 Publication	<1 %



Ch Uma Lavanya, Ashok Chatterjee.
"Persistent charge and spin currents in the 1D
Holstein-Hubbard ring at half filling and at

approach", Journal of Applied Physics, 2014

Publication

away from half filling by Bethe-ansatz approach", Physica E: Low-dimensional Systems and Nanostructures, 2021

	- Delication	
50	Kuntal Bhattacharyya, Ashok Chatterjee. "Polaronic and bound polaronic effects in the energy states of an electron in a two-dimensional parabolic quantum dot in the presence of Rashba spin-orbit interaction", AIP Publishing, 2019 Publication	Prof. ASE OK CHAITED SCHOOL OF PHYSIC UNIVERSITY OF HYDER HYDERABAD - 500 CHA
51	Soma Mukhopadhyay. "Suppression of Zeeman splitting in a GaAs quantum dot", Physical Review B, 03/1999 Publication	<1%
52	hdl.handle.net Internet Source	<1%
53	www.tapeworld.co.kr	<1%
54	Yanar, S "Polaronic effects in a Gaussian quantum dot", Superlattices and Microstructures, 200803	<1%
55	profdoc.um.ac.ir Internet Source	<1%
56	wrap.warwick.ac.uk Internet Source	<1%

- Barbara Wirthl, Sebastian Brandstaeter, Jonas Nitzler, Bernhard A. Schrefler, Wolfgang A. Wall. "Global sensitivity analysis based on Gaussian process metamodelling for complex biomechanical problems", International Journal for Numerical Methods in Biomedical Engineering, 2022

 Publication
- KRISTOPHER R. SCHUMACHER.

 "Homogeneous turbulence in ferrofluids with a steady magnetic field", Journal of Fluid

 Mechanics, 03/2008

 Publication

<1%

<1%

<1%

- R. Khordad, H. Bahramiyan. "Effect of pressure and electron–phonon interaction on optical properties of GaN triangular quantum wires", Optical and Quantum Electronics, 2015
- Ch. Uma Lavanya, Ashok Chatterjee.
 "Persistent Charge and Spin Currents in the
 1D Holstein-Hubbard ring at half filling and at
 away from half filling by Bethe-ansatz
 approach", Physica E: Low-dimensional
 Systems and Nanostructures, 2020
 Publication
- X W Zhang. "Hole Rashba effect and *g*-factor in InP nanowires", Journal of Physics D Applied Physics, 01/21/2007

62	archive.org Internet Source	<1%
63	lib.dr.iastate.edu Internet Source	<1%
64	"Adaptive and Natural Computing Algorithms", Springer Science and Business Media LLC, 2005 Publication	<1%
65	ebin.pub Internet Source	<1%
66	pure.tue.nl Internet Source	<1%
67	acikbilim.yok.gov.tr Internet Source	<1%
68	www.gymhjp.com Internet Source	<1%
69	Atef Boulila. "dynamique des systémes de solides ", Centre de publication universitaire	<1%
70	G.S. Kliros, P.C. Divari. "Beating of the oscillations in the magnetocapacitance of a MODFET with Rasba spin-orbit interaction", Microelectronics Journal, 2007 Publication	<1%

71

I. V. Sankar, Ashok Chatterjee. "Self-trapping phase diagram for the strongly correlated extended Holstein-Hubbard model in two-dimensions", The European Physical Journal B, 2014

<1%

Publication

Exclude quotes On

Exclude bibliography

Exclude matches

< 14 words